VNIVERSITAT DE VALÈNCIA

Numerical relativity simulations of tilted black hole-torus systems

Vassilios Mewes

Departament d'Astronomia i Astrofísica
Universitat de València

TESIS DOCTORAL

Directores:
José Antonio Font Roda
Pedro J. Montero Muriel

2016

JOSÉ ANTONIO FONT RODA, Profesor Titular de Astronomía y Astrofísica de la Universitat de València

y

PEDRO J. MONTERO MURIEL, Investigador Postdoctoral del Max-Planck-Institut für Astrophysik (Garching, Alemania)

CERTIFICAN:

Que la presente memoria, titulada *Numerical relativity simulations of tilted black hole–torus systems*, ha sido realizada en el Departamento de Astronomía y Astrofísica de la Universitat de València por Vassilios Mewes bajo su dirección y constituye su Tesis Doctoral para optar al grado de Doctor en Ciencias Físicas.

Valencia, 26 de Mayo de 2016

Fdo: José Antonio Font Roda Fdo: Pedro J. Montero Muriel

Für Evelyn.

Acknowledgements

This project would have never come to an end (or even started) had it not been for all the people who helped and guided me along the way.

First and foremost, I would like to thank my thesis supervisors, Prof. Toni Font and Dr. Pedro Montero, for all their help, encouragement and guidance throughout my doctoral studies, for suggesting the very interesting topics we have worked on together and for giving me the freedom to explore my own ideas.

I would like to thank the thesis committee and the external examiners for agreeing to review my thesis and for providing me with their valuable comments and corrections to the thesis manuscript.

I would like to thank Prof. Ewald Müller and the Max Planck Institute for Astrophysics for their hospitality during two extended research visits I enjoyed in Garching.

I thank my collaborators Prof. Nikolaos Stergioulas and Dr. Filippo Galeazzi, who have collaborated on the majority of the work presented in this thesis. Filippo has been invaluably supportive during the entire duration of the project and I would have been much more overwhelmed during the early stages of the thesis without his help.

I would like to thank the developers and maintainers of the Einstein Toolkit, for providing the community with their public toolkit for numerical relativistic astrophysics and for their superb support regarding all questions concerning the the toolkit I had during the years.

I thank the Department of Astronomy and Astrophysics at the University of Valencia for its hospitality and excellent work atmosphere, and especially the secretaries Feli and Manel for always helping me with paperwork and the mysterious ways of Spanish bureaucracy. I thank the professors in the department and the postdocs in the group for their help and insightful discussions during my time here.

I thank my office mates and the other PhD students in our group for interesting discussions on the subtleties of Spanish life and grammar, and lunches filled

with laughter, with special thanks going out to Juan Antonio Chistoso. Thanks to my Colombian roommates Alejandro, Andrés, Celso, Diego, and William, I have learnt to speak proper spanish during my time here in Valencia.

My time in Cambridge, which laid the academic foundation my doctoral studies have built upon, would have been much duller had it not been for countless discussions with Audrūnas and Enno, which have fortunately continued to this day.

A big hug to my friends Daniel E., Daniel W., Heike, Jonas, Julian, Lisa, Philipp, Robin, Sarah, Sergej, Sven, and Tabea who were always there for me and have visited me here in Valencia on such numerous occasions.

I thank my family, and especially my parents, for always believing in me and supporting me in all my endeavours and choices I have made. I would not be here if it was not for them.

Finally, I would like to thank you, Evelyn, for all you have done for me! Words fall truly short to express my gratitude for your endless endurance, support and love.

My doctoral studies have been funded by the Spanish Ministry of Science and Innovation (through the FPI-MICINN program). The research has also been funded by the Spanish Ministry of Economy and Competitiveness (MINECO) through grant AYA2013-40979-P, and by the Generalitat Valenciana (PROMETEOII-2014-069).

Abstract

Mergers of compact objects are among the most interesting events of relativistic astrophysics, being, in particular, the prime target for gravitational wave astronomy. In this thesis, we investigate the possible end-states of black hole-neutron star and binary neutron star mergers: thick accretion tori around spinning Kerr black holes. These black hole-torus systems are believed to be the engines of the brightest events in the Universe, so-called gamma-ray bursts. Our understanding of the evolution and stability of these systems relies crucially on accurate numerical relativity simulations of their dynamics, evolving both spacetime and matter fields. The main work in this thesis are such numerical relativity simulations of black hole–torus systems. We use equilibrium models of self-gravitating discs around black holes as initial data, which represent idealised (yet relevant) models of the actual post-merger discs found in self-consistent numerical relativity merger simulations. Traditionally, numerical simulations of these systems have been carried out under the assumption that the black hole spin and disc angular momentum are aligned. There are arguments, however, that many black hole-torus systems should be *tilted* instead, which means that the equatorial plane of the disc is no longer parallel to that of the black hole. These tilted black hole-torus systems form indeed self-consistently in numerical relativity simulations of misaligned black hole-neutron star mergers. In these tilted systems, the dynamics of the torus and black hole change completely as compared to the untilted case due to general relativistic effects arising from the structure of the Kerr spacetime. Specifically, due to differential Lense-Thirring precession, the disc may become *twisted* and *warped*. To capture the correct dynamical response of these effects on the disc evolution, it is therefore necessary to evolve the systems in general relativistic hydrodynamics simulations. Pioneering work in this field has been carried out by Fragile and collaborators, who performed the first relativistic simulations of tilted black hole-torus systems in the test-fluid approximation, which means that the spacetime was held fixed in time and the self-gravity of the disc ignored. Building on this seminal work, we

have performed in this thesis the first systematic study of tilted black hole-torus systems with a fully evolved spacetime. We observe many of the disc morphological features described in the test-fluid simulations of Fragile and collaborators. Additionally, we observe significant black hole precession and nutation as a result of the tilted disc evolution for all disc-to-black hole mass ratios considered in this thesis. The black hole spin direction is measured using a standard method in numerical relativity, which, as we show in this thesis, can be derived from Weinberg's pseudotensor. The black hole precession is seen to arise from the torque the disc exerts as it starts to precess due to the Lense-Thirring torque of the central black hole. When considering a non-rotating black hole, some of our initial models were known to be prone to develop the global, non-axisymmetric hydrodynamic Papaloizou-Pringle instability. We study these models in the tilted case in order to gauge the effect the black hole tilt has on the development of the instability. Our results show that the instability is a very robust feature of this physical system in the sense that it indeed develops for all initial black hole spin magnitudes and tilt angles we investigate. The contrary is also true, namely that a stable initial model remains so for the entire parameter space of the study. We investigate the precise mechanism of the instability and show that it manifests itself in a spiral density wave of constant pattern speed traveling through the differentially rotating disc. The density wave facilitates the outward transport of angular momentum from the inner region of the torus, where it has negative angular momentum with respect to the fluid, as it couples to the fluid via dissipation when its amplitude becomes non-linear and mild shocks develop. Our three-dimensional simulations show the presence of quasi-periodic oscillations in the instantaneous accretion rate, with frequencies in a range compatible with those observed in low mass X-ray binaries with either a black hole or a neutron star component. The frequency ratio of the dominant low frequency peak and the first overtone is $o_1/f \sim 1.9$, a frequency ratio not attainable when modelling the quasi-periodic oscillations as p-mode oscillations in axisymmetric tori.

Resumen

Las fusiones de objetos compactos se encuentran entre los eventos más interesantes de la astrofísica relativista, siendo, en particular, el principal objetivo de la astronomía de ondas gravitatorias. En esta tesis investigamos los posibles estados finales de la fusión de sistemas binarios formados por agujero negro-estrella de neutrones o por dos estrellas de neutrones: discos gruesos (o toros) de acrecimiento alrededor de agujeros negros en rotación tipo Kerr. Estos sistemas agujero negro-toro se cree que constituyen el motor central de los eventos más luminosos del Universo: los llamados estallidos de rayos gamma. Nuestro conocimiento sobre la evolución y la estabilidad de estos sistemas depende crucialmente de la realización de simulaciones numéricas precisas de su dinámica, en el contexto de la relatividad numérica, es decir, tanto el espacio-tiempo como la materia. El principal trabajo de esta tesis es llevar a cabo tales simulaciones en relatividad numérica de sistemas agujero negro-toro. Para ello utilizamos modelos de equilibrio de discos auto-gravitantes alrededor de agujeros negros como datos iniciales, los cuales representan modelos idealizados (aunque apropiados) de los discos post-fusión reales obtenidos de manera auto-consistente en simulaciones de fusión de binarias compactas en relatividad numérica. Tradicionalmente, la simulación numérica de estos sistemas se ha realizado bajo la hipótesis de que el espín del agujero negro y el momento angular del disco están alineados. Sin embargo, existen razones para creer que muchos de estos sistemas deberían estar *inclinados*, lo cual significa que el plano ecuatorial del disco ya no es paralelo al del agujero negro. Ciertamente, sistemas agujero negro-toro inclinados se han obtenido auto-consistentemente en simulaciones de relatividad numérica de la fusión de un agujero negro y una estrella de neutrones con los momentos angulares no alineados. En tales sistemas inclinados, la dinámica del sistema agujero negro-toro cambia completamente con respecto al caso alineado, debido a los efectos de relatividad general que surgen de la estructura del espacio tiempo de la métrica de Kerr. Especialmente, debido a la precesión diferencial de Lense-Thirring, el disco puede l legar a estar *trenzado* y *combado*. Para

capturar la respuesta dinámica correcta de estos efectos en la evolución del disco es necesario evolucionar los sistemas mediante simulaciones hidrodinámicas en relatividad general. El trabajo pionero en este campo fue llevado a cabo por Fragile y colaboradores, quienes realizaron las primeras simulaciones relativistas de sistemas agujero negro-toro inclinados en la aproximación fluido de prueba, es decir, asumiendo que el espacio-tiempo se mantiene inalterado en el tiempo e ignorando la auto-gravedad del disco. Basándonos en este influyente trabajo, hemos realizado en esta tesis el primer estudio numérico sistemático de sistemas agujero negro-toro inclinados en un espacio-tiempo totalmente evolucionado. Nuestro trabajo confirma la mayoría de las características morfológicas del disco descritas en las simulaciones con fluidos prueba de Fragile y colaboradores. Además, nuestros resultados muestran precesión y nutación significativas en el agujero negro como consecuencia de la evolución del disco inclinado para todas las proporciones entre las masas del disco y del agujero negro consideradas en esta tesis. La dirección del espín del agujero negro se mide utilizando un método estándar en relatividad numérica que, como se demuestra en la tesis, puede ser derivado a partir del pseudotensor de Weinberg. Hemos visto que la precesión del agujero negro surge del par de fuerzas que el disco ejerce cuando se inicia su movimiento de precesión debida al par de fuerzas tipo Lense-Thirring del agujero negro central. Por otro lado, simulaciones previas han mostrado que modelos iniciales que involucran agujeros negros sin rotación y sistemas alineados son propensos a desarrollar la inestabilidad global hidrodinámica no axisimétrica de Papaloizou-Pringle. En este trabajo estudiamos estos modelos en el caso inclinado para estimar el efecto que la inclinación del agujero negro tiene sobre el desarrollo de tal inestabilidad. Nuestros resultados muestran que la inestabilidad de Papaloizou-Pringle es una característica muy robusta de nuestro sistema físico puesto que, de hecho, se desarrolla para todas las magnitudes de espín y ángulos de inclinación iniciales investigados. Lo contrario también es cierto, es decir, un modelo inicialmente estable permanece estable para todo el espacio de parámetros considerados en nuestro estudio. En esta tesis investigamos en detalle el mecanismo de la inestabilidad y mostramos que ésta se manifiesta en la forma de una onda de densidad espiral, con una velocidad de patrón constante, que viaja a través del disco que gira con rotación diferencial. Esta onda de densidad facilita el transporte de momento angular hacia afuera desde las regiones internas del toro, donde tiene momento angular negativo con respeto al fluido, acoplándose al fluido mediante disipación una vez su amplitud se vuelve no-lineal y desarrollando choques moderados. Nuestras simulaciones tridimensionales muestran la presencia de oscilaciones cuasi-periódicas en la

tasa de acreción instantánea, con frecuencias en un rango compatible con las observadas en binarias de rayos X de baja masa con la componente compacta siendo o bien una estrella de neutrones o bien un agujero negro. La razón de frecuencias entre el pico de baja frecuencia dominante y el primer armónico es $o_1/f \sim 1.9$, una razón no reproducible cuando se modelan las oscilaciones cuasi-periódicas como modos p de oscilación de toros axisimétricos.

Publications

The following peer-reviewed publications and proceedings reports have been published during the duration of the doctoral fellowship:

- **V. Mewes**, F. Galeazzi, J. A. Font, P. J. Montero and N. Stergioulas,
  On the dynamics of tilted black hole-torus systems,
  Accepted for publication in MNRAS (2016)

- J. Adsuara, I. Cordero-Carrión, P. Cerdá-Durán, **V. Mewes** and M. A. Aloy,
  Optimal Scheduled Relaxation Jacobi method,
  Submitted to Communications in Computational Physics (2016)

- **V. Mewes**, J. A. Font, F. Galeazzi, P. J. Montero and N. Stergioulas,
  Numerical relativity simulations of thick accretion disks around tilted Kerr black holes,
  Phys. Rev. D **93**, 064055 (2016)

- N. Sanchis-Gual, J. C. Degollado, P. J. Montero, J. A. Font and **V. Mewes**,
  Quasistationary solutions of self-gravitating scalar fields around collapsing stars,
  Phys. Rev. D **92**, 083001 (2015)

- **V. Mewes**, J. A. Font and P. J. Montero,
  Measuring the black hole spin direction in 3D Cartesian numerical relativity simulations,
  Phys. Rev. D **91**, 124043 (2015)

- **V. Mewes**, P. J. Montero, N. Stergioulas, F. Galeazzi and J. A. Font,
  General Relativistic Simulations of Accretion Disks Around Tilted Kerr Black Holes,
  in Gravitational Wave Astrophysics,
  Proceedings of the Third Session of the Sant Cugat Forum on Astrophysics (2015)

Contents

List of Figures

List of Tables

Nomenclature

List of Symbols

$\Gamma^{\gamma}_{\alpha\beta}$	Christoffel symbols
x^{μ}	coordinates
$G_{\mu\nu}$	Einstein tensor
$g_{\mu\nu}$	spacetime metric
$\eta_{\mu\nu}$	Minkowski metric
$\mathcal{M}$	spacetime manifold
$R_{\mu\nu}$	Ricci tensor
R	3-dimensional Ricci scalar
${}^{(4)}R$	4-dimensional Ricci scalar
$R_{\alpha\beta\gamma\delta}$	Riemann tensor
$T_{\mu\nu}$	stress-energy tensor
$C_{\alpha\beta\gamma\delta}$	Weyl tensor
α	lapse function
β^{i}	shift vector
γ_{ij}	spatial metric
K_{ij}	extrinsic curvature
Σ_{t}	spacelike hypersurface
$\tilde{A}_{ij}$	conformally related traceless part of extrinsic curvature

ϕ	conformal factor
$\tilde{\gamma}_{ij}$	conformal spatial metric
$\tilde{\Gamma}^i$	conformal connection functions
E	matter energy density
h	specific enthalpy
ϵ	specific internal energy
l	specific angular momentum
W	Lorentz factor
P	pressure
ρ	rest-mass density
D	conserved rest-mass density
s	entropy
S_i	matter momentum density
S_{ij}	matter stress tensor
v^i	three-velocity
u^μ	four-velocity

Acronyms / Abbreviations

ADM	Arnowitt-Deser-Misner
AH	apparent horizon
BH	black hole
BBH	binary black hole
BHNS	black hole–neutron star
BNS	binary neutron star
BSSN	Baumgarte-Shapiro-Shibata-Nakamura
EH	event horizon

EOS equation of state

ET Einstein Toolkit

GRB gamma ray burst

GR General Relativity

GRHD general relativistic hydrodynamics

GRMHD general relativistic magnetohydrodynamics

GW gravitational wave

HRSC high-resolution shock-capturing

IVP initial value problem

LIGO Laser Interferometer Gravitational-Wave Observatory

LT Lense–Thirring

MoL method of lines

MRI magneto-rotational instability

NR numerical relativity

NS neutron star

PDE partial differential equations

PPI Papaloizou-Pringle instability

PPM piecewise parabolic method

QPO quasi-periodic oscillation

RI runaway instability

Part I

Introduction

Chapter 1

Astrophysical background

1.1 The detection of gravitational waves: a new window to the universe

On September 14, 2015 at 09:50:45 UTC, the two advanced Laser Interferometer Gravitational-Wave Observatories (LIGO) detected a transient gravitational wave (GW) signal produced by the merger of two black holes (BHs) [Abbott et al. 2016]. The event was named GW150914. This landmark detection confirmed the existence of GW by their direct observation for the first time. GWs had been predicted by Einstein [1918] as a direct consequence of his theory of general relativity (GR) [Einstein 1915, Einstein 1916]. Previous to the event GW150914, there was only an indirect confirmation of the existence of GWs by the discovery of the binary pulsar PSR B1913+16 [Hulse and Taylor 1975] and its energy loss via GW [Taylor and Weisberg 1982]. While the detection has confirmed yet another prediction of GR, it has also, even more importantly, opened a new window to the observation of the universe, allowing us to study cosmological and astrophysical systems via the GW they emit. Contrary to the electromagnetic messengers that have let us observe the universe so far, there is no opacity for GWs, as they propagate as perturbations of spacetime itself. Among the astrophysical systems to be observed by means of GW are binary BH (BBH) mergers such as the observed event GW150914, as well as BH-neutron star (BHNS) mergers, binary neutron star (BNS) mergers, accretion tori around BH and NS, and core-collapse supernovae, to name but a few.

To estimate parameters from detected signals, it is necessary to model the astrophysical sources and their emission of GW as accurately as possible in order to build large catalogs of waveforms for wide ranges of system parameters. For instance, the dynamics of a BBH coalescence can be divided in three distinct phases: the early inspiral, the actual merger phase and the subsequent ringdown of the remnant to a Kerr BH [Flanagan and Hughes 1998]. While the gravitational waveforms of the inspiral and ringdown can be accurately modelled using the Post-Newtonian formalism and BH perturbation theory, respectively, it is necessary to solve the nonlinear field equations of GR numerically to produce the waveforms of the actual merger phase [Berti, Cardoso, and Will 2006]. In matter spacetimes, such as BNS or BHNS mergers, the calculation of waveforms furthermore depends crucially on the physics used to model the matter.

1.2 Mergers of compact objects and BH–torus systems

Shortly after the first numerical relativity (NR) simulations of a complete BBH orbit presented in Brügmann, Tichy, and Jansen [2004], the first successful multiple orbit NR simulations of the actual merger of a BBH system were achieved in Pretorius [2005a], Campanelli et al. [2006], and Baker et al. [2006]. Since then, ever-growing computational resources and advances in the numerical methods used to simulate these systems have made the exploration of the vast initial parameter space possible (see e.g. Hinder [2010] and references therein for a recent overview of the status of BBH simulations). The initial parameters of BBH simulations are the BH mass ratio and the six components of their initial spin vectors. The investigation of these initial parameters has led to significant discoveries, as the occurrence of the orbital hang-up [Campanelli, Lousto, and Zlochower 2006] and the presence of the so-called super-kicks, where the final BH is displaced from the orbital plane after its formation with a higher speed than predicted by Post-Newtonian estimates. This happens for initial configurations with anti-aligned BH spins that lie in the orbital plane (see Brügmann et al. [2008] and references therein).

Stellar mass BH–torus systems are believed to be the end states of BNS or BHNS mergers, as well as of the rotational gravitational collapse of massive stars[1]. BNS mergers can also form an intermediate, transient structure known

[1]We note that there are more types of mergers that might lead to the formation of post-merger accretion tori, such as BH–white dwarf, NS–white dwarf, and binary white dwarf mergers (see, for instance Fryer et al. [1999], Paschalidis et al. [2011], and Raskin et al. [2012]).

as a hypermassive NS after the merger, whose large differential rotation leads to a delayed collapse to a BH (see, e.g. Shibata et al. [2006]), or to a magnetar (a NS with a extremely strong magnetic field) surrounded by an accretion disc (see, e.g. Giacomazzo and Perna [2013]. Our theoretical understanding of the formation of BH–torus systems and their evolution relies strongly on numerical work. The first BNS mergers in full GR (albeit for simplified matter models) were performed by Shibata and Uryū [2000], and following the BBH breakthrough in 2005, Shibata and Uryū [2006] performed the first NR BHNS mergers. If the NS does not plunge into the BH during the final merger phase of a BHNS binary, but is rather tidally disrupted by the BH, a thick accretion torus can form around the remnant Kerr BH (see Shibata and Taniguchi [2011] and references therein). Thick accretion tori also form in unequal mass BNS mergers (see Faber and Rasio [2012] and references therein). The formation of a thick, massive accretion torus in these systems is of particular interest as the remnant BH–torus system is believed to be a possible gamma-ray burst (GRB) engine [Woosley 1993, Janka et al. 1999, Aloy, Janka, and Müller 2005]. In particular, the BH–torus systems resulting from BNS and BHNS mergers are believed to be the birthplaces of short GRBs (SGRB), as the expected lifetime of the accretion torus is of the order of the duration of SGRBs, while long GRBs are more likely to be produced by "failed" Type Ib supernovae [Woosley 1993]. BH–torus systems emit GWs, which may eventually provide the direct means to study their actual formation and evolution. Observing these GWs will help to prove whether the hypothesis that these systems form the central engine of GRBs is correct, as due to their intrinsic high density and temperature electromagnetic observations are out of reach. Furthermore, once observed, the detected gravitational waveforms of the actual inspiral and coalescence in BNS and BHNS mergers will enhance our understanding of the actual equation of state (EOS) of NS [Read et al. 2009], thus providing valuable insights about the behaviour of matter at nuclear densities. For an overview of the event rate estimates of BNS and BHNS mergers that are observable with initial and advanced LIGO see e.g. Abadie et al. [2010], Dominik et al. [2013], and Dominik et al. [2015].

In recent years a significant number of NR simulations have shown the feasibility of the formation of such systems from generic initial data (see e.g. Rezzolla et al. [2010], Kyutoku et al. [2011], Hotokezaka et al. [2013b], Hotokezaka et al. [2013a], and Kastaun and Galeazzi [2015] for recent progress). In particular, the 3D simulations of Rezzolla et al. [2010] (see also references therein) have shown that unequal-mass BNS mergers lead to the self-consistent formation of *massive* accretion tori (or thick discs) around spinning BHs, thus meeting the

necessary requirements of the GRB's central engine hypothesis. However, if the energy released in a SGRB comes from the accretion torus, the BH–torus system has to survive for up to a few seconds [Rees and Meszaros 1994]. Any instability which might disrupt the system on shorter timescales, such as the runaway instability [Abramowicz, Calvani, and Nobili 1983] or the Papaloizou-Pringle instability (PPI) [Papaloizou and Pringle 1984], could pose a severe problem for the prevailing GRB models. Additionally, post-merger discs should be highly magnetised, due to efficient magnetic field amplification mechanisms active in BNS mergers [Kiuchi et al. 2015a]. Large accretion rates facilitated by the magneto-rotational instability (MRI), which might be active in accretion discs [Balbus and Hawley 1991], could further shorten the lifetime of the accretion torus.

The majority of compact merger simulations to date have led to the production of BH–torus systems in which the central BH spin and the torus angular momentum vector are aligned. This is the expected outcome for BNS mergers, where the direction of the remnant BH spin is perpendicular to the original orbital plane of the binary. For BHNS mergers, an aligned BH–torus system is produced if the BH has zero spin initially or if the BH spin is initially aligned with the orbital plane of the binary system. However, if the BH spin is initially *misaligned* with the orbital plane of the binary, *tilted* BH–torus systems have been shown to form self-consistently in full NR simulations [Foucart et al. 2011, Foucart et al. 2013, Kawaguchi et al. 2015]. Another possible scenario for the formation of tilted BH–torus systems is by means of asymmetric supernova explosions in binary systems [Fragos et al. 2010]. In fact, it is believed that most BH–torus systems should be tilted (see Fragile, Mathews, and Wilson [2001], Maccarone [2002], and Fragile et al. [2007] for arguments).

As shown in Foucart [2012], the disc mass in BHNS mergers increases with a larger initial BH spin and decreases with a larger initial BH mass. This is due to the size of the innermost circular stable orbit (ISCO) of the BH in the merger. The ISCO grows with BH mass and decreases with the spin magnitude of the BH. If the ISCO is large enough, the NS will be "swallowed" entirely by the BH before being tidally disrupted, leaving no accretion torus behind. Another factor in determining the tidal disruption of the NS is its compactness (the ratio of the NS mass and its radius). As seen in Foucart [2012], the larger the NS, the more favoured are massive post-merger discs. In order to estimate disc masses resulting from BHNS mergers, one needs thus an estimate for the initial BH masses in these system. One such method, via population synthesis considerations, favour larger BH masses [Belczynski et al. 2008, Belczynski et al.

2010, Fryer et al. 2012], with a peak around $8\,M_\odot$ and a mass gap between the lightest expected BHs and NS masses. This means that these massive BHs would need very large initial spins in order to be able to form massive remnant discs after the BHNS merger. However, the prediction of accurate remnant BH masses via population synthesis is difficult, as the BH mass crucially depends on the detailed supernova explosion mechanism [Kreidberg et al. 2012] which in turn is very model dependent on the actual presupernova evolution of rotating massive stars [Heger, Langer, and Woosley 2000].

1.3 Dynamics of tilted BH–torus systems

In a tilted BH–torus system, the dynamics of the system is fundamentally different from the aligned case due to general relativistic effects affecting inclined particle orbits in the Kerr spacetime, such as the Lense–Thirring (LT) effect [Lense and Thirring 1918]. The torque caused by the LT effect has a strong radial (r^{-3}) dependence and causes the disc to start precessing differentially, as a result of which it might become *twisted* and *warped*, affecting its dynamical behaviour (see Nelson and Papaloizou [2000] or Section 4.4.1 below for a definition of twist and warp). The inner regions of a thin disc might also be forced to move into the equatorial plane of the BH due to viscosity, via the so-called Bardeen-Petterson effect [Bardeen and Petterson 1975].

As the driving force of the tilted disc evolution are GR effects, one is guaranteed to include all relevant effects by evolving these systems in GR. Both general relativistic hydrodynamics (GRHD) and general relativistic magnetohydrodynamic (GRMHD) simulations of *tilted* thick accretion discs around Kerr BHs have been performed by Fragile and collaborators within the so-called Cowling (fixed spacetime, test–fluid) approximation (see e.g. Fragile and Anninos [2005] and Fragile et al. [2007]). In those seminal works, the authors carried out simulations to study both the dynamics and observational signatures of thick accretion tori around tilted Kerr BHs.

In thick, tilted discs around Kerr BHs, the evolution and propagation of warps can be described by bending waves rather than diffusion [Lubow, Ogilvie, and Pringle 2002] (see also the model of Foucart and Lai [2014] describing the linear warp evolution in tilted discs). In particular, in these systems the tilt angle does not approach zero in the vicinity of the central BH, as one would expect if the viscous Bardeen-Petterson effect would be at play [Ivanov and Illarionov 1997, Demianski and Ivanov 1997, Lubow, Ogilvie, and Pringle 2002]. This behaviour of the radial tilt profile in the inner region of thick, tilted accretion

discs has been observed in the inviscid GRHD simulations of Fragile and Anninos [2005]. Incorporating GR effects in the simulations of these systems is crucial to obtain correct disc evolutions; see for instance, the simulations of Nealon et al. [2016], where omitting or accounting for general relativistic apsidal precession completely changes the evolution of the tilt angle in the vicinity of the central BH. The response of the disc to the differential torque depends on the size and properties of the disc. Notably, if the sound crossing time in the disc is small compared to the timescale of the LT precession, which is the case for geometrically thick and radially slender discs, the response of the disc to the LT torque of the central BH is solid body precession [Fragile and Anninos 2005]. The precessing disc is exerting an equal and opposite torque on the central Kerr BH [King et al. 2005], which should therefore start to precess as well, at least in those systems in which the disc mass is not negligible and the spacetime therefore cannot be assumed to be a fixed background. As described in King et al. [2005], the LT torque alone does not act in a direction that results in disc alignment. However, there have been early arguments that the central BH should eventually align with the disc angular momentum [Rees 1978, Scheuer and Feiler 1996]. In particular, King et al. [2005] argued that the total torque cannot have a component in the direction of the BH spin, but can be broken down to a contribution that induces precession and a second, dissipative torque that tends to align the BH and the accretion disc.

The response of the BH to the torque exerted by the precessing disc can only be self-consistently analysed in GRHD simulations with a fully dynamical spacetime evolution. For discs with negligible mass compared to the central BH, the fixed-spacetime approximation in the seminal simulations of Fragile and collaborators is perfectly justified. However, for BHNS mergers with an initially low mass BH, the post-merger accretion disc can have a non-negligible mass compared to the remnant central BH, making the inclusion of the disc self-gravity necessary. To investigate these systems, and to extend the earlier works into the fully dynamical spacetime regime, we present here the first comprehensive study of tilted BH–torus systems with a fully evolved spacetime via 3D GRHD simulations. All simulations reported in the thesis have been carried out using the publicly available `Einstein Toolkit` (`ET`). In order to be able to monitor the disc evolution during our simulations, we have implemented a module for the `ET` performing the usual measure of the twist and tilt in the disc.

In order to quantify the response of the BH to the torque exerted by the disc, we need an accurate measure of the direction of the BH spin. One of the standard methods in NR to measure the magnitude of the angular momentum

of the BH horizon is described in Dreyer et al. [2003]. This method is based on the so-called isolated horizon formalism [Ashtekar, Beetle, and Fairhurst 1999] and its generalisation to dynamical horizons [Ashtekar and Krishnan 2003]. This method does not, however, give the direction of the BH spin in the 3D Cartesian reference frame of the computational grid of a NR simulation. One of the ways to measure the BH spin direction is via the so-called flat space rotational Killing vector method presented in Campanelli et al. [2007], where the authors showed that the method (while being coordinate based) reproduces the spin magnitude and direction on initial slices very well. The authors remark, however, that the method is not guaranteed to yield an accurate evaluation for generic gauges (such as the ones attained during NR simulations). For the simulations presented in this thesis we are in the need for an accurate measure of the BH spin direction for many orbits of the disc evolution in order to have an accurate description of the BH response to the disc torque. To achieve this goal we present below results showing that the method can be derived from Weinberg's pseudotensor [Weinberg 1972] and is equal, for an axisymmetric horizon, to computing the Komar angular momentum [Komar 1959], when the latter is expressed in a foliation adapted to axisymmetry.

1.4 Stability of accretion discs

Using perturbation theory, Papaloizou and Pringle [1984] found that tori with constant specific angular momentum (l) are unstable to non-axisymmetric global modes. Such modes have a co-rotation radius within the torus, located in a narrow region where waves cannot propagate. Waves can still tunnel through the co-rotation zone and interact with waves outside that region. The transmitted modes are amplified by reflections at the boundaries at the inner and outer edges of the torus.

In early simulations of the PPI in the non-linear regime, Hawley [1987] showed the formation of m counterrotating over-density lumps, where m is the azimuthal mode number. These over-density lumps were dubbed "planets". Goodman, Narayan, and Goldreich [1987] elucidated the precise mechanism of the instability and showed that the planets found in Hawley [1987] could be a new equilibrium configuration of the fluid after the saturation of the instability. The counterrotating over-density lumps manifest themselves as trailing spiral density waves of constant pattern speed. In a differentially rotating disc, this means that there is a region, namely at the co-rotation radius, where the spiral density wave is traveling with the same angular velocity as the fluid. Inside

the co-rotation radius, the wave travels slower, which means that it has *negative* angular momentum with respect to the fluid in that region. In the linear regime, the wave does not interact with the fluid, but once the wave amplitude becomes non-linear, mild shocks are formed and the wave can couple to the fluid of the disc via dissipation [Papaloizou and Lin 1995, Goodman and Rafikov 2001, Heinemann and Papaloizou 2012]. As it couples to the fluid, it removes angular momentum from the fluid in the region within the co-rotation radius and transports it outwards, thereby facilitating accretion.

Non-axisymmetric modes with an azimuthal mode number of $m = 1$ are special, as their appearance causes the centre of mass of the disc to no longer coincide with the centre of mass of the system. This results in a perturbed gravitational potential that causes a drift of the central compact object away from the centre of mass of the system [Adams, Ruden, and Shu 1989, Heemskerk, Papaloizou, and Savonije 1992]. The induced movement of the central mass can also enhance the strength of the $m = 1$ mode significantly [Adams, Ruden, and Shu 1989, Christodoulou and Narayan 1992]. This enhanced mode growth when the central BH is allowed to move provides another reason why simulations of BH–torus systems have to be evolved in fully dynamical spacetimes when the disc mass is not negligible, as the central BH remains fixed by definition in the Cowling approximation.

Korobkin et al. [2011] have studied non-axisymmetric instabilities in self-gravitating discs around BHs using three-dimensional hydrodynamical simulations in full GR. Their models incorporate both moderately slender and slender discs with disc-to-BH mass ratios ranging from 0.11 to 0.24. They observed the growth of unstable non-axisymmetric modes and also observed the movement of the central BH as a result of the growth of a $m = 1$ non-axisymmetric mode. Also employing NR simulations of both constant and non-constant l discs, Kiuchi et al. [2011] showed that the $m = 1$ mode survives for a long time after saturation in non-constant l discs, making the BH–torus system an emitter of large-amplitude, quasi-periodic GW that are potentially observable. In our comprehensive study of tilted accretion discs presented in this thesis, some of our initial disc models have been specifically chosen because they were known to be PP-unstable when the central BH was non-spinning. This allowed us to investigate what kind of effect the disc surrounding tilted Kerr BH will have on its stability.

BH–torus systems are characterised by the presence of a cusp-like inner disc edge where mass transfer driven by the radial pressure gradient is possible. If the cusp moves deeper inside the disc due to accretion, the mass transfer speeds up leading to a runaway process that destroys the disc on a dynamical timescale

(see Font and Daigne [2002] and Daigne and Font [2004] for test-fluid simulations in general relativity of the occurrence of this instability and Montero, Font, and Shibata [2010] for axisymmetric simulations where the self-gravity of the disc was first taken into account). In most recent NR simulations [Rezzolla et al. 2010, Hotokezaka et al. 2013b, Neilsen et al. 2014, Kastaun and Galeazzi 2015] the BH–torus systems under consideration did not manifest signs of runaway instabilities on dynamical timescales, because the non-constant l profiles of the massive discs that form self-consistently in the simulations seem to make them stable against the development of the runaway instability. This is because the disc is stabilised against the runaway instability when l is not constant [Daigne and Mochkovitch 1997], which was also observed numerically in Daigne and Font [2004]. Recently Korobkin et al. [2013] observed that by a suitable choice of model parameters, namely constant angular momentum tori exactly filling or slightly overflowing their Roche lobe, a rapid mass accretion episode with the characteristics of a runaway instability sets in. The astrophysical significance of such fine-tuned models is uncertain as they do not seem to be favoured as the end-product of self-consistent NR simulations of binary neutron star mergers [Rezzolla et al. 2010, Hotokezaka et al. 2013b, Kastaun and Galeazzi 2015, Sekiguchi et al. 2015].

In a follow up paper to their seminal work in 1984, Papaloizou and Pringle [1985] showed that the dynamical instabilities of constant l profile tori were still present in tori with non-constant l profiles, which, as indicated above, are more realistic outcomes of BNS and BHNS mergers. Furthermore, Zurek and Benz [1986] observed that discs with a larger exponent in the power-law distribution of l, $l \sim l^q$ than the critical value given in Papaloizou and Pringle [1985], $q > q_{\rm PP} = 2 - \sqrt{3}$, were still unstable, although angular momentum transport was slower in those cases. This means that global non-axisymmetric modes can indeed affect the disc evolution of post-merger BH–torus systems. For instance, in the recent GRHD simulations of Kawaguchi et al. [2015], the authors observe significant BH–disc alignment in one of the tilted post-merger BH–torus system they studied. These authors assume that angular momentum transport facilitated by a non-axisymmetric shock wave in the disc could provide the dissipation needed for the BH–disc alignment. Another example for the importance of non-axisymmetric instabilities is provided by the recent GRHD simulations of Paschalidis et al. [2015], where the authors observe the formation of a one-armed ($m = 1$) spiral arm instability in the hypermassive NS formed following a BNS merger.

Due to the importance of global non-axisymmetric modes in BH–torus systems, we investigate in this thesis the effects of the disc self-gravity around tilted BHs. Some of the initial models we have built were known to be unstable against the PPI in the untilted case [Korobkin et al. 2011]. Therefore, we investigate in particular the effects the BH tilt has on the development of these instabilities in the torus.

We end this introduction with a word on the initial disc models (see Section 6.1 below for full details). All the simulations reported in this thesis are performed using initial data constructed as equilibrium models of thick accretion discs around a Schwarzschild BH, using a construction described in Stergioulas [2011]. In order to obtain initial data that model a tilted BH–torus system, we replace the spacetime consisting of the non-rotating BH and self-gravitating disc spacetime by a Kerr spacetime with its symmetry axis tilted with respect to the disc angular momentum. We note that there is currently no known method of constructing tilted self-gravitating discs around Kerr BH, as such a tilted BH–torus system is not stationary by definition. Currently, the only way of self-consistently arriving at self-gravitating tilted BH–torus initial data is therefore via NR simulations of tilted BHNS mergers, such as the ones reported in Foucart et al. [2011], Foucart et al. [2013], and Kawaguchi et al. [2015]. While performing the mergers and investigating the subsequent post-merger disc evolution would have been possible using the `ET`, it would have rendered the study prohibitively expensive computationally and was therefore out of the scope of this work. We are not aware of publicly available tilted BH–torus data from self-consistent NR merger simulations either that we could have used as initial data.

1.5 Organisation of the thesis

The rest of the thesis is organised in three parts:

In Part II, we give a brief introduction to the field of NR, describing the spacetime evolution formalism in Chapter 2, GRHD in Chapter 3, and finally giving an overview of the computational framework in Chapter 4. This chapter briefly describes the `ET`, the numerical code which we use for all simulations presented in this thesis.

We present our results in three chapters in Part III. In Chapter 5, we present results regarding the measurement of BH spin direction in NR simulations. Our comprehensive parameter study of different accretion disc models around tilted Kerr BHs is presented in Chapter 6. In the final Chapter 7 of Part III, we analyse one of the models of Chapter 6 in more detail, using fluid tracer particles as a new means of analysing the disc evolution.

The discussion of the results and our outlook are presented in Part IV.

Finally, Part V contains two appendices. Appendix A contains a brief overview of hyperbolic partial differential equations (PDEs) and in Appendix B we give details on the actual implementation of the disc analysis thorn we have written.

1.6 Conventions

Where physical quantities are given without explicit units, we use units in which $c = G = M_\odot = 1$ throughout the thesis, where c, G and $M_\odot$ are the speed of light, the gravitational constant and the solar mass, respectively. Specifically, this means that units of length and time are given by $[\mathrm{L}] = M_\odot \sim 1.477\,\mathrm{km}$ and $[\mathrm{T}] = M_\odot \sim 4.92673 \times 10^{-6}\,\mathrm{s}$. A notable exception are frequencies, which we will give in units of Hz. We adopt a spacelike signature of the metric $(-,+,+,+)$. Lower case Latin indices run from 1 to 3, Greek indices run from 0 to 3 and upper case Latin indices indicate the number of equations in a hyperbolic system. We adopt the standard Einstein summation convention for the summation of repeated indices. Vector and tensor variables are indicated in boldface. Indices of objects living in three-dimensional hypersurfaces are raised and lowered with the spatial three-metric of the respective hypersurface.

Part II

Numerical relativity

One hundred years have passed since Albert Einstein formulated GR [Einstein 1915, Einstein 1916], deriving the equations of motion of the gravitational field. The field equations are a set of non-linear partial differential equations (PDEs) for the spacetime metric. The non-linearity is a consequence of the fact that the gravitational field itself carries energy and momentum. Obtaining exact solutions to the field equations is notoriously difficult. The most famous are the vacuum solutions of Schwarzschild [1916] and Kerr [1963]. The Schwarzschild solution is a spherically symmetric, static spacetime, describing the vacuum gravitational field around a non-rotating, uncharged mass. The Kerr spacetime is an axisymmetric, stationary solution, giving the vacuum gravitational field around a rotating mass. For an excellent introduction to the Kerr spacetime, see Visser [2007]. For an overview of exact solutions to the Einstein equations, see Kramer and Schmutzer [1980].

As noted in the introduction, ground based GW detectors have opened a new window to the observation of the universe. While the investigation of exact solutions to the field equations is an important field in itself, most exact solutions are stationary/static and as such do not emit GWs. It is therefore necessary to numerically solve the full non-linear field equations in order to model gravitational waveforms emitted in dynamical scenarios. This chapter gives an introduction to the methods and techniques developed in order to numerically integrate the field equations of GR.

The field of NR has come a long way from the first reformulation of the Einstein equations in a $3+1$ split by Darmois [1927] to the groundbreaking vacuum BBH simulations of Pretorius [2005a], Campanelli et al. [2006], and Baker et al. [2006]. For matter spacetimes, the first BNS mergers by Shibata and Uryū [2000] and BHNS mergers by Shibata and Uryū [2006] were equally important breakthroughs. As we can only give an overview of the field and the necessary techniques to solve the Einstein equations numerically, we refer the reader to the lectures notes of Gourgoulhon [2012] and the books by Alcubierre [2008] and Baumgarte and Shapiro [2010] for a general introduction to NR, as well as the Living Review articles on numerical hydrodynamics and magnetohydrodynamics in general relativity by Font [2008], on BNS mergers by Faber and Rasio [2012], as well as on BHNS mergers by Shibata and Taniguchi [2011].

This part of the manuscript is split in chapters describing the spacetime evolution, the evolution of GRHD and the computational framework that is used for the numerical simulations presented in this work.

Chapter 2

Spacetime Evolution

GR abandons the notion of a global flat space and a universal time in which the dynamics of matter take place, as is the case in Newtonian dynamics. Instead, the dynamics take place in a 4-dimensional spacetime consisting of events, which are 4-dimensional labels of 3 spatial and one temporal coordinate. Notably, space and time are brought on an equal footing. The mathematical structure of spacetime is that of a 4 dimensional pseudo-Riemannian manifold $\mathcal{M}$ equipped with a bilinear, symmetric form, the spacetime metric $\boldsymbol{g}$, together forming the set $(\mathcal{M}, \boldsymbol{g})$.

The equation of motion for the gravitational field is the following tensorial equation:

$$\boldsymbol{G} = 8\,\pi\,\boldsymbol{T}, \tag{2.1}$$

where $\boldsymbol{G}$ is the Einstein tensor and $\boldsymbol{T}$ the stress-energy tensor of the matter contained in the spacetime. A guiding principle in the development of the theory has been general covariance, as the laws of physics should not depend on the coordinates used in calculations. This is reflected in the fact that the *equation of motion* of the gravitational field is a tensorial equation. The Einstein equations determine the curvature of the manifold $\mathcal{M}$ for a given matter distribution described by the stress-energy tensor $\boldsymbol{T}$, while the curvature in turn determines the gravitational field felt by the matter distribution. This, as Zeidler [2011] remarks, can be formulated as a guiding principle of modern theoretical physics, namely as the realisation that *force equals curvature*.

Introducing the coordinates x^μ in $\mathcal{M}$, the line element (which measures distances and times between points in the manifold) is given in terms of the

spacetime metric as:

$$ds^2 = g_{\mu\nu} dx^\mu dx^\nu. \tag{2.2}$$

The Christoffel symbols of the Levi-Civita connection, which is torsion-free, are defined as

$$\Gamma^\gamma_{\alpha\beta} := \frac{1}{2}(\partial_\alpha g_{\beta\mu} + \partial_\beta g_{\alpha\mu} - \partial_\mu g_{\alpha\beta}) g^{\mu\gamma}, \tag{2.3}$$

where we have introduced the shorthand notation $\partial_\alpha := \frac{\partial}{\partial x^\alpha}$ and $g^{\mu\nu}$ is the inverse of the spacetime metric $g_{\mu\nu}$ in the sense that

$$g_{\alpha\nu} g^{\nu\beta} = \delta^\beta{}_\alpha, \tag{2.4}$$

with $\delta^\beta{}_\alpha$ being the Kronecker delta. As usual, indices are raised and lowered with the spacetime metric $g_{\mu\nu}$. The curvature of $\mathcal{M}$ is completely determined by the Riemann tensor $R^\delta{}_{\alpha\beta\gamma}$ given by

$$R^\delta{}_{\alpha\beta\gamma} := \partial_\alpha \Gamma^\delta_{\beta\gamma} - \partial_\beta \Gamma^\delta_{\alpha\gamma} + \Gamma^\delta_{\alpha\mu}\Gamma^\mu_{\beta\gamma} - \Gamma^\delta_{\beta\mu}\Gamma^\mu_{\alpha\gamma}. \tag{2.5}$$

From the Riemann tensor, we can construct the Ricci tensor $R_{\alpha\beta}$ of the spacetime, which is obtained by contracting the Riemann tensor once

$$R_{\alpha\beta} := R^\delta{}_{\alpha\delta\beta}, \tag{2.6}$$

and contracting the Ricci tensor once more gives the Ricci scalar or scalar curvature

$${}^{(4)}R := g^{\alpha\beta} R_{\alpha\beta}. \tag{2.7}$$

As the Ricci scalar does not carry indices by definition, we use the notation ${}^{(4)}R$ to indicate that it is a four-dimensional object of the manifold $\mathcal{M}$, distinguishing it from the 3-dimensional Ricci scalar R. Using the Ricci tensor and scalar curvature, we can express the Einstein tensor in the coordinates x^μ as follows

$$G_{\mu\nu} := R_{\mu\nu} - \frac{1}{2} g_{\mu\nu}\, {}^{(4)}R, \tag{2.8}$$

which gives the Einstein equations in coordinates

$$R_{\mu\nu} - \frac{1}{2} g_{\mu\nu}\, {}^{(4)}R = 8\,\pi\, T_{\mu\nu}. \tag{2.9}$$

Contracting Eq. (2.9) with $g_{\mu\nu}$ leads to

$${}^{(4)}R = -8\,\pi\, T^\lambda{}_\lambda \tag{2.10}$$

which means that the scalar curvature of the spacetime is directly related to the energy-momentum of the matter via the trace of $T_{\mu\nu}$. Substituting Eq. (2.10) back into Eq. (2.9), we are led to the following equivalent form of the Einstein

equations:

$$R_{\mu\nu} = 8\,\pi\,(T_{\mu\nu} - \frac{1}{2} g_{\mu\nu} T^{\lambda}{}_{\lambda}). \tag{2.11}$$

From this form of the Einstein equations, we see immediately that a vacuum spacetime ($T_{\mu\nu} = 0$) has a vanishing Ricci tensor.

The symmetric Einstein tensor $G_{\mu\nu}$ has ten independent components, so that Eq. (2.9) is a set of 10 algebraically independent equations. However, as a result of the Bianchi identities (see, e.g. Weinberg [1972]), the components of $G_{\mu\nu}$ are related by four differential identities,

$$G^{\mu}{}_{\nu;\mu} = 0, \tag{2.12}$$

where $_{;\mu}$ denotes the covariant derivative with respect to the metric $g_{\mu\nu}$. We are therefore left with $10 - 6$ independent equations for the spacetime metric, which means there are 4 degrees of freedom. These represent the gauge invariance of the theory, namely the diffeomorphisms of the 4 dimensional spacetime.

We note that by virtue of the Einstein equation (2.9), the local conservation of the Einstein tensor, Eq. (2.12), directly implies that the stress-energy tensor is locally conserved as well:

$$T^{\mu}{}_{\nu;\mu} = 0. \tag{2.13}$$

The fact that time and space are combined into events in GR, as well as the 4 dimensional gauge invariance make the numerical integration of the equations of motion of the gravitational field a daunting task. For dynamical vacuum spacetimes, we do not know the future end states of the system in order to be able to properly formulate boundary conditions. Furthermore, the presence of matter complicates the evolution of the system further, as the matter might be subject to the other forces of nature (the electromagnetic, electroweak and strong force) as well. Additionally, we know that there is an arrow of time, given by the second law of thermodynamics, namely that the entropy of an isolated system cannot decrease in time. We would therefore like to rewrite the field equations (2.9) in a way that enables us to integrate them forward in time, as we are required to integrate the internal evolution of the matter forward in time as well. We are thus led to consider if we can solve the Einstein equations as a Cauchy initial value problem (IVP):

Given the metric $g_{\mu\nu}$ and its "velocity" $\partial_0 g_{\mu\nu}$ at a single point in time $x^0 = t_0$ everywhere in space, can we integrate the field equations coupled to the matter evolution equations forward along x^0?

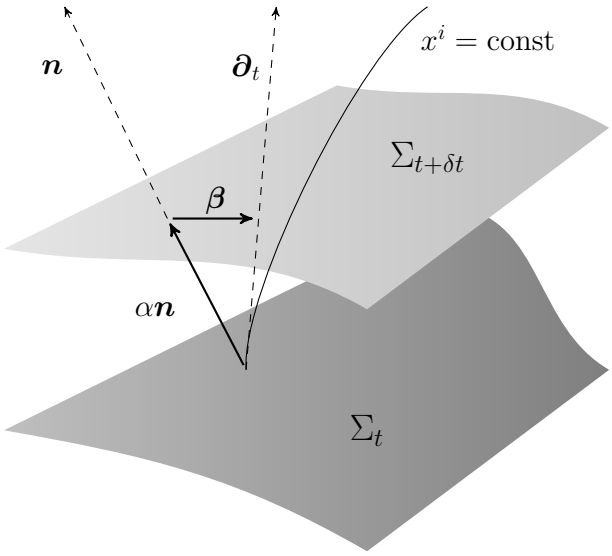

Figure 2.1 Diagram showing the 3+1 splitting of spacetime in a foliation adapted to the coordinates x^i of the spacelike hypersurface Σ_t. See main text for details.

2.1 The $3+1$ formalism of GR

By slicing the 4 dimensional spacetime as a family of non-intersecting 3-dimensional spacelike hypersurfaces Σ_t, one can reformulate finding the solution to the Einstein equations as the Cauchy IVP sought above. This is based on the works of Darmois [1927], Lichnerowicz [1944] and Choquet-Bruhat [1952]. In the description of the $3+1$ formalism below, we largely follow the derivations given in Gourgoulhon [2012], to which we refer the reader for full details.

In the $3+1$ formalism, the 4 dimensional spacetime manifold $\mathcal{M}$ is foliated by a set of non-intersecting spacelike hypersurfaces Σ_t, where t is a parameter indicating the elapsed time between neighbouring hypersurfaces. In the following we choose to foliate $\mathcal{M}$ in a manner that is adapted to the coordinates x^μ, expressing the tensorial equations in those coordinates, as we are ultimately interested in rewriting the field equations as PDEs in order to numerically integrate them. We denote the normal vector to the hypersurface as $\boldsymbol{n}$, and the tangent vector to the coordinate lines of $x^i = \text{const}$ as $\boldsymbol{\partial}_t$ (called the time vector [Gourgoulhon 2012]). The three central quantities in expressing the spacetime metric $g_{\mu\nu}$ in the $3+1$ formalism are then: The spatial 3-metric γ_{ij}, which determines the intrinsic geometry of Σ_t, the lapse function α, which is a measure of the temporal distance along the normal $\boldsymbol{n}$ between Σ_t and the neighbouring $\Sigma_{t+\delta t}$, and the shift vector β^i, which measures the

shift of the coordinates between the normal $\boldsymbol{n}$ and the time vector $\boldsymbol{\partial}_t$. Fig. 2.1 displays a diagram illustrating the resulting foliation. Indices of objects living on the hypersurface Σ_t are raised and lowered with the spatial metric γ_{ij}. The normal vector n^μ and the covariant normal vector n_μ are given by the following expressions in the coordinates x^μ

$$n^\mu = \left(\frac{1}{\alpha}, -\frac{\beta^i}{\alpha}\right), \tag{2.14}$$

$$n_\mu = (-\alpha, 0), \tag{2.15}$$

while the time vector is given by

$$\boldsymbol{\partial}_t = \alpha \boldsymbol{n} + \boldsymbol{\beta}. \tag{2.16}$$

From this, we see that the normal vector $\boldsymbol{n}$ is given by:

$$\boldsymbol{n} = \frac{1}{\alpha}(\boldsymbol{\partial}_t - \boldsymbol{\beta}). \tag{2.17}$$

In this 3+1 split, the 4 dimensional spacetime metric takes the following form:

$$g_{\mu\nu} = \left(\begin{array}{c|c} -\alpha^2 + \beta_i\beta^i & \gamma_{ij}\beta^j \\ \hline \gamma_{ij}\beta^j & \gamma_{ij} \end{array}\right), \tag{2.18}$$

and its inverse is given by

$$g^{\mu\nu} = \left(\begin{array}{c|c} -\alpha^{-2} & \beta^i\alpha^{-2} \\ \hline \beta^j\alpha^{-2} & \gamma^{ij} - \beta^i\beta^j\alpha^{-2} \end{array}\right), \tag{2.19}$$

where γ^{ij} is the inverse of 3-metric γ_{ij}. While the spatial metric γ_{ij} defines the intrinsic geometry of Σ_t, it gives no information on how Σ_t is embedded in the four dimensional manifold $\mathcal{M}$. This information is provided by the extrinsic curvature K_{ij}, which measures the evolution of the spatial metric between neighbouring hypersurfaces. The extrinsic curvature is a spatial tensor of Σ_t and is given by the Lie derivative of the spatial metric γ_{ij} along the direction of the normal $\boldsymbol{n}$:

$$\boldsymbol{K} = -\frac{1}{2\alpha}(\mathcal{L}_{\boldsymbol{\partial}_t} - \mathcal{L}_{\boldsymbol{\beta}})\,\boldsymbol{\gamma}, \tag{2.20}$$

where $\mathcal{L}_{\boldsymbol{\partial}_t}\boldsymbol{\gamma}$ and $\mathcal{L}_{\boldsymbol{\beta}}\boldsymbol{\gamma}$ are expressed in coordinates as follows:

$$\mathcal{L}_{\boldsymbol{\partial}_t}\boldsymbol{\gamma} = \partial_t\,\gamma_{ij}, \tag{2.21}$$

$$\mathcal{L}_{\boldsymbol{\beta}}\boldsymbol{\gamma} = D_i\beta_j + D_j\beta_i, \tag{2.22}$$

where D_i is the covariant derivative associated with the spatial metric γ_{ij}. In component notation, the extrinsic curvature is therefore given by:

$$K_{ij} = -\frac{1}{2\alpha}(\partial_t\,\gamma_{ij} - D_i\beta_j + D_j\beta_i), \tag{2.23}$$

showing that the extrinsic curvature is closely related to the time derivative of the spatial metric. In fact, this gives us an evolution equation for γ_{ij} stemming purely from the geometry of the foliation. Having defined the spacetime metric $g_{\mu\nu}$ in terms of the set $\{\alpha, \beta^i, \gamma_{ij}\}$, the embedding of Σ_t in $\mathcal{M}$ with the help of the extrinsic curvature K_{ij} has therefore given us the first evolution equation of the $3+1$ field equations:

$$(\partial_t - \mathcal{L}_{\boldsymbol{\beta}})\,\gamma_{ij} = -2\,\alpha\,K_{ij}. \tag{2.24}$$

To proceed, we need to define how to project the four dimensional tensors living in $\mathcal{M}$ onto the hypersurface Σ_t in order to be able to project the field equations onto the hypersurface. We can project four dimensional tensors in various ways; namely projecting along the tangents of the hypersurface using the orthogonal projector $\gamma^{\alpha}{}_{\beta}$:

$$\gamma^{\alpha}{}_{\beta} = \delta^{\alpha}{}_{\beta} + n^{\alpha} n_{\beta}, \tag{2.25}$$

or a projection along the normal to Σ_t using n^{μ}, or as a mix of the two projections. We first project the stress-energy tensor $T_{\mu\nu}$ onto the hypersurface, which gives rise to the following quantities related to the matter content of the spacetime:

$$E \equiv n^{\mu}\, n^{\nu}\, T_{\mu\nu} = \frac{1}{\alpha^2}\left(T_{00} - 2\,\beta^a T_{0a} + \beta^a \beta^b T_{ab}\right), \tag{2.26}$$

$$S_i \equiv -\gamma^{\mu}{}_{i}\, n^{\nu}\, T_{\mu\nu} = -\frac{1}{\alpha}(T_{0i} - T_{ia}\beta^a), \tag{2.27}$$

$$S_{ij} \equiv \gamma^{\mu}{}_{i}\, \gamma^{\nu}{}_{j}\, T_{\mu\nu} = T_{ij}, \tag{2.28}$$

$$S \equiv \gamma^{ij}\, S_{ij}. \tag{2.29}$$

These quantities are respectively, the matter energy density E, the matter momentum density S_i, the matter stress tensor S_{ij}, and the trace of the matter stress tensor S. Contracting the Einstein equations in the form of Eq. (2.11) twice with the orthogonal projector leads to

$$(\partial_t - \mathcal{L}_{\boldsymbol{\beta}})\,K_{ij} = -D_i D_j \alpha + \alpha\,(R_{ij} + K K_{ij} - 2K_{ia}K^{a}{}_{j} + 4\pi((S-E)\gamma_{ij} - 2S_{ij})) \tag{2.30}$$

Projecting Eq. (2.11) twice with the normal to the hypersurface results in:

$$R + K^2 - K_{ij}K^{ij} = 16\pi E, \tag{2.31}$$

which is the so-called **Hamiltonian constraint**. Finally, performing a mixed projection of Eq. (2.11) leads to the following equation:

$$D_j K^{j}{}_{i} - D_i K = 8\pi S_i, \tag{2.32}$$

which is the so-called **momentum constraint**. To arrive to these equations, one needs to make use of the *Gauss*, *Codazzi*, and *Ricci equations*. We refer the reader to Gourgoulhon [2012] for the full details of the derivation.

Eqs. (2.24) and (2.30) constitute the evolution equations of the 3+1 formalism, while Eqs. (2.31) and (2.32) are constraint equations that need to be fulfilled at every spatial hypersurface Σ_t. These four equations, written in the 3+1 formalism are equivalent to the original four dimensional Einstein equations (2.11).

For completeness (see Gourgoulhon [2012]), we explicitly give the various terms in the above equations by expressing the covariant derivative D_i associated with the spatial metric γ_{ij} in terms of partial derivatives using the Christoffel symbols associated with the connection of γ_{ij}, ${\Gamma^a}_{bc}$:

$$ {\Gamma^a}_{ij} = \frac{1}{2}\gamma^{ab}(\partial_i\gamma_{bj} + \partial_j\gamma_{ib} - \partial_b\gamma_{ij}). \tag{2.33} $$

Then

$$ D_iD_j\alpha = \partial_i\partial_j\alpha - {\Gamma^a}_{ij}\,\partial_a\,\alpha, \tag{2.34} $$

$$ D_aK^a{}_i = \partial_aK^a{}_i + {\Gamma^a}_{ab}\,K^b{}_i - {\Gamma^b}_{ai}\,K^a{}_b, \tag{2.35} $$

$$ D_iK = \partial_iK. \tag{2.36} $$

Furthermore, the Lie derivatives with respect to the shift vector, $\mathcal{L}_{\boldsymbol{\beta}}$, are given by

$$ \mathcal{L}_{\boldsymbol{\beta}}\,\gamma_{ij} = \partial_j\beta_i + \partial_i\beta_j - 2{\Gamma^a}_{ij}\,\beta_a, \tag{2.37} $$

$$ \mathcal{L}_{\boldsymbol{\beta}}\,K_{ij} = \beta^a\,\partial_aK_{ij} + K_{aj}\,\partial_i\beta^a + K_{ia}\,\partial_j\beta^a. \tag{2.38} $$

The Ricci tensor R_{ij} and the spatial scalar curvature R are given by

$$ R_{ij} = \partial_a{\Gamma^a}_{ij} - \partial_j{\Gamma^a}_{ia} + {\Gamma^a}_{ij}\,{\Gamma^b}_{ab} - {\Gamma^b}_{ia}\,{\Gamma^a}_{bj}, \tag{2.39} $$

$$ R = \gamma^{ij}\,R_{ij}. \tag{2.40} $$

The evolution and constraint equations constitute a set of second-order non-linear PDEs for the set of variables $\{\gamma_{ij}, K_{ij}, \alpha, \beta^i, E, S_i, S_{ij}\}$. We note that there are no time derivatives in the Hamiltonian and Momentum constraint equations. They are rather restrictions on the initial data on the initial spacelike hypersurface $\Sigma_{t=0}$. Loosely speaking, this means that the initial data needs to be a solution to the field equations in order to be able to obtain a meaningful time evolution. Due to the Bianchi identities, we are guaranteed that the constraints are identically fulfilled during the time evolution. However, this is only true in the continuum limit, while numerical systems tend to drift away from the constraint surface due to the accumulation of truncation errors.

In order to gain some insight into the meaning of the constraints, and in particular into the role played by the lapse and the shift, we will now briefly describe a *Hamiltonian* formulation of GR. Utilising the $3+1$ split, Dirac [1949] and Arnowitt, Deser and Misner (ADM) [1961] (republished in Arnowitt, Deser, and Misner [2008]), derived a Hamiltonian formulation of GR, where, in close analogy to quantum mechanics, the generator of time evolution is the Hamiltonian of the system. The starting point is the Hilbert action of GR

$$S_{\mathrm{GR}}[g_{\mu\nu}] = \frac{1}{16\pi}\int_{\mathcal{M}} {}^{(4)}R\sqrt{-g}\,d^4x, \tag{2.41}$$

where g is the determinant of $g_{\mu\nu}$. The action is a functional of the metric. In the $3+1$ formalism, we want to express the action $S_{\mathrm{GR}}[g_{\mu\nu}]$ in terms of the set $\{\gamma_{ij}, \alpha, \beta^i\}$. The spatial metric γ_{ij} will play the role of the generalised coordinates q, and we denote by p^{ij} the canonically conjugate momentum to γ_{ij}. We restrict ourselves to the vacuum case below, but the inclusion of matter proceeds analogously. The action in terms of the set $\{\gamma_{ij}, \alpha, \beta^i\}$ is then given by:

$$S_{3+1}[\gamma_{ij}, \alpha, \beta^i] = \frac{1}{16\pi}\int_{\mathbb{R}}\left(\int_{\Sigma_t} p^{ij}\dot{\gamma}_{ij}\,d^3x - H_\alpha - H_{\beta^i}\right)dt, \tag{2.42}$$

where H_α and H_{β^i} are obtained by "smearing" the gravitational super-Hamiltonian

$$H = \frac{1}{\sqrt{\gamma}}(p_{ij}p^{ij} - \frac{p^2}{2}) - \sqrt{\gamma}R, \tag{2.43}$$

where $\gamma \equiv \det(\gamma_{ij})$, and super-momentum

$$H_i = -2D_i p^j{}_i, \tag{2.44}$$

with the Lagrangian multipliers lapse

$$H_\alpha = \int_{\Sigma_t} \alpha\, H\, d^3x, \tag{2.45}$$

and shift [Kucha and Torre 1991]

$$H_{\beta^i} = \int_{\Sigma_t} \beta^i\, H_i\, d^3x. \tag{2.46}$$

As the variations of the action with respect to the lapse and shift need to vanish in order for the action to be extremal, and no term in the action explicitly depends on either α or β^i, apart from their use as Lagrangian multipliers, H_α and H_{β^i} must be identically zero:

$$\frac{\delta S_{3+1}}{\delta\alpha} = 0 \implies H = \frac{1}{\sqrt{\gamma}}\left(p_{ij}p^{ij} - \frac{p^2}{2}\right) - \sqrt{\gamma}R = 0, \tag{2.47}$$

and

$$\frac{\delta S_{3+1}}{\delta \beta^i} = 0 \implies H_i = -2D_j p^j{}_i = 0. \tag{2.48}$$

These are precisely the **Hamiltonian** and **momentum** constraints. The variation of the action with respect to γ_{ij} and p^{ij} leads to the Hamiltonian equations of motion for the spatial metric and the conjugate momentum in terms of the following Poisson brackets:

$$\dot{\gamma}_{ij} = \{\gamma_{ij}, H_\alpha + H_{\beta^i}\}, \tag{2.49}$$

$$\dot{p}^{ij} = \{p^{ij}, H_\alpha + H_{\beta^i}\}. \tag{2.50}$$

As Kucha and Torre [1991] remark, the Einstein equations remain valid when introducing coordinate conditions after the variation, which the ADM reformulation allows us to do. The coordinate conditions only prescribe the passage from one hypersurface Σ_t to another $\Sigma_{t+\delta t}$. For reference, we give the relation between the extrinsic curvature K_{ij} and the canonically conjugate momentum p_{ij}:

$$p^{ij} = \sqrt{\gamma}(K\,\gamma^{ij} - K^{ij}). \tag{2.51}$$

After having obtained the Einstein equations as PDEs in coordinates adapted to the coordinates introduced in the $3 + 1$ split of the spacetime, we could in principle go ahead and numerically integrate them, after having specified a set of initial data $\{\gamma_{ij}, K_{ij}, E, S_i, S_{ij}\}$ that satisfies the constraints. As we have seen, the lapse and shift are Lagrangian multipliers of the Hamiltonian reformulation and therefore not dynamic variables, the freedom to choose them freely reflects the original diffeomorphism invariance of the 4 dimensional theory. There are, however, various caveats:

Firstly, although we should in principle be able to freely choose the gauge in free evolution schemes, choosing the correct gauge for the numerical integration is crucial for the long-term stability of simulations. We will return to this issue in section 2.3 below.

Secondly, although the Bianchi identities guarantee that the constraints are fulfilled during the entire evolution, this is only strictly true in the continuum limit, and performing the numerical integration of the field equations with finite resolution will in general not preserve the constraints. When the constraints are not satisfied, we are no longer solving the Einstein equations. There exist therefore two different approaches to the numerical integration of the field equations: the so-called *free evolution schemes*, in which the level of constraint violations is only monitored during the evolution, and the so-called *constrained evolution schemes*, where the constraints are actively enforced during the evolution. Both

approaches have advantages and disadvantages. In free evolution schemes, the resulting nonlinear PDEs are hyperbolic, and therefore much easier and computationally cheaper to solve than the nonlinear mixed elliptic-hyperbolic PDEs arising in constraint evolution schemes. However, as said above, the constraints are only fulfilled in the continuum limit and numerical errors result in solutions that are not true solutions of the Einstein equations as the simulation proceeds. We use a free evolution scheme in this work, and will therefore not describe constrained evolution schemes further. For examples of constrained schemes for the numerical integration of the Einstein equations see Bonazzola et al. [2004] and Cordero-Carrión et al. [2009] and references therein.

Finally, when performing a free evolution using the discretised $3+1$ evolution equations (2.24) and (2.30) directly, the evolution is not stable. The reason is that the equations are only weakly hyperbolic and as such mathematically not well posed. The root of the problem is the appearance of the spatial Ricci tensor in these equations [Friedrich 1996], due to the fact that it contains mixed partial derivatives of the spatial metric. We will discuss this further in Appendix A, where we define the notion of hyperbolicity for first order systems of PDEs and provide a heuristic argument showing how indeed the mixed partial derivatives of the Ricci tensor influence the hyperbolicity of the $3+1$ evolution equations.

One way to eliminate these mixed derivatives is the *conformal-traceless reformulation* of the $3+1$ evolution equations, first presented by Nakamura, Oohara, and Kojima [1987]. The introduction of auxiliary variables removes the troublesome mixed partial derivatives in the Ricci tensor, and additionally, the trace of the extrinsic curvature, K, is evolved separately. One of the resulting, and arguably most widely used, free evolution scheme based on the conformal-traceless reformulation of the $3+1$ evolution equations is the so-called *BSSN* formulation [Baumgarte and Shapiro 1999, Shibata and Nakamura 1995][1]. As we exclusively use the BSSN formulation for all simulations in this work, we restrict ourselves to its description only, which we present in the following section.

As a final remark, we note that there exist other formulations of the Einstein equations not based on the $3+1$ formalism, such as the characteristic initial value problem (for a review see Winicour [2012]) or the generalised harmonic decomposition by Pretorius [2005b].

[1] Note that it is sometimes called BSSNOK, because it is based on the strategy of Nakamura, Oohara, and Kojima [1987] to simplify the spatial Ricci tensor.

2.2 The BSSN equations

The starting point of the conformal-traceless reformulation is a conformal decomposition of the spatial metric γ_{ij}, an idea dating back to Lichnerowicz [1944], by introducing a conformal factor ϕ and the conformal spatial metric

$$\tilde{\gamma}_{ij} = e^{-4\phi}\,\gamma_{ij}, \tag{2.52}$$

in a way that the determinant of the conformal metric, $\tilde{\gamma}$, is unity and the conformal factor is given by $\phi = \ln(\gamma)/12$. Defining the traceless part of the extrinsic curvature as

$$A_{ij} = K_{ij} - \frac{1}{3}\gamma_{ij}K, \tag{2.53}$$

the conformally related traceless part of the extrinsic curvature is given by

$$\tilde{A}_{ij} = e^{-4\phi}\,A_{ij}. \tag{2.54}$$

By taking the trace of the $3+1$ evolution equation for the spatial metric (2.24) one obtains an evolution equation for the trace of γ_{ij}:

$$\partial_t \ln(\gamma^i{}_i) = -2\,\alpha\,K + 2D_i\beta^i. \tag{2.55}$$

The evolution of the conformal factor ϕ is given by

$$\partial_t\phi = -\frac{1}{6}\alpha\,K + \beta^i\partial_i\phi + \frac{1}{6}\partial_i\beta^i. \tag{2.56}$$

In a similar fashion, by taking the trace of the evolution equation (2.30) of the extrinsic curvature and combining it with the Hamiltonian constraint (2.31), one obtains an evolution equation for the trace of the extrinsic curvature:

$$\partial_t K = -\gamma^{ij}\,D_j\,D_i\,\alpha + \alpha\left(\tilde{A}_{ij}\tilde{A}^{ij} + \frac{K^2}{3}\right) + 4\pi\alpha(E+S) + \beta^i\partial_i K. \tag{2.57}$$

Finally, combining the evolution equations for the trace of the extrinsic curvature (2.56) and the conformal factor (2.57) with the $3+1$ evolution equations (2.24) and (2.30), one arrives at the evolution equations for the conformal metric and the conformally related traceless extrinsic curvature:

$$\partial_t\tilde{\gamma}_{ij} = -2\alpha\tilde{A}_{ij} + \beta^a\partial_a\tilde{\gamma}_{ij} + \tilde{\gamma}_{ia}\partial_j\beta^a + \tilde{\gamma}_{aj}\partial_i\beta^a - \frac{2}{3}\gamma_{ij}\partial_a\beta^a, \tag{2.58}$$

$$\begin{aligned}\partial_t\tilde{A}_{ij} = {} & e^{-4\phi}\,[\alpha(R_{ij} - \frac{1}{3}\gamma_{ij}\,R) - 8\pi\,\alpha\,(S_{ij} - \frac{1}{3}\gamma_{ij}S) \\ & - (D_iD_j\alpha - \frac{1}{3}\gamma_{ij}D^aD_a\alpha)] + \alpha\,(K\,\tilde{A}_{ij} - 2\tilde{A}_{ia}\tilde{A}^a{}_j) \\ & + \beta^a\partial_a\tilde{A}_{ij} + \tilde{A}_{ia}\partial_j\beta^a + \tilde{A}_{aj}\partial_i\beta^a - \frac{2}{3}\tilde{A}_{ij}\partial_a\beta^a.\end{aligned} \tag{2.59}$$

Note that the Ricci tensor still appears unaltered in the above equation for the time evolution of $\tilde{A}_{ij}$, and specifically, the mixed derivatives of the metric have not yet been eliminated. To do so, one proceeds by splitting the Ricci tensor into two parts:

$$R_{ij} = R^{\phi}_{ij} + \tilde{R}_{ij}, \tag{2.60}$$

where R^{ϕ}_{ij} is given by

$$R^{\phi}_{ij} = -2\tilde{D}_i\tilde{D}_j\phi - 2\gamma_{ij}\tilde{D}^a\tilde{D}_a\phi + 4\tilde{D}_i\phi\tilde{D}_j\phi - 4\gamma_{ij}\tilde{D}^a\phi\tilde{D}_a\phi, \tag{2.61}$$

and $\tilde{D}_i$ is the covariant derivative associated with the conformal metric. Introducing the *conformal connection functions* $\tilde{\Gamma}^i$ [Baumgarte and Shapiro 1999], defined as

$$\tilde{\Gamma}^i \equiv \tilde{\gamma}^{ab}\,\tilde{\Gamma}^i{}_{ab} = -\partial_a\tilde{\gamma}^{ia}, \tag{2.62}$$

where the $\tilde{\Gamma}^i{}_{ab}$ are Christoffel symbols of the connection associated with the conformal metric $\tilde{\gamma}_{ij}$, the conformal Ricci tensor $\tilde{R}_{ij}$ can be expressed as:

$$\tilde{R}_{ij} = \frac{1}{2}\tilde{\gamma}^{ab}\partial_{ab}\tilde{\gamma}_{ij} + \tilde{\gamma}_{a(j}\partial_{j)}\tilde{\Gamma}^a + \tilde{\Gamma}^a\tilde{\Gamma}_{(ij)a} + \tilde{\gamma}^{ab}(2\,\tilde{\Gamma}^c_{a(i}\tilde{\Gamma}_{j)cb} + \tilde{\Gamma}^c_{ib}\tilde{\Gamma}_{caj}). \tag{2.63}$$

The only second derivatives of the metric left in the definition of $\tilde{R}_{ij}$ is the Laplace operator $\tilde{\gamma}^{ab}\partial_{ab}\tilde{\gamma}_{ij}$. The rest of the second derivatives have been recast in terms of the conformal connection functions $\tilde{\Gamma}^i$, which was the aim of the reformulation of the original $3+1$ evolution equations. The conformal connection functions are now considered as independent variables and need to be evolved. The evolution equation is obtained by performing a permutation of space and time derivatives in the definition (2.62):

$$\begin{aligned}\partial_t\tilde{\Gamma}^i =& -2\tilde{A}^{ia}\partial_a\alpha + 2\,\alpha\,(\tilde{\Gamma}^i{}_{ab}\tilde{A}^{ab} - \frac{2}{3}\tilde{\gamma}^{ia}\partial_a K - 8\pi\,\tilde{\gamma}^{ia}S_a + 6\tilde{A}^{ia}\partial_a\phi)\\ &+ \beta^a\partial_a\tilde{\Gamma}^i - \tilde{\Gamma}^a\partial_a\beta^i + \frac{2}{3}\tilde{\Gamma}^i\partial_a\beta^a + \frac{1}{3}\tilde{\gamma}^{bi}\partial_{ab}\beta^a + \tilde{\gamma}^{ba}\partial_{ba}\beta^i.\end{aligned} \tag{2.64}$$

Thus, in the BSSN reformulation of the $3+1$ evolution equations, the evolution variables are now the set:

$$\{\phi, \tilde{\gamma}_{ij}, K, \tilde{A}_{ij}, \tilde{\Gamma}^i\}. \tag{2.65}$$

The aim of the reformulation of the original $3+1$ equations was to obtain a mathematically well-posed system. To this end, the removal of the mixed derivatives in the Ricci tensor has been achieved with a conformal-traceless reformulation and the introduction of new auxiliary evolution variables. We should therefore be able to numerically integrate constraint-satisfying initial data forward in time using the BSSN equations. However, we have not yet

specified the gauge. As we show next, our choice of gauge is based on both physical and numerical reasons.

2.3 Choosing the gauge

The search for a suitable gauge has been guided by the following requirements: On physical grounds, the coordinate evolution should be *singularity avoiding*, while numerically, the BSSN system supplemented with evolution equations for the lapse and shift should be strongly hyperbolic. Choosing a suitable foliation as well as suitable evolution of the spatial coordinates will be equally important to guarantee long-term stable simulations. For a geometric interpretation of the lapse and shift, see for instance Fischer and Marsden [1972].

Let us start by analysing the gauge freedom with the simplest choice, the so-called Gaussian coordinates, which are defined by choosing the following constant lapse and shift: $\alpha = 1$, $\beta^i = 0$. Foliations with $\alpha = 1$ are also known as geodesic slicing. In this gauge, the lines $x^i = \text{const}$ are orthogonal to the hypersurface (see Fig.2.1), and the time elapsed between hypersurfaces is the proper time measured by Eulerian observers. In this gauge, the geodesics emanating from a hypersurface Σ_t are orthogonal to the hypersurface, and furthermore irrotational [Senovilla 1998]. While the $3+1$ evolution equations simplify tremendously when using Gaussian coordinates, they are not useful in the numerical integration, as they are not singularity avoiding when the initial data contains singularities, as is the case for BHs (see Smarr and York [1978]). But even in spacetimes initially not containing singularities, the solution to the field equations necessarily develops coordinate singularities in finite time [Komar 1956] when using Gaussian coordinates.

There have been several attempts to remedy the inability of geodesic slicing to avoid singularities, such as *maximal slicing*, which amounts to choosing a lapse that corresponds to a vanishing trace of the extrinsic curvature ($K = 0$). This leads to an elliptic equation for the lapse ($D_i D^i \alpha = \alpha\, K_{ij} K^{ij}$ in vacuum). An alternative is the *harmonic* slicing condition [Choquet-Bruhat and Ruggeri 1983], corresponding to the following evolution equation for the lapse:

$$(\partial_t - \mathcal{L}_{\boldsymbol{\beta}})\alpha = -K\,\alpha^2. \tag{2.66}$$

A generalisation of the harmonic slicing condition (2.66) was given in Bona et al. [1995]:

$$(\partial_t - \mathcal{L}_{\boldsymbol{\beta}})\alpha = -K\,\alpha^2\, f(\alpha), \tag{2.67}$$

where $f(\alpha)$ is an arbitrary function. Note that $f(\alpha) = 1$ recovers the original harmonic slicing condition. Choosing $f(\alpha) = 2/\alpha$ leads to

$$(\partial_t - \mathcal{L}_{\boldsymbol{\beta}})\alpha = -2\,K\,\alpha, \tag{2.68}$$

which admits the following solution (for $\beta^i = 0$):

$$\alpha = 1 + \ln(\gamma). \tag{2.69}$$

This slicing is therefore known as **1+log slicing**. It is singularity avoiding [Bona et al. 1995] and has become (with various variations) one of the standard choices for NR simulations. Notably, two of the three breakthrough BBH simulations, the ones of Campanelli et al. [2006] and Baker et al. [2006], have used variations of the 1+log slicing.

The role of the shift is more elusive, and in early works it has been routinely set to zero. When dealing with spacetimes containing BHs, however, this has the unwanted effect of producing large stretching of the coordinates near the BH, with the coordinates falling into the BH as the simulation proceeds, causing the horizon to continuously grow. In axisymmetric spacetimes of rotating BHs, there is further complication since a vanishing shift produces large shears close to the BH due to frame dragging [Alcubierre 2008].

One successful cure to the fall-in of the spatial coordinates has been the so-called $\tilde{\Gamma}$-freezing of Alcubierre and Brügmann [2001], which amounts to 'freeze' the evolution of the conformal connection functions $\tilde{\Gamma}$ in the sense that their time derivative is vanishing, i.e. $\partial_t \tilde{\Gamma} = 0$. This prescription leads to an elliptic evolution equation for the shift. To avoid solving a computationally expensive elliptic equation, Alcubierre et al. [2003] introduced the so-called **hyperbolic $\tilde{\Gamma}$-driver** condition:

$$\partial_t^2 \beta^i = k\,\partial_t \tilde{\Gamma} - (\eta - \partial_t \ln(k))\,\partial_t \beta^i, \tag{2.70}$$

where k and η are positive functions, the latter playing the role of a damping term. This results in a hyperbolic evolution equation for the shift. By introducing the auxiliary variable B^i, one can write the $\tilde{\Gamma}$-driver as a set of two first-order evolution equations:

$$\partial_t \beta^i = k\,B^i, \tag{2.71}$$

$$\partial_t B^i = \partial_t \tilde{\Gamma}^i - \eta\,B^i. \tag{2.72}$$

The damping parameter η is a free parameter (see van Meter et al. [2006] for results using different values of η). In practice, when using mesh-refinement, the η parameter introduces a step size limit for the time step, as noted in Schnetter

[2010], where damping η as a function of the coordinate radius r is presented as a simple and effective solution to this problem.

We have therefore almost reached the goal of having rewritten the $3+1$ evolution equations in a form that is well-posed, as well as having found suitable gauge conditions that allow the long-term evolution of constraint-satisfying initial data. There is one last missing ingredient, however: If we start with a spacetime containing a true singularity, such as the centre of a BH, or a spacetime that will develop a true singularity, for instance through the gravitational collapse of a NS, we need a prescription to deal with the singular geometry at the location of the singularity. One way is to excise a certain volume containing the singularity. Specifically, one can "remove" the entire volume enclosed by the surface of the BH from the computational domain, which was first performed in Seidel and Suen [1992]. This method effectively cured the problems of numerically evolving spacetimes containing singularities, but has two apparent deficits: First, when using Cartesian grids, one needs to construct a so-called "Lego-sphere" [Cook et al. 1993] which only approximates the axisymmetric EH, and second, one needs to find appropriate boundary conditions for moving excision regions [Szilágyi et al. 2007] when the BHs are moving in the computational grid.

The alternative to singularity excision is the so-called **moving puncture** method, which is the standard choice for most groups.

2.4 The moving puncture

In Brandt and Brügmann [1997], the authors described a novel construction of multiple BH initial data where the spatial metric γ_{ij} on the initial hypersurface is defined as

$$\gamma_{ij} = (\psi)^4 \, \delta_{ij}, \tag{2.73}$$

where the conformal factor ψ is split in two parts, $\psi = \Psi_{\rm BL} + u$. $\Psi_{\rm BL}$ is the Brill-Lindquist conformal factor [Brill and Lindquist 1963] and u is an everywhere regular function that represents the non-singular part of the solution at the centre of the BHs, the "punctures", namely

$$\psi = \Psi_{\rm BL} + u, \quad \Psi_{\rm BL} = \sum_{i=1}^{N} \frac{m_i}{2|\mathbf{r} - \mathbf{r}_i|}, \tag{2.74}$$

where m_i is the mass of the i-th puncture and N is the total number of BHs on the grid. Using this split, one can solve for u (using the Hamiltonian constraint) without imposing special boundary conditions at the punctures. In this approach, the punctures remain fixed on the computational grid. This means that for

BBHs in orbital motion, the punctures are fixed in a co-rotating frame, so that the coordinates themselves need to evolve in such a way as to represent the orbital motion of the BHs. In Campanelli et al. [2006] and Baker et al. [2006] the authors discovered a way of evolving the puncture initial data without the need for keeping the punctures fixed, but allowing them to move freely on the grid. The singular part of the conformal factor can be evolved together with the regular part, using the following modification of the $\tilde{\Gamma}$-driver condition which amounts to adding a shift advection term [Baker et al. 2006]:

$$\partial_t \beta^i = \frac{3}{4}\,\alpha\, B^i, \tag{2.75}$$

$$\partial_t B^i = \partial_t \tilde{\Gamma}^i - \beta^i \partial_a \tilde{\Gamma}^a - \eta\, B^i. \tag{2.76}$$

The geometry and regularity of moving punctures was analysed by Hannam et al. [2007] and their equivalence to moving BHs established in Thornburg et al. [2007].

With these ingredients, namely the **conformal-traceless reformulation** of the 3+1 evolution system, the **1+log slicing**, the **$\tilde{\Gamma}$-driver** coordinate evolution (for the well-posedness of the BSSN system with a dynamical evolution of the lapse and shift see Beyer and Sarbach [2004] and Gundlach and Martín-García [2006]) and the **moving puncture** method, it is possible to long-term evolve constraint-satisfying initial data.

2.5 GW extraction

One of the most important outcomes of NR simulations is the calculation of gravitational waveforms. Indeed, the estimates for the initial BH masses of the recently discovered BBH merger GW150914, as well as the estimate of the final BH mass and its spin have been possible by comparing the measured GW signal with a large catalog of GW signals obtained from GR [Abbott et al. 2016]. While the early inspiral phase is very accurately described in the post-Newtonian formalism (see, for instance Blanchet et al. [1996]), and the predicted waveforms agree well with the results from NR up until about the last orbit of the merger [Baker et al. 2007], the use of NR simulations is indispensable for an accurate modelling of the GW signal produced by the actual merger of compact objects.

Einstein [1918] predicted the existence of GW by obtaining wave-like solutions to the linearised field equations in the weak-field regime. We can split the

spacetime metric $g_{\mu\nu}$ as Minkowski space $\eta_{\mu\nu}$ plus a non-flat metric $h_{\mu\nu}$:

$$g_{\mu\nu} = \eta_{\mu\nu} + h_{\mu\nu}. \tag{2.77}$$

In the weak-field limit, we assume that $|h_{\mu\nu}| \ll 1$. We adopt the convention that indices are raised and lowered with $\eta_{\mu\nu}$ when working to first-order in $h_{\mu\nu}$ [Weinberg 1972]

$$\eta^{\mu\sigma}\, h_{\sigma\nu} \equiv h^{\mu}{}_{\nu}. \tag{2.78}$$

The first-order Ricci tensor $R^{(1)}_{\mu\nu}$ then becomes

$$R^{(1)}_{\mu\nu} \equiv \frac{1}{2}\left(\Box h_{\mu\nu} - \partial_\lambda \partial_\mu h^{\lambda}{}_{\nu} - \partial_\lambda \partial_\nu h^{\lambda}{}_{\mu} + \partial_\mu \partial_\nu h^{\lambda}{}_{\lambda}\right), \tag{2.79}$$

where $\Box$ is the d'Alembert operator. The Einstein field equations then read

$$\Box h_{\mu\nu} - \partial_\lambda \partial_\mu h^{\lambda}{}_{\nu} - \partial_\lambda \partial_\nu h^{\lambda}{}_{\mu} + \partial_\mu \partial_\nu h^{\lambda}{}_{\sigma} = 16\pi\,(T_{\mu\nu} - \frac{1}{2}\,\eta_{\mu\nu} T^{\lambda}{}_{\lambda}). \tag{2.80}$$

Choosing a *harmonic coordinate system*, which is defined as

$$g^{\kappa\lambda}\,\Gamma^{\mu}{}_{\kappa\lambda} = 0, \tag{2.81}$$

we have to first order

$$\partial_\lambda h^{\lambda}{}_{\nu} = \frac{1}{2}\,\partial_\mu h^{\lambda}{}_{\lambda}, \tag{2.82}$$

which reduces the field equation to

$$\Box h_{\mu\nu} = -16\pi\,(T_{\mu\nu} - \frac{1}{2}\,\eta_{\mu\nu} T^{\lambda}{}_{\lambda}), \tag{2.83}$$

which is precisely a wave equation for the weak-field perturbation $h_{\mu\nu}$. One solution is given by the retarded potential

$$h_{\mu\nu}(t, \boldsymbol{x}) = 4 \int d^3\boldsymbol{y} \frac{S_{\mu\nu}(t - |\boldsymbol{x} - \boldsymbol{y}|, \boldsymbol{y})}{|\boldsymbol{x} - \boldsymbol{y}|}, \tag{2.84}$$

where

$$S_{\mu\nu} \equiv (T_{\mu\nu} - \frac{1}{2}\,\eta_{\mu\nu} T^{\lambda}{}_{\lambda}). \tag{2.85}$$

As seen from the wave equation for $h_{\mu\nu}$ (2.83) and also from the form of the time argument in $S_{\mu\nu}(t - |\boldsymbol{x} - \boldsymbol{y}|, \boldsymbol{y})$, GWs travel with a speed equal to 1, i.e. the speed of light.

We now turn to the extraction of GWs from numerical simulations. There are three main approaches to the extraction of gravitational waveforms from numerical data: Using gauge invariant perturbations of the Schwarzschild metric, also called the Moncrief [1974] formalism (for a review, see Nagar and Rezzolla [2005]), the Newman-Penrose formalism [Newman and Penrose 1962] and the Cauchy-characteristic extraction [Babiuc et al. 2005] (for an implementation see Reisswig et al. [2009]).

We will restrict ourselves to the description of the Newman-Penrose formalism, as this is the method we use to extract GWs in our simulations. In this formalism the extraction is performed using one of the so called *Newman-Penrose scalars* or *Weyl scalars*, Ψ_4. The Weyl scalars are the 10 independent components of the four dimensional Weyl tensor ${}^{(4)}C_{\alpha\beta\mu\nu}$, which is defined as follows:

$$ {}^{(4)}C_{\alpha\beta\mu\nu} \equiv {}^{(4)}R_{\alpha\beta\mu\nu} - \left(g_{\alpha[\mu} {}^{(4)}R_{\nu]\beta} - g_{\beta[\mu} {}^{(4)}R_{\nu]\alpha} \right) + \frac{1}{3} g_{\alpha[\mu} g_{\nu]\beta} {}^{(4)}R, \quad (2.86) $$

where square brackets around indices refer to the antisymmetric part of the tensor. The Weyl tensor has the same symmetries as the Riemann tensor, and in addition it is traceless, ${}^{(4)}C_{\alpha\beta\alpha\nu} = 0$. The Weyl tensor of a conformal metric $\tilde{g}_{\mu\nu} = \psi\, g_{\mu\nu}$ is equal to the Weyl tensor of the original metric $g_{\mu\nu}$. In particular, this means that a conformally flat spacetime has a vanishing Weyl tensor.

The Weyl scalars are formed by contracting the Weyl tensor of the spacetime with a complex null tetrad. This means choosing a tetrad of four vectors $\{l^\mu, k^\mu, m^\mu, \bar{m}^\mu\}$ such that:

$$ l^\mu l_\mu = k^\mu k_\mu = m^\mu m_\mu = \bar{m}^\mu \bar{m}_\mu = 0. \quad (2.87) $$

If one further imposes that $-l^\mu k_\mu = 1 = m^\mu \bar{m}_\mu$, one has constructed a so-called Newman-Penrose null tetrad. One way to construct such a null tetrad is by choosing l^μ and k^μ to be two real vectors that are radially outgoing and ingoing null vectors, respectively. We then construct two complex spatial vectors, m^μ and $\bar{m}^\mu$ that are orthogonal to l^μ and k^μ. Using the null tetrad, we can then contract it with the Weyl tensor to obtain the Weyl scalars. As noted above, for the extraction of GWs we are interested in the Weyl scalar Ψ_4 only, as one can show that it corresponds to outgoing gravitational radiation (see for instance Baumgarte and Shapiro [2010]). In terms of the Weyl tensor and the constructed null tetrad, Ψ_4 is given by

$$ \Psi_4 = {}^{(4)}\tilde{C}_{\alpha\beta\mu\nu}\, k^\alpha\, \bar{m}^\beta\, k^\mu\, \bar{m}^\nu. \quad (2.88) $$

In particular, the gravitational strain is related to Ψ_4 via:

$$ \Psi_4 = \ddot{h}_+ - i\, \ddot{h}_\times, \quad (2.89) $$

where h_+ and $h_\times$ are the plus and cross polarisation of the GW, respectively, and the double dot symbol indicates the second time derivative. In order to calculate the Weyl scalar Ψ_4 from the $3+1$ numerical data of a simulation one needs to express ${}^{(4)}\tilde{C}_{\alpha\beta\mu\nu}$ in terms of the $3+1$ variables and construct a suitable tetrad. We first note that the Weyl tensor is equal to the Riemann tensor in vacuum, so both tensors can be interchanged in vacuum. This means we can use

the Gauss, Codazzi and Ricci equations to express the four-dimensional Riemann tensor ${}^{(4)}R_{\alpha\beta\mu\nu}$ in terms of the $3+1$ variables. Following Baker, Campanelli, and Lousto [2002], the relevant components are given by:

$$ {}^{(4)}R_{ijkl} = R_{ijkl} + 2\,K_{i[k}K_{l]j}, \tag{2.90} $$

$$ {}^{(4)}R_{0jkl} = 2\,\partial_{[k}K_{l]j} + 2\,K_{a[k}\Gamma^{a}{}_{l]j}, \tag{2.91} $$

$$ {}^{(4)}R_{0j0l} = R_{jl} - K_{ja}K^{a}{}_{l} + KK_{jl}. \tag{2.92} $$

Finally, to construct a suitable null tetrad, one may proceed as described in Baker, Campanelli, and Lousto [2002].

2.6 BH mass and spin

BH belong to the most interesting objects in the universe, yet they are characterised by just one or two parameters, for Schwarzschild and Kerr BHs, respectively. The defining property of a Schwarzschild BH is its mass M, while a Kerr BH is completely defined by its mass M and angular momentum J, with the Kerr parameter a being $a = J/M$. When monitoring BHs in numerical simulations, one would therefore like to measure these quantities with great accuracy. In the case of a single vacuum BH, we could just measure the total mass of the spacetime in order to infer the BH mass, but as soon as we have multiple BHs in our computational domain, or BHs surrounded by matter, we need to measure the mass and angular momentum of the BH using its intrinsic properties. One such possibility would be the calculation of the mass and angular momentum using the surface of the BH, the so called *event horizon* (EH). The defining property of the EH is that it causally disconnects the interior of the BH from the outside, as no light rays emitted from within the EH can reach infinity but rather fall back to the singularity, while light rays emitted from the outside can reach infinity [Hawking and Ellis 1975]. In this sense, the EH is a global property of the 4 dimensional space, and one needs the entire time evolution of the spacetime to locate it. While it is possible to use the numerical data of a simulation to integrate geodesics backward in time to obtain the EH [Anninos et al. 1995, Libson et al. 1996], it would be desirable to obtain information about the mass and angular momentum that can be calculated on every spacelike hypersurface as the simulation proceeds.

There is an additional way to define a horizon for a BH, the so-called *apparent horizon* (AH). The AH can be computed locally in time, that is on each hypersurface Σ_t. (See Thornburg [2007] and references therein for definitions and implementations of EH and AH finders.) To define the AH, one begins

with the definition of a *marginally trapped surface* (MTS), which may be defined as a closed spacelike 2-surface in Σ_t with the property that its future-pointing outgoing null geodesics have zero expansion Θ. In terms of the $3+1$ variables, the expansion is defined as [York 1989]:

$$\Theta \equiv D_i n^i + K_{ij}\, n^i\, n^j - K = 0, \tag{2.93}$$

where n^i is the unit normal to the surface. The AH is then defined as the outermost MTS in Σ_t. Given a spacetime containing an AH, Hawking and Ellis [1975] have shown that its existence necessarily implies the existence of an EH, and therefore the existence of a BH. Finding an AH during a simulation therefore means that the spacetime contains a BH. Note, however, that the converse is *not* true: The existence of an EH does not guarantee the existence of an AH, this can be seen from the absence of an AH in certain slicings of the Schwarzschild spacetime [Wald and Iyer 1991]. When found, the AH is also always contained within the EH, and coincides with the latter for a stationary spacetime.

Once we have located an AH, we want to obtain its quasi-local mass and angular momentum. The precise definitions are provided in the so-called *isolated* and *dynamical horizon formalism* [Ashtekar, Beetle, and Fairhurst 1999, Ashtekar and Krishnan 2003] (see Ashtekar and Krishnan [2004] for a review of the formalisms, and for the application of the isolated and dynamical horizon formalism to NR see Dreyer et al. [2003] and Schnetter, Krishnan, and Beyer [2006]).

The BH spin is calculated by performing the following surface integral on the AH of the BH

$$J_{\rm AH} = \frac{1}{8\pi} \int_S \left(\psi^a R^b K_{ab}\right) dS, \tag{2.94}$$

where ψ^a is an approximate rotational Killing vector on the horizon that has to be determined numerically (see Dreyer et al. [2003]), R^b is the outward pointing unit vector normal to the horizon, K_{ab} is the extrinsic curvature on the horizon surface and dS is the surface element.

Once the spin is known, we can calculate the horizon mass $M_{\rm AH}$:

$$M_{\rm AH} = \frac{1}{2\,R_{\rm AH}} \sqrt{R_{\rm AH}^4 + 4\,J_{\rm AH}^2}, \tag{2.95}$$

where $R_{\rm AH} = (A_{\rm AH}/(4\pi))^{1/2}$ is the areal radius of the AH. In the case of a Kerr spacetime, the mass of the AH coincides with the Christodoulou mass [Christodoulou 1970, Smarr 1973]. Moreover, the irreducible mass of the horizon is

$$M_{\rm irr} = \sqrt{\frac{A_{\rm AH}}{16\pi}}. \tag{2.96}$$

As the area of the AH cannot decrease, the conservation of the irreducible mass provides a very good check for the accuracy of the simulation.

2.7 Total energy of the system

After having discussed the quasi-local mass of individual BHs in the previous section, we now turn to a definition of the total mass or energy contained in a hypersurface Σ_t. If the spacetime is asymptotically flat (for details see Jaramillo and Gourgoulhon [2011]), one can define the total energy contained in the hypersurface Σ_t as the following surface integral, called the ADM energy:

$$E_{\mathrm{ADM}} = \frac{1}{16\pi} \lim_{r\to\infty} \iint_S \left(\partial_j \gamma_{ij} - \partial_i \gamma_{jj}\right) n^i dS, \tag{2.97}$$

where n^i is the outward normal to the surface and the integration has to be carried out in Cartesian-like coordinates. Numerically, especially when using large domains and mesh refinement, calculating the ADM energy using (2.97) using a large surface might not be very accurate, as the resolution is reduced near the outer boundaries of the domain. It would therefore be preferable to evaluate the ADM energy as a volume integral. Following the derivation in Ó Murchadha and York [1974], we can also calculate the total energy in Σ_t as the following volume integral:

$$E_{\mathrm{ADM}} = \frac{1}{16\pi} \int_{\Sigma_t} \partial_l \left(\alpha\sqrt{\gamma}\gamma^{ij}\gamma^{kl}(\gamma_{ik,j} - \gamma_{ij,k})\right) d^3x. \tag{2.98}$$

In Yo, Baumgarte, and Shapiro [2002], the authors derive an equivalent volume integral for the total energy using the BSSN variables.

Chapter 3

General relativistic hydrodynamics

After having discussed the evolution of the spacetime, whose curvature represents the gravitational force felt by the matter fields, we now turn to the description of the intrinsic matter evolution. Most matter fields in astrophysical scenarios can be modelled as a fluid, including stars, neutron stars, and accretion discs. Therefore, we need a GRHD formalism describing the matter evolution which will be coupled to the evolution of the spacetime via the Einstein field equations. We incorporate all non-gravitational interactions of the matter fields in the stress-energy tensor $T_{\mu\nu}$ when coupling the matter to the evolution of the gravitational field. In this work, we have restricted those non-gravitational interactions to be those of the evolution of the fluid only, neglecting other possible contributions such as electromagnetic fields or radiation transport. Neglecting these is a highly idealised assumption, as we know that accretion tori are likely to be highly magnetised (as already indicated in the Introduction) and that neutrino cooling will play a significant role in the thermal properties of the torus due to the very high densities and temperatures found in these systems (see Foucart et al. [2014] for BHNS merger simulations with neutrino cooling).

In ordinary fluid dynamics, the fluid evolution is described by the Navier-Stokes equations. We will model the matter as a *perfect fluid*, which corresponds to the assumption that the fluid has no viscosity, and that there is no heat conduction in the fluid. Under these assumptions, the Navier-Stokes equations reduce

to the so-called *Euler equations*. We first describe the classical Euler equations and then proceed to the general relativistic form of the Euler equations[1].

In classical fluid dynamics, a perfect fluid is subject to the following three conservation laws: The conservation of mass, given by the *continuity equation*:

$$\partial_t \rho + \partial_a (\rho\, v^a) = 0, \tag{3.1}$$

where ρ is the fluid density, and v^i its velocity, the conservation of momentum, expressed in the *momentum (Euler) equation*:

$$\partial_t (\rho\, v_i) + \partial_a (\rho\, v_i\, v^a + p\, \delta^a{}_i) = 0, \tag{3.2}$$

where p is the fluid pressure, and the conservation of the total energy:

$$\partial_t E + \partial_a (v^a (E + p)) = 0, \tag{3.3}$$

where E is the total energy of the fluid, which can be written as:

$$E = \frac{1}{2} \rho\, v_a\, v^a + \rho\, \epsilon, \tag{3.4}$$

where ϵ is the specific internal energy of the fluid. The conservation of the total energy therefore reads

$$\partial_t \left(\frac{1}{2} \rho\, v_a\, v^a + \rho\, \epsilon \right) + \partial_a \left(v^a \left(\frac{1}{2} \rho\, v_a\, v^a + \rho\, \epsilon + p \right) \right) = 0. \tag{3.5}$$

We define the 5 dimensional *state vector* $\boldsymbol{w}$ as

$$\boldsymbol{w} = \begin{bmatrix} \rho \\ \rho\, v_i \\ \left(\frac{1}{2} \rho\, v_a\, v^a + \rho\, \epsilon \right) \end{bmatrix}, \tag{3.6}$$

and similarly define the 5×3 *flux matrix* $\boldsymbol{F}$, which is a function of $(\boldsymbol{w})$, as

$$\boldsymbol{F}(\boldsymbol{w}) = \begin{bmatrix} \rho\, v^a\, \delta^1{}_A \\ (\rho\, v_i\, v^a + p\, \delta^a{}_i)\, \delta^i{}_A \\ (\frac{1}{2} \rho\, v_a\, v^a + \rho\, \epsilon + p)\, v^a\, \delta^5{}_A \end{bmatrix}, \tag{3.7}$$

where we adopt the convention that upper case Latin indices run from 1 to n, where n is the dimension of $\boldsymbol{w}$. The $\delta^A{}_B$ therefore selects the rows of the flux matrix, which correspond to the equations of the system. Using the state vector and flux matrix as defined above, the classical Euler equations can then be written as the following system of first-order hyperbolic PDEs

$$\partial_t w_A + \partial_a F^a{}_A(w) = 0. \tag{3.8}$$

[1] In magnetised discs, the MRI is likely to provide an effective viscosity [Balbus and Hawley 1991]. Foucart et al. [2014] estimate the viscous timescale in their post-merger accretion tori to be ~ 0.1s, which is significantly longer than the simulations presented in this thesis.

A set of PDEs written in the above form is called a system of *conservation laws*. In the next section, we describe how the Euler equations (3.8) can be rewritten in a general relativistic manner in the 3 + 1 formalism. We follow the derivation laid out in Banyuls et al. [1997] (for further details and information on additional approaches see Font [2008]).

3.1 The general relativistic Euler equations in the 3 + 1 formalism

The starting point of the derivation of the general relativistic Euler equations are, analogously to their Newtonian version, the conservation of rest-mass density (the continuity equation) and the conservation of the fluid energy-momentum. A general relativistic perfect fluid has a rest-mass current J^μ and stress-energy tensor $T_{\mu\nu}$ given by

$$J^\mu = \rho\, u^\mu, \tag{3.9}$$

$$T^{\mu\nu} = \rho\, h\, u^\mu\, u^\nu + p\, g^{\mu\nu}, \tag{3.10}$$

where ρ is the fluid rest-mass density, u_μ the fluid four-velocity, P the fluid pressure and h the fluid enthalpy

$$h = 1 + \epsilon + \frac{p}{\rho}. \tag{3.11}$$

The general relativistic continuity equation and the conservation of energy-momentum are then given by

$$J^\mu{}_{;\mu} = 0, \tag{3.12}$$

$$T^{\mu\nu}{}_{;\mu} = 0. \tag{3.13}$$

As the system is underdetermined, we need to close it with an equation of state (EOS) that relates the fluid rest-mass density, pressure and internal energy, $p = p(\rho, \epsilon)$.

The three-velocity of the fluid as measured by observers at rest in the spatial hypersurface Σ_t (so-called *Eulerian observers*) is

$$v^i = \frac{u^i}{\alpha\, u^0} + \frac{\beta^i}{\alpha}, \tag{3.14}$$

and the corresponding Lorentz factor of the fluid, W, is defined as

$$W \equiv \alpha\, u^0 = \frac{1}{\sqrt{1 - \gamma_{ij} v^i v^j}}. \tag{3.15}$$

The set of variables $\{\rho, v^i, \epsilon\}$ describing the fluid is called the set of *primitive variables*. This set does not correspond to the fluid properties as measured by Eulerian observers in Σ_t, which are described by the so-called *conserved variables*: the conserved baryon number D, the conserved momentum density in the i-th direction S^i and the total energy E. In terms of the primitive variables, these are given by the following definitions:

$$D = \rho\, W, \tag{3.16}$$

$$S^i = \rho\, h\, W^2\, v^i, \tag{3.17}$$

$$E = \rho\, h\, W^2 - P. \tag{3.18}$$

Defining the state vector $\boldsymbol{U}(\boldsymbol{w})$ as

$$\boldsymbol{U}(\boldsymbol{w}) = \begin{bmatrix} D \\ S_i \\ \tau \end{bmatrix}, \tag{3.19}$$

the 5×3 flux matrix $\boldsymbol{F}(\boldsymbol{w})$ and source vector $\boldsymbol{S}(\boldsymbol{w})$ are given by

$$\boldsymbol{F}(\boldsymbol{w}) = \begin{bmatrix} D\,\hat{v}^i\,\delta^1{}_A \\ (S_j\,\hat{v}^i + P\,\delta^i_j)\,\delta^j_A \\ (\tau\,\hat{v}^i + P\,v^i)\,\delta^5{}_A \end{bmatrix}, \tag{3.20}$$

$$\boldsymbol{S}(\boldsymbol{w}) = \begin{bmatrix} 0 \\ T^{\mu\nu}(\partial_\mu g_{\nu i} - \Gamma^\lambda_{\mu\nu} g_{\lambda i}) \\ \alpha(T^{\mu 0}\partial_\mu(\ln\alpha) - T^{\mu\nu}\Gamma^0_{\mu\nu}) \end{bmatrix}, \tag{3.21}$$

where $\tau \equiv E - D$ and $\hat{v}^i \equiv v^i - \beta^i/\alpha$. Therefore, it is possible to write the conservation laws of energy-momentum and the continuity equation as a conservation law by means of the conserved variables, resulting in the following first-order, flux-conservative hyperbolic system of equations [Banyuls et al. 1997]:

$$\frac{1}{\sqrt{-g}}\left[\partial_0(\sqrt{\gamma}\,U_A) + \partial_i(\sqrt{-g}\,F^i_A)\right] = S_A, \tag{3.22}$$

where $g \equiv \det(g_{\mu\nu}) = \alpha\sqrt{\gamma}$. This constitutes the general relativistic version of the Euler equations in the $3+1$ formalism, which is known as the so-called *Valencia formulation*.

3.2 High-resolution shock-capturing methods

Systems of nonlinear hyperbolic PDEs such as the Euler equations or the GRHD equations (3.22) are characterised by the fact that smooth initial data can develop

discontinuities in the variables in finite time[2]. The reason the GRHD equations in the *Valencia formulation* were written in conservative form is that, in such a form, a numerical scheme that converges guarantees the correct Rankine-Hugoniot conditions across discontinuities, which is called the *shock-capturing* property. This property is at the heart of high-resolution shock-capturing (HRSC) methods that guarantee that the physics of the flow will be correctly modelled by the numerical scheme in the presence of discontinuities in the fluid variables. Moreover, finite difference schemes written in conservation form guarantee that the convergence of the solution (if it exists) will be to one of the *weak solutions* of the system of PDEs [Lax and Wendroff 1960]. Weak solutions are characterised by being solutions to the integral form of the conservation system. The set of all weak solutions is too large to be of practical use, as many (numerically) admissible weak solutions will not represent physically relevant solutions. Thus there is need for an additional (thermodynamic) condition, the so-called *entropy condition* (namely that the entropy of a fluid element must increase when crossing a discontinuity) to guarantee that the numerical scheme will converge to the physical solution. The convergence of the numerical scheme is closely related to its stability, and one useful measure is the *total-variation* (TV) stability (see e.g. LeVeque [1992] for a detailed discussion).

Additionally, numerical schemes written in conservation form guarantee that the conserved quantities of the system are numerically conserved in the absence of sources or sinks. This means that the change of the state vector U_A in time in a domain $\mathcal{V}$ that does not contain sources or sinks will be given by the fluxes F^i_A through the boundaries of the domain $\partial\mathcal{V}$, a three dimensional surface which is defined as the standard-oriented hyper-parallelepiped consisting of two spacelike surfaces $\{\Sigma_{x^0}, \Sigma_{x^0+\Delta x^0}\}$ and the timelike surfaces $\{\Sigma_{x^i}, \Sigma_{x^i+\Delta x^i}\}$ joining the two temporal slices together. System (3.22) is thus expressed in integral form

$$\int_{\mathcal{V}} \frac{1}{\sqrt{-g}}\, \partial_0(\sqrt{\gamma}\, U_A)\, d\mathcal{V} + \int_{\mathcal{V}} \frac{1}{\sqrt{-g}}\, \partial_i(\sqrt{-g}\, F^i_A)\, d\mathcal{V} = \int_{\mathcal{V}} S_A\, d\mathcal{V}, \qquad (3.23)$$

[2]While it is known that physical shocks (discontinuities in the spacetime) do not exist in GR, there is nevertheless the possibility of the formation of gauge shocks when the kinematical variables (lapse and shift) are evolved as hyperbolic equations, such as the $1+\log$ slicing (2.67) and the $\tilde{\Gamma}$-driver (2.70) described in Section 2.3 above. Alcubierre [2003] has investigated the formation of shocks for the family of $1+\log$ slicing conditions and found a member that is shock avoiding. Additionally, it appears as if the formation of shocks in the evolution of the lapse is suppressed due to under-resolution caused by the shift in the puncture method in 3D simulations [Garfinkle, Gundlach, and Hilditch 2008]. When performing the shift evolution via the $\tilde{\Gamma}$-driver, it seems that $\tilde{\Gamma}$ acts as an effective "shock-absorber" [van Meter et al. 2006], as this shift evolution equation have proven to be very stable.

where $d\mathcal{V} = \sqrt{-g}\, d^4x$. This is the starting point to devise HRSC schemes to solve it. Specifically, the flux integrals in (3.23) are given by

$$\begin{aligned}\int_{\mathcal{V}} \frac{1}{\sqrt{-g}}\, \partial_i(\sqrt{-g}\, F^i_A)\, d\mathcal{V} = &\int_{\Sigma_{x^1+\Delta x^1}} \sqrt{-g}\, F^1_A\, dx^2\, dx^3 - \int_{\Sigma_{x^1}} \sqrt{-g}\, F^1_A\, dx^2\, dx^3,\\ &+ \int_{\Sigma_{x^2+\Delta x^2}} \sqrt{-g}\, F^2_A\, dx^1\, dx^3 - \int_{\Sigma_{x^2}} \sqrt{-g}\, F^2_A\, dx^1\, dx^3,\\ &+ \int_{\Sigma_{x^3+\Delta x^3}} \sqrt{-g}\, F^3_A\, dx^1\, dx^2 - \int_{\Sigma_{x^3}} \sqrt{-g}\, F^3_A\, dx^1\, dx^2.\end{aligned} \tag{3.24}$$

This means that the time integration of the conserved variables is given by the interface fluxes of matter and energy-momentum of the fluid, as well as the (cell-centred) sources. One can therefore approximate those *numerical* fluxes (which depend on the solution at the cell interfaces) as the time-averaged fluxes across cell interfaces during a timestep as

$$(\hat{F}^i_A)_{i+\frac{1}{2}} \approx \frac{1}{\Delta t} \int_{t^n}^{t^{n+1}} F^i_A(U_A(x^{i+\frac{1}{2}}, x^0)). \tag{3.25}$$

In general, the approximation to the real solution on a grid with finite resolution will be a piecewise continuous function, which means that the fluxes can be obtained by solving local Riemann problems at cell interfaces, an idea first described in Godunov [1959].

Riemann problems are IVPs with discontinuities in the solution. During the evolution, a discontinuity in the fluid variables decays into shock waves, rarefaction waves and contact discontinuities. Shock waves move from the higher to lower density regions, while rarefaction waves move in the opposite direction. Contact discontinuities are characterised by a discontinuity in the density, while both pressure and velocity are constant across them. In order to solve the Riemann problem, we need to obtain the spectrum (eigenvalues and eigenvectors) of the first-order system. As explained in Appendix A, we need to bring system (3.22) into the following quasi-linear form

$$\partial_t U_A + m^{aB}{}_A(U)\, \partial_a U_B + S_A(U) = 0, \tag{3.26}$$

in order to compute the spectrum and eigenvectors of the matrix $m^{aB}{}_A(U)$. Once obtained, the Riemann problem is solved analytically to obtain the numerical fluxes. In order to rewrite the system in quasi-linear form, one obtains the *Jacobian* of the system by taking partial derivatives of the flux matrix with respect to the state vector. The resulting three (one for each spatial dimension)

5×5 Jacobian matrices are then combined into the block matrix ${m^{aB}}_{A}(U)$

$$ {m^{iB}}_{A}(U) = \alpha \, \partial_{U_A} F^{iB}(U), \tag{3.27} $$

which has real (but degenerate) eigenvalues and a complete set of eigenvectors [Banyuls et al. 1997] (the Jacobian ${m^{iB}}_{A}(U)$ is therefore diagonizable and system (3.22) is therefore strongly hyperbolic). The features of the solution travel at characteristic speeds given by the eigenvalues of the Jacobian ${m^{iB}}_{A}(U)$.

Specifically, for a fluid moving in the x-direction, the eigenvalues are given by

$$ \lambda_0 = \alpha v^x - \beta^x \quad \text{(triple)}, \tag{3.28} $$

$$ \lambda_\pm = \frac{\alpha}{1 - v^2 c_s^2} \left(v^x (1 - c_s^2) \pm c_s \sqrt{(1 - v^2)[\gamma^{xx}(1 - v^2 c_s^2) - v^x v^x (1 - c_s^2)]} \right) - \beta^x, \tag{3.29} $$

where $v^2 = \gamma_{ab} v^a v^b$ and c_s is the sound speed in the fluid, whose square is given by

$$ c_s^2 = \left. \frac{\partial p}{\partial E} \right|_s = \frac{1}{h} \left(\left. \frac{\partial p}{\partial \rho} \right|_\epsilon + \frac{p}{\rho^2} \left. \frac{\partial p}{\partial \epsilon} \right|_\rho \right). \tag{3.30} $$

Note that the Newtonian limit of the eigenvalues (in which $\alpha \to 1, \beta^i \to 0, v^x \ll 1$) is correctly recovered ($\lambda_0 = v^x, \lambda_\pm = v^x \pm c_s$).

In practice, obtaining the numerical fluxes using the analytical solution of the Riemann problem is often not feasible, in particular in multidimensional simulations. One avoids finding the exact solution and uses linearised (approximate) Riemann solvers instead, which still make use of the spectrum and the eigenvectors of the first-order system. Examples of approximate Riemann solvers are the Harten-Lax-van Leer-Einfeldt (HLLE) solver [Harten, Lax, and Leer 1983, Einfeldt 1988], the approximate solver of Roe [1981] and the Marquina flux formula [Donat and Marquina 1996, Aloy et al. 1999].

The fluid data at the cell interfaces needed to obtain the numerical fluxes via the solution of local Riemann problems could simply be obtained as the average of the data at neighbouring cell centres (which only yields overall first-order methods). A wide variety of higher order cell-reconstruction methods are available in the literature (see e.g. Toro [2013]). Examples of higher order reconstruction schemes are the piecewise-parabolic method (PPM) [Colella and Woodward 1984] and essentially non-oscillatory (ENO) methods [Harten et al. 1987]. Regardless of their spatial order for smooth solutions, these reconstruction techniques always reduce to first-order in the presence of physical shocks and local extrema of the fluid variables (such as the central density of a NS, for instance).

While the choice of variables is crucial to obtain the GRHD evolution equations in conservative form, it is usually the primitive variables that are reconstructed at the cell interfaces. To do this, one needs a conservative-to-primitive scheme which inverts Eqs. (3.16)-(3.18), involving numerical root-finding. Once we have obtained the numerical fluxes via the solution of local Riemann problems, we update the solution of the conserved variables by one timestep with the numerical fluxes and the sources. This is usually done employing high-order, conservative Runge-Kutta schemes [Shu and Osher 1988].

We finish this chapter with a summary of the steps necessary to advance the solution by a timestep in a numerical GRHD scheme coupled to the spacetime evolution:

- Advance spacetime evolution in time
- Calculate the source vector $S_A(U)$ at all grid points
- Reconstruct primitive variables at cell interfaces using high-order reconstruction methods
- Set up local Riemann problems using the reconstructed primitive variables at cell interfaces as initial data
- Calculate the numerical fluxes at cell interfaces by solving the local Riemann problems using approximate Riemann solvers
- Advance the solution of the conserved variables in time by using the obtained numerical fluxes and sources
- Recover primitive variables
- Update the stress energy-tensor $T_{\mu\nu}$ with the new matter field configuration
- Update spacetime variables in time using the new matter field configuration as source

Chapter 4

Computational framework

The simulations reported in this thesis are performed using the publicly available [`Einstein Toolkit` n.d.] code (described in detail in Löffler et al. [2012], to which we refer the reader for a complete overview of the components of the `ET`). In the following, we provide a brief summary of the main components of the toolkit we use in our simulations.

The `ET` is a code for relativistic astrophysics simulations, which is based on the modular [`Cactus Computational Toolkit` n.d.] [Goodale et al. 2003, Allen et al. 2011]. `Cactus` provides a very small core of base functionalities (the so-called "flesh") coupled to general modules commonly called "thorns". Simulations of astrophysical systems often span a very wide range of distance scales, making large domains with high resolutions necessary. In the BH–torus systems we are investigating in this thesis, we need very high resolution to capture the correct dynamics of the system, while GW extraction needs to be performed in the "wave zone", that is, far away from the sources of the gravitational field. In 3D simulations, large domains with high resolution quickly become prohibitively expensive in terms of both memory and computational power requirements. We are therefore in need of mesh refinement, where the resolution is gradually decreased away from the origin. Adaptive mesh refinement (AMR) in the `ET` is provided by the [`Carpet` n.d.] driver [Schnetter, Hawley, and Hawke 2004, Schnetter et al. 2006], which employs the Berger-Oliger algorithm [Berger and Oliger 1984] with subcycling in time. Using AMR is crucial when the resolution in the domain needs to be dynamically adapted to the system (for instance to add finer mesh refinement levels during the late stages of a NS collapse or to follow the BHs with the finest meshes in a BBH simulations as they move through the computational domain). In our simulations, we need to follow the

central BH of the BH–torus system as it starts moving due to the development of the PPI in the disc.

The `ET` provides numerical solvers that use the infrastructure of `Cactus` and `Carpet` to numerically evolve the Einstein equations (2.9). The main ingredients are methods to evolve the Einstein equations based on the $3+1$ formalism described in Chapter 2 coupled to methods to solve the GRHD equations in the Valencia formulation described in Chapter 3. These tasks are performed by the `McLachlan` and `GRHydro` codes, respectively. In addition, there are numerous thorns performing diagnostics during simulations. We will describe these thorns below and describe in detail a new thorn for the `ET` that was written as part of this thesis with the aim of analysing the disc evolution of the simulations reported in this thesis. We follow the description of the disc analysis thorn by a short introduction to the fluid tracer particles that we have employed in the simulations of Chapter 7.

4.1 McLachlan

The left hand side of the Einstein field equations (2.9) is evolved using the `McLachlan` code [Brown et al. 2009, Reisswig et al. 2011], solving the BSSN equations. The `McLachlan` code is generated automatically from tensorial equations using the `Kranc` code [Husa, Hinder, and Lechner 2006].

Using `McLachlan`, we evolve the BSSN evolution equations using a fourth-order accurate, centred finite-differencing operator, while the advection terms for the shift vector are evolved with a fourth-order upwind stencil. We apply fifth-order Kreiss-Oliger dissipation to all spacetime variables to achieve overall fourth-order accuracy for the spacetime evolution. Using the BSSN evolution system together with the $1+\log$ and $\tilde{\Gamma}$-driver gauge evolution conditions, the `McLachlan` code can evolve stably a single puncture for several light crossing times, see e.g. Löffler et al. [2012].

The specific evolution equations used in `McLachlan` are the following:

$$\partial_0 \alpha = -\alpha^2 \, f(\alpha, \phi, x^\mu)(K - K_0(x^\mu)) \,, \tag{4.1}$$

$$\partial_0 K = -\gamma^{ij} \tilde{D}_i \, \tilde{D}_j \, \alpha + \alpha(\tilde{A}^{ij} \, \tilde{A}_{ij} + \frac{1}{3} K^2) + 4\pi(E + \gamma^{ij} \, S_{ij}) \,, \tag{4.2}$$

$$\partial_0 \beta^i = \alpha^2 \, G(\alpha, \phi, x^\mu) \, B^i \,, \tag{4.3}$$

$$\partial_0 B^i = e^{-4\,\phi} \, H(\alpha, \phi, x^\mu) \, \partial_0 \tilde{\Gamma}^i - \eta^i(B^i, \alpha, x^\mu) \,, \tag{4.4}$$

$$\partial_0 \phi = -\frac{1}{6} \left(\alpha \, K - \partial_k \beta^k \right) \,, \tag{4.5}$$

$$\partial_0 \tilde{\gamma}_{ij} = -2\,\alpha\,\tilde{A}_{ij} + 2\,\tilde{\gamma}_{k(i}\partial_{j)}\beta^k - \frac{2}{3}\,\tilde{\gamma}_{ij}\,\partial_k\beta^k\,, \tag{4.6}$$

$$\begin{aligned}\partial_0 \tilde{A}_{ij} = {} & e^{-4\,\phi}\left(\alpha\,\tilde{R}_{ij} + \alpha\,R^{\phi}_{ij} - \tilde{D}_i\tilde{D}_j\alpha\right)^{\mathrm{TF}} \\ & + \alpha\,K\,\tilde{A}_{ij} - 2\,\alpha\,\tilde{A}_{ik}\,\tilde{A}^k_{\ j} + 2\,\tilde{A}_{k(i}\partial_{j)}\beta^k \\ & - \frac{2}{3}\tilde{A}_{ij}\,\partial_k\beta^k - 8\,\pi\,\alpha e^{-4\,\phi}\,S^{\mathrm{TF}}_{ij}\,,\end{aligned} \tag{4.7}$$

$$\begin{aligned}\partial_0 \tilde{\Gamma}^i = {} & -2\,\tilde{A}^{ij}\,\partial_j\alpha \\ & + 2\,\alpha\left(\tilde{\Gamma}^i_{kl}\,\tilde{A}^{kl} + 6\,\tilde{A}^{ij}\,\partial_j\phi - \frac{2}{3}\,\tilde{\gamma}^{ij}\,K_{,j}\right) \\ & - \tilde{\Gamma}^j\,\partial_j\beta^i + \frac{2}{3}\,\tilde{\Gamma}^i\,\partial_j\beta^j + \frac{1}{3}\,\tilde{\gamma}^{ik}\,\beta^j_{,jk} + \tilde{\gamma}^{jk}\,\beta^i_{,jk} \\ & - 16\,\pi\,\alpha\,\tilde{\gamma}^{ik}\,S_k\,,\end{aligned} \tag{4.8}$$

where f, K_0, G, H and η^i are functions controlling the gauge evolution, the $^{\mathrm{TF}}$ superscript denotes the trace-free part of an expression and we have used the following shorthand notation, $\partial_0 = \partial_t - \beta^j\,\partial_j$. The coupling to the stress-energy tensor $T^{\mu\nu}$ is done via the projections (2.26)-(2.29). This system constitutes the so-called ϕ-variant of the BSSN formulation (see Pollney et al. [2011] for other possible variations).

The 1+log slicing (2.67) for the evolution of the lapse corresponds to the following choice of f and K_0

$$f(\alpha, \phi, x^\mu) \equiv \frac{2}{\alpha}\,, \tag{4.9}$$

$$K_0(x^\mu) \equiv 0\,, \tag{4.10}$$

and the $\tilde{\Gamma}$-driver shift condition (2.70) for the evolution of the shift is achieved by choosing

$$G(\alpha, \phi, x^\mu) \equiv \frac{3}{4\,\alpha^2}\,, \tag{4.11}$$

$$H(\alpha, \phi, x^\mu) \equiv e^{-4\,\phi}\,, \tag{4.12}$$

$$\eta^i(B^i, \alpha, x^\mu) \equiv \eta\,B^i\,q(r)\,, \tag{4.13}$$

where $q(r)$ is a function that attenuates the $\tilde{\Gamma}$-driver depending on the radius [Schnetter 2010] and η is a damping parameter. The strong hyperbolicity of the BSSN system implemented in `MacLachlan` has been discussed in Brown et al. [2009]. For the simulations reported in Chapter 6 we use a dynamically evolved damping parameter η using the formulation of Alic et al. [2010], adapted to a single puncture. The simulations of Chapter 7, however, are performed using the standard $\tilde{\Gamma}$-driver evolution of the shift, with a fixed and radially damped η.

The change in the gauge evolution is motivated by greater compatibility with the standard `McLachlan` code and also serves as an important check to quantify the influence of the gauge evolution on the physics of the BH–torus system.

We apply Sommerfeld outgoing boundary conditions for all BSSN evolution variables with an extrapolation to include the part of the boundary conditions that does not behave like a simple outgoing wave [Alcubierre et al. 2000], implemented in the `NewRad` thorn. The boundary condition assumes a radial outgoing wave with wave speed v_0, so that any tensor component of the evolution variables A can be modelled as

$$A = A_0 + \frac{u(r - v_0 t)}{r}, \tag{4.14}$$

where A_0 is the value at infinity and u a spherically symmetric perturbation. The value at infinity and wave speed depend on each variable and have to be specified (for example, $\alpha_0 = 1$ and $\beta^i{}_0 = 0$). Assuming this behaviour of the fields implies the following differential equation:

$$\partial_t A = -v_0 \frac{x^i}{r} A - v_0 \frac{A - A_0}{r}. \tag{4.15}$$

To account for contributions to the boundary that do not behave as pure waves, it is necessary to incorporate extra parts decaying with a certain power of the radius, defining a corrected source term $(\partial_t A)^*$ as follows:

$$(\partial_t A)^* = (\partial_t A) + \left(\frac{r}{r - n^i \partial_i r} \right)^p n^i \partial_i (\partial_t A), \tag{4.16}$$

where n^i is the unit normal to the respective boundary face. As stated in Löffler et al. [2012], using $p = 2$ usually works well in practice, which is the value we use for all simulations reported in this thesis. This type of boundary condition gives stable evolutions if applied far enough from the sources of the gravitational field. The outer boundaries produce errors traveling inwards, hence the need to place the outer boundaries sufficiently far away to causally disconnect them from the central regions of the domain.

4.2 GRHydro

The evolution of the hydrodynamics is performed by `GRHydro` [Baiotti et al. 2005, Löffler et al. 2012, Mösta et al. 2014], a code that solves the GRHD equations in flux-conservative form, in the so-called Valencia formulation [Banyuls et al. 1997, Font 2008], using HRSC methods.

We use the PPM [Colella and Woodward 1984] to reconstruct the primitive variables at the cell interfaces and Marquina's flux formula [Donat and Marquina 1996, Aloy et al. 1999] to compute the numerical fluxes. Differently from the original implementation [Baiotti, Hawke, and Rezzolla 2007], we reconstruct the quantities Wv^i instead of the three-velocities v^i. This guarantees that the velocities reconstructed at the cell boundaries remain subluminal even under extreme conditions like those encountered near the AH of the BH [Galeazzi et al. 2013]. We have found this measure to be crucial in guaranteeing long-term stable evolutions of the fluid near the AH.

The corresponding first-order flux-conservative hyperbolic evolution system evolved in `GRHydro` is:

$$\frac{\partial \boldsymbol{U}}{\partial t} + \frac{\partial \boldsymbol{F}^i}{\partial x^i} = \boldsymbol{S}\,, \tag{4.17}$$

with the vector of conserved quantities

$$\boldsymbol{U} = [D, S_i, \tau]\ , \tag{4.18}$$

and the vector of fluxes

$$\boldsymbol{F}^i = \left[D\,\hat{v}^i, S_j\,\hat{v}^i + \delta^i_j\,p, \tau\,\hat{v}^i + p\,v^i\right]\ , \tag{4.19}$$

with $\hat{v}^i = \alpha v^i - \beta^i$. In `GRHydro`, the components of the vector of sources are calculated using the extrinsic curvature in order to remove all time derivatives that are present in (3.21), resulting in

$$\boldsymbol{S} = \begin{bmatrix} 0 \\ \frac{\alpha}{2} S^{kl}\partial_i \gamma_{kl} + S_k \partial_i \beta^k - (\tau + D)\,\partial_i \alpha \\ \alpha S^{kl} K_{kl} - S^j \partial_j \alpha \end{bmatrix}\ . \tag{4.20}$$

As necessary in GRHD computations, the primitive variables are calculated from the conserved quantities at each time step of the evolution using a root-finding procedure (see Mösta et al. [2014] and references therein for details).

In our simulations the torus is initially described by a polytropic EOS

$$p = K\rho^\Gamma\,, \tag{4.21}$$

where K is the polytropic constant and Γ the adiabatic exponent. The polytropic EOS describes a cold, degenerate gas of (noninteracting) fermions in both the non-relativistic and ultra-relativistic limit [Shapiro and Teukolsky 1986] and the polytropic EOS can be used to model NS as non-ideal Fermi gases [Alcubierre 2008]. While this EOS is only a poor approximation to the real EOS describing matter at near nuclear densities, there are still large theoretical uncertainties concerning the real EOS of NS and very dense matter as encountered in our

discs. NS are therefore still often modelled by polytropic EOS (see, e.g. Faber and Rasio [2012]) and the initial data have been built with these considerations in mind as well. During the evolution we allow for non-isotropic changes in the fluid flow such as shocks and for this reason we use an ideal gas EOS,

$$p = (\Gamma - 1)\rho\epsilon\,, \tag{4.22}$$

where Γ is the same adiabatic index as in (4.21). As indicated in Tables 6.1 and 6.2, we use $\Gamma = 4/3$ for the evolution of all our models. A Gamma-law EOS with $\Gamma = 4/3$ is commonly adopted to describe a single-component perfect gas in the relativistic regime. Our work focuses in particular on the comparison with previous work on tilted accretion discs by Fragile and Anninos [2005], as well as the works of Korobkin et al. [2011] and Kiuchi et al. [2011] where this value of Γ was also adopted.

As a grid-based code `GRHydro` cannot evolve regions without matter content as the determinant of the Jacobian (3.27) becomes zero in those regions. As is customary, a low density atmosphere (typically several orders of magnitude below the maximum density of the initial data) fills those grid points that should belong to vacuum regions. In all our simulations we set the density of the atmosphere to 10^{-8} times the initial maximum rest-mass density in the torus. Although fully evolved, the dynamical effects of the atmosphere regions can be neglected.

The set of complex time-dependent PDEs of the GRHD evolution coupled to the BSSN equations is integrated using the method of lines (MoL) [Hyman 1976] using a $4:2$ multi-rate Runge-Kutta (RK) algorithm that evolves the spacetime using a fourth-order RK and the fluid using a second-order RK.

4.3 Diagnostics

We measure the BH mass during the evolution using the `AHFinderDirect` thorn which implements the AH finder described in Thornburg [2003]. The BH spin magnitude and direction are measured using the `QuasiLocalMeasures` thorn [Dreyer et al. 2003, Schnetter, Krishnan, and Beyer 2006] (see also the review of quasi-local methods in Szabados [2009]). We measure the spin direction using the so-called flat-space rotational Killing vector method of Campanelli et al. [2007], which can be derived using Weinberg's pseudotensor in Gaussian coordinates and is equal to the Komar angular momentum integral when the latter is expressed in a foliation adapted to the axisymmetry of spacetime [Mewes, Font, and Montero 2015], see Chapter 5. To track the time-dependent location

of the puncture during the evolution, we use the `PunctureTracker` thorn. GWs are extracted using a multipole expansion of the Weyl scalar Ψ_4 at different, user specified radii. The thorns `Multipole` and `WeylScal4` compute the respective quantities. The accuracy of the `WeylScal4` thorn is described in Hinder, Wardell, and Bentivegna [2011], recovering correctly the radial fall-off rates for the Weyl scalars predicted by the peeling theorem. We calculate the mass accretion rate $\dot{M}$ as the instantaneous flow of matter through the AH, using the `Outflow` thorn. We monitor the error in our simulations using the Hamiltonian and momentum constraint, calculated in the thorn `ML_ADMConstraints`. The two constraints are calculated directly from Eqs. (2.31) and (2.32) using finite-differencing.

It is difficult to judge how large the constraint violations may become during a simulation before one can no longer trust the results. In some works, normalised Hamiltonian and momentum constraints are used to monitor the error evolution (see, e.g. Etienne et al. [2008]) where the Hamiltonian and momentum constraint are divided by the Euclidean norm of all terms entering their calculation. We note that when using mesh refinement levels and large computational domains, this normalisation is not useful, as some terms in Eqs. (2.31) and (2.32) are being calculated directly using finite differences of γ_{ij} or K_{ii}. These quantities are therefore computed with a different accuracy in different mesh refinement domains while the rest of the terms is simply being read off the grid. As a result, normalising the constraints by the Euclidean norm of all the terms included in the computation causes them to approach one away from the origin, as the resolution becomes coarser with each refinement level. In practice, one is therefore concerned with the growth of constraint violations rather than their absolute values, which, for the reasons indicated above, are not a useful measure. Rapidly growing constraint violations usually indicate that a crash is soon to happen in the simulation.

4.4 The disc analysis thorn

One of the main tasks of this work has been the development of a thorn for the `ET` to analyse the disc evolution during the simulations we performed. The thorn and its capacities have grown during the duration of this work and we will therefore describe its latest version.

The following global quantities are calculated: The total disc rest mass M_0, the total disc gravitational mass M, the total disc angular momentum $J_{\rm Disc}$, the total rotational kinetic energy T of the disc, and the total internal energy of the disc $E_{\rm int}$. These quantities are defined as follows (see, for instanceBaumgarte

and Shapiro [2010]):

$$M_0 = \int D\,\sqrt{\gamma}\,d^3x\,, \tag{4.23}$$

$$M = \int (-2\,T^0{}_0 + T^\mu{}_\mu)\,\alpha\,\sqrt{\gamma}\,d^3x\,, \tag{4.24}$$

$$J_{\rm Disc} = \int T^0{}_\phi\,\alpha\,\sqrt{\gamma}\,d^3x\,, \tag{4.25}$$

$$T = \int \frac{1}{2}\,\frac{u^\phi}{u^0}\,T^0{}_\phi\,\alpha\,\sqrt{\gamma}\,d^3x\,, \tag{4.26}$$

$$E_{\rm int} = \int \epsilon\,D\,\sqrt{\gamma}\,d^3x\,. \tag{4.27}$$

To quantify the growth of non-axisymmetric modes in the disc, we compute 3D Fourier integrals of the density, as described in Baiotti et al. [2007]. The amplitude of the m-th mode is given by:

$$D_m = \int \rho\,e^{-i\,m\,\phi}\,\sqrt{\gamma}\,d^3x\,. \tag{4.28}$$

The mode calculation in Eq. (4.28) implicitly assumes the total disc angular momentum to be aligned with the z-axis. For arbitrary orientations of the disc, this leads to wrong results in the calculation of the modes. We therefore also calculate the amplitude of the non-axisymmetric modes using the total disc angular momentum vector as our reference axis.

When using computational domains that are very large, the total mass of the atmosphere can be a non-negligible fraction of the total rest-mass of the torus. We therefore have to ignore cells corresponding to the atmosphere when integrating the global quantities above and in the calculations of the non-axisymmetric modes in the disc.

4.4.1 Twist and tilt

In order to keep track of the response of the tilted accretion disc and to check for LT precession and the occurrence of the Bardeen-Patterson effect, we measure two angles, the twist (precession) and tilt (inclination) of the disc [Nelson and Papaloizou 2000]. We closely follow the description of the angles given by Fragile and Anninos [2005], with a modification in the calculation of the twist, and furthermore adapt the way they are calculated.

The main idea is to split the disc up into a series of annuli and calculate the angular momentum vector of the matter, $\mathbf{J}_{\rm Disc}(r)$, for each individual annulus.

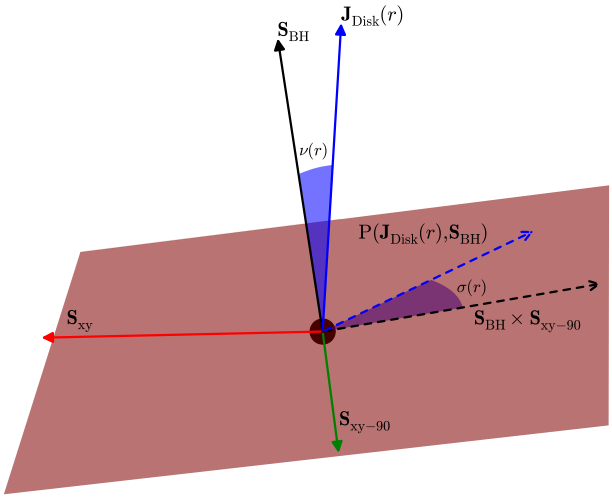

Figure 4.1 The figure visualises the various vectors and projections we use to calculate the twist and tilt in the disc. Note that all vectors in the figure have been scaled to unity for better visualisation.

Using this vector, we define two angles, the twist $\sigma(r)$

$$\sigma(r) = \angle(\mathbf{S}_{\rm BH} \times \mathbf{S}_{\rm xy-90}, \mathrm{P}(\mathbf{J}_{\rm Disc}(r), \mathbf{S}_{\rm BH}))\,, \tag{4.29}$$

and the tilt $\nu(r)$

$$\nu(r) = \angle(\mathbf{S}_{\rm BH}, \mathbf{J}_{\rm Disc}(r))\,, \tag{4.30}$$

where

$$\mathrm{P}(\mathbf{a}, \mathbf{n}) = \mathbf{a} - \frac{\mathbf{a}\cdot\mathbf{n}}{|\mathbf{n}|^2}\,\mathbf{n}\,, \tag{4.31}$$

is the projection of vector $\mathbf{a}$ onto the plane with normal $\mathbf{n}$.

The vector $\mathbf{S}_{\rm BH} \times \mathbf{S}_{\rm xy-90}$ is constructed in the following way: We project the BH spin $\mathbf{S}_{\rm BH}$ onto the xy-plane, $\mathbf{S}_{\rm xy} = \mathrm{P}(\mathbf{S}_{\rm BH}, \mathbf{z})$ and then rotate the resulting vector $\mathbf{S}_{\rm xy}$ by $\pi/2$ about the z-axis. The cross product of $\mathbf{S}_{\rm BH}$ and $\mathbf{S}_{\rm xy-90}$ then lies in the equatorial plane of the BH (the plane orthogonal to the BH spin) and the twist $\sigma(r)$ at $t = 0$ is 0 throughout the disc. A sketch showing the construction of these vectors and twist and tilt angles is provided in Fig. 4.1. The reference coordinate system for the actual calculations is centred about the BH origin.

The twist $\sigma(r)$ is then a measure of how much the angular momentum vector of each annulus has precessed in the (dynamically changing) equatorial plane of the BH, while the tilt $\nu(r)$ gives the angle between the BH spin and the angular momentum vectors for each annulus. The disc is said to be *twisted* if the twist

becomes a function of radius, $\sigma = \sigma(r)$, and is said to be *warped* if the tilt becomes a function of radius, $\nu = \nu(r)$.

The angular momentum vector for each annulus is calculated following the procedure outlined in the section on spin in [Weinberg 1972] (pages 46f.). We calculate $\mathbf{J}_{\rm Disc}(r)$ from the anti-symmetric angular momentum tensor

$$L^{\mu\nu} = \int d^3x (x^\mu T^{\nu 0} - x^\nu T^{\mu 0}) \tag{4.32}$$

in the following way:

$$J_x = L^{23}, \; J_y = L^{31} \;\text{ and }\; J_z = L^{12} \,. \tag{4.33}$$

The relevant components of the stress-energy tensor $T^{\mu\nu}$ are

$$T^{i0} = \rho \, h \, \left(\frac{W^2}{\alpha} \, v^i - \frac{W}{\alpha} \, \beta^i \right) + P \, \frac{\beta^i}{\alpha^2} \,. \tag{4.34}$$

We note that our procedure differs slightly from that given in Fragile and Anninos [2005], where the components of the disc shell angular momentum vectors were computed using the intrinsic spin as follows:

$$S_\alpha = \frac{1}{2} \, \epsilon_{\alpha\beta\gamma\delta} \, J^{\beta\gamma} \, U^\delta \,, \tag{4.35}$$

where $\epsilon_{\alpha\beta\gamma\delta}$ is the 4-dimensional Levi-Civita symbol and $U^\delta = p^\delta / (-p_\beta p^\beta)^{\frac{1}{2}}$ is the total 4-velocity of the system, with p^α being the 4-momentum.

Using the intrinsic spin, the contribution to the total angular momentum stemming from choosing a reference point is accounted for in the linear momentum of the centre of mass of the system. We choose to use the angular momentum tensor $L^{\mu\nu}$, calculated about the centre of the BH instead, using Eq. (4.32) in the calculation of $\sigma(r)$ and $\nu(r)$. We therefore pick a reference frame centred on the BH, as it is moving around the grid and we are interested in the total angular momentum of the disc shell about the BH centre. We note that the calculation of the twist and tilt angles is in fact gauge dependent. We have checked the impact of the gauge choice on the twist and tilt angles by measuring the angles for the initial data with different lapse and shift profiles to find that the angles are calculated correctly (as the initial tilt and twist profiles are parameters of our initial data), which also serves as an important consistency check for the correct measure of the initial angles. We also compute the instantaneous precession and nutation rates for both the BH spin vector $\mathbf{S}$ and the total disc angular momentum vector $\mathbf{J}_{\rm Disc}$ (which we calculate by summing the components of all shells). For the BH, we compute its precession and nutation about the z-axis, while the total precession and nutation of the disc angular momentum vector $\mathbf{J}_{\rm Disc}$ is calculated about the BH spin axis.

We refer the reader to Appendix B for details on the actual implementation of the disc analysis thorn.

4.5 Fluid tracer particles

In the simulations reported in Chapter 7, we use fluid tracers particles placed in the disc at the beginning of the simulation that are advected with the flow. Employing tracers provides an additional valuable means to analyse the disc evolution. In order to compute the evolution of the tracer particles in our system we adopt a simple test particle approximation to convert from the Eulerian representation of the fluid flow, in which the hydrodynamics variables are evolved on the computational grid, into the the Lagrangian one needed to compute the velocity of the particles. This method is often use in the context of core-collapse supernovae simulation to describe the evolution of the unbound material subject to r-process nucleosynthesis (see Travaglio et al. [2004] and Nakamura et al. [2015]). These passively advected particles allow us to record their velocity, internal energy and pressure by interpolating the corresponding quantities from the underlying grid. We adopt a linear interpolation to project the physical quantities computed on the grid onto the tracer particles.

Using the local 3-velocity of the fluid, $\boldsymbol{v}$, lapse α, and shift vector $\boldsymbol{\beta}$ we can evolve the position of the particle by simply integrating

$$\frac{d\boldsymbol{x}}{dt} = \tilde{\boldsymbol{v}}(\boldsymbol{x}) \ , \tag{4.36}$$

where $\tilde{\boldsymbol{v}} \equiv \alpha\boldsymbol{v} - \boldsymbol{\beta}$ is the advection speed with respect to the coordinates [Foucart et al. 2014]. For the time evolution of the tracers, we use a second-order accurate in time Adams-Bashforth explicit integrator which requires two previous time steps, t^{n-1} and t^n, to compute the position vector, $\boldsymbol{x}$, of the particles at t^{n+1}. As a result, we can express the evolution equation for the position as

$$\boldsymbol{x}^{n+1} = \boldsymbol{x}^n + \frac{3}{2}\Delta t \left(\tilde{\boldsymbol{v}}^n - \tilde{\boldsymbol{v}}^{n-1}\right) \ , \tag{4.37}$$

where Δt represent the time step relative to the finest mesh refinement where the tracer particle is located.

Using this prescription, the tracers are then advected with the fluid flow during the evolution of the disc. The tracers are output in `hdf5` snapshots at user-specified time intervals during the evolution, which allows one to perform the disc analysis as a post-processing step rather than during the simulation. The analysis of the disc via the tracer particles performs very well in the bulk regions of the disc and accurately reflect the total mass, energy and angular momentum

of the disc during the evolution. For the analysis of complicated flow details in low density regions (such as the accretion streams observed in Fragile and Anninos [2005] and Chapter 6), however, the disc analysis thorn of Section 4.4 performs much more accurate as it analyses the disc morphology using the full 3D data during the evolution. Due to the much larger output files resulting from the output of the 3D spacetime and hydrodynamics variables, the disc analysis has to be performed during the simulation rather than as a post-processing step. Depending on the number of tracers, it might be computationally cheaper to advect the tracer particles with the flow and later analyse them rather than performing the complicated disc analysis during the simulation. This might significantly reduce the runtime of the evolution simulations. Due to the manageable file sizes of the tracer output, the tracers are furthermore a very powerful tool for the visualisation of the disc evolution.

Part III

Results

Chapter 5

Measuring the BH spin direction in 3D Cartesian NR simulations

The results of this chapter have been originally published in:
V. Mewes, J. A. Font and P. J. Montero
Phys. Rev. D **91**, 124043 (2015).

The direction of the BH spin in NR is commonly measured by the approach suggested by Campanelli et al. [2007]. In this approach the BH spin direction is simply defined as the Euclidean unit vector tangent to the coordinate line joining the two poles on the horizon (i.e. the two points where the axially symmetric vector ψ^a given in Eq. (2.94) vanishes). The approximate Killing vector field ψ^a on the horizon is obtained numerically using spherical-polar coordinates and the accuracy in the spin direction is typically about a few angular grid zones. This definition of the spin vector reproduces the Bowen-York spin parameter on the initial slice and gives satisfactory results as long as the BH horizon does not become too distorted. Moreover, Campanelli et al. [2007] present another method for finding the spin magnitude and direction, using flat-space coordinate rotational Killing vectors to calculate the Cartesian components of the BH spin and its magnitude from the Euclidean norm of the resulting vector. The flat-space Killing vector method has the practical advantage that the vector ψ^a used in the surface integral (2.94) is given analytically and is constant, therefore it does not have to be found numerically on each timeslice.

We show below how the flat-space Killing vector method can be derived by performing a surface integral of Weinberg's energy-momentum pseudotensor [Weinberg 1972][1]. By using the 3+1 split of spacetime and Gaussian coordinates, it is possible to express the angular momentum of a given volume using Weinberg's energy-momentum pseudotensor in a simple form that allows for a straightforward calculation of the spin vector of the BH horizon. Weinberg's energy-momentum pseudotensor is a symmetric pseudotensor derived by writing Einstein's equations using a coordinate system that is quasi-Minkowskian, which means that the four-dimensional metric $g_{\mu\nu}$ is approaching the Minkowski metric $\eta_{\mu\nu}$ at infinity. Although it is not generally covariant, the pseudotensor is Lorentz covariant, and with the appropriate choice of coordinates it provides a measure of the total angular momentum of the system.

5.1 Angular momentum with Weinberg's pseudotensor

Weinberg's energy-momentum pseudotensor is obtained by writing the Einstein equations in a coordinate system that is quasi-Minkowskian in Cartesian coordinates, so that the metric $g_{\mu\nu}$ approaches the Cartesian Minkowski metric $\eta_{\mu\nu} = \mathrm{diag}(-1, 1, 1, 1)$ at infinity as follows

$$g_{\mu\nu} = \eta_{\mu\nu} + h_{\mu\nu}\,, \tag{5.1}$$

where $h_{\mu\nu}$ does not necessarily have to be small everywhere. By writing the Einstein equations in parts linear in $h_{\mu\nu}$ (one is usually interested in evaluating integrals containing the pseudotensor as surface integrals far from the sources of the gravitational field), one arrives at an energy-momentum pseudotensor $\tau^{\mu\nu}$, which is the total energy-momentum "tensor" of the matter fields, $T_{\lambda\kappa}$, and of the gravitational field, $t_{\lambda\kappa}$,

$$\tau^{\mu\nu} = \eta^{\mu\lambda}\eta^{\nu\kappa}\left[T_{\lambda\kappa} + t_{\lambda\kappa}\right] = \frac{1}{8\pi}\frac{\partial}{\partial x^{\sigma}}Q^{\sigma\mu\nu}, \tag{5.2}$$

where $Q^{\sigma\mu\nu}$ is the superpotential given by

$$Q^{\sigma\mu\nu} = \frac{1}{2}\left(\frac{\partial h^{\lambda}_{\lambda}}{\partial x_{\mu}}\eta^{\sigma\nu} - \frac{\partial h^{\lambda}_{\lambda}}{\partial x_{\sigma}}\eta^{\mu\nu} - \frac{\partial h^{\lambda\mu}}{\partial x^{\lambda}}\eta^{\sigma\nu}\right.$$

[1] In GR, pseudotensors are objects akin to the stress-energy tensor $T^{\mu\nu}$ which contain the energy-momentum contribution of the gravitational field itself. They are therefore non-covariant objects, as the gravitational field can be made to vanish at any point in space by choosing a freely falling reference frame.

$$+ \frac{\partial h^{\lambda\sigma}}{\partial x^{\lambda}}\eta^{\mu\nu} + \frac{\partial h^{\mu\nu}}{\partial x_{\sigma}} - \frac{\partial h^{\sigma\nu}}{\partial x_{\mu}}\Bigg), \tag{5.3}$$

and indices of linearised quantities are raised and lowered with $\eta_{\mu\nu}$.

Using the pseudotensor, the volume integrals giving the total four-momentum (of matter sources and gravitational field) of the volume V are given by

$$P^{\mu} = \int_V \tau^{0\mu} d^3x = -\frac{1}{8\pi}\int_V \left(\frac{\partial Q^{i0\mu}}{\partial x^i}\right) d^3x. \tag{5.4}$$

Furthermore, the pseudotensor $\tau^{\mu\nu}$ defined by Eq. (5.2) is symmetric, which allows one to use it to calculate the total angular momentum in a volume V using the following volume integral:

$$\begin{aligned} J^{\mu\nu} &= \int_V \left(x^{\mu}\tau^{0\nu} - x^{\nu}\tau^{0\mu}\right) d^3x \\ &= -\frac{1}{8\pi}\int_V \left(x^{\mu}\frac{\partial Q^{i0\nu}}{\partial x^i} - x^{\nu}\frac{\partial Q^{i0\mu}}{\partial x^i}\right) d^3x. \end{aligned} \tag{5.5}$$

As Weinberg remarks, the physically interesting Cartesian components of the angular momentum contained in the volume are

$$J_x \equiv J^{23}, \quad J_y \equiv J^{31}, \quad J_z \equiv J^{12}. \tag{5.6}$$

Using the divergence theorem, the volume integral can be transformed to the following surface integral over the bounding surface:

$$\begin{aligned} J^{ij} = -\frac{1}{16\pi}\iint_S \Bigg(&- x_i\frac{\partial h_{0j}}{\partial x^k} + x_j\frac{\partial h_{0i}}{\partial x^k} + x_i\frac{\partial h_{jk}}{\partial t} \\ &- x_j\frac{\partial h_{ik}}{\partial t} + h_{0j}\delta_{ki} - h_{0i}\delta_{kj}\Bigg) n^k dS, \end{aligned} \tag{5.7}$$

where n^i is the unit normal to the surface of integration and dS the surface element.

The convergence of the four-momentum volume integrals (5.4) involving the pseudotensor $\tau^{\mu\nu}$ critically depends on the rate at which the metric $g_{\mu\nu}$ approaches the Minkowski reference metric at large distances. Given the following behaviour of $h_{\mu\nu}$ as $r \to \infty$,

$$h_{\mu\nu} = \mathcal{O}(r^{-1}), \tag{5.8}$$

$$\frac{\partial h_{\mu\nu}}{\partial x^{\sigma}} = \mathcal{O}(r^{-2}), \tag{5.9}$$

$$\frac{\partial^2 h_{\mu\nu}}{\partial x^{\sigma}\partial x^{\rho}} = \mathcal{O}(r^{-3}), \tag{5.10}$$

where $r = (x^2 + y^2 + z^2)^{\frac{1}{2}}$, it can be shown that the energy-momentum "tensor" of the gravitational field, $t_{\mu\nu}$, behaves at large distances as

$$t_{\mu\nu} = \mathcal{O}(r^{-4}), \tag{5.11}$$

which in turn shows that the four-momentum volume integral (5.4) converges. The convergence of the total angular momentum volume integral (5.5) and of the corresponding surface integral (5.7) is more problematic, due to the appearance of x^μ in the volume integral. This is also observed in the convergence properties of the integrals of the ADM quantities [Arnowitt, Deser, and Misner 2008], where the surface integrals for the ADM mass and linear momentum converge when imposing fall-off conditions like those of Eq. (5.8), while the calculation of the ADM angular momentum generally requires stronger asymptotic fall-off conditions autociteJaramillo2011. We shall return to the issue of the convergence of Eq. (5.7) after we have expressed it in terms of the 3+1 variables and in Gaussian normal coordinates in the next section.

5.2 The angular momentum pseudotensor integral in Gaussian coordinates

We can express the total angular momentum given by Eq. (5.7) in Gaussian normal coordinates (also called synchronous coordinates), which represent free-falling observers. By using the 3+1 decomposition of the four-dimensional metric $g_{\mu\nu}$ in Eq. (2.18) and from the requirement that the metric $g_{\mu\nu}$ approaches Cartesian Minkowski space at infinity (5.1), we see that in the 3+1 decomposition $h_{\mu\nu}$ is given by

$$h_{\mu\nu} = \left(\begin{array}{c|c} -\alpha^2 + \beta_i\beta^i + 1 & \gamma_{ij}\beta^j \\ \hline \gamma_{ij}\beta^j & \gamma_{ij} - \delta_{ij} \end{array}\right). \tag{5.12}$$

If we now express the angular momentum surface integral, Eq. (5.7), in terms of the 3+1 variables we find that J^{ij} can be written as

$$\begin{aligned} J^{ij} = -\frac{1}{16\pi}\iint_S \Bigg(& - x_i \frac{\partial(\gamma_{jm}\beta^m)}{\partial x^k} + x_j \frac{\partial(\gamma_{im}\beta^m)}{\partial x^k} \\ & + x_i \frac{\partial(\gamma_{jk} - \delta_{jk})}{\partial t} - x_j \frac{\partial(\gamma_{ik} - \delta_{ik})}{\partial t} \\ & + \gamma_{jm}\beta^m\delta_{ki} - \gamma_{im}\beta^m\delta_{kj}\Bigg) n^k dS. \end{aligned} \tag{5.13}$$

Moreover, using the definition of Gaussian coordinates in terms of the 3+1 variables, we see that in these coordinates $h_{00} = h_{0i} = h_{i0} = 0$. In this gauge,

Eq. (5.13) considerably simplifies to

$$J^{ij} = -\frac{1}{16\pi} \iint_S \left(x_i \frac{\partial \gamma_{jk}}{\partial t} - x_j \frac{\partial \gamma_{ik}}{\partial t} \right) n^k dS. \tag{5.14}$$

We can now use the definition of the extrinsic curvature K_{ij},

$$K_{ij} = -\frac{1}{2\alpha} \left(\frac{\partial \gamma_{ij}}{\partial t} - \mathcal{L}_\beta \gamma_{ij} \right), \tag{5.15}$$

where $\mathcal{L}_\beta$ is the Lie derivative with respect to the shift vector β^i, to see that the time derivative of the spatial metric $\partial \gamma_{ij}/\partial t$ in Gaussian coordinates is simply

$$\frac{\partial \gamma_{ij}}{\partial t} = -2K_{ij}. \tag{5.16}$$

Substituting Eq. (5.16) in Eq. (5.14), we find that

$$J^{ij} = \frac{1}{8\pi} \iint_S (x_i K_{jk} - x_j K_{ik})\, n^k dS. \tag{5.17}$$

Finally, using Eq. (5.6), the three components of the Cartesian angular momentum vector of a volume are given by

$$J_x = J^{23} = \frac{1}{8\pi} \iint_S (yK_{3k} - zK_{2k})\, n^k dS\,, \tag{5.18}$$

$$J_y = J^{31} = \frac{1}{8\pi} \iint_S (zK_{1k} - xK_{3k})\, n^k dS\,, \tag{5.19}$$

$$J_z = J^{12} = \frac{1}{8\pi} \iint_S (xK_{2k} - yK_{1k})\, n^k dS\,. \tag{5.20}$$

Introducing the components of the three Cartesian Killing vectors of the rotational symmetry of Minkowski space

$$\xi_x = (0, -z, y) \tag{5.21}$$

$$\xi_y = (z, 0, -x) \tag{5.22}$$

$$\xi_z = (-y, x, 0) \tag{5.23}$$

we can rewrite the surface integrals of the three Cartesian components of the angular momentum in the following way:

$$J_i = \frac{1}{8\pi} \iint_S K_{jk} (\xi_i)^j n^k dS\,. \tag{5.24}$$

Thus, Weinberg's identification of the (2,3), (3,1) and (1,2) components as being the physically interesting ones is now clearly seen from Eq. (5.24), as it is the rotational Killing vectors of Minkowski space that enter in the calculation of the Cartesian components of the total angular momentum of the volume.

Note that this form of the angular momentum is remarkably similar to that of the ADM angular momentum [Jaramillo and Gourgoulhon 2011]:

$$J_i = \frac{1}{8\pi} \lim_{r\to\infty} \iint_S \left(K_{jk} - K\gamma_{jk}\right) (\xi_i)^j n^k dS\,. \tag{5.25}$$

If the integration is done over a sphere, the components of the surface normal n^k are given by

$$n^i = \left(\frac{x}{r}, \frac{y}{r}, \frac{z}{r}\right), \tag{5.26}$$

so that $(\xi_i)^j$ and n^k are orthogonal vectors,

$$\gamma_{jk}(\xi_i)^j n^k = (\xi_i)^k n_k = 0 \quad \forall\, i. \tag{5.27}$$

Therefore, the part of the integral containing the trace of K_{ij} in Eq. (5.25) vanishes for spherical surfaces and therefore equations (5.24) and (5.25) are identical. We have thus shown that by using Weinberg's pseudotensor in Gaussian coordinates we obtain the total ADM angular momentum evaluated at spatial infinity, when the integration surface is a sphere. We might still need to impose a stricter asymptotic behaviour than the asymptotic Euclidean flatness described in Jaramillo and Gourgoulhon [2011] (for instance the quasi-isotropic or asymptotic maximal gauge), but as Gourgoulhon [2012] noted, the $K_{jk}(\xi_i)^j n^k$ part of Eq. (5.25) converges in practice. We are, however, interested in evaluating Eq. (5.24) quasi-locally, that is, associated with finite 2-surfaces (in our actual applications, these will be apparent horizons of black holes [Mewes et al. 2016]).

For an axisymmetric spacetime, the angular momentum can be calculated via the so-called Komar angular momentum [Komar 1959], which is defined as (following again the notation of Jaramillo and Gourgoulhon [2011] and Gourgoulhon [2012]):

$$J_K = \frac{1}{16\pi} \iint_S \nabla^\mu \phi^\nu dS_{\mu\nu}, \tag{5.28}$$

where ϕ^ν is the axial Killing vector. Note the extra factor of 2 in the denominator, known as Komar's anomalous factor [Katz 1985]. The Komar angular momentum integral does not have to be evaluated at spatial infinity, but is valid for every surface. In Jaramillo and Gourgoulhon [2011] and Gourgoulhon [2012] it is shown that using a slicing adapted to the axisymmetry of the spacetime, and expressing Eq. (5.28) in terms of the 3+1 variables, the Komar angular momentum becomes

$$J_K = \frac{1}{8\pi} \iint_S K_{ij} \phi^i n^k dS. \tag{5.29}$$

In Gourgoulhon [2012] the above integral is evaluated for a Kerr BH in spherical Boyer-Lindquist coordinates, and the angular momentum is found to be

$J_K = Ma$, as expected, where M and a are the BH mass and spin parameter, respectively. As the two integrals (5.24) and (5.29) have exactly the same structure, and the latter is coordinate (but not foliation) invariant, we arrive at the conclusion that the introduction of Gaussian coordinates has led to a coordinate invariant expression for the angular momentum derived from Weinberg's pseudotensor, namely the Komar angular momentum[2]. Note the absence of the anomalous factor of 2 in our final expression (5.24). It therefore seems that it is possible to relax the restriction of using Cartesian coordinates in calculations involving Weinberg's pseudotensor.

5.3 Measuring the angular momentum in NR simulations

It is easy to check that not only the choice of Gaussian coordinates simplifies the calculation of the total angular momentum via Weinberg's pseudotensor, but also that it makes straightforward the implementation of the above expressions in a NR 3D Cartesian code based on the 3+1 decomposition. For instance, if using the widely adopted BSSN formulation [Nakamura, Oohara, and Kojima 1987, Shibata and Nakamura 1995, Baumgarte and Shapiro 1999], the extrinsic curvature K_{ij} of the spatial slices is closely related to one of the evolved variables, namely the traceless part of the conformally related extrinsic curvature. We note that in present-day NR simulations one does not typically use Gaussian coordinates for the actual numerical evolutions. This has to do with the fact that Gaussian coordinates can only be used in the close vicinity of a spatial hypersurface, as the geodesics emanating from the hypersurfaces will eventually cross and form caustics in a finite time [Gourgoulhon 2012]. Furthermore the foliation is not singularity-avoiding, which means Gaussian coordinates are unsuitable for the numerical evolution of spacetimes containing curvature singularities. Instead, the gauge conditions most commonly employed today in NR belong to the family of the so-called moving puncture gauges, which consist of the "1+log" condition for the lapse function [Bona et al. 1995] and the Gamma driver condition for the shift vector [Alcubierre et al. 2003]. However, one can use the numerical solution

[2]Integrals over all space containing the pseudotensor have to be evaluated in Cartesian-like coordinates in order to give finite results. Specifically, when using spherical coordinates, the integrals (5.4) and (5.5) might diverge. See the discussion on the integration of the Ricci scalar R in Gourgoulhon and Bonazzola [1994] for a detailed discussion of this issue and strategies to allow the use of non-Cartesian coordinates in these type of integrals.

for the extrinsic curvature K_{ij} in Eq. (5.24) due to the freedom to choose any gauge for calculations done on each timeslice.

In addition, Eq. (5.24) is actually equivalent to the method proposed by Campanelli et al. [2007] for the calculation of the angular momentum of a volume using flat-space coordinate rotational Killing vectors (cf. Eq. (5.21)). To see this, consider the definition of the Killing vectors in Cartesian coordinates given in Campanelli et al. [2007]:

$$\psi^a_x = [0, -(z - z_c), (y - y_c)], \tag{5.30}$$

$$\psi^a_y = [(z - z_c), 0, -(x - x_c)], \tag{5.31}$$

$$\psi^a_z = [-(y - y_c), (x - x_c), 0], \tag{5.32}$$

where (x_c, y_c, z_c) is the coordinate centroid of the AH, which has to be subtracted to avoid including contributions from a possible orbital angular momentum of the BH about the centre of the computational grid in the calculation of its spin. Upon substituting their flat-space coordinate rotational Killing vectors into Eq. (2.94), we find that

$$J_x = \frac{1}{8\pi} \iint_S (yK_{3b} - zK_{2b})\, n^b dS\,, \tag{5.33}$$

$$J_y = \frac{1}{8\pi} \iint_S (zK_{1b} - xK_{3b})\, n^b dS\,, \tag{5.34}$$

$$J_z = \frac{1}{8\pi} \iint_S (xK_{2b} - yK_{1b})\, n^b dS\,, \tag{5.35}$$

where we have set $x_c = y_c = z_c = 0$ for simplicity. We see that the two sets of expressions for the Cartesian components of the angular momentum vector of the AH, those from Weinberg's pseudotensor evaluated in Gaussian coordinates and those from the flat space rotational Killing vector method, are equivalent and equal to the Komar angular momentum in an axisymmetric spacetime.

Chapter 6

NR simulations of tilted BH–torus systems

The results of this chapter have been originally published in:
V. Mewes, J. A. Font, F. Galeazzi, P. J. Montero and N. Stergioulas
Phys. Rev. D **93**, 064055 (2016).

6.1 Initial data and setup

The initial setup for the simulations presented in this chapter is a thick, self-gravitating axisymmetric accretion disc in equilibrium around a rotating BH. Such a system is built following the approach laid out in Stergioulas [2011] that we briefly describe below. The solver to build the initial data (ID) first computes models of self-gravitating, massive tori around non-rotating BHs. For BH–torus initial data, the accuracy is usually evaluated by the deviations of the constraints rather than some Virial-like expressions as the ones derived in Gourgoulhon and Bonazzola [1994] and Bonazzola and Gourgoulhon [1994], though it might be interesting to derive explicit forms of the GR Virial theorem for the BH–torus initial data in the future. For our simulations of tilted discs around rotating BHs we retain the hydrodynamical content of a model and replace the spacetime by a tilted Kerr spacetime in quasi-isotropic coordinates. The generated ID is then interpolated onto Cartesian coordinates and evolved with the `ET`. We are not aware of a method to generate self-consistent data for self-gravitating

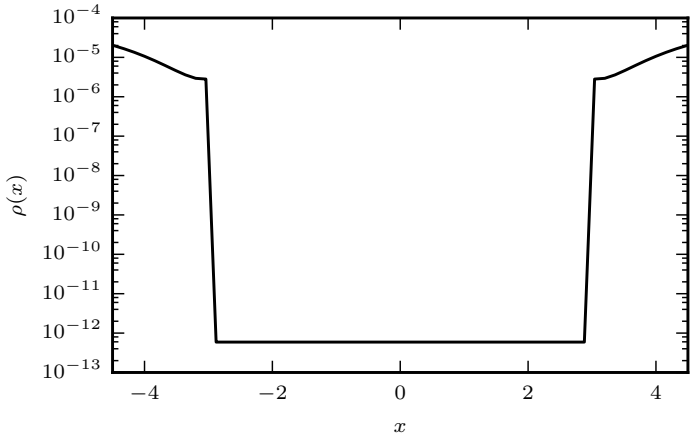

Figure 6.1 Innermost region of the initial rest-mass density profile along the x-axis for model `C1Ba0b0`. The disc ends at 3.03 and the AH is initially located at $x = 0.46$.

tilted discs around Kerr BHs and therefore resort to this method[1]. In order to keep the constraint violations as low as possible, we use disc models with rest masses of only a few percent of the BH mass and with small to moderate BH spins. When replacing the original spacetime of the ID with the tilted Kerr spacetime in the computational domain, both the torus rest-mass M_0 and the torus gravitational mass $M_{\rm T}$ will change somewhat, due to the fact that the volume element of the spacetime, as well as the lapse, have changed. In order to assess the difference in M_0 and $M_{\rm T}$ due to the replacement of the spacetime we calculate both quantities using Eqs. (4.23) and (4.24). We find the largest difference in M_0 and $M_{\rm T}$ in model `C1Ba03b30` (see a list of models in Table 6.1 below), where we obtain the following fractional differences: $\Delta M_0 \approx -3\%$ and $\Delta M_{\rm T} \approx -3\%$.

6.1.1 Self-gravitating accretion discs

Our ID are self-gravitating discs around a Schwarzschild BH in quasi-isotropic (QI) coordinates [Stergioulas 2011]. The ID is fully described by the four metric potentials $\lambda(r,\theta)$, $B(r,\theta)$, $\alpha(r,\theta)$ and $\omega(r,\theta)$ that characterise the metric of a stationary, axisymmetric spacetime in spherical polar QI coordinates,

$$ds^2 = -e^{2\nu}dt^2 + e^{2\alpha}(d\bar{r}^2 + \bar{r}^2 d\phi^2) + \frac{B^2}{e^{2\nu}}\bar{r}^2 sin^2\theta(d\phi - \omega dt)^2\,, \qquad (6.1)$$

[1] A possible attempt to construct these initial models might be to solve the constraint equations with a matter source representing a warped disc in steady-state.

where the isotropic radius $\bar{r}$ is given in terms of the areal radius r by

$$\bar{r} = \frac{1}{2}\left(r - M + \sqrt{r^2 - 2Mr}\right) , \tag{6.2}$$

where M is the mass of the BH. The ID also provides the pressure p and orbital angular velocity $\Omega = u^\phi/u^t$, measured by an observer at infinity at rest. The evolution time is measured in terms of the initial orbital period at the radius of the initial maximum of the rest-mass density, ρ_c. These two quantities, together with the EOS, are sufficient to obtain the remaining hydrodynamical quantities. The ID is constructed using the polytropic EOS given by (4.21). The value of the constant K (see Table 6.1) in the polytropic EOS essentially fixes the central density in the construction of our ID, leading to values expected in post-merger accretion tori (see, e.g. the values reported in Rezzolla et al. [2010]). The components of the 3-velocity in Cartesian coordinates are given by

$$v^i = \left(y\left(\frac{\omega - \Omega}{\alpha}\right), -x\left(\frac{\omega - \Omega}{\alpha}\right), 0\right) \tag{6.3}$$

where α is the lapse function. The Lorentz factor is calculated directly from the 3-velocity

$$W = \frac{1}{\sqrt{1 - v_i v^i}} = \frac{1}{\sqrt{1 - (\omega - \Omega)^2 \frac{B^2}{e^{4\nu}}(x^2 + y^2)}} . \tag{6.4}$$

The matter content of the ID only fills the computational domain up to the event horizon of the BH. In our simulations we do not excise the BH but rather treat it as a puncture. We noticed that when evolving the BH as a puncture with matter content without excision, the simulations were not long-term stable and failed at early stages of the evolution due to errors in the matter evolution at the location of the puncture. The reason is a very rapid pile up of matter at this location, which leads to non-physical values of the hydrodynamical variables at the puncture. These lead to failures in the `GRHydro` evolution code during the conversion from conserved to primitive variables. In Faber et al. [2007] a successful method to evolve hydrodynamics in the presence of punctures was presented. This method checks for unphysical values of the hydrodynamical variables at the immediate vicinity of the puncture and resets them to physical values. In practice it checks for the positivity of the conserved energy ($\tau \geq 0$) and an upper bound for $|S|^2$:

$$\gamma^{ij} S_i S_j \leq \tau(\tau + 2\rho). \tag{6.5}$$

In our simulations, we use a similar treatment inside the BH horizon, namely we specify a fraction of the volume of the AH in which we reset the matter fields to atmosphere values and the stress-energy tensor $T^{\mu\nu}$ to zero, which is

essentially the same technique as described in Reisswig et al. [2013]. In this way, we avoid using a moving excision boundary for the hydrodynamical variables as in Löffler, Rezzolla, and Ansorg [2006]. From the point of view of the evolution it is safe to do this, as the evolution of the hydrodynamics inside the horizon cannot influence the evolution outside the horizon. In fact, we checked that the fraction of the AH in which we apply such atmosphere resetting has no effect on the evolution, as expected. We checked this by applying the atmosphere reset for different fractions of the AH. In all cases, the evolution outside the AH was unaffected, confirming that the region inside the AH is causally disconnected. This has been employed for instance in the so-called "turduckening" of initial BH data [Brown et al. 2009]. For the practical implementation of this approach we use a spherical surface that contains the shape of the AH and apply the atmosphere method in a fraction of the minimum radius of that surface. Our procedure is illustrated in Fig. 6.1 where we plot the initial density profile along the x-axis for model `C1Ba0b0` of our sample (see Tables 6.1 and 6.2). The AH is initially located at $x = 0.46$ and there exists a smooth density profile across the horizon. The remaining hydrodynamical quantities are treated in the same way. By using this approach we are able to evolve matter fields in the presence of punctures for very long times without the need for moving hydrodynamical excision zones.

6.1.2 Tilted Kerr spacetime in improved quasi-isotropic coordinates

We set up a Kerr BH tilted about the x-axis by an angle β_0 in the improved quasi-isotropic coordinates proposed by Liu, Etienne, and Shapiro [2009]. In those coordinates, the radius of the horizon does not shrink to zero in the extreme Kerr limit, but approaches $r = M/4 > 0$. The initial mass M of the Kerr BH is chosen to be equal to the value used in the ID calculation of the self-gravitating torus. The spin parameter a varies for different runs. The list of 21 models we use in our investigation is summarised in Tables 6.1 and 6.2.

We perform the rotation of the BH about the x-axis in the following way: we first rotate by an angle β_0 the coordinates x, y, z to the tilted coordinates,

$$\hat{\boldsymbol{x}} = \mathbf{R}\,\boldsymbol{x} \implies \begin{pmatrix} \hat{x} \\ \hat{y} \\ \hat{z} \end{pmatrix} = \begin{pmatrix} 1 & 0 & 0 \\ 0 & \cos\beta_0 & -\sin\beta_0 \\ 0 & \sin\beta_0 & \cos\beta_0 \end{pmatrix} \begin{pmatrix} x \\ y \\ z \end{pmatrix} . \tag{6.6}$$

We then calculate the spatial metric γ_{ij} and extrinsic curvature K_{ij} by performing coordinate transformations of the respective expressions given in Liu, Etienne,

Table 6.1 Main characteristics of our initial models. From left to right the columns indicate the name of the model, the BH mass $M_{\rm BH}$, the disc-to-BH mass ratio q, defined as the ratio of the total gravitational mass of the torus of the original ID and the irreducible mass of the Schwarzschild BH, the inner and outer disc radii $r_{\rm in}$ and $r_{\rm out}$, the maximum rest-mass density $\rho_{\rm c}$ and the polytropic constant of the EOS K. All models are evolved with a Γ-law ideal fluid EOS with $\Gamma = 4/3$. Models indicated with a $*$ were simulated using half the canonical resolution of $\Delta x = 0.02$. See main text for details.

Name	$M_{\rm BH}$	q	$r_{\rm in}$	$r_{\rm out}$	$\rho_{\rm c}$ $(\times 10^{-5})$	K
`D2a01b0`	1.0002	0.044	3.42	30.1	1.05	0.323
`D2a01b5`	1.0002	0.044	3.42	30.1	1.05	0.323
`D2a01b15`	1.0002	0.044	3.42	30.1	1.05	0.323
`D2a01b30`	1.0002	0.044	3.42	30.1	1.05	0.323
`D2a05b5`	1.0002	0.044	3.42	30.1	1.05	0.323
`D2a05b15`	1.0002	0.044	3.42	30.1	1.05	0.323
`D2a05b30`	1.0002	0.044	3.42	30.1	1.05	0.323
`C1Ba0b0`	0.9569	0.160	3.03	22.7	5.91	0.180
`C1Ba01b5`	0.9569	0.160	3.03	22.7	5.91	0.180
`C1Ba01b15`	0.9569	0.160	3.03	22.7	5.91	0.180
`C1Ba01b30`	0.9569	0.160	3.03	22.7	5.91	0.180
`C1Ba03b5*`	0.9569	0.160	3.03	22.7	5.91	0.180
`C1Ba03b15*`	0.9569	0.160	3.03	22.7	5.91	0.180
`C1Ba03b30*`	0.9569	0.160	3.03	22.7	5.91	0.180
`NC1a0b0*`	0.9775	0.110	3.60	33.5	1.69	0.170
`NC1a01b5*`	0.9775	0.110	3.60	33.5	1.69	0.170
`NC1a01b15*`	0.9775	0.110	3.60	33.5	1.69	0.170
`NC1a01b30*`	0.9775	0.110	3.60	33.5	1.69	0.170
`NC1a03b5*`	0.9775	0.110	3.60	33.5	1.69	0.170
`NC1a03b15*`	0.9775	0.110	3.60	33.5	1.69	0.170
`NC1a03b30*`	0.9775	0.110	3.60	33.5	1.69	0.170

and Shapiro [2009] (in spherical polar coordinates) to our tilted Cartesian coordinates $\hat{x}^i$. We set the initial shift β^i to 0 and choose the following initial lapse profile:

$$\alpha = \frac{2}{1 + (1 + \frac{M}{2r})^4} \,. \tag{6.7}$$

We find that this initial lapse profile greatly helps with the conservation of irreducible mass and spin during the initial gauge transition the system undergoes. The bigger the difference between the initially chosen lapse profile and the profile the system attains after the transition to the puncture coordinates, the larger the errors in irreducible mass and spin. As all quantities have been set up in the tilted coordinates $\hat{x}^i$, we also need to apply rotations to vectors and tensors, in

Table 6.2 Main characteristics of our initial models (continued). From left to right the columns indicate the name of the model, the orbital period $P_{\rm orb}$ in code units and (milliseconds) and orbital frequency $f_{\rm orb}$ at the radius of the initial $\rho_{\rm c}$, the specific angular momentum profile in the equatorial plane of the disc $l \equiv -u_\phi/u_0$ (in terms of the Schwarzschild radial coordinate R), the BH spin parameter a, and the initial tilt angle β_0. All models are evolved with a Γ-law ideal fluid EOS with $\Gamma = 4/3$. Models indicated with a $*$ were simulated using half the canonical resolution of $\Delta x = 0.02$. See main text for details.

Name	$P_{\rm orb}$	$f_{\rm orb}$ (Hz)	l-profile	a	β_0 (deg)
D2a01b0	150 (0.74)	1360	3.75 (const)	0.1	0
D2a01b5	150 (0.74)	1360	3.75 (const)	0.1	5
D2a01b15	150 (0.74)	1360	3.75 (const)	0.1	15
D2a01b30	150 (0.74)	1360	3.75 (const)	0.1	30
D2a05b5	150 (0.74)	1360	3.75 (const)	0.5	5
D2a05b15	150 (0.74)	1360	3.75 (const)	0.5	15
D2a05b30	150 (0.74)	1360	3.75 (const)	0.5	30
C1Ba0b0	157 (0.77)	1300	3.67 (const)	0.0	0
C1Ba01b5	157 (0.77)	1300	3.67 (const)	0.1	5
C1Ba01b15	157 (0.77)	1300	3.67 (const)	0.1	15
C1Ba01b30	157 (0.77)	1300	3.67 (const)	0.1	30
C1Ba03b5*	157 (0.77)	1300	3.67 (const)	0.3	5
C1Ba03b15*	157 (0.77)	1300	3.67 (const)	0.3	15
C1Ba03b30*	157 (0.77)	1300	3.67 (const)	0.3	30
NC1a0b0*	242 (1.19)	843	3.04 $R^{0.11}$	0.0	0
NC1a01b5*	242 (1.19)	843	3.04 $R^{0.11}$	0.1	5
NC1a01b15*	242 (1.19)	843	3.04 $R^{0.11}$	0.1	15
NC1a01b30*	242 (1.19)	843	3.04 $R^{0.11}$	0.1	30
NC1a03b5*	242 (1.19)	843	3.04 $R^{0.11}$	0.3	5
NC1a03b15*	242 (1.19)	843	3.04 $R^{0.11}$	0.3	15
NC1a03b30*	242 (1.19)	843	3.04 $R^{0.11}$	0.3	30

order to obtain the correct components of the shift, spatial metric and extrinsic curvature in the original x^i coordinate system that is going to be used in the simulations. We obtain the components of the shift vector with

$$\boldsymbol{\beta} = \mathbf{R}\,\hat{\boldsymbol{\beta}}\,, \tag{6.8}$$

and the components of the spatial metric and extrinsic curvature with

$$\boldsymbol{\gamma} = \mathbf{R}\,\hat{\boldsymbol{\gamma}}\,\mathbf{R}^{\mathsf{T}}\,, \tag{6.9}$$

$$\boldsymbol{K} = \mathbf{R}\,\hat{\boldsymbol{K}}\,\mathbf{R}^{\mathsf{T}}\,, \tag{6.10}$$

where $\mathbf{R}$ is the rotation matrix from $\hat{x}^i$ to x^i.

Our choice of the initial BH spin magnitude is currently limited by our computational method and is therefore somewhat smaller than spins expected in certain astrophysical scenarios. For example, as the simulations of misaligned BHNS mergers of Foucart et al. [2011], Foucart et al. [2013], and Kawaguchi et al. [2015] have shown, accretion discs form in these systems only for relatively high (> 0.7) initial BH spins; see also Foucart [2012] for disc mass predictions from BHNS mergers. These initial spins in astrophysical merger scenarios are larger than the spins investigated in our study $a \in [0, 0.5]$. However, the smaller the BH mass, the smaller the BH spins that are necessary to tidally disrupt the NS during the BHNS merger. The BHs in our study have all masses close to the solar mass. The reasons for our choice of smaller spins are the very demanding resolution requirements when evolving highly spinning BHs (see, e.g. Lousto et al. [2012]). Furthermore, spin conservation seems to be affected non-linearly with higher spin magnitude [Marronetti et al. 2008], which we have also observed in Mewes et al. [2015]. The choice of astrophysically more realistic BH spin magnitudes would have been prohibitively expensive (see, e.g. Lousto et al. [2012] for details) and is beyond the scope of our study of self-gravitating accretion discs around tilted Kerr BHs. Nevertheless, our results with dimensionless spin values of 0.5 should provide a first qualitative understanding of what may happen at dimensionless spin values of 0.7.

It is believed that there is a mass gap between the heaviest remnant NS and lightest remnant BH in supernova explosions (see, for instance, the recent supernovae simulations spanning a large parameter space of progenitors in Ugliano et al. [2012] and Ertl et al. [2016]). Specifically, the mass gap found in Ugliano et al. [2012] is between $\sim 1.8 M_\odot$ and $\sim 6.5 M_\odot$. However, we note that the existence of this mass gap in BH masses has been questioned in Kreidberg et al. [2012]. While the peak of BH masses in these considerations is still around $8\,\mathrm{M}_\odot$, very small BH masses in mergers are at least not ruled out as in previous studies. Furthermore, the BH mass predictions population synthesis models are based on assumptions about the exact details of the supernova explosion mechanism (see for instance Belczynski et al. [2012], where no mass gap is found using a delayed supernova explosion model assuming a 100-150 ms instability growth time). As we explained in the introduction, the smaller the BH mass, the smaller the BH spin needs to be in order to tidally disrupt the NS during the merger in order to leave a thick accretion torus around the BH. It therefore seems that some of the combination of BH spins and mass-ratios studied in this work (while having been primarily motivated on computational grounds) are a possible (although maybe not the most likely) outcome from BHNS mergers.

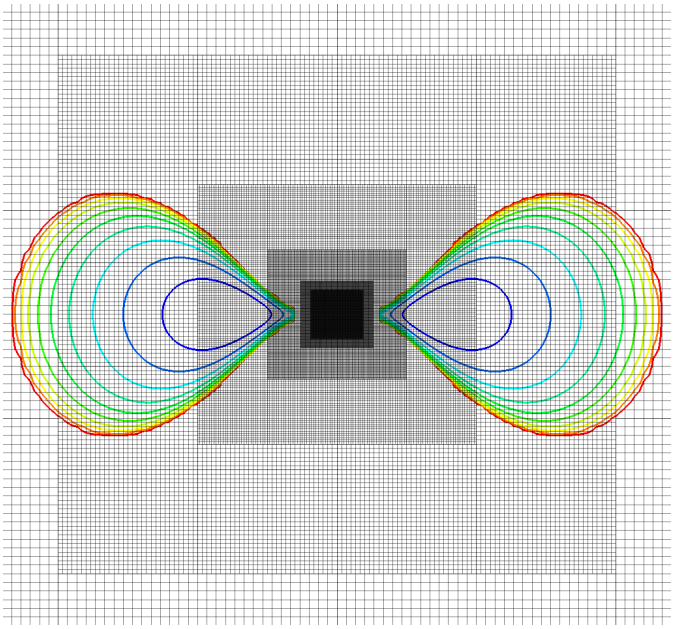

Figure 6.2 Contour plot in the xz plane of the initial rest-mass density profile in the disc for model `C1Ba0b0`. The innermost contour (blue line) corresponds to a density of 2.1×10^{-5} while the outermost contour (red line) corresponds to 5.9×10^{-10} (code units). The AMR grid structure, showing the 6 innermost mesh refinement levels (out of 13), is shown as well in the figure. The box is 46 units of length across. See main text for details on the actual resolution of the different grids.

Based on these considerations, model `D2`, the lightest in our study, is the most astrophysically relevant model of the three models studied.

We remark that our models are idealised approximations to the BH–torus systems formed in BHNS and BNS mergers. The biggest differences are the final BH mass resulting from BHNS mergers and the rotation profile of the accretion disc formed in these mergers. Two of our discs have constant specific angular momentum profiles, which are unlikely to be found in real astrophysical discs. See for instance the evolution of the specific angular momentum profiles in the post-merger torus NR simulations of BNS in Rezzolla et al. [2010], where non-axisymmetric structures redistribute angular momentum in the very early stages of the torus evolution (see also Section 6.2.8 below). The chosen mass ratios in our ID are attainable for BNS post-merger discs, but, as explained above, probably not viable models for tilted BH–torus systems.

We choose the initial tilt angle $\beta_0 \in [5°, 30°]$. In the simulations of tilted BHNS mergers of Foucart et al. [2011], the authors found that for initial inclinations $< 40°$, the mass of the resulting accretion disc would be around $10 - 15\%$

of the initial NS mass, whereas higher initial inclinations produced a sharp drop in the mass of the resulting disc. For those pre-merger inclinations $< 40°$, the resulting tilt of the post-merger disc was around $10°$. In the recent simulations of tilted BHNS mergers of Kawaguchi et al. [2015], the authors report a post-merger disc with a tilt $\approx 20 - 30°$, for an initial tilt of $\approx 60°$. These findings seem to be in accordance with the probability distributions of post-merger tilt angles for BH-NS mergers obtained in Stone, Loeb, and Berger [2013], which show a sharp cut-off in the probability distribution for post-merger tilt angles $> 50°$.

The two initial disc models `D2` and `NC1` are inside the Roche lobe, while model `C1B` overfills the Roche lobe slightly initially. We have not seen any indication for the occurrence of the runaway instability in any of the simulations presented in this work.

6.1.3 Numerical setup

The use of mesh-refinement techniques is of fundamental importance in our simulations where different physical scales need to be accurately resolved. For this reason, we use the `Carpet` driver that implements a vertex-centred AMR scheme adopting nested grids [Schnetter, Hawley, and Hawke 2004]. Figure 6.2 shows isocontours of the initial rest-mass density profile for a representative disc model (`C1Ba0b0`) in a vertical cut (xz-plane) together with the initial innermost AMR grid structure. In our simulations, we use 13 levels of mesh refinement, with the outer boundary placed at 4096. In computational grids that are not radially compactified and are therefore of finite size, the location of the outer boundary determines the maximum time of evolution before the system might be affected by possible junk radiation propagating inwards from the outer boundary. For disc models `C1B` and `D2`, our computational domain is large enough to causally disconnect the outer boundary from the BH–torus system. For model `NC1`, which has a larger orbital period at the pressure maximum, the simulation time is larger than the light-crossing time of the domain. However, we have checked that there is no growth of the constraints associated with the arrival of junk radiation from the outer boundary. We perform a comprehensive series of simulations using two different resolutions, high resolution runs with a highest resolution of $\Delta x = 0.02$ and simulations with half this resolution, see Tables 6.1 and 6.2. Every refinement level except the innermost one is half the size of the preceding level. The innermost refinement level, as can be seen in Fig. 6.2, is more than half the size of the next refinement level. All simulations have been performed using a CFL factor of 0.25. In the outermost 6 refinement levels, we use the

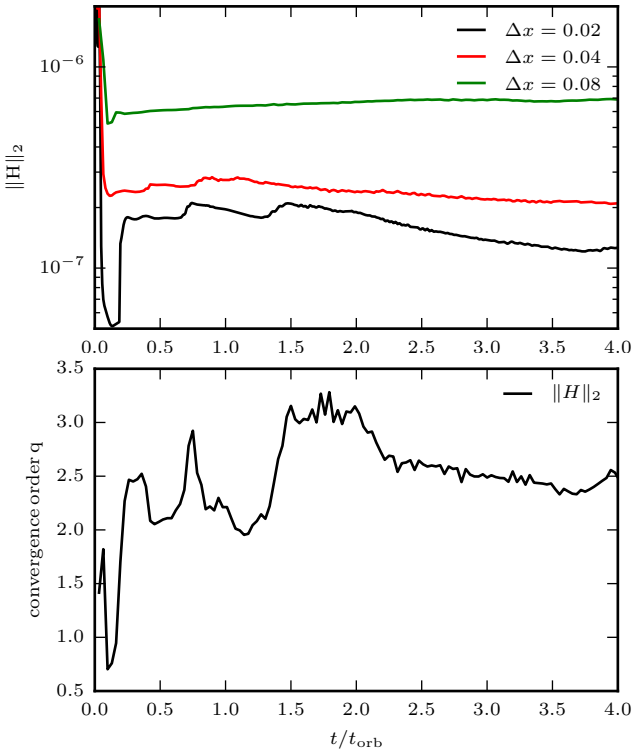

Figure 6.3 Convergence properties: *Top panel:* dependence on grid resolution for the $L2$-norm of the Hamiltonian constraint. *Bottom panel:* corresponding order of convergence. Model `C1Ba01b30` has been used for this figure.

same time step as in level 7, in order to prevent instabilities in the spatially varying damping parameter η. Using the same (smaller) time step in the outer levels is necessary, even though the spatially varying η parameter of Alic et al. [2010] takes into account the time step limitation of the η parameter described in Schnetter [2010]. In the following section, we provide details of the accuracy and convergence properties of our simulations using this numerical setup.

6.1.4 Accuracy and convergence

In Fig. 6.3 we plot the time evolution of the $L2$-norm of the Hamiltonian constraint (top panel) and the convergence order of this quantity (bottom panel) for the first four orbits of model `C1Ba01b30`. The plot shows the results obtained by using both the canonical (finest grid resolution $\Delta x = 0.02$) and two lower ($\Delta x = 0.04$ and $\Delta x = 0.08$) resolutions. We follow Galeazzi et al. [2013] and

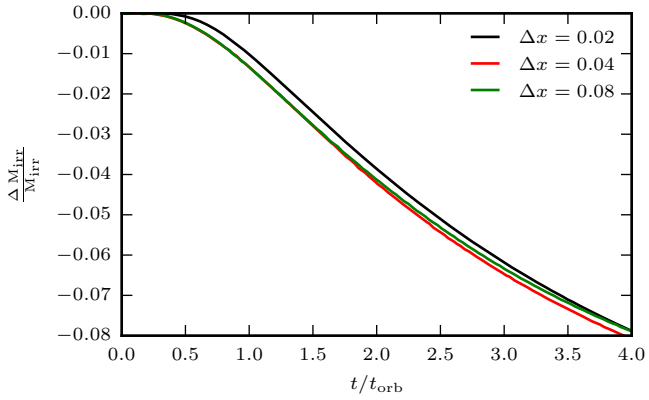

Figure 6.4 Dependence of the irreducible mass of the BH on grid resolution for model `C1Ba01b30` plotted for the first 4 orbits.

define the convergence order q as

$$q = \frac{1}{\log(f)} \log \left(\frac{\| \|\mathrm{H}\|_2^{\mathrm{low}} - \|\mathrm{H}\|_2^{\mathrm{med}} \|}{\| \|\mathrm{H}\|_2^{\mathrm{med}} - \|\mathrm{H}\|_2^{\mathrm{high}} \|} \right) , \tag{6.11}$$

where f is the refinement factor $f = \Delta x_{\mathrm{low}}/\Delta x_{\mathrm{med}} = \Delta x_{\mathrm{med}}/\Delta x_{\mathrm{high}} = 2$. From Fig. 6.3 we see that the order of convergence shows some variability between a minimum of ~ 1 and a maximum of about 3. The spacetime evolution is fourth order, while the evolution of the hydrodynamics is only second order accurate and reduces to first order in the presence of shocks. We observe higher than second order convergence in the $L2$-norm of the Hamiltonian constraint. This could be ascribed to the spacetime evolution which, due to the small disc-to-BH mass ratio and to the inconsistent ID setup, could dominate the error budget in our simulations. Furthermore, it is difficult to assess the order of convergence of our simulations at later times once the PPI sets in, since the truncation error of the different resolutions could excite the exponential growth of the non-axisymmetric modes at different times causing the study of convergence to be difficult, as one would compare different physical systems.

The fractional change in the irreducible mass of the BH for model `C1Ba01b30` is plotted in Fig. 6.4. The most striking feature of this figure is the absence of an initial drop of the irreducible mass due to the inconsistent choice of ID, contrary to the behaviour found in the simulations of Korobkin et al. [2011]. The initial drop found by Korobkin et al. [2011] (which is about 8-10%) happened in the first orbit and was due to their metric blending technique in the ID setup. After that significant initial drop, the irreducible mass in Korobkin et al. [2011] increases

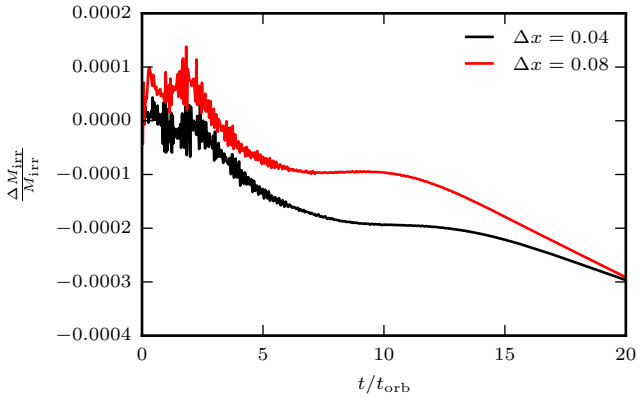

Figure 6.5 Evolution of the fractional error in the irreducible mass of a vacuum Kerr BH with the same mass as that of model `C1B` and a Kerr parameter of $a = 0.3$. Results are shown for two different resolutions.

again to remain at around 97.5% of its initial value during the evolution. Such a precise control of the irreducible mass conservation may be related to the use of a (quasi) spherical grid. In contrast, in our setup without AH excision, there is no oscillatory behaviour in the evolution of the irreducible mass at the early stages of the evolution, as the ID in quasi-isotropic coordinates dynamically adapts to the puncture gauge[2]. Nevertheless, the irreducible mass is seen to start decreasing in a smooth fashion from $0.5t_{\rm orb}$ onwards. By the total time of 4 orbital periods shown in Fig. 6.4, the irreducible mass has decreased to a minimum of about 92% of its initial value, to subsequently increase as the simulation proceeds as matter and angular momentum accrete onto the BH. Moreover, Fig. 6.4 shows that this (unphysical) drop in the irreducible mass does not converge away with resolution.

In order to investigate this issue, we have performed two additional *vacuum* ($T^{\mu\nu} = 0$) simulations of a BH with the same mass as of that of the `C1B` models and with an initial Kerr parameter of $a = 0.3$. In Fig. 6.5 we plot the corresponding fractional error in the irreducible mass for two (finest grid) resolutions, $\Delta x = 0.04$ and 0.08, for a total time of 20 orbits. Similar to our results for the BH–torus setup, we observe no convergence in the unphysical drop of the irreducible mass during the first ≈ 10 orbits, while the irreducible mass decreases slower for the higher resolution run in the later stages of the evolution, as expected. We note, however, that the magnitude of the fractional

[2]In order to avoid the initial gauge transition, one could try to use the trumpet slices for a Kerr BH described in Dennison, Baumgarte, and Montero [2014] as initial data.

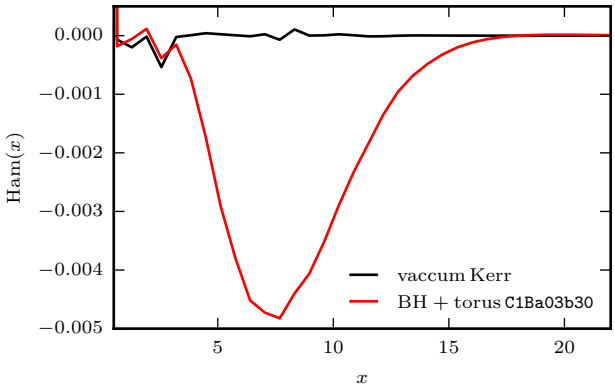

Figure 6.6 Initial radial profile of the Hamiltonian constraint for a vacuum Kerr BH and for model `C1Ba03b30` along the x-axis from the AH outwards.

error in the vacuum tests is much smaller (about two orders of magnitude) than that observed in our BH–torus runs.

Unphysical loss of irreducible mass for constraint-violating ID has been reported before in the literature (see, e.g. Mundim et al. [2011], Reifenberger and Tichy [2012], and Okawa, Witek, and Cardoso [2014]). It has been interpreted as if the effect of the constraint violations were equivalent to the presence of a negative mass in the system. The absorption of the violations by the BH causes the area of the AH, and therefore also the irreducible mass, to decrease. As stated in Section 6.1, our ID is manifestly constraint-violating and, furthermore, the constraint violations do *not* converge away with resolution. In Fig. 6.6 we plot the initial profile of the Hamiltonian constraint for the vacuum BH run with $\Delta x = 0.04$ and for the corresponding BH–torus `C1Ba03b30` model. We clearly see a large constraint violation (compared to the vacuum case) in the region where the disc initially resides. By interpreting the loss of irreducible mass as caused by the absorption of constraint violations, the lack of convergence in the irreducible mass drop in our BH–torus systems can be explained. As we have also seen in the vacuum tests, this transient feature connected to the initial constraint violations (much smaller in this case) is very long lived. In our BH–torus models the loss of irreducible mass only flattens out once enough matter has been accreted. Such large fractional errors are not reported in simulations where the BH–torus system forms after the evolution of a binary BHNS or BNS merger, which highlights the undesired effect of employing constraint-violating ID.

6.2 Results

6.2.1 Surface plots

We start describing the morphology and dynamics of a representative model of our sample. The evolution of model `C1Ba01b30` is shown in Fig. 6.7. This figure displays surface plots of the logarithm of the rest-mass density at six different stages of the evolution. The final panel shows the morphology of the system after the disc has completed 20 orbits around the BH. The interpolation of the ID from QI spherical polar coordinates to Cartesian coordinates, along with the inclusion of a moderate BH spin in the originally non-rotating BH, results in a significant perturbation of the equilibrium model that triggers a phase of oscillations of the torus around its equilibrium. These oscillations are present throughout the simulation and, as the disc is initially filling its Roche lobe, they induce a small accretion process of matter through the cusp towards the BH. This does not reduce significantly the total rest-mass of the torus as we show below. The oscillations are damped due to numerical viscosity and also by the formation of shocks developing in density waves that propagate inside the disc and convert kinetic energy into thermal energy. These oscillations therefore only trigger nonphysical accretion during the very early times of the simulation. The outward-propagating shocks, also found in the simulations of Korobkin et al. [2011], are produced by in-falling material along the funnel walls which reaches inner high-density regions and bounces back. One such shock wave can be clearly seen on the right portion of the disc in the 12 orbits panel of Fig. 6.7. The initial tilt of the BH spin ($\beta_0 = 30^\circ$) twists and warps the innermost parts of the disc closer to the BH. This gradual effect becomes evident on the time series shown in Fig. 6.7 and by the final 20 orbits the disc is significantly misaligned with the (horizontal) y-axis.

In Fig. 6.8 we show surface plots of the rest-mass density for the models `C1B`, `NC1` and `D2` for the lower spin simulations ($a = 0.1$) at the final time of the evolution $t/t_{\rm orb} = 20$. The effects of the initial BH tilt on the morphology of the disc at the final time are more clearly pronounced for the heavier models `C1B` (top row) and `NC1` (middle row). Although the spin of the BH is very small and the spacetime is therefore nearly spherically symmetric, the initial tilt angle nevertheless causes a different evolution. In contrast, the significantly lighter model `D2` is seen to be hardly affected by the initial tilt by the end of the evolution for these low spin simulations.

Similarly, in Fig. 6.9, we plot the same rest-mass density surface plots as in Fig. 6.8 for all our models with higher initial spin. Comparing the evolution of

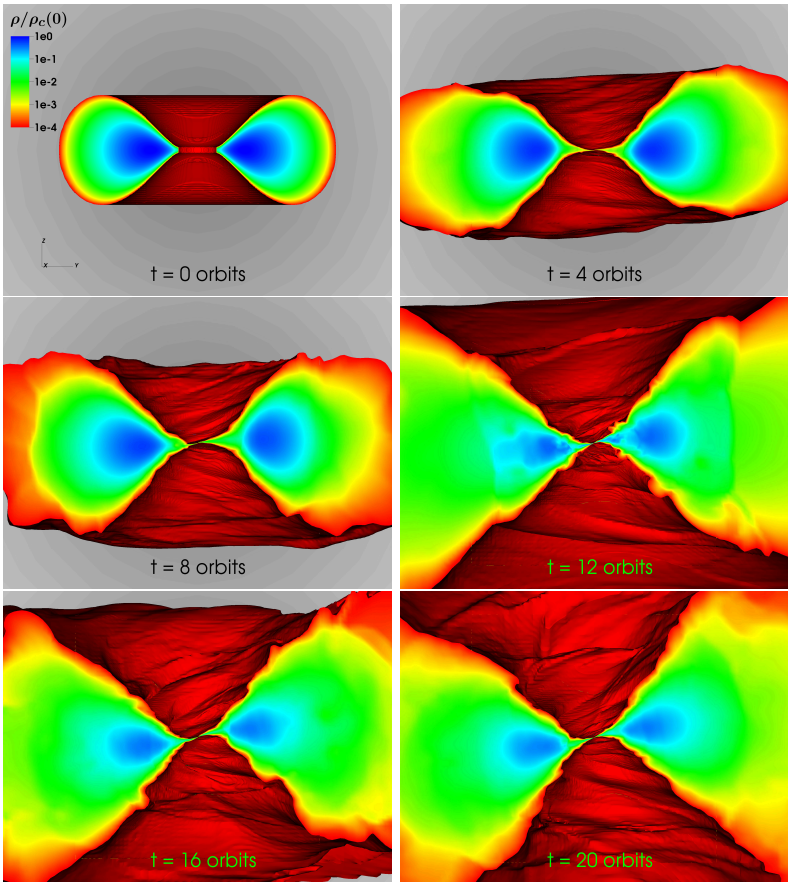

Figure 6.7 Surface plots of the logarithm of the rest-mass density for model `C1Ba01b30` at six different snapshots of the evolution, $t/t_{\rm orb} = 0, 4, 8, 12, 16$ and 20. The domain shown in all panels is 60 across the y-axis and 45 across the z-axis, which also indicates the upward direction in the plots. The surface of the disc is set at a density of $10^{-4}\rho_{\rm c}$ and half the disc is removed for visualisation purposes. The BH lies at the cutting plane of each panel. The evolution shows the development of two accretion streams on to the BH as the disc inclination increases during the evolution with respect to the initial equatorial plane.

the disc morphology with the lower initial spin figure, we see that there are now significant changes in the morphology when increasing the initial tilt angle β_0 for all models. The effects of evolving the disc in the tilted Kerr spacetime are now more pronounced, as the higher spin causes a significant deviation from spherical symmetry in the spacetime. In particular, the disc model `D2` is now also clearly affected by the BH spin. As it represents the lightest disc in our study, its evolution is most similar to the evolutions observed in Fragile and Anninos [2005], which were performed using BHs of significantly higher spins than in the

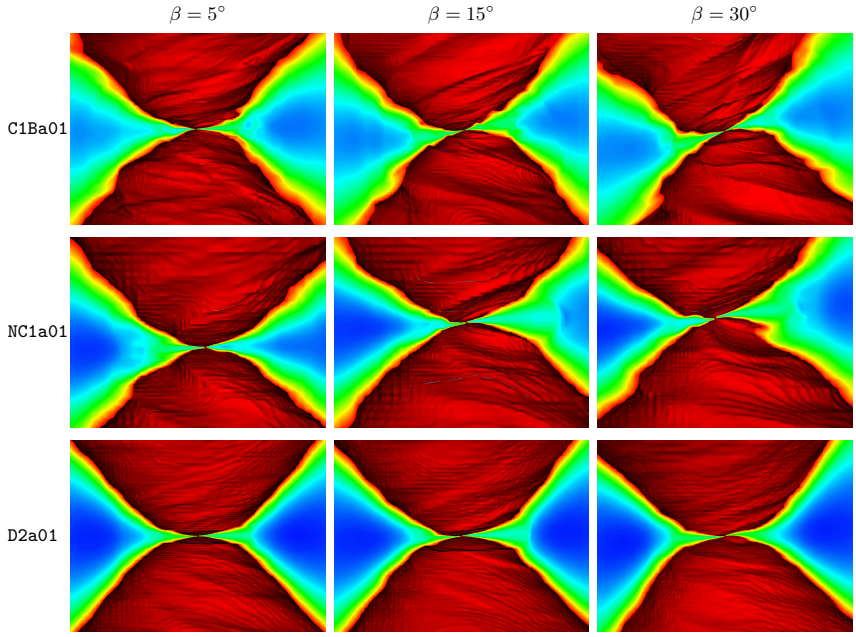

Figure 6.8 Surface plots of the (normalised) rest-mass density at the final time of the evolution $t/t_{\rm orb} = 20$ for models `C1B` with $a = 0.1$ (top row), `NC1` with $a = 0.1$ (middle row), and `D2` with $a = 0.1$ (bottom row). From left to right the columns correspond to initial tilt angles $\beta_0 = 5°, 15°$, and $30°$, respectively. The domain shown in all panels is 20 across the y-axis and 15 across the z-axis, which also indicates the upward direction in the plots. The color palette and corresponding normalised density used are the same as in Fig. 6.7.

simulations presented here. Low mass discs therefore do exhibit twisting and warping, but not at very low spins. The growth of non-axisymmetric modes associated with the PPI (see below) in the two more massive models `C1B` and `NC1` causes an alignment of the overall disc angular momentum vector with the BH spin. This interesting effect will be discussed in Section 6.2.6 below, where we comment on the BH precession and nutation properties.

In Figures 6.10 and 6.11 we plot linearly spaced isocontours and the logarithm of the rest-mass density in the plane perpendicular to the total angular momentum vector of the disc. This kind of "equatorial" plots allows for a better visualisation of the possible growth of non-axisymmetric structures in the disc. We note that due to the twisting and warping of the disc as a result of the initial BH tilt, the choice of the plane on to which project the isocontours for an adequate visualisation is not straightforward and careless choices (as e.g. the simple choice of the equatorial xy-plane) may hide important pieces of information on the dynamics and morphology. The top row of Fig. 6.10 corresponds

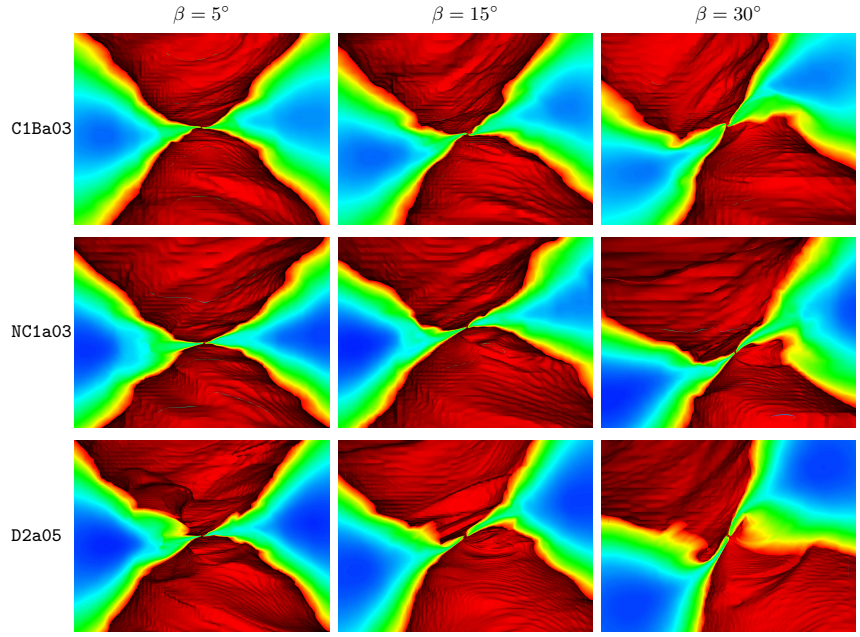

Figure 6.9 Surface plots of the (normalised) rest-mass density at the final time of the evolution $t/t_{\rm orb} = 20$ for models `C1B` with $a = 0.3$ (top row), `NC1` with $a = 0.3$ (middle row), and `D2` with $a = 0.5$ (bottom row). From left to right the columns correspond to initial tilt angles $\beta_0 = 5°, 15°$, and $30°$, respectively. The domain shown in all panels is 20 across the y-axis and 15 across the z-axis, which also indicates the upward direction in the plots. The color palette and corresponding normalised density used are the same as in Fig. 6.7.

to models `C1Ba01b5` (left), `C1Ba01b15` (middle), and `C1Ba01b30` (right), and all of them are displayed at the time at which the growth of the fastest growing non-axisymmetric structure in the disc saturates (see Fig. 6.15 in Section 6.2.4 below where we discuss the mode growth of the PPI for the different models of our sample). The middle row of Fig. 6.10 corresponds to models `NC1a01b5` (left), `NC1a01b15` (middle), and `NC1a01b30` (right), also shown at the time the fastest growing mode has maximum amplitude, while the bottom row shows models `D2a01b5` (left), `D2a01b15` (middle), and `D2a01b30` (right), which are displayed at the final time of the evolution ($t = 20t_{\rm orb}$) when the amplitudes of the corresponding PPI modes (if present) are largest. Correspondingly Fig. 6.11 shows the same type of isocontour plots as Fig. 6.10 but for the models with higher initial spin. The top row of Fig. 6.11 corresponds to models `C1Ba03b5` (left), `C1Ba03b15` (middle), and `C1Ba03b30` (right), the middle row of Fig. 6.10 corresponds to models `NC1a03b5` (left), `NC1a03b15` (middle), and `NC1a03b30` (right) and the bottom row shows models `D2a05b5` (left), `D2a05b15` (middle),

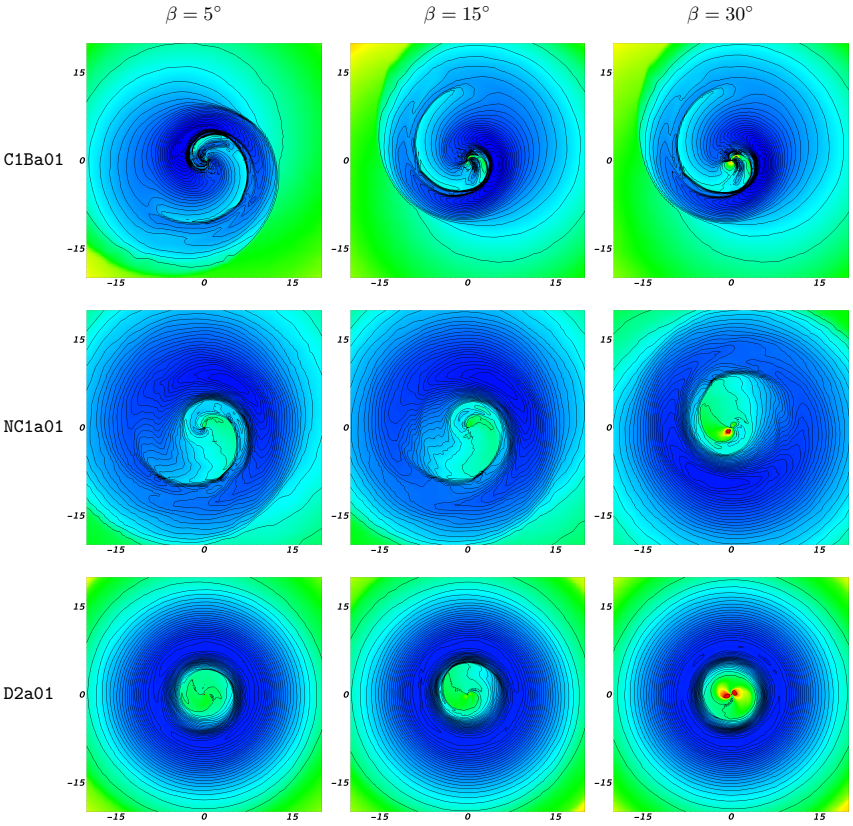

Figure 6.10 Linearly spaced isocontours in plots showing the logarithm of the rest-mass density in the plane perpendicular to the total angular momentum vector of the disc. From left to right the rows show models `C1Ba01b5`, `C1Ba01b15` and `C1Ba01b30` (top), `NC1a01b5`, `NC1a01b15` and `NC1a01b30` (middle), and `D2a01b5`, `D2a01b15`, and `D2a01b30` (bottom). The color palette and corresponding normalised density used are the same as in Fig. 6.7. The morphological structures shown in the different panels reflect the dominant PPI mode at the time of maximum non-axisymmetric mode amplitude. See main text for further details.

and `D2a05b30` (right). As in Fig. 6.10, the times shown are at either saturation of the fastest growing non-axisymmetric structure or when the maximum mode amplitudes are largest.

The inspection of the different panels displayed in Figs. 6.10 and 6.11 shows noticeable differences in the flow morphology. On the one hand all six models `C1B` (top rows in both figures), corresponding to initial BH spins of $a = 0.1$ and $a = 0.3$, respectively, exhibit a very prominent spiral density wave once the stationary accretion phase is reached. This structure, which is visible for all three tilt angles considered, $\beta = 5°, 15°$ and $30°$, is associated with the growth of the $m = 1$ non-axisymmetric PPI mode, which is the fastest-growing mode and

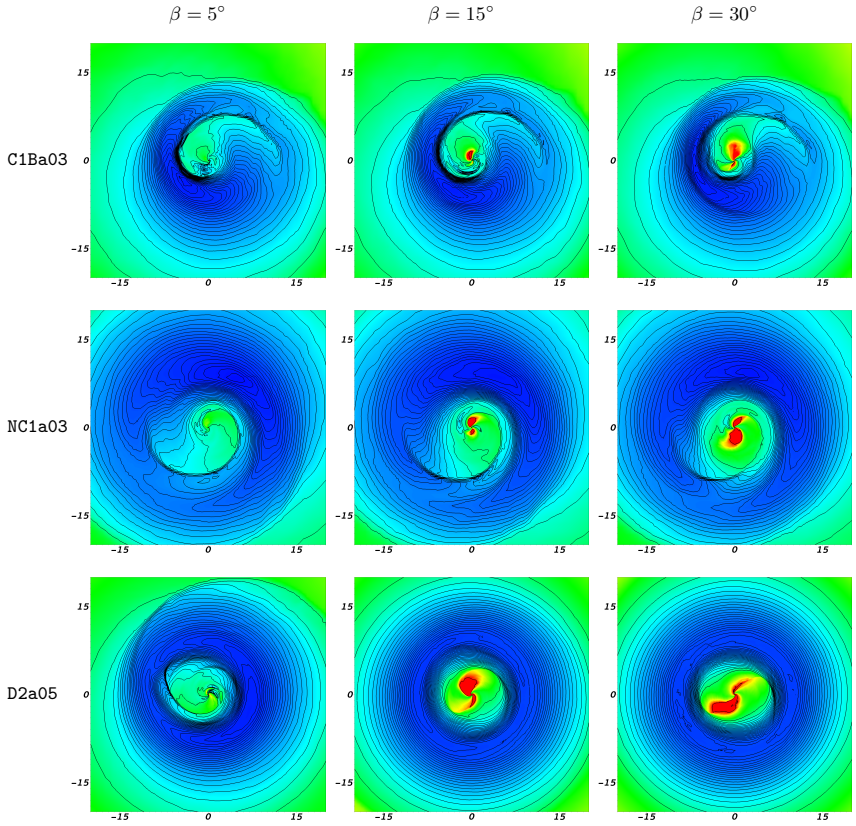

Figure 6.11 Linearly spaced isocontours in plots showing the logarithm of the rest-mass density in the plane perpendicular to the total angular momentum vector of the disc. From left to right the rows show models `C1Ba03b5`, `C1Ba03b15` and `C1Ba03b30` (top), `NC1a03b5`, `NC1a03b15` and `NC1a03b30` (middle), and `D2a05b5`, `D2a05b15`, and `D2a05b30` (bottom). The color palette and corresponding normalised density used are the same as in Fig. 6.7. The morphological structures shown in the different panels reflect the dominant PPI mode at the time of maximum non-axisymmetric mode amplitude. See main text for further details.

has the largest amplitude (see also Fig. 6.14). The middle rows, corresponding to the six models `NC1`, show the development of a spiral arm as well, however not as clearly pronounced as in the case of `C1B`. On the other hand the isodensity contours of all three models `D2` displayed in the bottom row of Fig. 6.10 for a BH spin $a = 0.1$ barely show any morphological deviation from the initial axisymmetry. Only the innermost regions closest to the BH show some slight non-axisymmetric structure, particularly for the model with the largest tilt angle ($\beta = 30°$) shown on the right panel. The disc of model `D2` is considerable lighter than that of model `C1B`, and model `NC1` has an initial non-constant specific angular momentum profile and according to Kiuchi et al. [2011] more massive

tori with $l = \text{const}$ profiles favour the appearance of the PPI with respect to less massive tori (see in particular Figs. 2 and 3(a) of Kiuchi et al. [2011] for their model `C1` which has very similar properties regarding size and BH-to-disc mass ratio to our model `C1B`). Our results seem to only partially confirm those previous findings as there seems to be some weak dependence of a moderate $m = 2$ PPI growth with increasing tilt angles. A possible origin of the $m = 2$ mode growth in these models might be connected to our Cartesian grid. However, the dependence of the growth on initial tilt angle seems to indicate that this is a physical effect. To gauge the effect of the Cartesian grid, one would have to compare the disc evolutions of our models with new simulations performed in spherical grids.

The dependence on the BH spin seems however to be more significant for the light model `D2`, as shown in the panels at the bottom row of Figures 6.10 and 6.11. For the higher spin runs shown in Fig. 6.11, all three panels show non-axisymmetric morphological features. All three snapshots correspond to the same final time of the evolution ($t = 20t_{\rm orb}$) and the dynamical differences between the three models are only due to the initial BH tilt angle. For $\beta = 5^\circ$ (left panel) the $m = 1$ spiral structure is visible and dominant but, at the same time, the $m = 2$ mode seems to have reached an almost similar amplitude (see the bottom panel of Fig. 6.14). Such $m = 2$ feature becomes clearly dominant the larger the BH inclination becomes, as depicted in the central regions of the middle and right panels.

6.2.2 Maximum rest-mass density evolution

We next show the evolution of the maximum rest-mass density in the discs in Fig. 6.12, normalised to the corresponding initial central density of each model (see Tables 6.1 and 6.2). For model `D2` (bottom panel), the effect of tilting the BH has very little effect on the evolution of $\rho_{\rm max}$ for a BH spin of $a = 0.1$. However, for $a = 0.5$, the evolution of $\rho_{\rm max}$ differs for the different initial tilt angles. Model `D2a05b5` exhibits an upward drift from 10 orbits onwards to bring ρ_{max} to the level of the lower spin runs towards the end of the simulation. This might be connected to the growth of the m=1 non-axisymmetric mode in this model, as discussed in the previous section. In the initial stages of the evolution, ρ_{max} is higher for larger tilt angles, a dependence that is also observed in the accretion rate (see Section 6.2.3). The maximum rest-mass density stays below its initial value for almost the entire evolution for both models `D2` and `NC1` (middle panel). This is very different in model `C1B` (top panel) where the

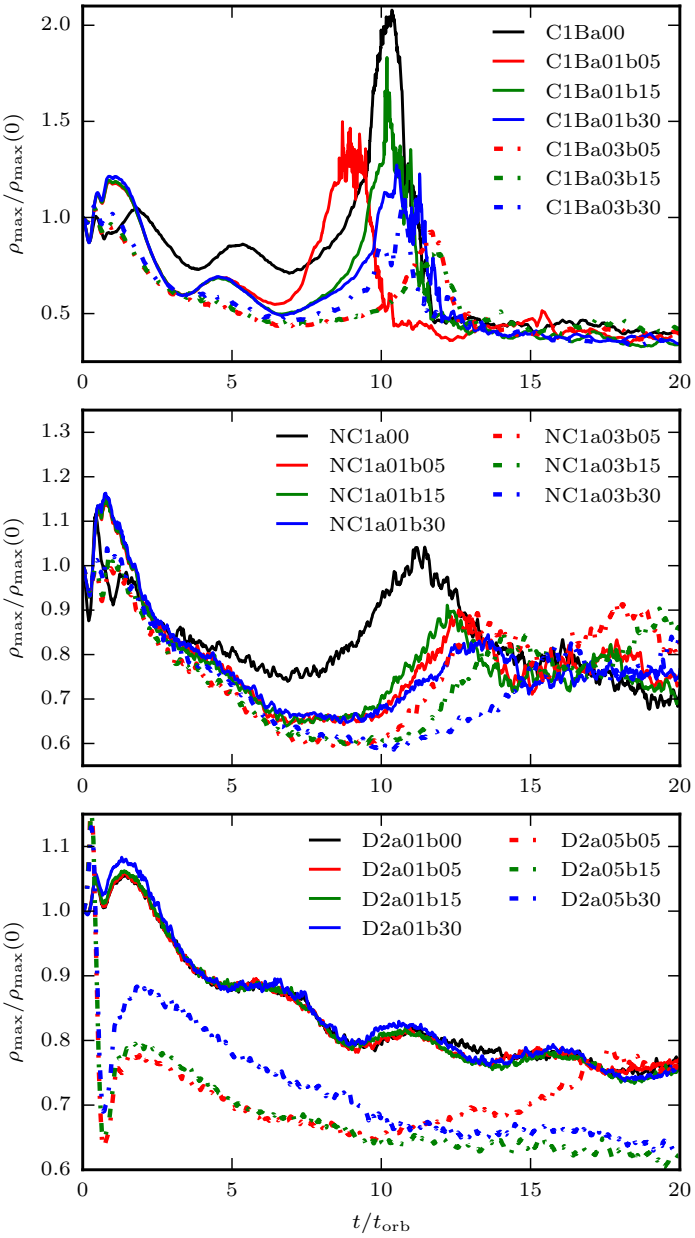

Figure 6.12 Evolution of the maximum rest-mass density, normalised by its initial value, for models `C1B` (top), `NC1` (middle) and `D2` (bottom). The dashed curves correspond to the high spin models of our sample.

occurrence and saturation of the PPI has a drastic effect on the evolution of ρ_{max}. When the PPI starts growing, a situation which is accompanied by an exponential growth of the accretion rate, ρ_{max} grows to up to twice its initial value, reaching the highest value for the untilted model `C1Ba00`. It subsequently settles to a value that is very similar for all initial spins and tilt angles, but the time of growth and the shape of the "lump" in the density evolution are different for the different spins and initial tilt angles. Model `NC1` shows features from both models `D2` and `C1B` described above. Similarly to model `D2`, ρ_{max} stays below its initial value for almost the entire evolution, with model `NC1a00` being an exception where it grows above the initial value briefly. There is, as in models `C1B`, a rapid growth in the central density, albeit somewhat smaller for the non-constant angular momentum discs, associated with the growth of the PPI in all the models. The magnitudes at which the mode growth saturates are similar, while the time at which the growth sets in depends on the initial spin and tilt angle.

6.2.3 Evolution of the accretion rate

Fig. 6.13 shows the time evolution of the mass accretion rate for all models of our sample, in units of $\mathrm{M}_{\odot}/s$. The colours used for the different models as well as the line style follow the same convention as in the rest-mass density evolution figure (Fig. 6.12). The top panel displays the mass flux for models `C1B`, the middle panel for models `NC1`, and the bottom panel for models `D2`. The mass flux is computed as the instantaneous flux of matter across the AH surface which is parameterised in spherical coordinates by the polar angle θ and azimuthal angle ϕ and is given by:

$$\dot{M} = 2\pi r^2 \int_0^{2\pi} \int_0^{\pi} D\, v^r \, \sin\theta \, d\phi \, d\theta \,, \tag{6.12}$$

where r is the radius of the AH and v^r is the radial velocity of the fluid crossing the sphere. In the actual implementation in the `Outflow` thorn, the relevant quantities are interpolated onto the respective spherical surface (the AH in our case) and the integration is performed as a two dimensional surface integral in spherical coordinates (see the thorn documentation at the `Einstein Toolkit` [n.d.] website for details). All three panels of Fig. 6.13 show that after a transient initial phase the mass accretion rate is seen to tend asymptotically to a fairly constant value.

In the previous fixed spacetime simulations of Fragile and Anninos [2005] it was found that the tilt and the twist of the discs are not strongly responsive to $\dot{M}$.

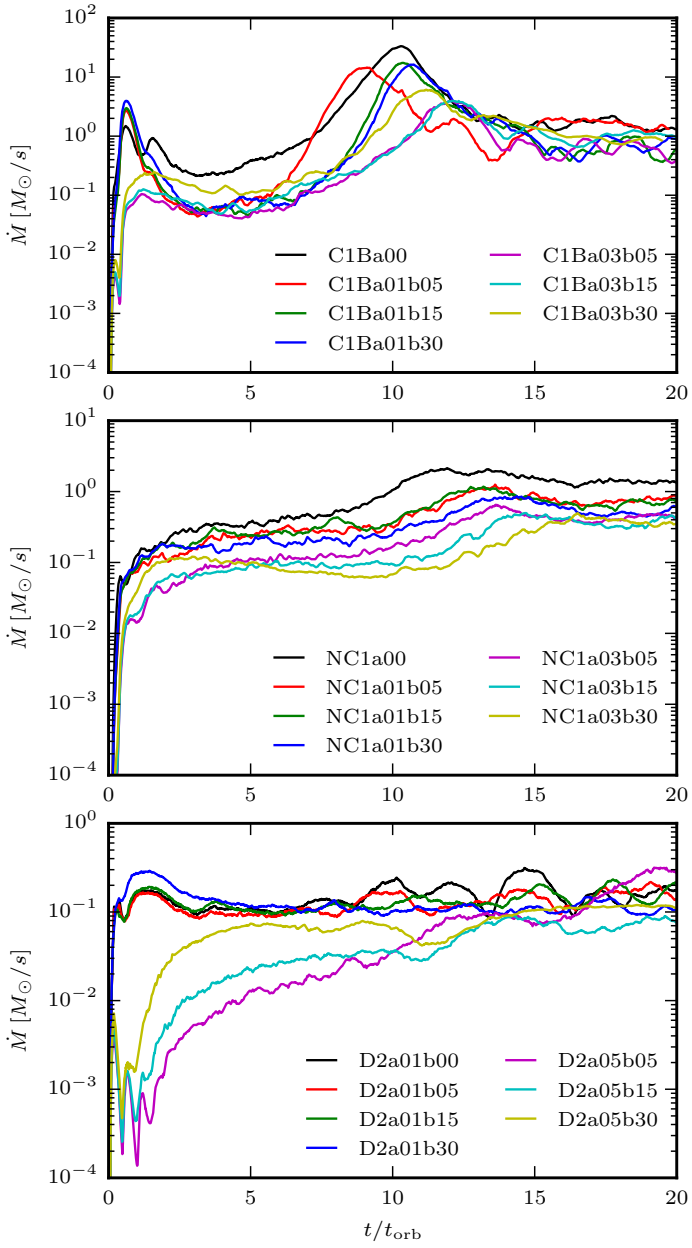

Figure 6.13 Evolution of the accretion rate in $M_\odot/s$ for models `C1B` (top), `NC1` (middle) and `D2` (bottom).

Our results for a dynamical spacetime validate those earlier findings, as the final dispersion found in $\dot{M}$ once this quantity reaches steady-state values is relatively

small irrespective of the BH spin and inclination angles ($\dot{M}\,[\mathrm{M}_\odot/s] \in [0.2, 1.5]$ for models `C1B` and `NC1`, and $[0.06, 0.2]$ for model `D2`). However, the transition to the steady-state does seem to show a clear dependence on the BH spin. We find that the initial $\dot{M}$ values are consistently smaller the larger the BH spin, about 2 orders of magnitude for models `D2` after $\sim$1 orbit and about half that value for the more massive discs `C1B` and `NC1`. Another trend, which is most clearly seen in model `D2`, is the initial dependence of the accretion rate on the tilt angle as well. We find that the higher the initial tilt angle, the higher the accretion rate in the early stages of the evolution. This is because the innermost stable circular orbit (ISCO) of a rotating Kerr BH has an ellipsoidal shape, attaining the smallest size at the equatorial plane of the BH. For prograde orbits such as those considered in our work, the specific angular momentum at the ISCO decreases with higher BH spin. Matter is accreted when its specific angular momentum is lower than that at the ISCO, which means that higher BH spins present larger centrifugal barriers for the matter to be accreted. For inclined orbits, the specific angular momentum at the respective ISCO for a given inclination angle increases with larger inclination (up to its maximum value at the pole of the BH) and the accretion rate becomes therefore higher for larger inclinations. While the transition stage is physically not relevant (as real post-merger discs would not show such an episode) it is nevertheless reassuring that we observe the correct physics during the transition.

A common feature present in the mass-flux plots of the simulations of Fragile and Anninos [2005] was a late-time "bump" which the authors attributed to the reflection of an outgoing wave within the disc at the outer edge. That feature does not seem to be so apparent in our models apart from maybe model `C1B` which shows a bump around $t \sim 10 t_{\mathrm{orb}}$ somewhat similar to that reported by Fragile and Anninos [2005]. However, in our interpretation, the phase of rapid growth in $\dot{M}$ in less than about 5 orbits seems to have a different origin. This conclusion is reached by comparing the time at which the growth of the PPI saturates (discussed in Figs. 6.14 and 6.15 in the following section) with the saturation time of the accretion rate for model `C1B`, which yields a significant close agreement. We note that this peak in the accretion rate is the highest of all our models, $\sim 30\mathrm{M}_\odot/\mathrm{s}$, lasting for less than about 1 ms. Therefore, we identify the exponential growth and subsequent saturation of the mass accretion rate with the growth and saturation of the PPI in our models.

The total rest mass accreted during the evolution ranges within $M_{\mathrm{acc}} \in [0.022, 0.033]$, $[0.005, 0.013]$ and $[0.0006, 0.002]$ for models `C1B`, `NC1` and `D2`, respectively. The accretion is facilitated by the outward transport of angular

momentum, which we describe in section 6.2.8 below. The growth of the PPI, to which we attribute the high peak accretion rates, is very effective in transporting angular momentum outwards. While we have performed our study without considering magnetic fields, it is known that magnetic fields are very effective at transporting angular momentum in accretion discs [Balbus and Hawley 1991], via the development of the MRI [Velikhov 1959, Chandrasekhar 1960]. Not taking into account the effects of magnetic fields in accretion discs seems to underestimate the accretion rate [Gold et al. 2014], see also recent GRMHD simulations of BHNS mergers in Paschalidis, Ruiz, and Shapiro [2015] and Kiuchi et al. [2015b] and the accretion rates reported therein. The accretion rates we observe are well above the Eddington limit and in a range compatible with that needed to power GRBs [Popham, Woosley, and Fryer 1999].

6.2.4 PPI growth in the disc and BH motion

In their seminal paper on the PPI, Papaloizou and Pringle [1984] showed that vertically thick, radially slender tori with constant specific angular momentum profiles are unstable against the development of global non-axisymmetric modes. Two of our models, `C1B` and `D2`, have constant specific angular momentum profiles, while model `NC1` has a radial dependence of $l \sim R^q$, where $q = 0.11$. Zurek and Benz [1986] showed that tori with non-constant angular momentum profiles might become PP-unstable as well. In order to check for the onset and the growth of non-axisymmetric instabilities, we monitor the mode amplitudes computed using Eq. (4.28), which is basically a Fourier decomposition of the azimuthal distribution of the density in the disc [Zurek and Benz 1986]. In simulations of accretion tori susceptible to the development of the PPI performed on spherical grids, it is customary to induce the instability with small initial non-axisymmetric density or velocity perturbations. *Any* non-axisymmetric perturbation will trigger the growth of the instability provided the torus is not stable against it. We do not actively seed the PPI in any of our models. Instead, there are two main sources of perturbations in our simulations, both connected to the fact that we evolve the BH-disc system in a Cartesian grid. First, the exact axisymmetry of the ID is lost when we interpolate the ID onto the Cartesian grid of the evolution, introducing small, non-axisymmetric perturbations in all interpolated quantities. This is due to the fact that in Cartesian grids neighbouring cells lie on concentric shells only in the limit of infinite resolution. The second source of perturbation is the so-called junk-radiation leaving the BH while the gauge evolves from the values specified by the ID to the puncture

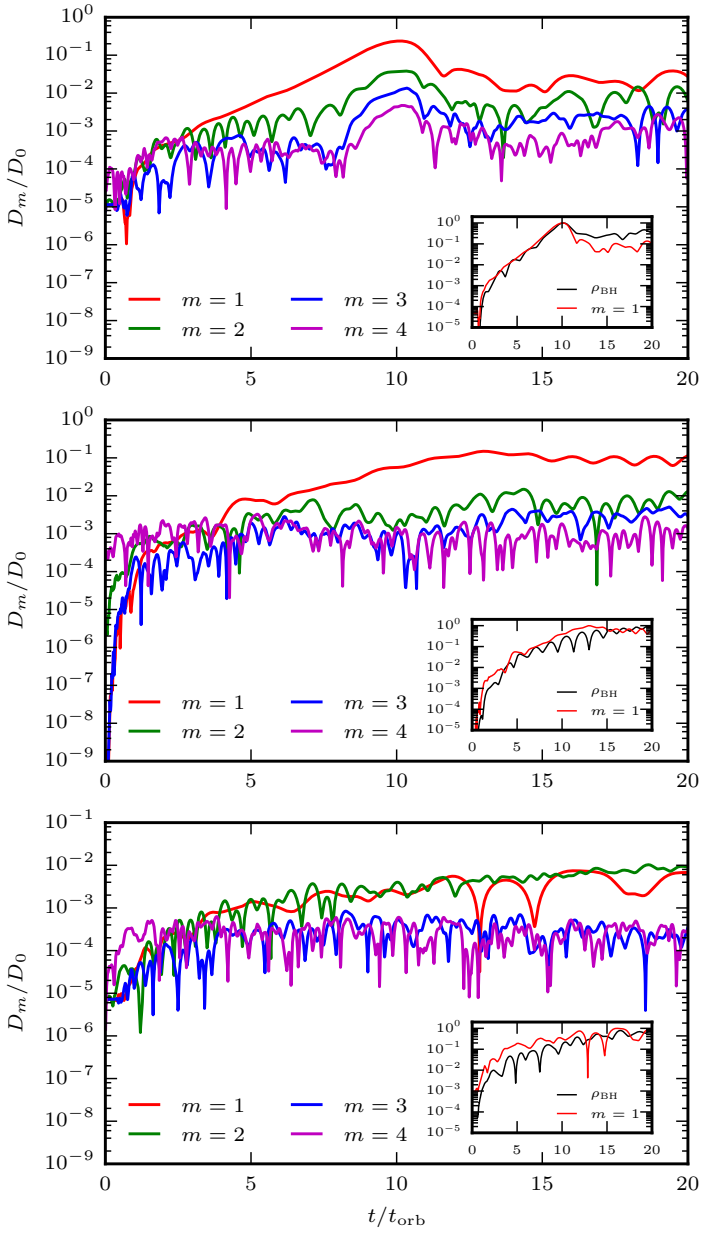

Figure 6.14 Evolution of the first four non-axisymmetric (PPI) modes scaled by the total rest-mass density (D_0) for models `C1Ba01b30` (top), `NC1a01b30` (middle) and `D2a01b30` (bottom). The inset shows the evolution of the $m = 1$ mode and the polar distance of the centre of the BH from the origin, both having been rescaled with their respective maximum values attained during the evolution.

gauge attained during the evolution. Here, we need to distinguish between models evolved around Schwarzschild BHs and the models evolved around tilted Kerr BHs. For the former, the junk-radiation leaving the BH initially should be axisymmetric. Indeed, when analysing this initial burst of radiation with the Weyl scalar Ψ_4, we find that the amplitudes of the $\Psi_4^{l,0}$ multipoles (which are axisymmetric) are the largest. Nevertheless, the initial junk-radiation has also non-vanishing amplitudes in the other $\Psi_4^{l,m}$ multipoles. Again, the reason for the presence of these non-axisymmetric $\Psi_4^{l,m}$ multipoles seems to be connected to the evolution in the Cartesian grid, and specifically to the existence of mesh refinement boundaries, which are *not* axisymmetric even in the continuum limit (see Zlochower, Ponce, and Lousto [2012] for interference patterns produced by the radiation crossing mesh refinement boundaries). Finally, in the case of the disc being around a tilted Kerr BH, the junk-radiation reaching the disc is now truly non-axisymmetric even without taking into account the effects of the Cartesian grid and the mesh refinement boundaries, as the axis of rotation is tilted with respect to the $z = 0$ plane.

We show in Fig. 6.14 the evolution of the amplitude of the first four non-axisymmetric modes D_m ($m = 1 - 4$) in the disc for models `C1Ba01b30` (top), `NC1a01b30` (middle) and `D2a01b30` (bottom). Those amplitudes are computed using Eq. (4.28). In addition, in the inset of all three plots we also show as a black solid curve the evolution of the polar distance of the centre of the BH from the origin of the computational grid, which we label $\rho_{\rm BH}$. We note that the $m = 4$ mode is dominant in the very early stages of the evolution for all models. This is due to the Cartesian grid. At the later stages, the (physical) $m = 1$ and $m = 2$ (for models `D2`) become dominant, as expected.

Model `C1Ba01b30` is the one that most clearly is found to develop the PPI, as signalled by the exponential growth of the $m = 1$ mode. Modes $m = 2 - 4$ also show a phase of exponential growth lasting for about 2 orbital periods (between $t \sim 8 - 10\, t_{\rm orb}$) but the saturation amplitudes reached are 1 to 2 orders of magnitude smaller than for $m = 1$. As mentioned in the previous section, the growth of the PPI is accompanied by an exponential growth of the mass accretion rate (see Fig. 6.13). For this model the PPI clearly saturates at around $t \sim 10\, t_{\rm orb}$, when the amplitude of the $m = 1$ mode quickly drops by an order of magnitude. After that, the amplitude of all the modes we have analysed remains rather constant. The strength of the $m = 2 - 4$ modes becomes similar at late times while the $m = 1$ mode still retains a significantly larger amplitude.

The polar distance of the BH from the origin for model `C1Ba01b30` closely follows the behaviour of the $m = 1$ fastest growing PPI mode. This distance is

found to grow at the same actual rate as the $m = 1$ mode, because the circular motion of the $m = 1$ over-density hump (well visible in the top-rightmost panel of Fig. 6.10) causes the BH to start moving in a spiral trajectory. After mode saturation the polar distance of the BH from the origin remains almost constant, reflecting a similar trend in the $m = 1$ evolution. This spiral motion of the BH as a result of the development of the PPI has also been observed in the simulations of Korobkin et al. [2011].

For the non-constant angular momentum model `NC1a01b30` (middle panel) the growth rate of the $m = 1$ mode is smaller, although it is still the dominant mode, as in model `C1Ba01b30`. The growth of the mode saturates somewhat later at around $t \sim 12.5\, t_{\rm orb}$ but, contrary to the evolution of `C1Ba01b30`, it does not drop significantly after saturation, remaining fairly constant thereafter. Furthermore, it remains the dominant mode at late times while the three remaining modes attain similar amplitudes. The evolution of the polar distance of the BH from the origin shows a small secular drift after the saturation of the PPI.

On the other hand, model `D2a01b30` (bottom panel) shows a very distinct behaviour. The amplitude of all four modes and the polar distance of the BH remain below the values attained in models `C1Ba01b30` and `NC1a01b30`, typically in the range between 1 to 2 orders of magnitude. Furthermore, the $m = 1$ and $m = 2$ modes grow at approximately the same rate and to similar final values during the evolution. The growth rate of $\rho_{\rm BH}$ is very similar to the growth rate of the modes $m = 1$ and $m = 2$. We also note that at early times the $m = 4$ mode shows the largest amplitude (purple line; not so clearly noticeable in the previous two models), perhaps an artefact of the Cartesian grid we use in our simulations. Nevertheless, the amplitude of this mode at late times is sufficiently smaller than the dominant amplitudes (mostly that of the $m = 1$ mode) to safely consider its effect on the dynamics negligible. From the mode analysis, we can therefore say that model `D2` is essentially PP-stable. We will return to this point in section 6.2.8, where we analyse the angular momentum transport in the models.

The results we have just described connect the exponential growth and saturation of the mass accretion rate with the growth and saturation of the PPI in the models where it has unambiguously taken place. To further justify this, we plot in Fig. 6.15 the evolution of the $m = 1$ mode for all models considered in our sample. Focusing on the evolution of the models `C1B` displayed in this figure (top panel) we can clearly see that the temporal order of the saturation of the mode growth closely coincides with the various peaks present in the mass

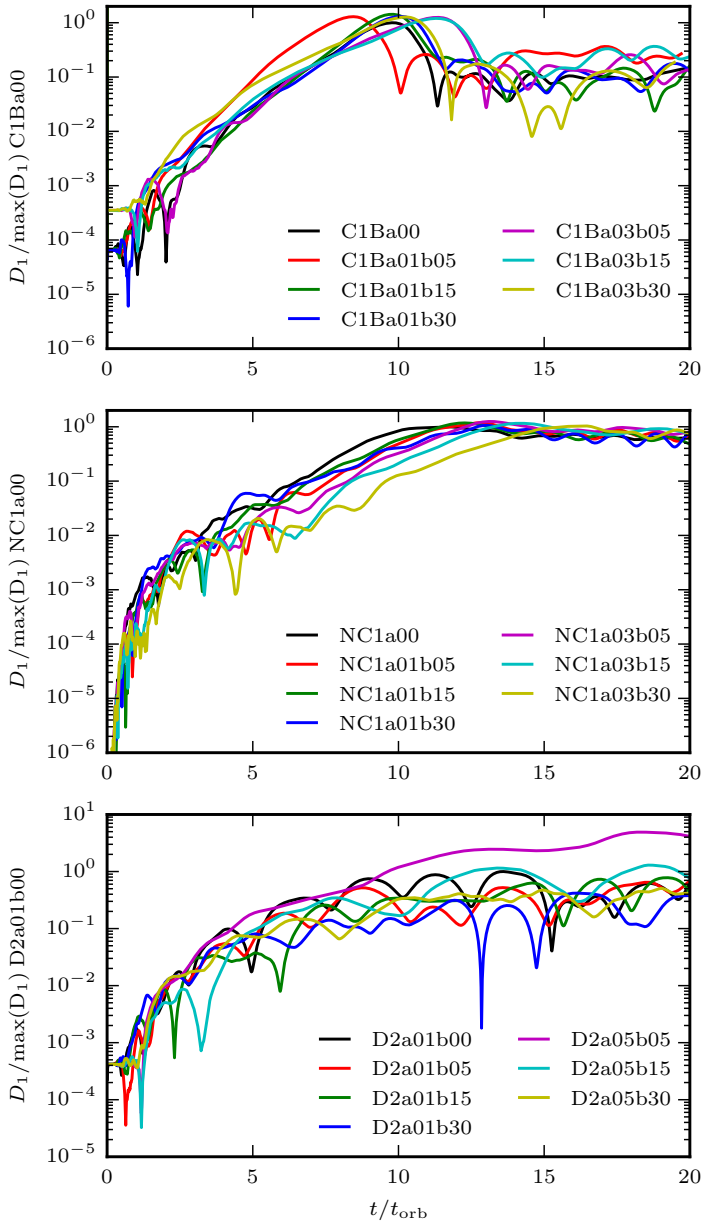

Figure 6.15 Evolution of the non-axisymmetric $m = 1$ mode for all models, namely `C1B` (top), `NC1` (middle) and `D2` (bottom), rescaled to the maximum amplitude of the D_1 mode of the respective untilted models.

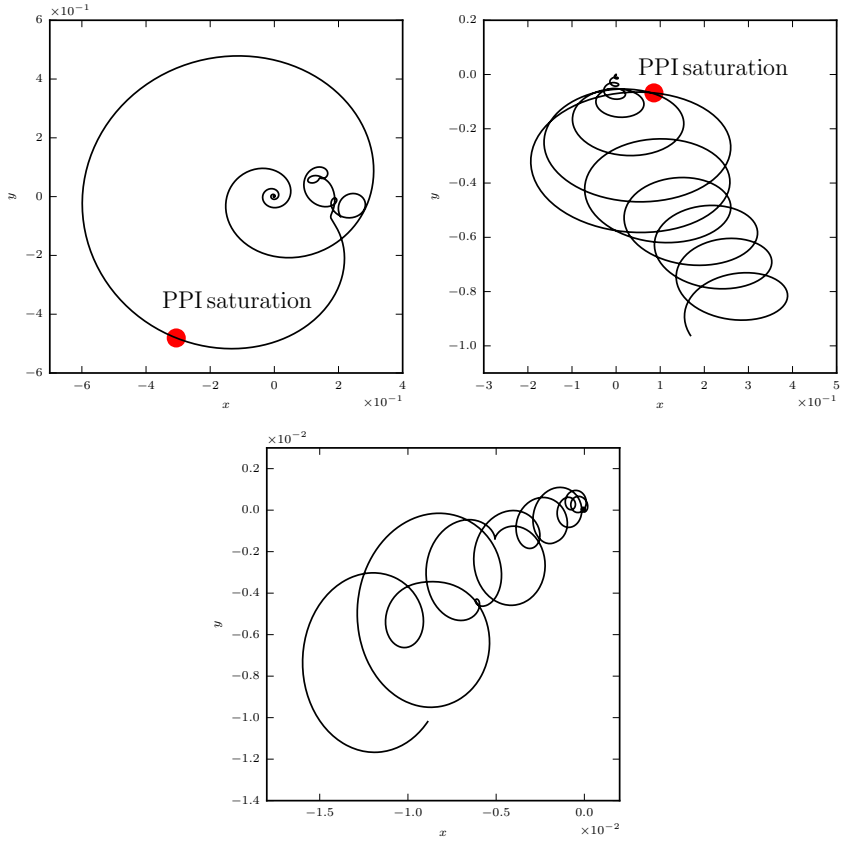

Figure 6.16 Position of the BH centre on the xy plane for models `C1Ba01b30` (left), `NC1a01b30` (middle) and `D2a01b30` (right). For models `C1Ba01b30` and `NC1a01b30`, the red dot indicates the point in the trajectory when the PPI saturates. Note that the scale ratio is not preserved in the figures for clarity in the visualisation and that the length scale is significantly different in every panel.

accretion rate evolutions shown in Fig. 6.13 (compare curves of the same color). The comparison among the three types of models also shows that the saturation mode growth for models `C1B` is only slightly larger than for models `NC1`, their late-time values being fairly similar, but about 2 orders of magnitude larger than in models `D2`. The slope of the mode growth is also steeper in models `C1B`, while the behaviour of the mode evolution in the case of the light tori `D2` almost seems to indicate that the development of non-axisymmetric instabilities is only marginal for such models. A striking feature worth highlighting from the middle panel of Fig. 6.15 is the non-existing dependence of the late time $m = 1$

mode amplitude on the BH spin and tilt angle for the non-constant angular momentum tori `NC1`.

To demonstrate the connection between the growth of non-axisymmetric modes in the disc with the motion of the BH, we plot in Fig. 6.16 the position of the BH centre on the xy plane for models `C1Ba01b30` (top), `NC1a01b30` (middle) and `D2a01b30` (bottom). This figure shows several interesting features connected to the growth of the modes in the tori. The motion of the BH is caused by the formation of a "quasi-binary system" between the BH and the $m = 1$ over-density lump, which was also observed in Korobkin et al. [2011]. Note that the motion of the BH is well within the initial inner disc radius (see Table 6.1). It is the binary motion that causes the long-term emission of GWs reported in Kiuchi et al. [2011]. We will return to this in the discussion of the GW emission connected to the PPI in section 6.2.9. For model `C1Ba01b30`, the development of the dominant $m = 1$ structure in the disc exerts a small kick in the BH. As a result the BH starts moving in a spiral trajectory until the PPI saturates and the mode amplitude drops, at which point the BH is roughly located at $(x, y) = (-0.3, -0.5)$. After saturation, the xy position of the BH is a combination of linear and circular motion. In model `NC1a01b30`, the linear motion is stronger from the beginning, causing a linear shift in the growing spiral motion. Upon saturation of the PPI, the circular motion continues with a smaller radius, in accordance to the evolution of the $m = 1$ mode which remains at a rather f value after saturation and up until the end of the evolution. Finally, for model `D2a01b30` we have a superposition of circular and linear motion again, as the modes $m = 1$ and $m = 2$ are of almost equal magnitude during the evolution. Here, the overall distance covered by the BH is significantly smaller than for the heavier models `C1Ba01b30` and `NC1a01b30`, as the mode amplitudes are much smaller for `D2` and the disc is also lighter. From our simulations, we see that more massive discs favour the development of the PPI. This might be in connection with the enhanced $m = 1$ mode strength due to the motion of the BH described above. We will investigate the effect of the BH motion on the mode growth rate and maximum amplitude in more detail in Chapter 7. The strength of the $m = 1$ mode growth will affect almost every diagnostic that we investigate in the subsequent sections. The growth of the PPI has therefore far reaching consequences on the disc evolutions.

We argue that the non-axisymmetric instability we observe in our models is indeed the PPI based on the azimuthal mode evolution in the disc and the development of the $m = 1$ over-density lump. However, we do not claim to have presented a direct, undeniable proof that the instability observed in our

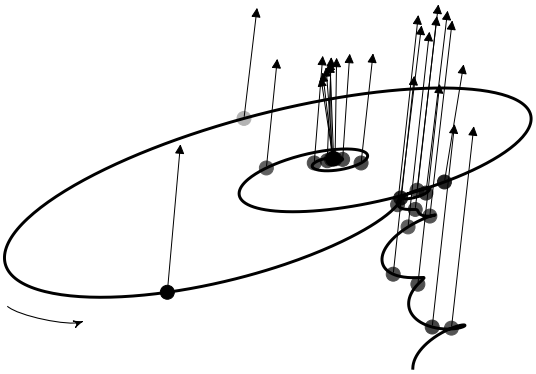

Figure 6.17 Full 3D trajectory of the BH along with its spin vectors for model `C1Ba01b30`. The curved arrow indicates the direction of the BH's motion. The magnitude of the spin vectors has been rescaled with a constant factor for visualisation purposes.

simulations is the analytical PPI studied in Papaloizou and Pringle [1984]. To do so, we should have compared the predicted growth rates of the PPI for our models in the linear regime to those observed in our simulations, and should have checked for the occurrence of the so-called non-axisymmetric I-modes (see Christodoulou and Narayan [1992] and Korobkin et al. [2011]) during the disc evolution. We also note that there exist other instabilities in self-gravitating discs which display spiral arm formation in the disc or even disc fragmentation, such as the axisymmetric local Toomre instability (a gravitational instability) [Toomre 1964]. Although Christodoulou and Narayan [1992] have shown that the Toomre instability is unlikely to affect radially slender accretion tori such as the ones considered in our study, we will analyse the gravitational stability of our discs in the following. A disc will be gravitationally unstable if the so-called Toomre parameter Q becomes less that unity, where Q is defined as

$$Q \equiv \frac{\kappa c_s}{\pi \Sigma}, \tag{6.13}$$

where κ is the epicyclic frequency, c_s the local sound speed in the disc, and Σ the surface density of the disc. For thick accretion tori, this measure of the disc stability against its self-gravity might not be adequate. Hachisu, Tohline, and Eriguchi [1987] derived a different criterion for gravitational stability, valid for both thick and thin discs, $\kappa^2/(\pi\rho) < 1$. As outlined in Christodoulou and Narayan [1992], we should choose Ω_0 (the orbital velocity at the pressure maximum) as the epicyclic frequency κ, and not the usual definition ($\kappa^2 \equiv (1/r^3)dl^2/dr$), as we are interested in the development of non-axisymmetric

modes. Defining the Jeans (gravitational) angular velocity at the pressure maximum as $\Omega_{\rm J}^2 \equiv 4\pi\rho$, Christodoulou and Narayan [1992] showed that the disc is gravitationally stable if $\Omega_{\rm J}/\Omega_0 \lesssim 2.4$. Using Ω_0 as the epicyclic frequency, the stability criterion of Hachisu, Tohline, and Eriguchi [1987] corresponds to $\Omega_{\rm J}/\Omega_0 < 2$. Evaluating $\Omega_{\rm J}/\Omega_0$ for our initial models, we find the following values: $\Omega_{\rm J}/\Omega_0 = 0.274$, 0.681, and 0.561 for disc models `D2`, `C1B` and `NC1`, respectively. We therefore conclude that out initial models are stable against their self-gravity. The discs remain gravitationally stable during the duration of the simulations, as we have not seen any evidence for gravitational fragmentation.

6.2.5 PPI saturation and BH kick

The complete 3D trajectory of the BH and its spin vector is plotted for model `C1Ba01b30` in Fig. 6.17. In this plot each small sphere with an attached arrow corresponds to the position of the BH and the magnitude (scaled for better visualisation) and direction of its spin vector. The positions are plotted at equal time intervals, so we see that the BH is moving much faster during the final stages of the PPI than before its occurrence or after its saturation. We can also see that there is a motion in the vertical direction, which is caused by the fact that the "binary" motion of the BH and $m = 1$ over-density lump does not lie in the equatorial plane anymore due to the initial tilt. While the PPI is growing, the BH–torus system therefore moves up and down in an oscillatory fashion. As we have seen in the $m = 1$ mode plots for models `C1B` (see the top panel of Fig. 6.15), the saturation of the PPI is very fast. The rapid saturation of the PPI (and the corresponding destruction of the $m = 1$ over-density lump) result in a mild vertical kick of the BH+torus system. To see that this is indeed connected to the saturation of the PPI, we plot in Fig. 6.18 the linear momentum radiated away by gravitational waves in the z-direction for models `C1Ba01`. From the plot, we can clearly see that the time of maximum emission of linear momentum corresponds exactly to the time the PPI saturates for each model. The radiated linear momentum has been calculated with the `pyGWAnalysis` package of the ET [Reisswig and Pollney 2011].

6.2.6 BH precession and nutation

Contrary to the test-fluid simulations of Fragile and Anninos [2005] and Fragile et al. [2007], as we are evolving the full spacetime, we can monitor the response of the BH to the evolution of the disc in the initially tilted configuration. In particular we can measure the total precession of the BH spin about the z-axis

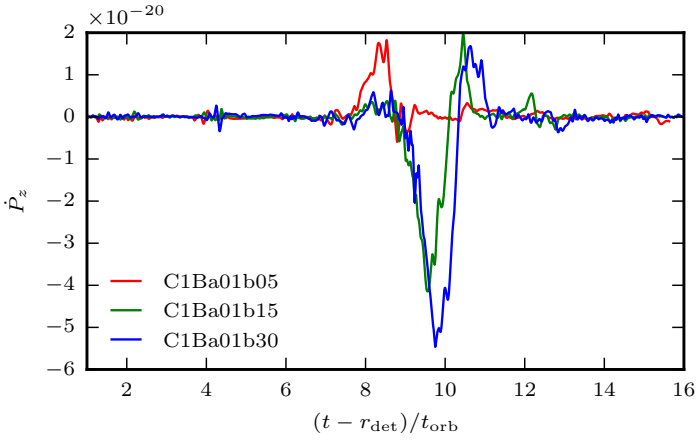

Figure 6.18 Radiated linear momentum in the z-direction for models `C1Ba01`.

($\sigma_{\rm BH} = \angle(y - \text{axis}, \mathbf{S}_{\rm xy})$) and its rate, as well as the inclination of the spin with respect to the z-axis $\nu_{\rm BH} = \angle(z - \text{axis}, \mathbf{S}_{\rm BH})$ and the corresponding nutation.

In Fig. 6.19 we plot the evolution of the precession rate $\dot{\sigma}_{\rm BH}$ of the BH about the z-axis for models `C1B` (top), `NC1` (middle) and `D2` (bottom panel) in radians per orbital period. The first thing to mention is that the constant angular momentum discs `D2` and `C1B` show a clear dependence of the precession rate with the initial BH spin magnitude. Namely, for models `D2` and `C1B`, the larger the spin the smaller the precession rate. However, for the non-constant angular momentum torus `NC1` the precession rate is very similar irrespective of the spin magnitude, particularly at the early stages ($t < 10\,t_{\rm orb}$). In models `D2` the evolution of $\dot{\sigma}_{\rm BH}$ is very smooth, and changes sign for the higher spin runs after about 17 orbits, whereas it remains fairly constant for the lower spin simulations.

A fact worth emphasising is that there is essentially no dependence of the precession rate on the tilt angle for constant angular momentum tori. This is particularly true for models `D2` but also models `C1B` show this lack of dependence up until the growth of the PPI. In all models `C1B` we observe a prominent modulation of the precession rate when the PPI enters the final stages of its growth and then saturates, as well as the change in sign for the higher spin runs. The magnitude of the precession rate is about an order of magnitude higher compared to models `D2`, which we attribute to the higher disc-to-BH mass ratio models `C1B` possess. The evolution of the BH precession rate for models `NC1` seems to fit in between the two other models. The magnitude of the precession rate is similar for the two BH spins considered in models `NC1`. We also note from

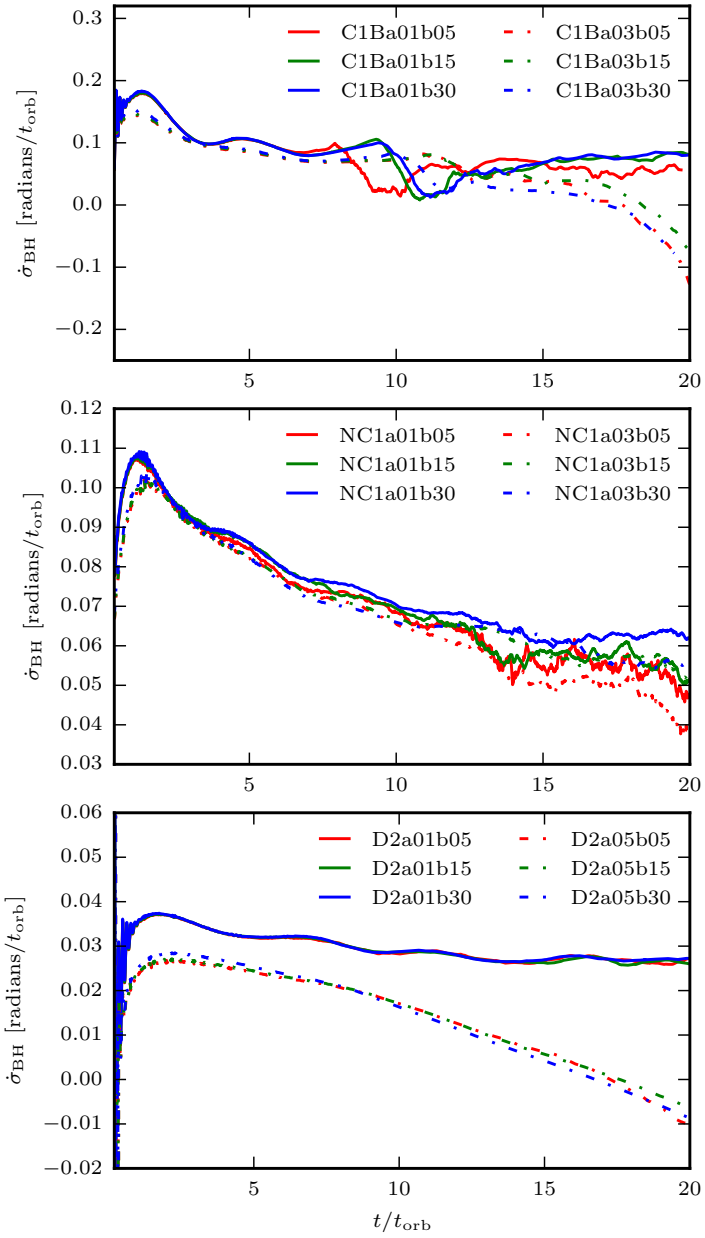

Figure 6.19 Evolution of the precession rate of the BH spin about the z-axis for models `C1B` (top), `NC1` (middle) and `D2` (bottom) in units of radians/$t_{\rm orb}$.

Fig. 6.19 that models `C1Ba01` and `D2a01` attain a fairly constant precession rate by the end of our simulations, namely $\sim 20\,$Hz and $\sim 6\,$Hz for models `C1Ba01`

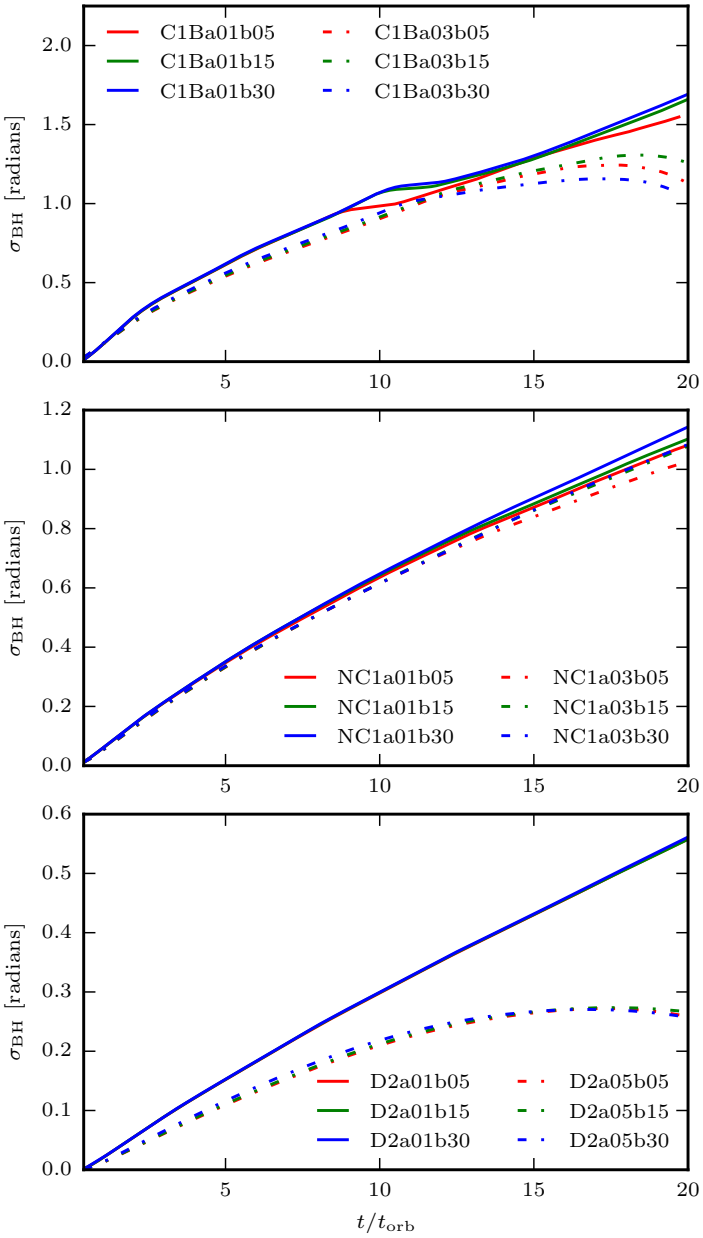

Figure 6.20 Total precession of the BH spin about the z-axis for models `C1B` (top), `NC1` (middle) and `D2` (bottom) in units of radians.

and `D2a01`, respectively. These are the frequencies for the BH masses indicated in Table 6.1.

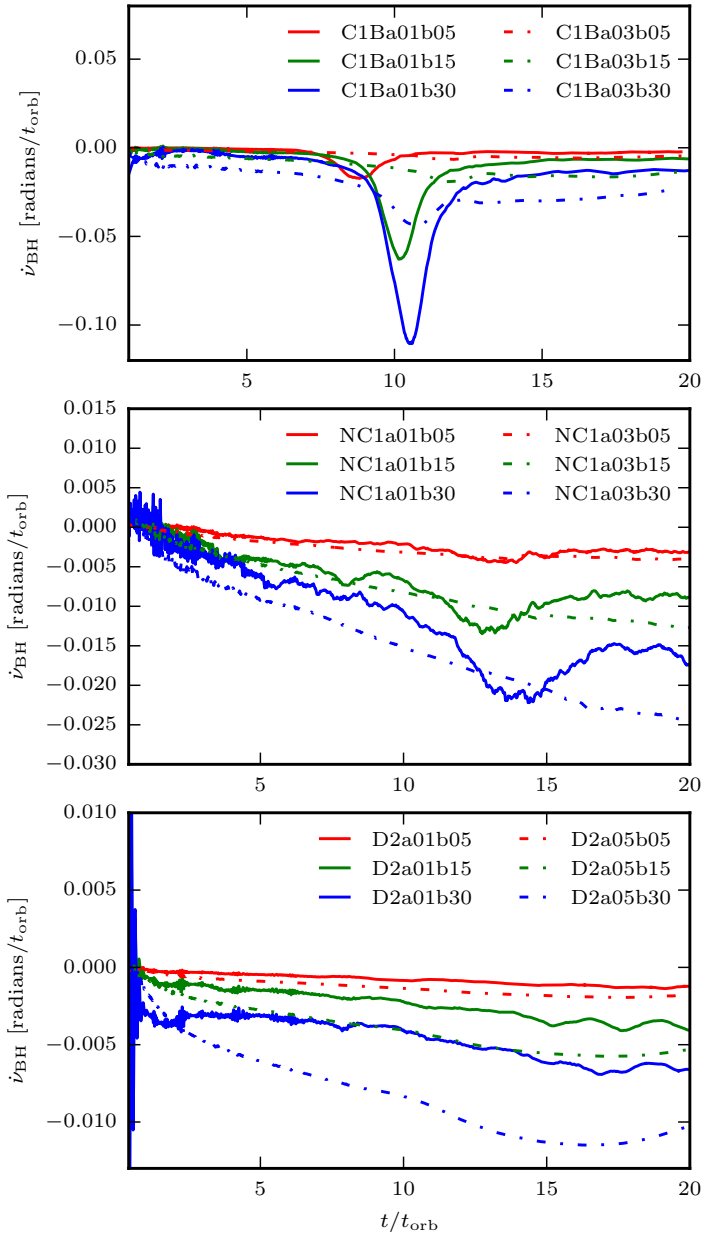

Figure 6.21 Evolution of the nutation rate of the BH spin about the z-axis for models `C1B` (top), `NC1` (middle) and `D2` (bottom) in units of radians/$t_{\rm orb}$.

The total precession of the BH spin about the z-axis is shown in Fig. 6.20. The lower spin models `C1Ba01`, that show the highest BH precession rate, have

completed a quarter of a full precession cycle by the end of our simulations at $t = 20t_{\rm orb}$. Given that the precession rate for those models appears to settle to a rather constant value (see Fig. 6.19) we would need a prohibitively expensive evolution of about 80 orbital periods for a full precession cycle of the BH for those models. If we assume that the precessing Kerr BH radiates GW as a freely precessing rigid body, it will radiate at $\dot{\sigma}_{\rm BH}$ and $2\,\dot{\sigma}_{\rm BH}$ in the $l = 2$, $m = 1, 2$ multipole modes [Zimmermann and Szedenits 1979]. This means we would have to evolve the BH–torus system for at least one full BH precession cycle in order to see the slow modulation of the GW signal caused by the BH precession. It remains an interesting open issue to see if the upcoming advanced GW detectors will be able to measure these GWs in the low tens of Hz.

The imprint of the growth of non-axisymmetric instabilities in the disc on the BH response can be seen even clearer in Fig. 6.21. This figure shows the evolution of the nutation rate for all models, that is, the evolution of the temporal variation of the tilt angle of the BH with the z-axis, $\dot{\nu}_{\rm BH}$. For models `C1B` (top panel) there is a clear period of alignment of the BH spin with the z-axis around the time when the PPI starts to grow. This is signalled by the rapid fall and rise of the nutation rate around the $10\,t_{\rm orb}$ mark for the slow spin ($a = 0.1$) BHs, but it is also (less) visible in the more rapidly rotating BHs (dashed lines). Upon saturation of the instability the nutation rate becomes almost constant and fairly close to being again zero for the $a = 0.1$ BH models (see solid lines). This behaviour is consistent with the evolution of the BH tilt angle itself displayed in Fig. 6.22, which, for the case of models `C1B` with small spins, shows two distinct zones of constant spin inclination, particularly for models with $\beta_0 = 5^\circ$ and 15° (model with $\beta_0 = 30^\circ$ still shows a negative slope at late times). The transition to zero nutation rate in the $a = 0.3$ `C1B` models after PPI saturation seems to take a longer time than that displayed in Fig. 6.21.

In addition Fig. 6.21 also shows that the maximum nutation rate attained increases with increasing initial tilt angle. This is very clearly seen in models `C1B` but it is also visible in most of the models `D2` and `NC1`. In particular the evolution of $\dot{\nu}_{\rm BH}$ for the non-constant angular momentum models `NC1` with $a = 0.3$ (dashed curves) does not seem to reach a local maximum, at least during the timescales we can afford to simulate. This is despite these models are also affected by the PPI. This might be explained by the fact that the non-axisymmetric $m = 1$ mode does not drop as sharply after the saturation of the PPI in the models `NC1` as it does in the `C1B` models (see Fig. 6.15). The growth of the mode in the disc seems to cause an alignment of the BH spin with the z-axis. Furthermore, the nutation rate is much larger for the `C1B` models. Finally, in the absence of

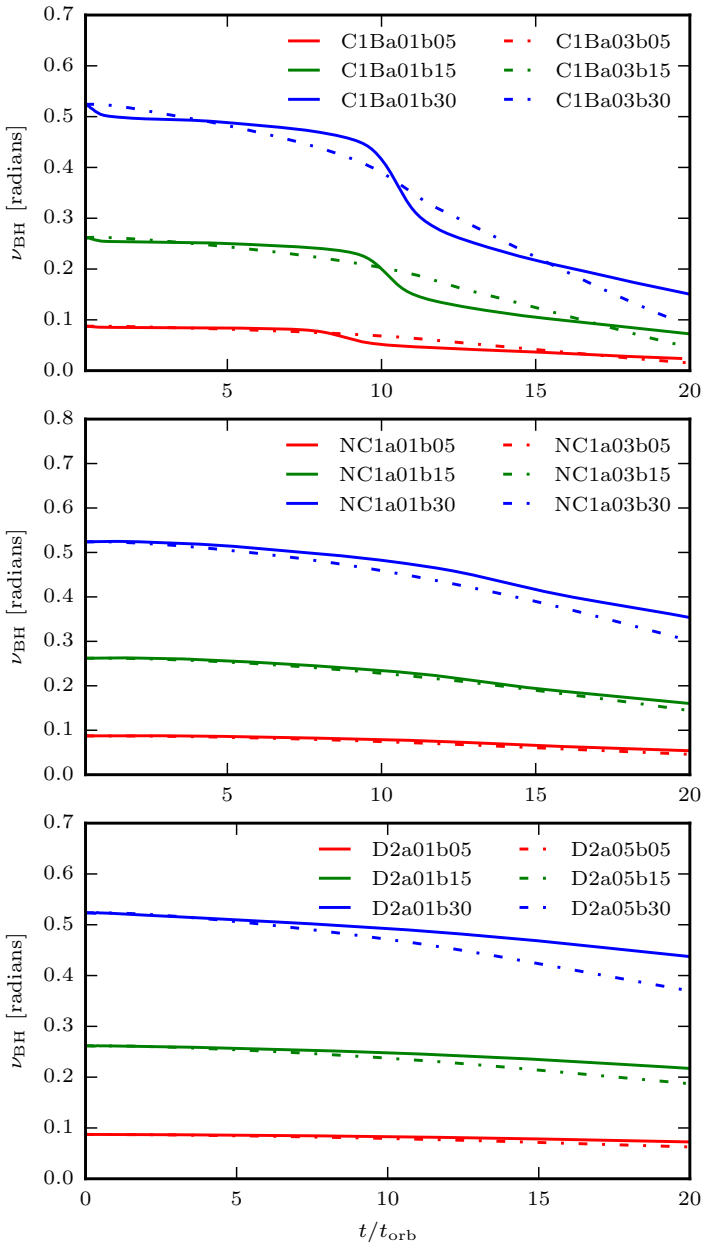

Figure 6.22 Evolution of the tilt angle of the BH spin with respect to the z-axis for models `C1B` (top), `NC1` (middle) and `D2` (bottom) in units of radians.

any strong growth of PPI modes, models `D2` do not show strong modulation of

the nutation rate, which is therefore closely connected to the existence of $m = 1$ non-axisymmetric modes in the disc.

The corresponding evolution of the inclination of the BH spin away from the z-axis is seen in Fig. 6.22. The panels show that a significant realignment of the BH spin with the z-axis takes place by the end of the simulations in models `C1B`, i.e. in those models that develop the PPI most significantly. For all models we see that the final inclination is smaller the bigger the initial tilt angle is, for equal spin magnitudes. This trend also seems to be more pronounced the higher the initial spin magnitude is.

6.2.7 Disc twist and tilt

We turn now to describe in this section the response of the discs as they evolve in the tilted spacetime, using the diagnostics we have introduced in Section 4.4. In Figures 6.23 and 6.24, we plot the evolution of the tilt and precession of the total angular momentum vector of the disc $J_{\rm Disc}$. This vector is the sum of the angular momentum vectors of each shell, as described in Section 4.4. We will refer to these as the global disc tilt and global disc precession around the BH spin, in order to distinguish them from the twist $\sigma(r)$ and tilt $\nu(r)$ angles in the individual disc shells.

The evolution of the global disc tilt, shown in Fig. 6.23, shows resemblances with the evolution of the tilt of the BH spin (see Fig. 6.22). For models `C1B` (top panel) we see that the development of the PPI not only causes a partial realignment of the BH spin with the z-axis, but also a realignment of the BH spin and disc angular momentum. This alignment seems to become constant towards the end of the simulation than the alignment of BH spin and the z-axis. We also note that the amount of realignment is reversed for the global disc tilt for models `C1B`. Here the higher initial spin magnitude leads to less alignment, in contrast with the evolution of the BH tilt. On the other hand, the alignment between BH spin and total disc angular momentum for models `NC1` (middle panel) is less pronounced as the realignment of the BH spin with the z-axis. As in the case of models `C1B`, the trend of more alignment with higher spin for the BH tilt is inverted for the evolution of the global disc tilt. There are also oscillations in the evolution of the global disc tilt for models `NC1`, which are not visible in the other two set of models. These oscillations seem to be caused by the persistent $m = 1$ non-axisymmetric mode in models `NC1`. Finally, for models `D2` (bottom panel), neither the initial spin magnitude nor the initial tilt angle seem to affect the evolution of the global disc tilt, which is furthermore hardly

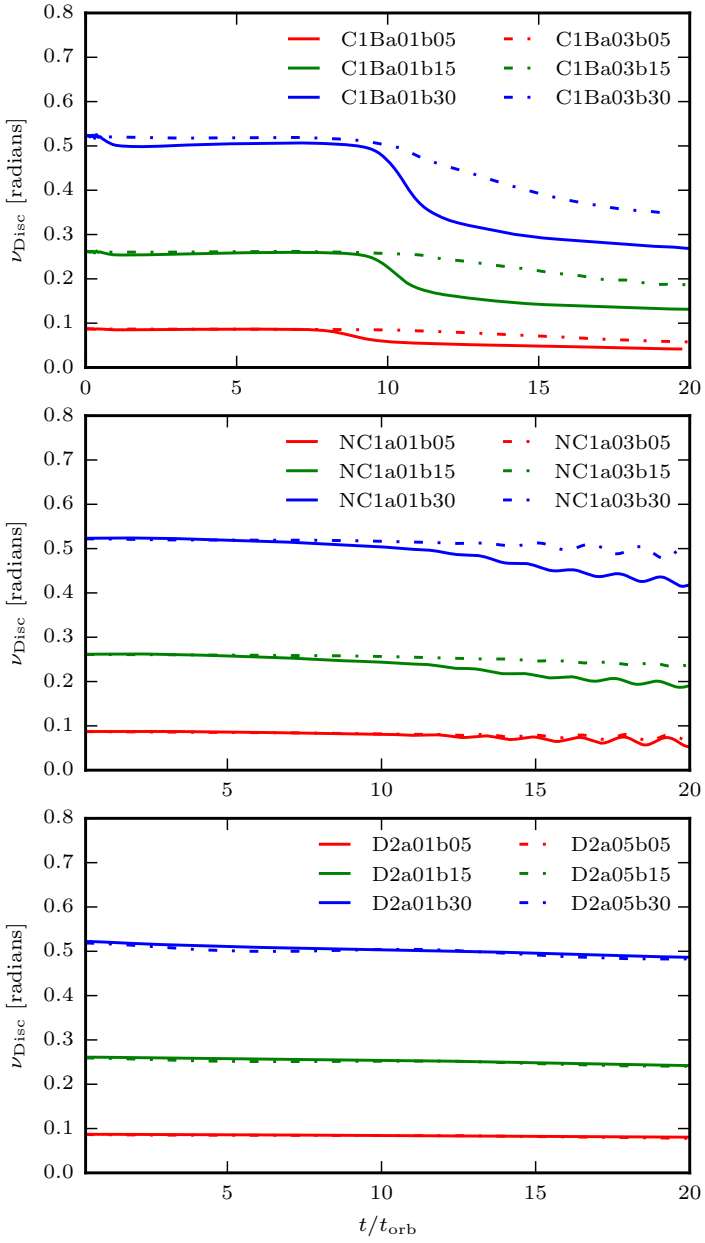

Figure 6.23 Evolution of the tilt angle $\nu_{\rm Disc}$ between then BH spin and the total disc angular momentum $J_{\rm Disc}$ for models `C1B` (top), `NC1` (middle) and `D2` (bottom) in units of radians.

changed during the entire evolution for all initial spins. The development of the PPI therefore seems to cause an alignment of the BH spin with the total disc

angular momentum, which is larger for smaller initial spins. We will analyse the role played by the PPI in the BH-disc alignment more carefully in Chapter 7. As both $\nu_{\rm BH}$ and $\nu_{\rm Disc}$ decrease during the growth of the PPI, it is clear that both the BH spin and disc angular momentum are modulated during the alignment period.

In Fig. 6.24 we plot the global precession of the total disc angular momentum vector about the BH spin axis for models `C1B` (top), `NC1` (middle) and `D2` (bottom panel). For all models, the higher the spin (dashed curves), the larger the global precession, as expected. The initial tilt angle does not seem to influence strongly the evolution for models `C1B` and `D2`, while the evolution for `NC1` shows oscillations towards the end of the evolution. Note that these oscillations are superimposed on the slow growth of the precession, which is always growing, as expected. The oscillations are caused by the wobbling and smaller precession cycles about the direction of the global vector. These oscillations are then visible in the projection of the disc angular momentum vector onto the equatorial plane of the BH. The amplitude of the oscillations is larger the smaller the initial tilt angle. The non-axisymmetric modes that survive much longer in the case of models `NC1` could be causing these oscillations in the global disc tilt and precession.

In Fig. 6.25 we show spacetime $(t - r)$ diagrams of the radial disc tilt profile for the entire time evolution for all tilted models in order to see whether and which disc models become warped during their evolution. The initial radial tilt profile is flat and the panels cover the initial radial extent of each model. For models `C1B` (top two rows) we see that by the end of the simulations the radial tilt for larger radii is significantly lowered compared to the initial tilt angle. Furthermore, there is a clear distinction in the radial tilt profile before and after the saturation of the PPI for the lower spin models ($a = 0.1$), in accordance with what we have observed for the global disc angular momentum tilt (see Fig. 6.23). For the higher spin models ($a = 0.3$) the tilt profile evolution is broken up into two regions as well. In these cases, the peak close to the origin reemerges after the saturation of the PPI. Likewise, models `NC1` (two middle rows) also show a peak close to the origin, but contrary to the previous set of models, the late time tilt profiles are oscillating in the regions closest to the BH. The oscillations are stronger for both, radii closer to the origin and smaller initial BH spin. As described before, we believe that these oscillations are a consequence of the long-lasting non-axisymmetric $m = 1$ mode in the disc.

The oscillations of the tilt angle close to the origin in models `NC1` will be investigated in detail in Chapter 7. To complete the analysis of Fig. 6.25, we note that models `D2` (two bottom rows) become clearly warped, with all models

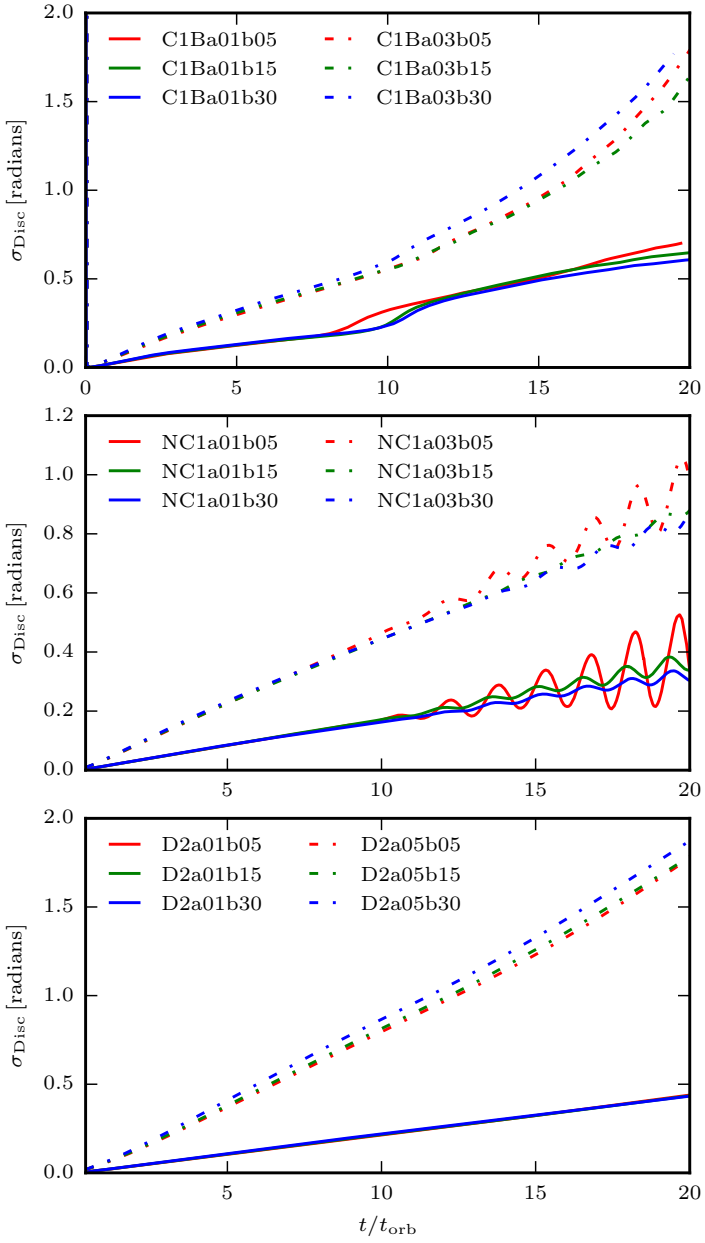

Figure 6.24 Evolution of the total precession of the total disc angular momentum $J_{\rm Disc}$ around the BH spin for models `C1B` (top), `NC1` (middle) and `D2` (bottom) in units of radians.

showing a peak near the origin. The profiles of the low spin models `D2a01` are very similar in shape for the three initial tilt angles. The peak in models

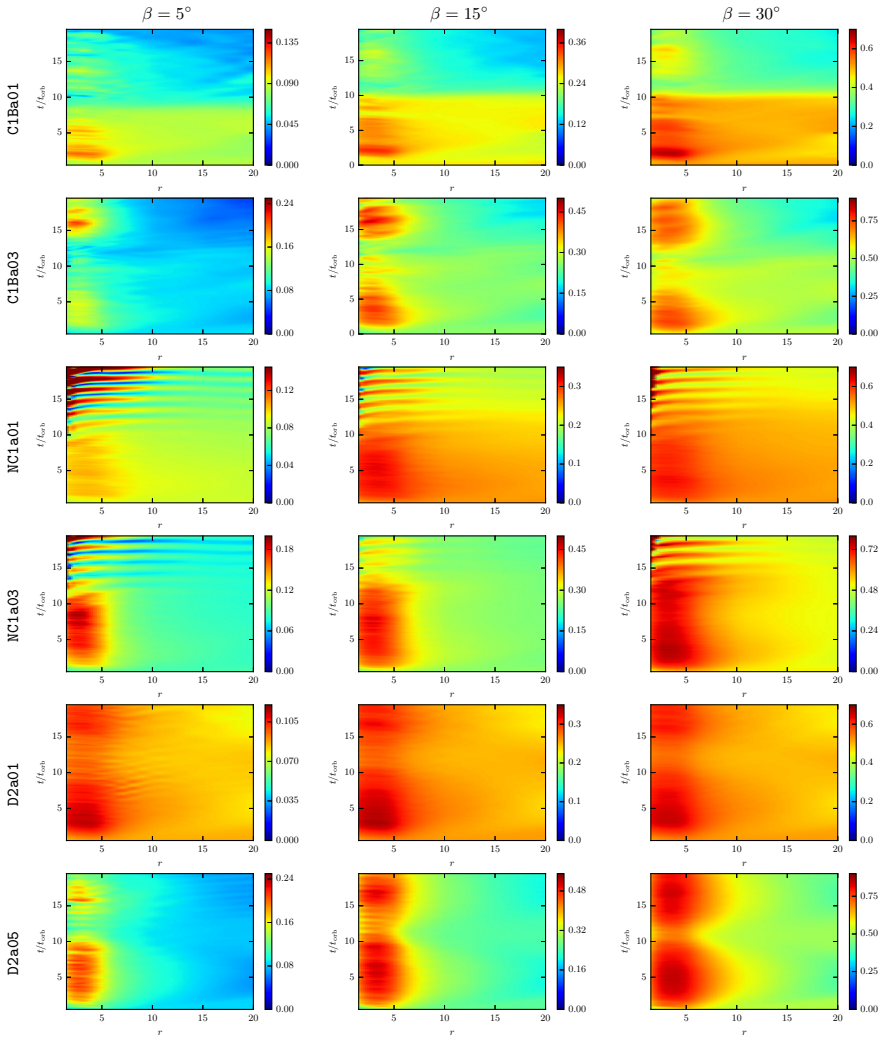

Figure 6.25 Spacetime $t - r$ diagrams of the radial disc tilt profile $\nu(r)$ for models `C1Ba01`, `C1Ba03` (top two panels), `NC1a01`, `NC1a03` (middle two panels), and `D2a01` and `D2a05` (bottom two panels). From left to right the panels show the initial tilt angles β_0 of 5°, 15° and 30°. Each panel shows the radial profile of the disc tilt for the entire time evolution.

`D2a05` is seen to oscillate stronger the smaller the initial tilt angle. Note that for none of the models we see an alignment of the inner region of the disc with the equatorial plane of the BH (this would mean $\nu(r) = 0$ there). We therefore find no occurrence of the Bardeen-Petterson effect in our simulations, at least in the timescales considered. This is in agreement with the results found in the fixed-spacetime inviscid simulations with no angular momentum transport

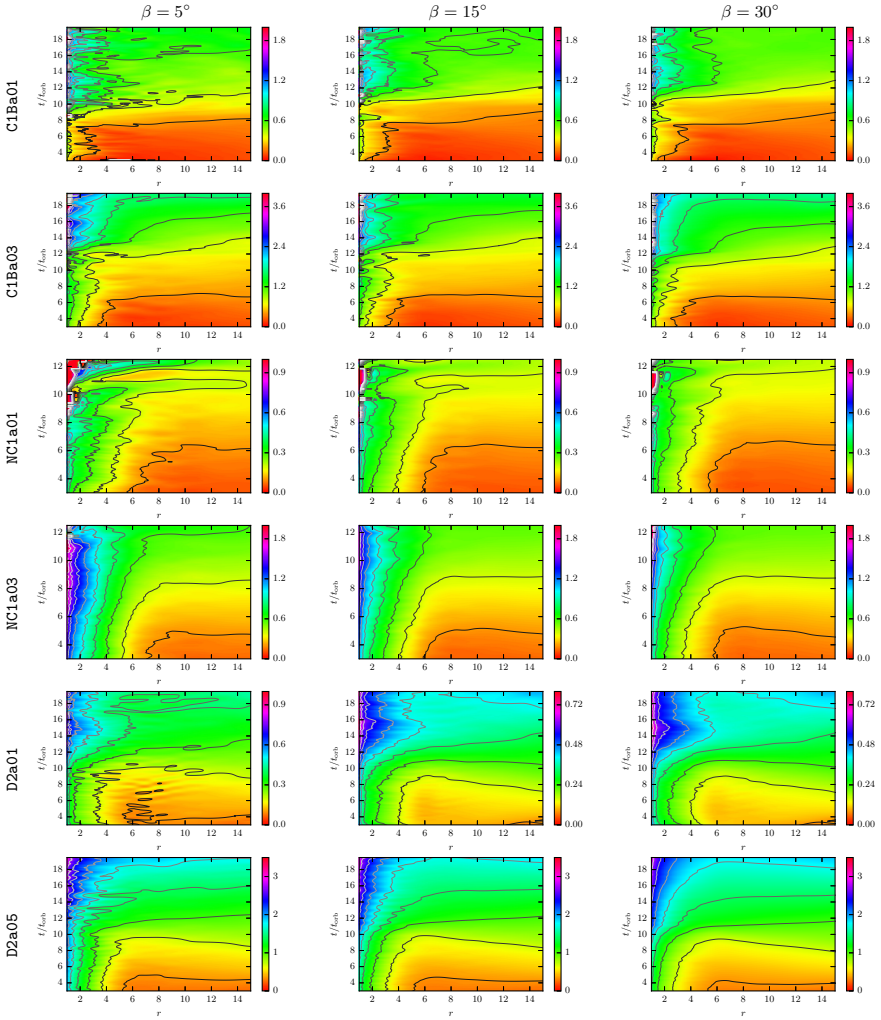

Figure 6.26 Spacetime $t - r$ diagrams of the radial disc twist profile $\sigma(r)$ for models `C1Ba01`, `C1Ba03` (top two panels), `NC1a01`, `NC1a03` (middle two panels), and `D2a01` and `D2a05` (bottom two panels). From left to right the panels show the initial tilt angles β_0 of 5°, 15° and 30°. Each panel shows the radial profile of the inner region disc twist from 3 orbits onwards.

of Fragile and Anninos [2005] and also with the GRMHD simulations of Fragile et al. [2007] that included angular momentum transport driven by the MRI. The observed profile and evolution of the disc warp seems to be in qualitative agreement with the analytic work on warp propagation as bending-waves in tilted thick accretion discs (see, for instance, the analytic tilt profiles in Ivanov and Illarionov [1997], Demianski and Ivanov [1997], and Lubow, Ogilvie, and Pringle [2002], the analytic model of linear warp evolution of Foucart and Lai [2014]

and the application of the linear warp evolution model in Franchini, Lodato, and Facchini [2016]). In these models, the tilt profile is non-zero near the BH with a hilltop profile. Our discs are in the bending-wave regime as they are thick and we do not take the fluid viscosity into account. We note that while the Bardeen-Petterson effect is not manifest in our models, we nevertheless do observe a *global* partial realignment of the BH spin with the disc angular momentum, caused by the growth of the PPI. This alignment of the disc angular momentum with the BH spin has also been observed in the post-merger evolution of a tilted accretion disc in Kawaguchi et al. [2015]. The authors conclude that the transport of angular momentum by non-axisymmetric shock waves in the disc might be responsible for such a Bardeen-Petterson-like effect. We will come back to this issue in Chapter 7 below. Finally, to check for Lense-Thirring precession, we plot the evolution of the inner region disc twist $\sigma(r)$ from $t = 3$ orbits onwards for all our tilted models in Fig. 6.26. We see that all models become twisted (as $\sigma(r)$ varies with r) in the regions for radii up to 5. The plots further indicate solid precession of the discs, as the radial profile of $\sigma(r)$ is increasing smoothly in time almost independently of the radius in the outer regions of the disc and does not remain 0 for large radii. This is consistent with the solid-body precession found in the fixed spacetime simulations of Fragile and Anninos [2005]. Models `D2` actually show a slightly growing twist for larger radii. In this trend, the higher initial spin models show flatter profiles, while there is some radial modulation of the profiles for the lower spin simulations. A striking feature of the plots is the smaller difference in accumulated twist for large radii between different initial spin magnitude for models `NC1`. In models `C1B` and `D2` the higher spin models show a much higher twist at large radii than their low spin counterparts (see also Fig. 6.24, where this is seen in the evolution of global twist of the disc angular momentum vector as well). As the long survival of the $m = 1$ mode in the `NC1` models seems to have an effect on the evolution of the twist, we plot this evolution only up to the saturation of the PPI for these models in order to properly visualise the solid body precession of the disc.

6.2.8 Angular momentum transport

In this section we investigate the transport of angular momentum in the discs. To illustrate the transport of angular momentum during the evolution of our models, we plot spacetime $t - r$ diagrams showing the magnitude of the angular momentum in radial shells, computed using Eq. (4.33). Such diagrams are displayed in Fig. 6.27. The magnitude of the angular momentum in each shell,

$\|J(r)\|$, has been rescaled to the global maximum value attained in any shell during the evolution. Fig. 6.27 shows the evolution of $\|J(r)\|$ for the three untilted models `C1Ba0b0` (top panel), `NC1a0b0` (middle panel) and `D2a01b0` (bottom panel). This figure reveals that compared to the latter two models, model `C1Ba0b0` shows a radical redistribution of angular momentum in the radial direction. This drastic difference is due to the development of the PPI in model `C1Ba0b0`. Following the initial perturbation we see that the contours of $\|J(r)\|$ start growing in a wave-like manner, transporting angular momentum outwards. This happens up until the saturation of the PPI at about 10 orbital periods. As noted by Balbus [2003] during the growth phase the PPI is thought to be an effective mechanism for angular momentum transport in thick accretion discs, where a right combination of rotation and pressure at the boundaries of the disc allows the growing non-axisymmetric modes to transport angular momentum outwards. Zurek and Benz [1986] showed as well that the development of non-axisymmetric instabilities is closely connected to the transport of angular momentum. After saturation, the new distribution of angular momentum seems PP-stable and does not exhibit drastic changes for the rest of the evolution.

We can compare the evolution of $\|J(r)\|$ to the development of the $m = 1$ non-axisymmetric mode in the disc, which drops to a value of around 1% of its maximum value after saturation (see top panel of Fig. 6.15). As described in Balbus [2003], the development of the PPI crucially relies on the properties of both the inner and outer boundaries of the disc. Blaes [1987] showed that a small amount of accretion (which modifies the inner boundary of the disc) was sufficient to saturate the growing PPI. Furthermore, wider tori are known to be less violently unstable than slender tori [Hawley 1991]. In subsections 6.2.3 and 6.2.4 we already showed that the accretion rate and the growth of the $m = 1$ non-axisymmetric mode saturate at the same time, but the $t - r$ diagram of Fig. 6.27 also shows that the angular momentum isocontours in the outer regions of the disc are being pushed outwards with growing amplitude as well. It therefore seems that both mechanisms are saturating the PPI simultaneously in model `C1Ba00`.

Model `NC1a0b0`, displayed in the middle panel of Fig. 6.27, has a non-constant specific angular momentum distribution, and shows a very different evolution of $\|J(r)\|$. The inner region of the disc shows a gentle reduction of angular momentum during the entire evolution and no sudden and drastic redistribution is found as the one that occurred in model `C1Ba0b0`. The outer contour grows to encompass the entire outer domain shown in the plot. Another difference is the almost complete absence of variability of the inner region of the disc,

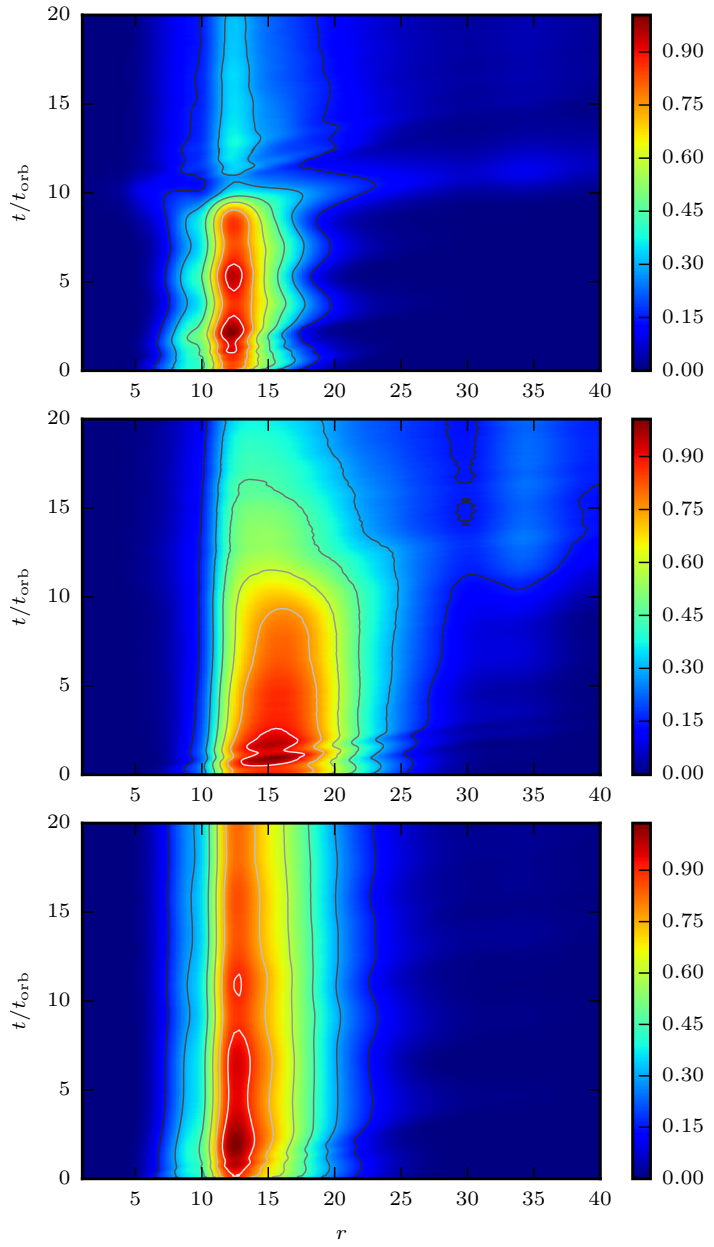

Figure 6.27 Spacetime $t - r$ diagram showing the time evolution of the radial profile of the angular momentum magnitude $\|J(r)\|$ for untilted models `C1Ba0b0` (top panel), `NC1a0b0` (middle panel) and `D2a01b0` (bottom panel).

which is in contrast to model C1Ba0b0, where oscillatory behaviour is seen in the inner boundary of the disc too. The specific angular momentum profile of model NC1a0b0 is between constant and Keplerian, with Keplerian discs being essentially PP-stable. Model NC1a0b0 still develops the PPI, albeit in a milder manner than model C1Ba0b0, with the torus of model NC1a0b0 being initially wider. Finally, model D2a01b0 (bottom panel), the lightest of our models, is PP-stable as already shown in subsection 6.2.4. The corresponding spacetime diagram of $\|J(r)\|$ shows no pronounced outward transport of angular momentum as the evolution proceeds, the profile remaining very similar to its initial configuration. The inner region with a high angular momentum magnitude is thinned out slightly, and the profile spreads a bit overall, but the changes are nowhere nearly as pronounced as for models C1Ba0b0 and NC1a0b0. As we have seen in the analysis of the modes, the amplitude of the $m = 1$ mode drops sharply upon the saturation of the PPI in the C1Ba00 model. The subsequent evolution of the angular momentum profile remains constant, similar to what we observe for the entire evolution of the PP-stable model D2a01b0. There is a clear split between the stages of the evolution: the first during which the PPI develops and saturates, and the subsequent evolution of an essentially PP-stable torus. Model NC1a00, on the other hand, shows a very different behaviour: as already seen in the mode analysis, the $m = 1$ mode amplitude remains roughly at its saturation value for the rest of the evolution, which is lower than the values attained by models C1B. The persistent $m = 1$ mode is seen to continuously transport angular momentum outwards till the end of the simulation. The restructuring of the disc by the transport of angular momentum is more long-lived, compared to the drastic change the saturation of the PPI brings about in model C1Ba00. These findings seem to confirm those found in Zurek and Benz [1986]. Using the same kind of spacetime diagrams we have also checked the dependence of the angular momentum transport on the BH spin a and on the initial tilt angle β_0 for all models of our sample. We find that the angular momentum transport shows weak dependence with the tilt angle (the higher the tilt angle the slowest the transport) and shows essentially no dependence with the spin, at least for the moderate values of the BH spin we could afford in our study. This is a remarkable result, as it demonstrates that models C1B and NC1 are PP-unstable for a wide range of initial BH spin magnitudes and tilt angles.

We note that our GRHD simulations are underestimating the real angular momentum transport likely to occur in astrophysical accretion discs due to our lack of accounting for viscosity (for instance via the MRI). The sources of viscosity in our discs are due to the developing non-axisymmetric modes and

numerical viscosity. The latter seems to play only a minor role, as can be seen from the accretion rates reported for models `C1Ba00`, `NC1a00` and `D1a01b00`, which is about an order of magnitude lower for the PP-stable model `D1a01b00` than for the other two. The timescale at which the viscosity provided by the MRI operates is difficult to estimate. In Foucart et al. [2014], the authors estimate a viscous timescale of ~ 0.1 s in their BHNS post-merger torus. This would correspond to about $130\, t_{\rm orb}$ for disc model `C1B`. We should take the evolution of magnetic fields into account for longer simulations in our discs (to complete a full BH spin precession cycle, for instance).

6.2.9 Gravitational waves

In this section, we explicitly report frequencies and times in SI units. Note that the results presented here have been obtained using the BH masses listed in Table 6.1. None of the results have been rescaled for different BH masses.

The recent numerical simulations of Kiuchi et al. [2011] have shown that the growth and saturation of the PPI makes BH–torus systems emitters of large amplitude, quasi-periodic GW, potentially detectable by forthcoming ground-based and spacecraft detectors. It was found in particular that the $m = 1$ non-axisymmetric structure survives with an appreciable amplitude after saturation of the PPI, which leads to the emission of quasi-periodic GWs with a large amplitude[3]. In this section we turn our attention to analyse the implications of the PPI in our tilted BH–torus systems regarding the emission of GWs, namely the dependence of the resulting gravitational waveforms and spectra on the BH spin magnitude and initial tilt angle.

In Fig. 6.28 we plot the real part of the $(l, m) = (2, 2)$ mode of the outgoing part of the complex Weyl scalar Ψ_4 for models `C1Ba01` and `NC1a01` and for all initial tilt angles β_0. This quantity has been computed at an extraction radius $r = 640$ (945 km). Fig. 6.28 shows that, in agreement with Kiuchi et al. [2011], all models display strong emission of gravitational waves and that the emission persists for many dynamical timescales well after the saturation of the PPI. The peak amplitude for models `C1Ba01` is about an order of magnitude higher than for models `NC1a01`.

We recall that model `C1B` has a slightly higher initial disc-to-BH mass ratio than model `NC1` ($q = 0.16$ and 0.11, respectively) and that the development of the

[3]First estimates through full GRHD simulations of the GW detectability by the PPI instability in self-gravitating BH–torus systems were obtained in Korobkin et al. [2011] where the nonlinear saturation phase was almost reached. See also van Putten [2001] for earlier proposals and alternative estimates of the gravitational waves emitted by non-axisymmetric instabilities in such systems.

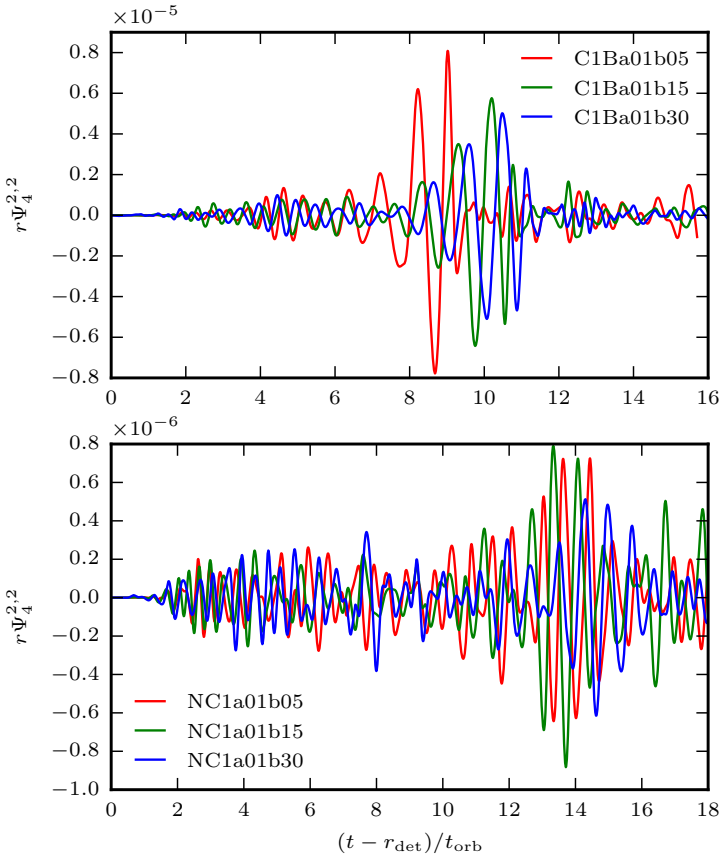

Figure 6.28 Time evolution of the $l = m = 2$ mode of the real part of the Weyl scalar Ψ_4 multiplied by the extraction radius ($r = 640$). The top panel shows models `C1Ba01` and the bottom panel models `NC1a01`.

PPI in models `C1B` is more pronounced than in the non-constant specific angular momentum models `NC1` (see Fig. 6.10). These two features are responsible for the difference in the peak amplitudes between the two initial models. We also note that the peak amplitude in the `C1Ba01` models, reached at PPI saturation, is much higher than the amplitude of the remaining signal, whereas in models `NC1a01` the variations are not so pronounced. As we showed in Fig. 6.15, upon PPI saturation the dominant $m = 1$ PPI mode drops to about 1% of its peak value in models `C1B`, while it remains at a similar strength for models `NC1`.

Fig. 6.28 also shows that the GW signal depends weakly on the initial tilt angle, particularly for the non-constant specific angular momentum models `NC1`. The smallest peak amplitudes are attained for the most tilted BH spacetime

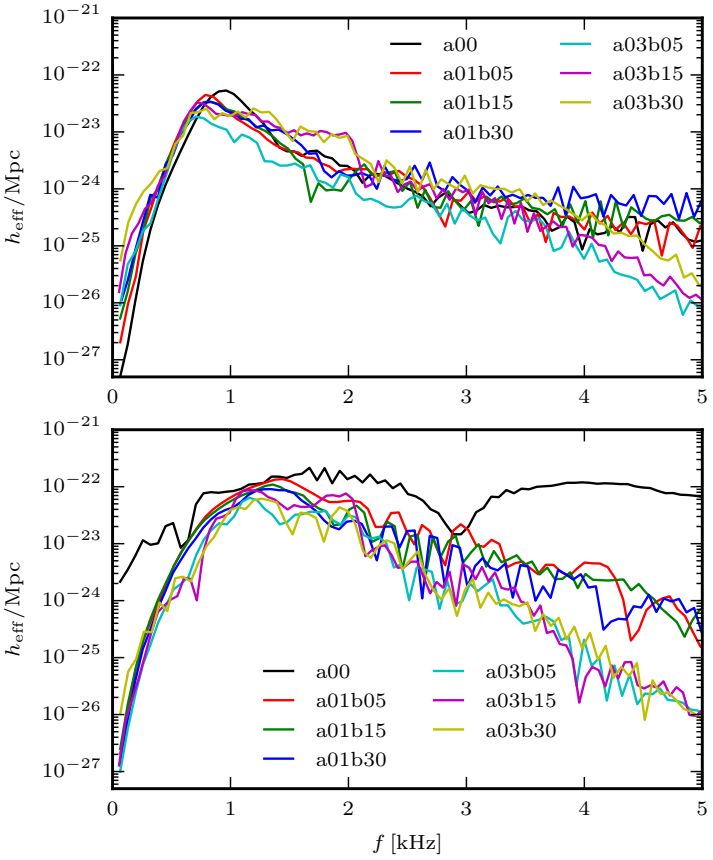

Figure 6.29 Spectrum of the effective strain for models `C1B`, showing the $l = 2, m = 1$ modes (top) and $l = m = 2$ modes (bottom) for the source located at 1 Mpc.

($\beta_0 = 30°$). In any event, the differences found in the values spanned by the peak amplitudes with regard to β_0 are not too significant.

We use the fixed frequency integration (FFI) described in Reisswig and Pollney [2011] in the integration of the Ψ_4 data to obtain the GW strain. In Figs. 6.29-6.31 we plot the effective strain $h_{\rm eff}$/Mpc as a function of frequency for all models, placing the sources at 1 Mpc, in order to see any possible imprint of the initial spin magnitude and tilt angle on the GW spectrum. As described above, we use the same timestep for the time integration of the spacetime and GRHD evolution equations in the 7 outermost refinement levels (which means that in those outer refinement levels $\Delta t = 1.58 \times 10^{-6}$ s and 3.16×10^{-6} s for higher and lower resolution runs, respectively). At our extraction radius, the timestep in the respective mesh refinement level is therefore sufficiently small to

sample the GW multipole signal with a δt of 6.32×10^{-6} s (1.26×10^{-5} s) for the higher (lower) resolution runs, respectively, where δt is the output timestep of the GW data from the simulation. Due to the Nyquist criterion, we can therefore resolve the GW spectra up to ≈ 80 (40) kHz[4]. The top panels of Figs. 6.29 and 6.30 correspond to the $(l, m) = (2, 1)$ mode and the bottom panels to the $(l, m) = (2, 2)$ mode. The highest power is usually found at a frequency of about 1kHz. For the effective strain of the $(l, m) = (2, 1)$ mode for models `C1B` shown in the top panel of Fig. 6.29, we can clearly identify two trends. On the one hand there is a difference at high frequencies between the models with either no or low ($a = 0.1$) initial BH spin (models `C1Ba00` and `C1Ba01`) and the high spin models ($a = 0.3$). The spectra for these two groups show a different slope from $f \sim 2$kHz onwards. On the other hand, for models `C1Ba00` and `C1Ba01`, an increase in the initial tilt angle leads to an increase in the power for frequencies $f > 2$kHz. This also seems to be present at lower frequencies although it is somewhat less clear. Correspondingly, the power spectra of the $(l, m) = (2, 2)$ mode shown in the bottom panel of Fig. 6.29 neatly splits the models into three groups, according to the initial spin magnitude of the BH. We find that the slope of the spectra becomes steeper from $f \sim 2$kHz onwards the higher the BH spin. In all cases, the slope of the effective strain with the frequency shows essentially no dependence with the initial tilt angle for the various groups of models characterised by the same BH spin. The power in model `C1Ba00` is at least an order of magnitude larger for all frequencies than that of the tilted models. This is because the spiralling motion in the equatorial plane of both the BH and the $m = 1$ over-density PPI "planet" emits GWs predominantly in the $l = m = 2$ mode which is emitted in the direction perpendicular to the equatorial plane. This is an optimal situation for the model with aligned BH and disc spins, as the coordinate system in which we perform the multipole expansion of the GW is aligned with the z-axis. However for the tilted models the "orbit" of the BH and of the over-density lump in the disc is not confined to

[4]We note that this analysis serves to establish that we would be able to resolve the GW spectra up to ≈ 80 (40) kHz using the timestep at the extraction radius. Physically, there is no reason to expect such high frequencies in the spectra of the GW signals of our BH–torus systems. To analyse the maximum expected frequencies, we assume the maximum fluid orbital frequency in our systems to be the orbital frequency at the ISCO, $\nu_{\rm ISCO}$, which, for the BH masses indicated in Table 6.1, is between $\nu_{\rm ISCO} \sim 2.2$ kHz for a non-spinning BH and $\nu_{\rm ISCO} \sim 16$ kHz for a maximally spinning Kerr BH [Remillard and McClintock 2006]. For our initial models with a maximum initial Kerr parameter of $a = 0.5$, we therefore expect the maximum orbital frequency to be ~ 4 kHz. The emitted GW will have a frequency twice as large, so we would thus expect to obtain GW frequencies of up to 8 kHz. In order to concentrate on the lower-frequency properties of the spectrum (namely the radiation at the orbital frequency at the initial pressure maximum and the frequency of the PPI pattern speed), we plot the GW spectra for frequencies up to 5 kHz.

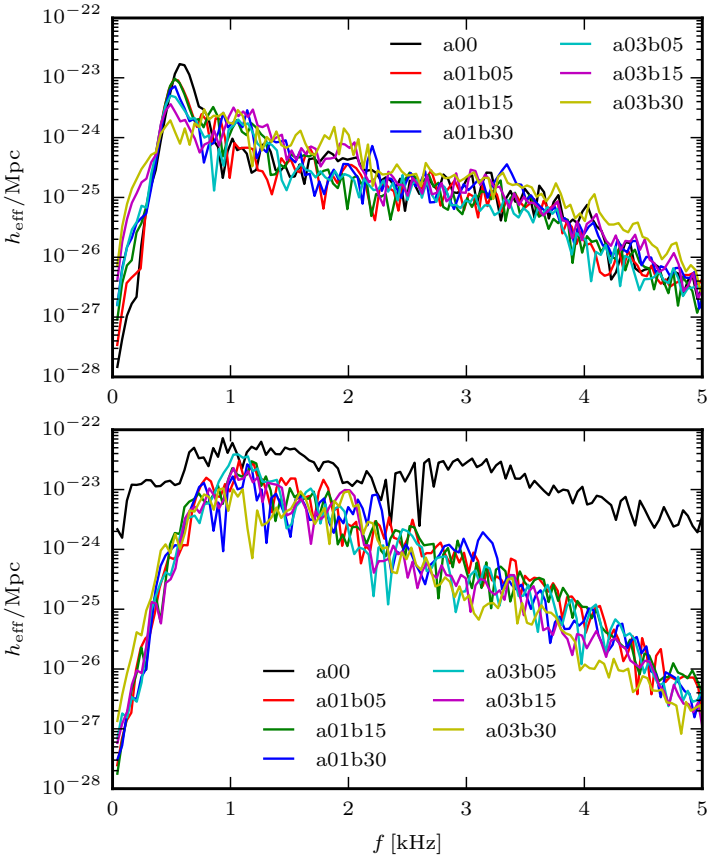

Figure 6.30 Spectrum of the effective strain for models `NC1`, showing the $l = 2, m = 1$ modes (top) and $l = m = 2$ modes (bottom) for the source located at 1 Mpc.

the equatorial plane anymore because of the reaction of the disc to the tilted BH spin. This results in a decrease in the GW power. In order to have a fair comparison of the GW power emitted in the untilted and tilted systems, one would need to extract the waves in a (time-changing) coordinate system adapted with its z-axis aligned with the total angular momentum of the system.

The spectra of the non-constant specific angular momentum models `NC1` displayed in Fig. 6.30 are markedly different to those of constant specific angular momentum tori. Namely, their dependence on the frequency is similar for all modes (same slope) irrespective of the initial tilt angle and of the BH spin. No split in two or three families is found according to the BH spin. The effective strain of the $(l, m) = (2, 1)$ mode for models `NC1` shows a plateau in the low frequency part (up to ~ 0.5kHz) for models `NC1a03b15` and `NC1a03b30`. The

spectra show a prominent peak around 0.6kHz for all models but these two. The height of the peak drops with growing initial spin and initial inclination angle, which might as well be an artefact due the multipole expansion in the untilted coordinate system. For the $l = m = 2$ mode we find that the curve for the untilted model `NC1a00` lies more than an order of magnitude above the curves corresponding to the initially tilted discs, as seen also for the `C1Ba00` model in the previous figure.

Finally, in Fig. 6.31 we show the effective strains of the $(l, m) = (2, 1)$ mode (top panel), (2,2) mode (middle panel) and (3,1) mode (bottom panel) for models `D2`. In the spectra of the $(l, m) = (2, 1)$ mode there is a clear variation with the initial tilt and BH spin magnitude, with both increasing the power of the mode for all frequencies shown. The fact that the power increases with growing tilt angle seems to indicate that this behaviour is really a physical consequence of the tilted disc evolution. Contrary to model `C1B` and similar to model `NC1`, we find now that model `D2` does not show the grouping of models depending on the BH spin, and the associated frequency dependence (i.e. steeper slopes for higher spins). As this model is PP-stable and has an initially constant distribution of specific angular momentum, its dynamics is somewhat between that of the other two models. The spectra of the $l = m = 2$ mode (middle panel) show in particular a very different behaviour to those shown for models `C1B` and `NC1`, namely that the model with zero initial inclination does not show significantly larger power than the models with $a = 0.1$ and $a = 0.5$. Since models `D2` do not develop the PPI, there is no strong emission of GW in the $l = m = 2$ mode due to the absence of the spiral motion of both BH and over-density 'planet' that is present for the other two initial models.

Therefore, the power spectrum of the untilted model `D2a01b0` does not exceed that of the rest of the other tilted `D2` models. The two models `D2a05b15` and `D2a05b30` both show two peaks in the low frequency part of the spectrum.

The absence of the PPI in the `D2` models results in a GW emission where the $l = m = 2$ mode is not the dominant mode. To show this, we plot the effective strain of the $(l, m) = (3, 1)$ mode in the bottom panel of Fig. 6.31. The power is comparable with that of the $(l, m) = (2, 1)$ and $l = m = 2$ modes, which is not the case for models `C1B` and `NC1` that both develop the PPI. The plot of the effective strain of the $(l, m) = (3, 1)$ mode shows that same trend as that of the $(l, m) = (2, 1)$ mode, i.e. the power density increases with spin magnitude and initial tilt angle. Furthermore, we can see clear quasi-periodic oscillations in the low frequency part of the spectrum for models `D2a05`. These oscillations might be the result of two non-axisymmetric modes being present in disc models `D2`, as

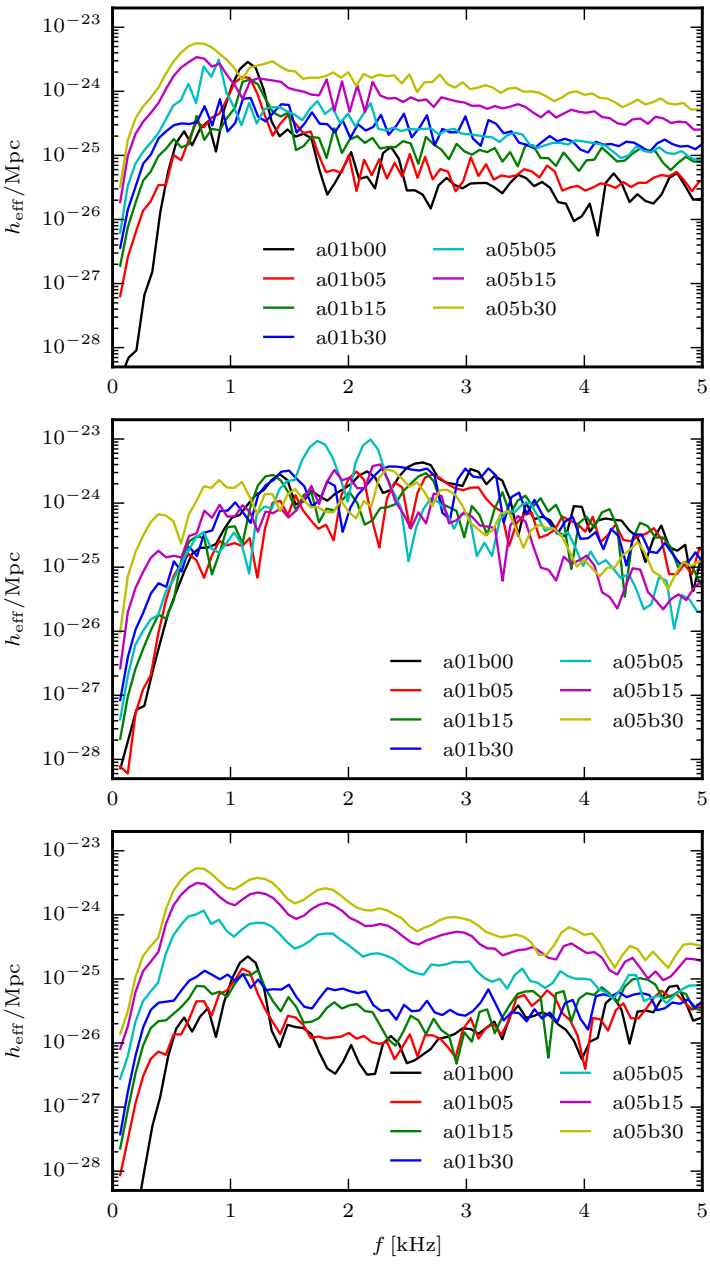

Figure 6.31 Spectrum of the effective strain for models D2, showing the $l = 2, m = 1$ modes (top panel) and $l = m = 2$ modes (middle panel) and $l = 3, m = 1$ modes (bottom panel) for the source located at 1 Mpc.

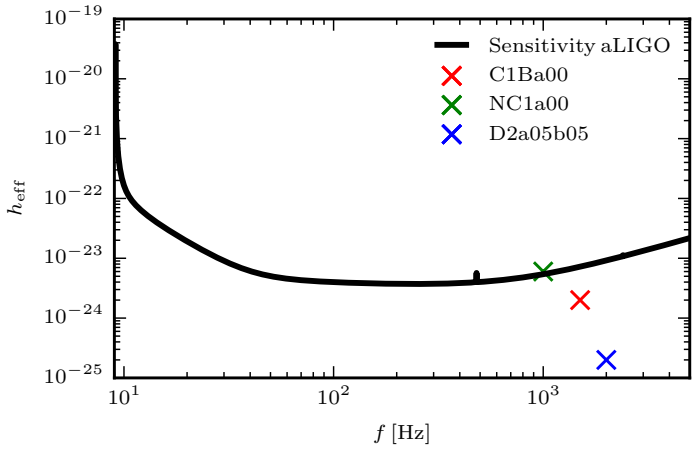

Figure 6.32 Plot showing the peak amplitudes of the effective strain, inferred from the accretion timescale, for the three different initial models. The sensitivity curve for advanced LIGO with zero-detuning and high-power configuration is shown in black. The small bump at ~ 500 Hz in the sensitivity curve is the fundamental vibrational mode of the test mass suspension fibres [LIGO Scientific Collaboration et al. 2015].

the $m = 1$ and $m = 2$ mode are of roughly equal strength (see Fig. 6.14). The spectra of all models shown are not very smooth and show small peaks. To check if these are due to numerical effects or actual imprints of the fluid evolution would probably require much higher resolution simulations than those presented in this work.

In order to estimate the detectability of the GWs emitted by these systems, we follow the analysis in Kiuchi et al. [2011]. We assume that the BH–torus system of models `NC1` will radiate GWs for the entire accretion timescale $t_{\rm acc}$ (which is the time needed for the entire disc to accrete). This is because in these models, the $m = 1$ over-density lump and the BH form a long-lasting quasi-binary system. Assuming that the accretion rate will remain at the level it attained by the end of the simulations (see Fig. 6.13), a lower limit for the accretion timescale for models `NC1` is $t_{\rm acc} \approx 0.1$ s. Note that this is only about four times longer than the duration of the simulations reported here. It also coincides with the viscous timescale reported in Foucart et al. [2014], which means that additional physics such as the MRI are likely to shorten this timescale in real accretion discs.

From the timescale, we can estimate the number of GW oscillations at the peak frequency, which yields ≈ 100 cycles[5] as a lower limit for models `NC1`.

[5]The peak frequency for models `NC1` is around 1 kHz, which means that the source should emit ~ 100 wave cycles at the peak frequency during the accretion timescale.

The peak amplitude of the GW strain will then be amplified by $\sqrt{N_{\rm cycles}} \approx 10$, while we assume no such amplification neither for models `C1B` (where the PPI is rapidly damped after saturation) nor for models `D2` (which are PP-stable). We note that these estimates are in very good agreement with the corresponding findings reported in Kiuchi et al. [2011]. The corresponding peak amplitudes for the BH–torus systems located at a distance of 50 Mpc, together with the advanced LIGO (aLIGO) sensitivity curve, are plotted in Fig. 6.32, showing that the GWs emitted by models `NC1` could be detectable due to the long-lasting emission of GWs due to the persistent $m = 1$ mode. We also note that the planned factor-of-3 upgrade of aLIGO [Hild 2012, Adhikari 2014, Miller et al. 2015] will further improve the detectability in the future.

To put the occurrence of BH–torus systems resulting from BHNS mergers into perspective, we note that the current, realistic merger rate of BHNS up to a distance of 50 Mpc is about $3.75 \times 10^{-3}\,{\rm yr}^{-1}$ (see Abadie et al. [2010] and references therein). The actual number of BHNS mergers that result in BH–torus systems is likely to be lower than this, as not all BHs in these mergers will have sufficiently low masses and/or sufficiently high spins to tidally disrupt the NS during inspiral, therefore leaving no torus behind.

Chapter 7

Analysing the tilted BH–torus dynamics with fluid tracers

The results of this chapter have been originally published in:
V. Mewes, F. Galeazzi, J. A. Font, P. J. Montero and N. Stergioulas
Accepted for publication in MNRAS

In this chapter, we investigate the dynamics of one titled BH–torus model of Chapter 6 (`NC1a03b05`) in more detail using fluid tracer particles as an additional means to analyse the disc evolution.

7.1 Initial data and setup

Model `NC1a03b05` has a non-constant l-profile and was shown to exhibit the development of a long-lasting non-axisymmetric $m = 1$ mode in Chapter 6. The parameters of this model are given in Tables 6.1 and 6.2. In the simulations presented in this chapter, we evolve the model for up to 32 orbital periods (significantly longer than we did in the simulations reported in Chapter 6) in two different ways to gauge the influence of the self-gravity of the fluid in the evolution of this model. The first evolution takes into account the solution of the coupled system of Einstein equations and GRHD equations, and thus corresponds to a fully dynamical spacetime evolution. For the second evolution we assume the test-fluid (Cowling) approximation in which the spacetime is

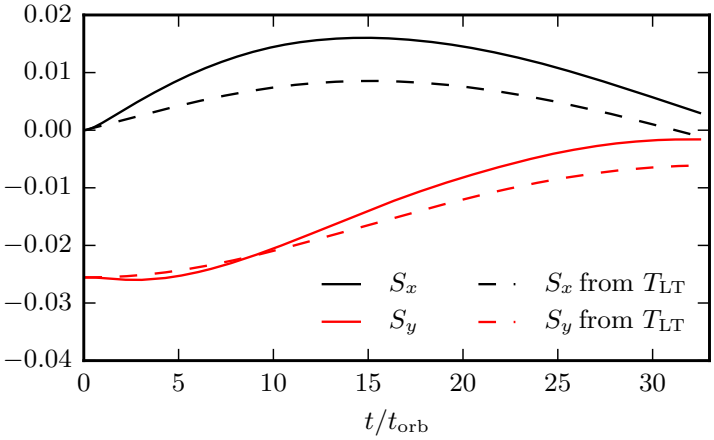

Figure 7.1 Evolution of the x and y components of the BH spin $\boldsymbol{S}$ and the evolution of the spin components resulting from the LT torque exerted by the disc.

fixed and only the GRHD equations are solved. As initial data for this second simulation we use the data of the fully evolved spacetime run that has been checkpointed at $t = 1.5t_{\rm orb}$. This is to ensure that we are evolving the same system once the gauge perturbations have left the region where the torus resides, and in particular to provide the same perturbation that triggers the growth of the non-axisymmetric instability in both runs.

Initially we place 250000 tracers at random locations in the accretion disc, where the probability distribution is weighted according to the underlying rest-mass density distribution. This results in all tracer particles being of equal mass (3.97×10^{-7}) initially and during the evolution. The bulk motion of the tracers is able to capture accurately the motion of the underlying fluid flow especially when it is not turbulent and strong shocks are not present.

7.2 BH precession from Lense-Thirring torque

The main driver of the tilted disc evolution is the LT precession. At the lowest post-Newtonian order of spin-orbit interactions, a particle in an inclined orbit around a central Kerr BH will be subject to the following torque [Kidder 1995, Merritt and Vasiliev 2012]:

$$\boldsymbol{T}_{\rm LT} = 2\frac{\boldsymbol{S} \times \boldsymbol{J}}{r^3}, \tag{7.1}$$

where $\boldsymbol{S}$ is the BH spin, $\boldsymbol{J}$ is the angular momentum vector of the particle, and r is the distance of the particle from the BH centre. This is the LT torque exerted

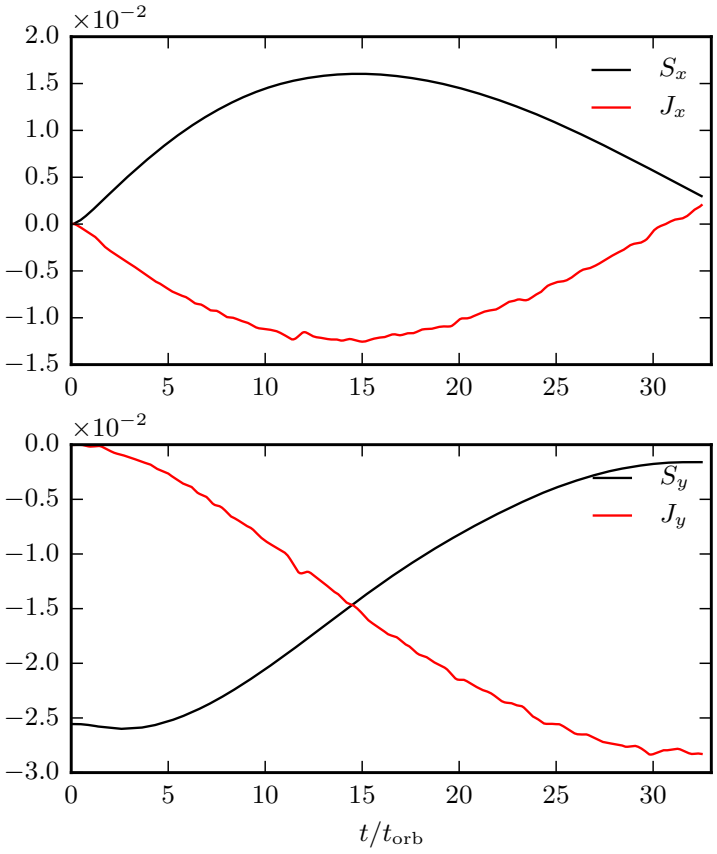

Figure 7.2 Evolution of the x and y components of the BH spin $\boldsymbol{S}$ and total disc angular momentum $\boldsymbol{J}_{\rm disc}$.

by the central BH on the particle. As a result of this torque, the orbital angular momentum of the particle will start to precess around the BH spin. As there is a strong radial dependence on the magnitude of the torque, the inner regions of a tilted accretion disc will become twisted, i.e. they will differentially precess around the central BH. However, as shown in the results of Fragile and Anninos [2005] and in Chapter 6, the sound crossing time in the disc is shorter than the LT timescale, which results in a global disc response to the LT torque produced by the Kerr BH, leading to solid body precession of the disc. By Newton's third law, the disc exerts a torque of equal magnitude and opposite direction on the BH, causing it to precess as well.

To check whether the precession of the BH we observe in our simulations has a physical origin, we compare the time evolution of the x and y components of

the BH spin, S_x, S_y, with the evolution of the BH spin that would have resulted from summing up the cumulative spin change resulting from the LT torque of the disc at each timestep:

$$\boldsymbol{S}_{\rm LT}(t) = \boldsymbol{S}(0) + \int_0^t \boldsymbol{T}_{\rm LT} dt. \tag{7.2}$$

As the disc is approximately precessing as a solid body, we calculate the torque coming from the disc total angular momentum vector, $\boldsymbol{J}_{\rm disc}$, and choose the radius in Eq. (7.1) to be that of the location of the initial density maximum, $r = 10.2$. The results are shown in Figure 7.1. This figure shows that the time evolution of the BH spin components agree well with the torque exerted on the BH by the disc. In Fig. 7.2 we show the time evolution of the x and y components of $\boldsymbol{S}$ and $\boldsymbol{J}_{\rm disc}$. Clearly, the sum of the spin components and disc angular momentum components along the two directions is seen to be approximately constant for the evolution, in agreement with the fact that the LT torque is the main driver for both disc and BH precession.

7.3 $m = 1$ non-axisymmetric instability

7.3.1 Spiral density wave

Two of the three models we studied in Chapter 6 were found to develop a global non-axisymmetric instability with $m = 1$ being the dominant azimuthal mode. One such instability is the instability of tori with constant specific angular momentum profiles, the Papaloizou-Pringle instability [Papaloizou and Pringle 1984]. Early numerical investigations of Hawley [1987] showed that the non-linear regime of the PPI resulted in the formation of counterrotating over-density lumps. The precise mechanism of the instability was elucidated in Goodman, Narayan, and Goldreich [1987], where the authors showed that the planets found in Hawley [1987] might be a new equilibrium configuration of the fluid. The instability was subsequently investigated numerically by Hawley [1991] as well as in the recent, fully general relativistic simulations of Kiuchi et al. [2011], Korobkin et al. [2011], and Mewes et al. [2016].

In this section we show that the growth of the $m = 1$ mode in the disc results in the formation of a spiral density wave with a constant global pattern speed Ω_P. As the disc is differentially rotating this means that there is a location in the disc, the so-called corotation radius $r_{\rm co}$, where the spiral density wave has the same orbital velocity as the fluid in the disc. Inside $r_{\rm co}$ the wave travels slower than the fluid, which means that it has negative angular momentum with

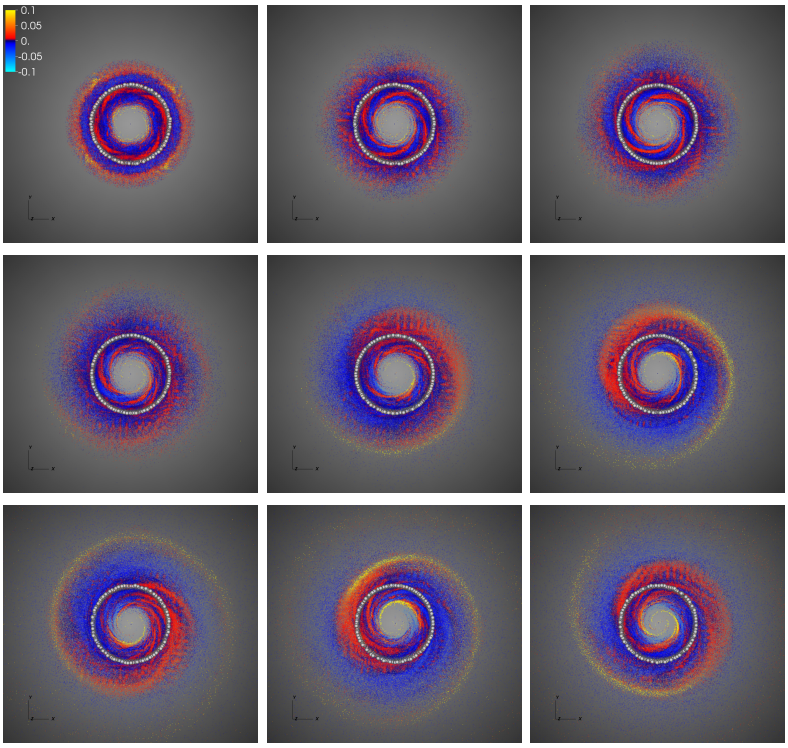

Figure 7.3 Fractional change in the rest mass density $\Delta\rho/\rho$ between two timesteps, shown at 9 different snapshots of the evolution, $t/t_{\rm orb} = 1, 4, 8, 12, 16, 20, 24, 28$, and 32 (from the top-left panel). The domain shown in all panels is 100 across both x-axis and y-axis. The grey circles show the tracers at the location of the corotation radius $r_{\rm co}$. The formation of a spiral density wave from the growth of the $m = 1$ mode is noticeable.

respect to the fluid. While the wave amplitude is linear, it does not interact with the fluid, but once non-linear amplitude effects come into play, the spiral density wave can couple to the fluid via dissipation [Papaloizou and Lin 1995, Goodman and Rafikov 2001, Heinemann and Papaloizou 2012]. When this happens, the wave begins to transport angular momentum outwards as the fluid loses angular momentum to the wave inside the corotation radius. The development and persistence of the spiral density wave is shown in Figure 7.3. The figure shows the fractional change in density between two successive snapshots of the tracer particles $\Delta\rho/\rho$ at 9 different times of the disc evolution, as well as the tracer particles that are located at $r_{\rm co}$ (grey circles). The location of the corotation radius is defined as the radius where the $m = 1$ pattern speed and the fluid orbital velocity are equal. As usual, the non-axisymmetric modes in the disc are analysed by means of an azimuthal Fourier transform of the rest-mass density

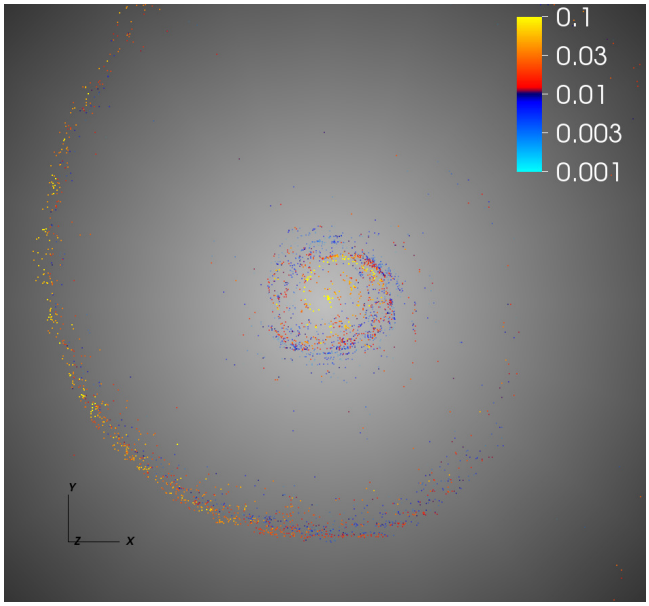

Figure 7.4 Fractional change in the fluid entropy s between two timesteps, for tracers with $\Delta\rho/\rho > 0.1$, shown at $t/t_{\rm orb} = 32$.

ρ [Zurek and Benz 1986, Heemskerk, Papaloizou, and Savonije 1992]:

$$D_m = \int \alpha \sqrt{\gamma}\, \rho\, e^{-i\, m\, \phi}\, d^3x\,, \tag{7.3}$$

Similarly, the mode analysis performed using the tracers is performed by means of the following sum

$$D_m = \sum_j^N m_j\, e^{-i\, m\, \phi}, \tag{7.4}$$

where m_j is the mass of each tracer particle. From the mode amplitudes, the pattern speed of an azimuthal mode with mode number m is defined as (see, for instance Heemskerk, Papaloizou, and Savonije [1992])

$$\Omega_P = \frac{1}{m}\frac{d\phi_m}{dt}, \tag{7.5}$$

where the phase angle ϕ_m is given by

$$\phi_m = \tan^{-1}\left(\frac{\mathrm{Im}(-D_m)}{\mathrm{Re}(D_m)}\right). \tag{7.6}$$

For our simulation, we obtain an orbital period of the $m = 1$ pattern of $P_P \sim 1.96$ ms, which is slightly shorter than twice the initial orbital period of the disc at the location of the density maximum (see Table 6.2). We note that we have chosen

the same range of the fractional change in the rest-mass density in all snapshots shown, which corresponds to the interval $[-0.1, 0.1]$. At these wave amplitudes, non-linear effects are negligible compared to the linear effects [Masset and Tagger 1997]. This plot range has however been chosen for visualisation purposes and the wave amplitudes are actually much larger than 0.1 after the saturation of the $m = 1$ growth, reaching almost unity. At these wave amplitudes non-linear effects are important and the spiral density wave can couple to the fluid via dissipation. To show the development of weak shocks, we plot the fractional change in the entropy $s = p/\rho^{\Gamma}$ for tracers with $\Delta\rho/\rho > 0.1$ in Figure 7.4. From this plot, we clearly see an increase in the fluid entropy in the inner and outer regions of the spiral density wave. We note that the mesh refinement boundaries of our computational grid also produce entropy changes due to dissipation. However, these changes are about an order of magnitude smaller than the physical increase of entropy due to the development of shocks in the spiral density wave.

7.3.2 Gravitational torque and motion of the central BH

We next turn to the interaction of the non-axisymmetric $m = 1$ mode and the central BH. The moving over-density planet in the disc represents a time-changing non-axisymmetric gravitational potential. Following Roedig et al. [2012], we estimate the total gravitational torque on the BH exerted by the tracer particles in the following way:

$$\boldsymbol{T}_G = \sum_i^N M_{\rm BH} m_i \frac{\boldsymbol{r}_{\rm BH} \times (\boldsymbol{r}_i - \boldsymbol{r}_{\rm BH})}{|\boldsymbol{r}_i - \boldsymbol{r}_{\rm BH}|^3}, \tag{7.7}$$

where the sum runs over all tracer particles.

The resulting components of the gravitational torque $\boldsymbol{T}_{\rm G}$ and the time derivative of the components of the BH orbital angular momentum $\dot{\boldsymbol{L}}_{\rm BH}$, are shown in Figure 7.5. This figure clearly shows that the orbital angular momentum of the BH is caused by the gravitational torque of the non-axisymmetric matter distribution in the disc. The orbital angular momentum components of the BH are calculated using the flat space coordinate rotational Killing vectors on the AH [Campanelli et al. 2007] (which gives the Komar angular momentum in axisymmetry [Mewes, Font, and Montero 2015]) without the subtraction of the position of the BH centre and the subsequent subtraction of the intrinsic spin of the AH. While this is by no means a gauge invariant measure of the orbital angular momentum of the BH, it agrees very well with the Newtonian

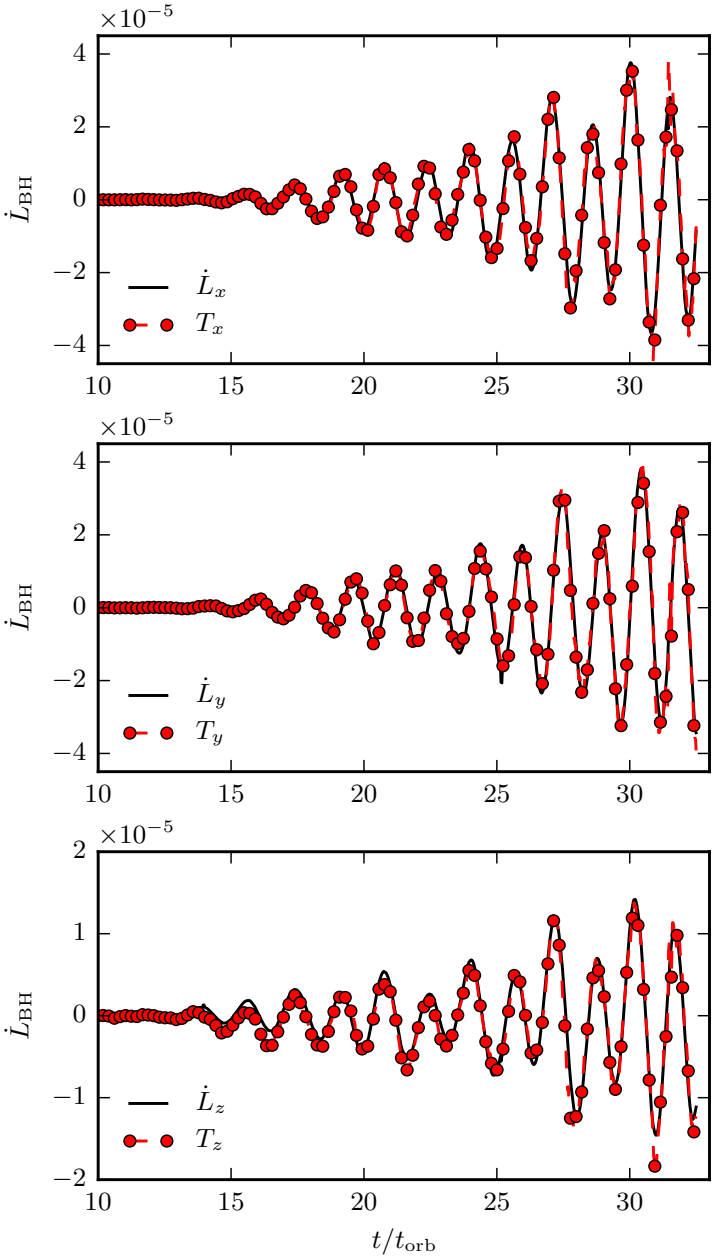

Figure 7.5 Time derivative of the components of the BH orbital angular momentum vector $\boldsymbol{L}_{\rm BH}$ and the components of the gravitational torque computed from the non-axisymmetric matter distribution $\boldsymbol{T}_{\rm G}$.

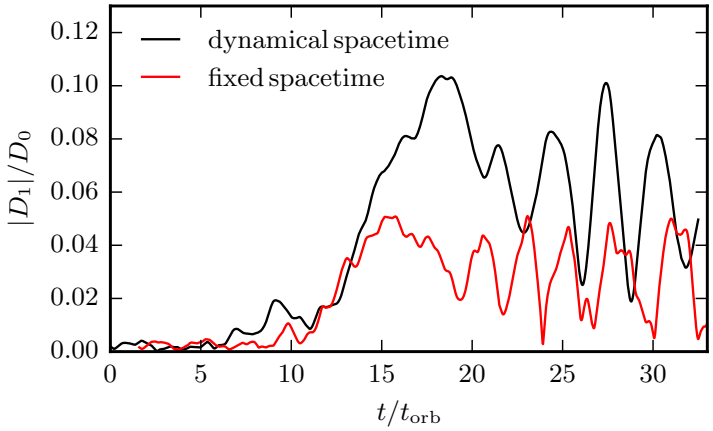

Figure 7.6 Evolution of the $m = 1$ mode for the dynamical spacetime simulation (black line) and the fixed spacetime simulation (red curve), calculated with the tracer particles. We note that we are using a linear scale for the vertical axis in this plot, contrary to the mode plots shown in Chapter 6.

calculation of the BH orbital angular momentum as

$$\boldsymbol{L}_{\rm BH} = M_{\rm BH}\, \boldsymbol{r}_{\rm BH} \times \boldsymbol{v}_{\rm BH}. \tag{7.8}$$

The disc acquires some bulk orbital angular momentum (equal and opposite to that of the BH) as a result of the growth and the longevity of the $m = 1$ mode as well. During the later stages of the evolution, after the saturation of the $m = 1$ mode growth, this bulk orbital angular momentum of the disc becomes comparable to the fluid angular momentum in the x and y direction. We note that it is precisely the evolution of the bulk orbital angular momentum that we mistakenly identified as tilt and twist oscillations in Mewes et al. [2016]. This was due to an error in the reading of the location of the BH centre in the disc analysis code described in Section 4.4, which ultimately resulted in the calculation of the disc angular momentum about the origin rather than about the BH centre.

As a result of this error in the disc analysis used for the results presented in Mewes et al. [2016], we speculated that the observed global oscillations in the tilt and twist might be due to the development of the Kozai-Lidov (KL) [Kozai 1962, Lidov 1962] effect. This effect results in the periodic exchange of the inclination and eccentricity of a particle orbit around a central mass that is itself in an orbit with a third mass (called the perturber). The effect is a direct consequence of the conservation of the total angular momentum of the system. As the KL effect has recently been observed to operate in inclined

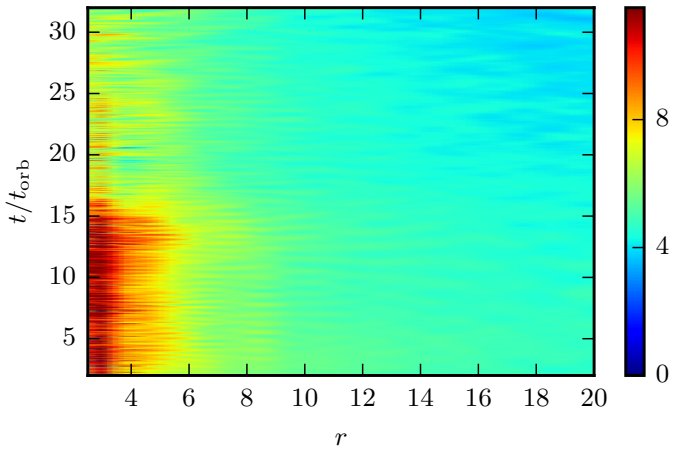

Figure 7.7 Spacetime diagram of the radial profile of the tilt angle $\nu(r)$. The tilt angle is shown in degrees.

hydrodynamical discs around a central mass which is in a binary with another mass [Martin et al. 2014], we assumed in Mewes et al. [2016] that the KL effect might also be in operation in our discs as the long-lasting $m = 1$ mode forces the central BH to move in a quasi-binary orbit with the over-density planet in the disc. To demonstrate the operation of the KL effect and to explain the oscillations in more detail has been one of the main motivations for carrying out new simulations and employing the tracer particles as a new tool for the analysis of the disc. As explained above, we have clarified the origin of the global tilt and twist oscillations as being connected to the bulk orbital angular momentum the disc acquires when forming the quasi-binary system with the BH. The KL effect is therefore not seen to be in operation in our discs.

The effect of the motion of the central BH on the strength of the $m = 1$ mode is shown in Figure 7.6. This figure displays the time evolution of the normalised magnitude of the D_1 mode for our two simulations. While growth rates of the $m = 1$ mode strength are very similar for the two runs, the maximum mode amplitude is about two times higher in the fully dynamical spacetime simulation (where the BH is allowed to move). We note that the growth rate and maximum $m = 1$ mode amplitude in the simulation presented here is smaller than the one reported in Chapter 6 for the same model. The difference arises from the use of a constant damping parameter in the standard Γ-driver shift condition, which is known to be less accurate than dynamical damping parameters for large mass-ratio BBH simulations (see for instance Gold and Brügmann [2013]). The dynamics of the high mass-ratio quasi-binary system composed of the central BH

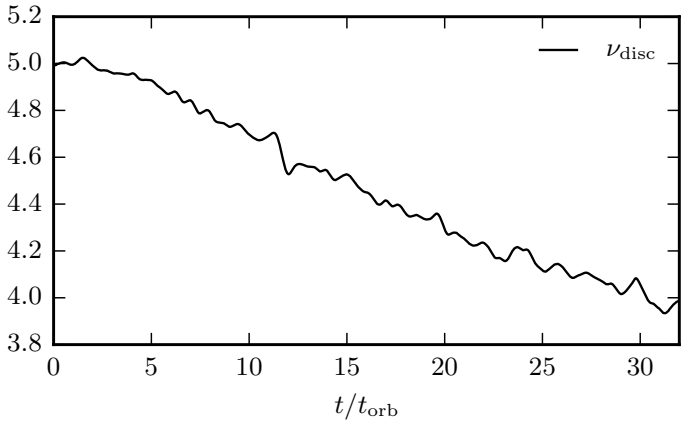

Figure 7.8 Time evolution of the tilt angle of the disc, $\nu_{\rm disc}$, shown in degrees.

and the moving over-density planet in the disc should therefore be described with better accuracy using the dynamical damping parameter employed in Chapter 6. It seems that the fixed damping parameter restricts the BH motion, resulting in a smaller mode power. We note, however, that the actual development of the instability and the overall properties of the disc after its saturation remain unaffected by the choice of gauge, as they should.

7.3.3 Disc alignment

As shown in King et al. [2005], the direction of the torque responsible for disc (and therefore also BH) precession does not act in the direction to align the disc angular momentum with the central BH. The alignment torque ultimately results from the inclusion of the effects of viscosity or dissipation, and its magnitude depends, as King et al. [2005] remark, on the actual disc properties. As our fluid evolution does not explicitly account for viscosity, viscous and dissipative effects might therefore only arise due to numerical viscosity and dissipation in shocks. As we have seen in Section 7.3.1, the spiral density wave that results from the development of the $m = 1$ mode provides dissipation that is stronger than the one arising from the numerics. Another factor working towards alignment of the BH spin and the disc is the accretion of angular momentum, which is a negligible effect in our simulations due to the very low amount of total mass accreted during the evolution.

In Figure 7.7, we plot a spacetime diagram showing the evolution of the tilt angle profile $\nu(r)$ obtained from the tracers. Similar to the disc analysis

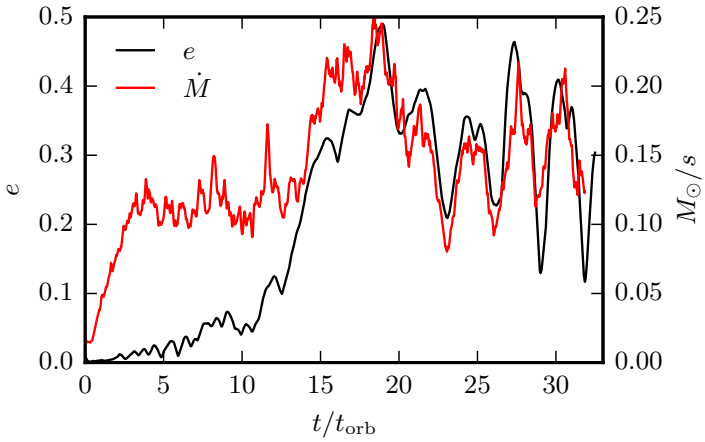

Figure 7.9 Evolution of the sum of disc eccentricity e_1 and disc ellipticity e_2 and the rest mass accretion rate $\dot{M}$ in units of $M_\odot/s$. The accretion rate has been shifted by $0.65\,t_{\rm orb}$ in time for a better visualisation of the correlation between its modulation and e.

explained in Nelson and Papaloizou [2000] and Fragile and Anninos [2005] and employed in Chapter 6, we split the domain in radial shells and calculate the components of the total angular momentum of all tracers within a given shell to obtain the tilt profile. We clearly see the expected, non-zero oscillating tilt profile predicted by the warp propagation as bending waves during the early stages of the simulation. The tilt amplitude close to the central BH is significantly reduced from about $15t_{\rm orb}$ onwards. This could be connected to the time when the developing spiral density wave becomes non-linear for the first time, coupling to the fluid inside the corotation radius and lowering the tilt amplitude. We do not see a complete global alignment as observed in Kawaguchi et al. [2015] during the time of the evolution. However, as Figure 7.8 shows, there is a clear monotonic drop in the global tilt angle $\nu_{\rm disc}$ from $t = 2\,t_{\rm orb}$ onwards, which is when the $m = 1$ non-axisymmetric mode starts growing. Kawaguchi et al. [2015] noted that the alignment timescale was comparable or shorter than the precession timescale of the disc. We note that our disc is precessing slower than the ones studied in Kawaguchi et al. [2015], as our initial BH spin is much smaller than that of the central BH they obtain in their BHNS merger simulations. In our dynamical spacetime simulation, both the disc angular momentum and BH spin have completed half a precession cycle within $32\,t_{\rm orb}$, while the global tilt angle $\nu_{\rm disc}$ has not dropped by half within the same period. A difference between our disc evolution and the ones described in Kawaguchi et al. [2015] is the accretion timescale, which in their case is comparable to the precession

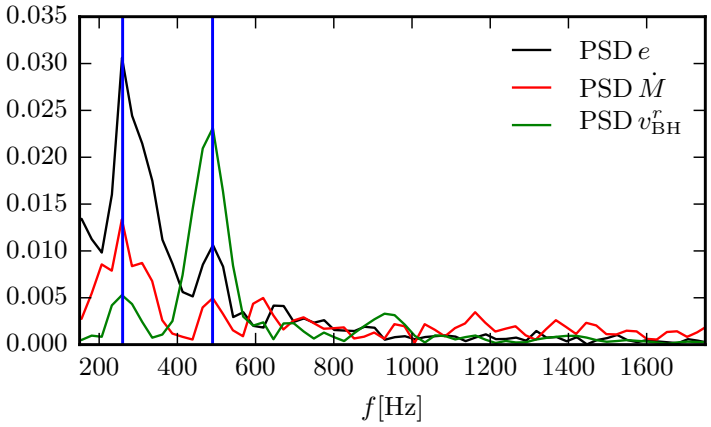

Figure 7.10 Power spectrum density of e, the rest mass accretion rate $\dot{M}$ and the radial BH velocity $v^r_{\rm BH}$.

timescale and, therefore, to the alignment timescale. We do not observe this behaviour in our simulations, as the total rest mass accreted during the evolution (2.6×10^{-3}) is very small compared to the initial disc rest mass (1.02×10^{-1}). Assuming that the accretion rate remains constant for the lifetime of the disc, the accretion timescale would be ≈ 10 times larger than the precession timescale of the disc.

7.4 QPOs in the accretion rate

As already observed in Chapter 6, the growth of the $m = 1$ non-axisymmetric mode in the disc strongly influences the instantaneous accretion rate. As the accretion rate can be assumed to be a measure of X-ray luminosity (see, for instance van Paradijs, Penninx, and Lewin [1988] and Méndez et al. [1999]), finding QPOs in the accretion rate and correlating them with the disc evolution might serve as a model to explain the QPOs observed in LMXBs (see e.g. van der Klis [2006] and references therein). The origin of these QPOs is still not fully understood, and there are various models trying to explain the observed X-ray variability in these sources (see Lai and Tsang [2009] for a detailed summary of the proposed models, Belloni and Stella [2014] for a recent review of QPOs in LMXBs and Mishra et al. [2015] and Mazur et al. [2016] for recent models). As matter accretion implies the development of a radial flow, we follow MacFadyen and Milosavljević [2008] and calculate the eccentricity e_1 and ellipticity e_2 of

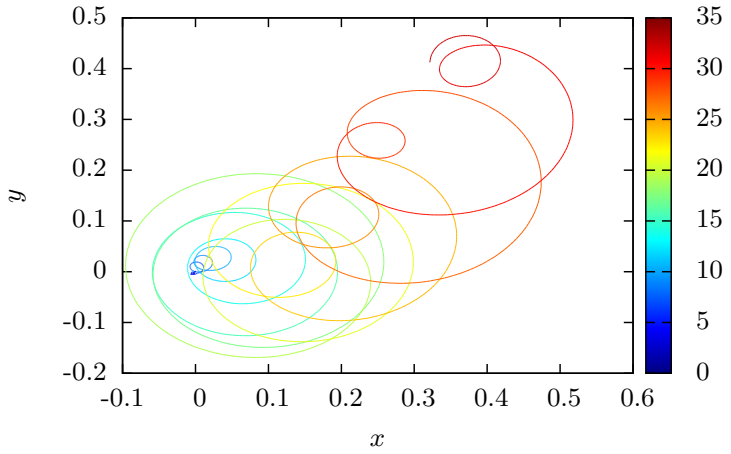

Figure 7.11 Trajectory of BH projected onto xy-plane. The colorbar indicates the time in $t_{\rm orb}$ along the trajectory.

the tracer particles as

$$e_n = \frac{|\sum_j^N m_j v^r e^{in\phi}|}{\sum_j^N m_j v^\phi}\,, \tag{7.9}$$

where v^r and v^ϕ are the radial and azimuthal components of the 3-velocity, respectively. We denote the sum of disc eccentricity and ellipticity by

$$e \equiv e_1 + e_2. \tag{7.10}$$

The evolution of e together with the mass accretion rate $\dot{M}$ is plotted in Figure 7.9. As in Chapter 6, we calculate the accretion rate as the following surface integral at the AH:

$$\dot{M} = 2\pi r^2 \int_0^{2\pi}\int_0^{\pi} D\, v^r\, \sin\theta\, d\phi\, d\theta\,. \tag{7.11}$$

The mass accretion rate in Fig. 7.9 has been shifted by $0.65 t_{\rm orb}$ to better illustrate that the accretion rate is clearly modulated by e and shows distinct QPOs. As expected, the applied shift is backwards in time, as the evolution of $\dot{M}$ trails the evolution of e. The power spectral densities (PSD) of e, $\dot{M}$ and the radial velocity of the BH are shown in Figure 7.10. The PSD show a clear dominant peak at $\sim 260\,$Hz with a first overtone at $\sim 490\,$Hz for e and $\dot{M}$. The frequency ratio of the dominant low frequency peak and the overtone is $o_1/f \sim 1.9$. The double peak in the PSD arises from the modulation of the strength of the $m = 1$ mode (see Fig. 7.6). The modulation causes changes in the eccentricity of the orbital motion of the BH as well, which is displayed in Fig. 7.11.

Periodicity in the accretion rate due to the inner region of a circumbinary accretion disc becoming eccentric has also been observed in Farris et al. [2014], as well as in the MHD simulations of Machida and Matsumoto [2008], where the authors attribute the QPOs in the accretion rate to the development of a $m = 1$ non-axisymmetric mode. We note that the QPO frequencies extracted from our simulation are for a fiducial model with a central BH mass of $\sim 1\,M_\odot$ (see Table 6.1). The observed frequencies in these systems usually scale as M^{-1}, where M is the mass of the central compact object, as in the p-mode torus oscillation model of Rezzolla et al. [2003]. Assuming the M^{-1} frequency scaling to be universal (see for instance Abramowicz et al. [2004] and Zhou et al. [2015] for arguments and observational support), this would mean that the QPOs we observe in the accretion rate would be at ~ 26 Hz and ~ 49 Hz if we rescale our results for a $10\,M_\odot$ BH. These frequencies are compatible with the results of Machida and Matsumoto [2008], who found 10 Hz QPOs for a $10\,M_\odot$ BH. Therefore, the QPOs we observe resulting from the modulation of the $m = 1$ mode strength could help explain the low-frequency QPO sector of the fast X-ray variability seen in LMXBs.

On the other hand, if we assume the accretor to be a NS, after rescaling our results for typical NS masses, the QPOs in the accretion rate would also have frequency peaks in a range compatible with those observed in LMXBs. Note that models based on the p-mode oscillations of axisymmetric tori cannot explain the observed twin QPOs in LMXBs with a NS as an accretor, with a fundamental frequency smaller than 500 Hz, since the fundamental mode frequency decreases as the size of the disc increases or as the distribution of the disc specific angular momentum approaches the Keplerian profile [Montero and Zanotti 2012]. Therefore, the o_1/f frequency ratio in axisymmetric models shows a tendency to concentrate towards the $3:2$ ratio line as the fundamental mode frequency tends to zero. However, deviations from axisymmetry may relax this constraint, and there exist several works where the idea that the QPOs in accretion discs might be connected to non-axisymmetric modes has been put forward (see for instance Li, Goodman, and Narayan [2003], Tagger and Varnière [2006], Machida and Matsumoto [2008], Lai and Tsang [2009], and Henisey, Blaes, and Fragile [2012]). By rescaling our results for a $1.4\,\mathrm{M}_\odot$ NS, the fundamental mode would lie at ~ 185 Hz while the first overtone would be at ~ 350 Hz. Such values, extracted from the modulation in the accretion rate triggered by the development of a non-axisymmetric $m = 1$ instability, lie thus within the range needed to explain, for instance, the observed QPOs in sources like Cir X-1 or XTE J1807-294.

Part IV

Discussion and outlook

Chapter 8

Discussion

In the sections below, we provide a detailed, individual discussion of our results presented in the three chapters of Part III.

8.1 Measuring the BH spin direction in 3D Cartesian NR simulations

As we have shown in Chapter 5, the flat-space rotational Killing vector method of Campanelli et al. [2007] can be derived from Weinberg's pseudotensor when using Gaussian coordinates. These coordinates have two interesting properties that make them particularly useful for the evaluation of the angular momentum pseudotensor integral, Eq. (5.7). First, the complicated integral (5.7) reduces to the much simpler expressions given by Eq. (5.24) and this final expression is equal to the Komar angular momentum integral in a foliation adapted to the axisymmetry of the system. As a result, one does not need the knowledge of the shift vector and of its spatial derivatives on the surface of integration, which in practice would involve more quantities that one would need to interpolate onto the horizon surface for the calculation of the spin, thus also avoiding the numerical error associated with the computation of the finite difference approximation to those spatial derivatives. Second, Gaussian coordinates trivially satisfy the necessary falloff conditions for the lapse and shift. Moreover, by using Gaussian coordinates we recover the ADM angular momentum evaluated at spatial infinity, provided we use a spherical surface of integration.

It is generally known that the various energy-momentum pseudotensors proposed in the literature are not covariant and care has to be taken when evaluating

them in different coordinate systems and gauges (see Szabados [2009] for a review on quasi-local mass and angular momentum in GR, where the problems arising when using pseudotensors for the calculation of mass and angular momentum are also discussed). The derivation of Weinberg's pseudotensor relies crucially on the reference space being Cartesian Minkowski. In his textbook, Weinberg [1972] states that a spherical polar coordinate system would lead to a gravitational energy density concentrated at infinity. This is ultimately due to the non-covariance of the pseudotensor. Additionally, the choice of gauge is also crucial to obtain meaningful results. Gaussian coordinates guarantee the correct asymptotic behaviour of the lapse and shift, irrespective of the asymptotic behaviour the numerically evolved lapse and shift may posses, which are, as previously stated, not explicitly used in the calculation of the AH spin on the respective timeslice. Furthermore, we have shown that Gaussian coordinates transform the pseudotensor angular momentum surface integral (5.13) to the Komar angular momentum integral (5.29) which is coordinate independent. The use of Gaussian coordinates (as an explicit gauge-fixing) seems to therefore remove the coordinate restrictions of the pseudotensor.

When Campanelli et al. [2007] introduced the flat-space rotational Killing vectors for the calculation of the BH spin direction, the authors stated that they could not guarantee the correct results for all times because the method is not gauge invariant. However, as we have shown in Chapter 5, the method can actually be derived from the integration of Weinberg's total angular momentum pseudotensor over the AH surface when using Gaussian normal coordinates in the integration. As a result, the method does not depend on the evolving lapse and shift, as the gauge is fixed to the Gaussian normal coordinates on the respective timeslice. We stress that the evolution of the lapse and shift during the free evolution of the spacetime does not enter the calculation, given the coordinates evolve in such a way that an AH is found at all times during the evolution, which is usually the case in puncture evolutions with the BSSN system. There is a dependence on the gauge evolution via the extrinsic curvature K_{ij} that is interpolated onto the AH for the calculation of the spin direction, but the same is true for the expression of the spin magnitude in Eq. (2.94).

Schnetter, Krishnan, and Beyer [2006] showed that Eq. (2.94) gives the spin magnitude provided an approximate Killing vector can be found on the horizon and is gauge independent on the respective time-slice if the approximate Killing vector field ψ^a is divergence-free. In Chapter 5 we have shown that both methods (i.e. either via Weinberg's pseudotensor in Gaussian coordinates or via flat-space rotational Killing vectors) yield the Komar angular momentum when

the latter is expressed in a foliation adapted to the axisymmetry. We note that the restriction to axisymmetry turns out in practice not to be a major weakness, as NR simulations have repeatedly shown that the remnants of BBH mergers and perturbed Kerr BHs typically settle down to the axisymmetric Kerr solution quickly [Schnetter, Krishnan, and Beyer 2006, Owen 2009]. Moreover, both methods provide a measure of the BH spin magnitude and direction that is not explicitly dependent on the lapse and the shift on the respective time-slice. As both methods use the fixed rotational Killing vectors of Minkowski space, they measure the spin contribution from the axisymmetry of the AH, which is the only meaningful way to measure its angular momentum as it is not clear how non-axisymmetric perturbations of the AH influence the actual spin value.

8.2 NR simulations of tilted BH–torus systems

In Chapter 6 we have presented the results of an extended set of NR simulations of massive accretion discs around tilted Kerr BHs. We considered three different thick accretion discs of varying mass and specific angular momentum magnitude and distribution, along with different BH configurations with two spin magnitudes a and four initial tilt angles β_0. On the one hand, the motivation for this work has been to extend the investigations of Fragile and Anninos [2005] and Fragile et al. [2007] performed in the test-fluid approximation to full GR, thereby analysing the influence of the self-gravity of the disc on the BH–torus dynamics. On the other hand, our work has also served to enlarge the parameter space of the existing NR simulations of thick accretion tori around BHs [Korobkin et al. 2011, Kiuchi et al. 2011] by accounting for *tilted* BH–torus systems for the first time.

For the models with disc-to-BH mass ratios of $0.044 - 0.16$ we studied, we find that the assumption of using a fixed background spacetime is not justified. We observed significant precession and nutation of the tilted BH, which means that the tilted BH–torus evolution cannot be accounted for in fixed spacetime simulations. For some of our models the precession rate attained a fairly constant value by the end of the simulation. The BH nutation rate was also seen to be strongly modulated for those models that develop the PPI, showing that the development of non-axisymmetric modes in the disc exerts a torque on the BH.

Our simulations revealed that the development of the PPI is universal for the range of initial spin magnitudes and tilt angles investigated. Models `C1B` and `NC1`, both PP-unstable when the central BH is non-rotating or untilted, remained PP-unstable when the BH was rotating or tilted, for all initial spin magnitudes and tilt angles investigated. The reverse also seems to be true:

model D2, which is PP-stable for an untilted, non-rotating central BH remained PP-stable for the entire parameter space of initial spins and tilt angles considered in our study. As we mentioned before, model D2, having the smallest mass ratio in our study, is the most likely outcome of BHNS mergers based on astrophysical considerations. Thus, our findings are relevant to gauge the importance of the PPI in thick post-merger accretion discs around black holes. In agreement with the NR simulations of Kiuchi et al. [2011], the growth of the $m = 1$ PPI mode manifested itself in the formation of a counter-rotating over-density lump that formed a "quasi-binary" with the BH during its existence. This caused the BH to move in a spiral trajectory for as long as the "planet" existed. For models C1B, the "planet" dispersed quickly upon the saturation of the PPI, while in models NC1 the over-density structure persisted much longer, with the $m = 1$ mode amplitude remaining at its level of saturation till the end of the simulations. When the PPI develops around a tilted Kerr BH, the binary motion of BH and "planet" is not restricted to the xy-plane but also shows some vertical motion. For models C1B in particular, the rapid destruction of the non-axisymmetric structure caused a mild kick to the BH–torus system in the vertical direction which was also imprinted in the time evolution of the linear momentum radiated away by gravitational waves in the opposite direction.

The evolution of the disc around the tilted BH can cause a significant twisting (differential precession) and warping (spatially varying tilt) in the disc. We monitored the evolution of the twist $\sigma(r)$ and tilt $\nu(r)$ of radial shells during the simulations, using an analysis thorn we developed for the ET. For models C1B (NC1) we found a phase of rapid (mild) realignment of the total angular momentum vector of the disc, $J_{\rm Disc}$, and the BH spin, $J_{\rm BH}$, during the growth of the PPI. We attribute this alignment to the development of the $m = 1$ structure in the disc. In their recent NR simulations of tilted BHNS mergers and the corresponding post-merger disc evolution, Kawaguchi et al. [2015] also observed significant alignment of the tilted accretion disc and the central BH, in a timescale comparable to the accretion timescale of the system. While there was no mode analysis presented, the authors argued that angular momentum transport caused by a non-axisymmetric shock wave in the disc should work in favour of disc–BH alignment. Our simulations also confirmed the presence of significant differential disc twisting due to LT precession. For all models, the cumulative twist is higher for higher initial BH spins, as expected, and the outer regions of the discs precess as a solid body. This solid body precession was also observed in Fragile and Anninos [2005] and is a consequence of the sound crossing time in the disc being small compared to the timescale of the

LT precession, which is the case for the geometrically thick and radially slender discs we studied in this thesis. The evolution of the tilt profiles of models `D2` was similar to what Fragile and Anninos [2005] observed, with the development of a peak in the innermost region of the disc. This behaviour is in agreement with the evolution and propagation of warps being described by bending waves rather than diffusion [Lubow, Ogilvie, and Pringle 2002]. For models `C1B`, the PPI caused a drastic change in the tilt profile upon saturation. We did not observe the Bardeen-Petterson effect in any of our models, as the tilt angle $\nu(r) \neq 0$ in the inner region of the discs, in agreement with the model of Ivanov and Illarionov [1997], Demianski and Ivanov [1997], and Lubow, Ogilvie, and Pringle [2002].

The PPI is thought to activate the outward transport of angular momentum. This is indeed the case in our simulations, as the evolution of the angular momentum profiles shows. For model `C1Ba0b0`, angular momentum profile contour lines in the the outer parts of the disc were seen to start moving outwards in a wave-like manner up until the sudden saturation of the PPI. After saturation there was no more transport of angular momentum and the evolution resembled that of the PP-stable model `D2a01b0`. For model `NC1a0b0` the persistence of the $m = 1$ structure in the disc caused a continuous transport of angular momentum outwards for the entire simulation of the disc.

As Kiuchi et al. [2011] showed, the development of the PPI and the corresponding over-density $m = 1$ lump in the disc cause the long-term radiation of GWs, predominantly in the $l = m = 2$ multipole mode, as expected from the radiation emitted by a binary system. Our simulations confirmed these results, showing that models `C1B` and `NC1` do indeed radiate mainly in that particular mode. The rapid destruction of the $m = 1$ structure in models `C1B` caused the amplitude of the emitted GW signal to drop significantly after the PPI saturated, while the peak amplitude was closely correlated with the time of saturation. Models `NC1` on the other hand, continued to emit at an amplitude similar to that attained at saturation, as the $m = 1$ structure survived until the end of the simulations. We also calculated the effective strains of the GW signals. While models `C1B` showed different spectra for different initial spin magnitudes and tilt angles, there seemed to be no such trend for models `NC1`. For those two set of models, the GW emission was predominantly in the $l = m = 2$ mode while in models `D2` we also found also significant power in the $l = 3$, $m = 1$ mode. In addition, the strain spectra of models `D2` showed a clear trend to higher values with increasing initial spin and tilt angle. We follow the analysis of Kiuchi et al. [2011] and assume that if the $m = 1$ structure survives for the entire accretion

timescale, the peak strain of the GW signal will be amplified by the square root of the number of GW cycles emitted at the peak frequency. The GWs emitted by models `NC1` could currently be detectable for BH–torus systems located at distances up to 50 Mpc. Finally, we briefly touched on the issue of the possible modulation of the GW signal caused by the BH precession. For the fastest precessing models of our sample, models `C1Ba01`, we showed that in order to see such an effect, we would need to perform a simulation lasting for about 80 orbits to obtain a complete BH precession cycle, assuming the precession rate remains constant beyond the 20 orbit mark we could afford in our simulations.

8.3 Analysing the tilted BH–torus dynamics with fluid tracers

In Chapter 7 we have investigated in detail the BH–torus dynamics of model `NC1a03b05`. We employed fluid tracer particles as a powerful new tool to analyse the disc dynamics. The tracers provide a complementary tool to the existing disc analysis thorn described in Section 4.4.

Using the tracers, which accurately describe the bulk morphology of the fluid in the disc, we showed that the BH precession we reported in Chapter 6 was indeed caused by a torque resulting from the disc precessing as a solid body, which in turn resulted from the LT torque the BH exerts on the disc. This is expected, as the disc should exert an equal and opposite torque on the BH. For sufficiently high disc-to-BH mass ratios, tilted BH–torus systems should therefore contain precessing central BHs, and the BHs should precess for at least the accretion timescale of the disc.

The main characteristic of model `NC1` is its non-constant l profile. As already observed in the NR simulations of Kiuchi et al. [2011] and also in Chapter 6 these models form a long-lived over-density "planet" as the result of the growth of the PPI. Using the tracers, we showed that the growth of the $m = 1$ non-axisymmetric instability manifests itself as a spiral density wave of constant pattern speed in the differentially rotating disc. The pattern period was shown to be slightly smaller than the initial fluid period at the location of the maximum rest-mass density of the disc. While the spiral wave remains of small amplitude, it travels through the fluid without interaction. Once the wave amplitude becomes large enough for non-linear effects to become important (in some regions the fractional change in rest-mass density became as high as 0.9), the wave couples to the fluid via the formation of mild shocks, which can be seen clearly as an

increase in the fluid entropy. As the disc is differentially rotating, the spiral density wave has *negative* angular momentum w.r.t. the fluid inside the region that is smaller than the so-called co-rotation radius; therefore the wave can transport fluid angular momentum outwards and becomes the main driver for accretion.

The density wave also represents a time-changing non-axisymmetric gravitational potential. As observed in Korobkin et al. [2011] and Chapter 6 this gravitational potential causes the BH to move along a spiral trajectory. Using the tracers, we calculated the total gravitational pull exerted by the disc on the BH and showed that the resulting torque agrees very well with the observed motion of the BH. This is an important confirmation that the BH movement is of physical origin, and not caused by numerical effects or the evolution of the gauge variables lapse and shift. BH–disc alignment within the accretion timescale was observed in the NR simulations of tilted post-merger discs in Kawaguchi et al. [2015]. Correspondingly, in the simulations reported in Chapters 6 and 7 we also saw partial realignment of the BH–torus system. In all cases, there was no explicit viscosity in the fluid evolution. As the torque acting to align the BH spin with the disc must be of dissipative nature, the only way to achieve BH–torus alignment is via numerical dissipation or dissipation via shocks in the fluid. The spiral density wave that results from the growth of the $m = 1$ mode provides such a channel, and Kawaguchi et al. [2015] speculated that shocks in non-axisymmetric waves might be responsible for the observed alignment of the BH–torus system in their simulations. This is a strong argument to carefully check for non-axisymmetric structures in post-merger disks, as they seem to influence the evolution of the system profoundly.

Our simulations also revealed the presence of distinct QPOs in the evolution of the accretion rate, in a frequency range compatible with that of X-ray luminosity QPOs in LMXBs. When rescaling the frequency of the observed QPOs in our simulation for a $10M_\odot$ BH, the extracted frequencies are compatible with the range of low-frequency QPOs in those systems. Furthermore, the same rescaling for typical NS masses also gives QPOs with frequencies compatible with those observed in sources like Cir X-1 or XTE J1807-294. The frequency ratio of the dominant low frequency peak and the first overtone found in our three-dimensional simulations was $o1/f \sim 1.9$, a frequency ratio not attainable when modelling the QPOs as p-mode oscillations in axisymmetric tori. As the flow needs to develop a non-zero radial velocity component in order to accrete, we have also analysed the sum of disc eccentricity and ellipticity using the tracers and showed that its evolution exhibits the same QPO structure at exactly the

same frequencies. While the origin of the variability of the eccentricity (which was also exhibited in the radial motion of the BH) is still unclear, the fact that the accretion rate is so clearly modulated could be the starting point to devise a new model to explain the observed QPOs in LMXBs.

Chapter 9

Outlook

There are numerous direct extensions to the work presented in this thesis on NR simulations of tilted BH–torus systems. We plan on performing long-term simulations in the future in order to, firstly, obtain the complex GW signal from the kind of precessing BH–torus systems we have started to explore here (namely, the imprint of BH precession on the waveform), and, secondly, to obtain clearer PSD of the accretion rate, which might help to shed some light onto the origin of HFQPOs in LMXRBs. As explained in the manuscript, we have restricted ourselves in this study to modelling the matter in the torus using GRHD and the ideal fluid EOS. For thick discs formed following BNS or BHNS mergers, this EOS is a poor approximation. We are planning on extending our work to more realistic EOSs (including the effects of composition and pressure from trapped neutrinos) such as the one described in Paschalidis et al. [2011]. Furthermore, it is most likely that post-merger discs should be highly magnetised, as there are efficient magnetic flied amplification mechanisms in BNS mergers [Kiuchi et al. 2015a]. In this regard, Fragile et al. [2007] have already performed GRMHD simulations of tilted, magnetised BH–torus systems in the Cowling approximation. Moving into the regime of GRMHD simulations with a fully dynamical spacetime will be interesting especially in connection with precessing jets that might naturally emerge from these systems.

The role played by magnetic fields in connection with non-axisymmetric hydrodynamical instabilities such as the PPI is also not yet fully understood. The interest in the PPI quickly diminished after the discovery that the MRI is active in accretion discs [Balbus and Hawley 1991]. However, Fu and Lai [2011] suggest that highly magnetised tori might still be unstable to global hydrodynamic instabilities even if they are stable against the development of

the MRI. Elucidating these global non-axisymmetric instabilities through NR simulations of hot, magnetised accretion tori around BHs is one of the direct and obvious extensions of the work presented in this thesis.

For these future simulations, we want to improve our ID and/or experiment with spacetime evolution schemes that offer constraint damping, such as the Z4 [Bona et al. 2003, Bona and Palenzuela 2004], CCZ4 [Alic et al. 2012] or fCCZ4 systems [Sanchis-Gual et al. 2014]. Another possibility could be moving excision simulations using the constrained evolution scheme described in Bonazzola et al. [2004] and Cordero-Carrión et al. [2009]. This is due to our observation that the constraint violations of our initial tilted BH–torus data (which act as a type of negative mass) are absorbed by the BH during the evolution, causing an unphysical loss of irreducible mass. Constraint damping schemes might help in radiating away the constraint violations. Constructing tilted BH–torus data is however a daunting task on the other hand, as the system is not stationary. For small mass-ratios, it might therefore be sufficient to resolve the constraints of the ID. A possible idea is to write a new, general purpose elliptic solver in the `ET`, building on the scheduled relaxation Jacobi (SRJ) method of Yang and Mittal [2014]. The SRJ method solves elliptic equations by using a scheduled sequence of relaxation weights in the Jacobi iterative method. The method is easy to implement and trivially parallelised. In Adsuara et al. [2016] we have analytically derived the optimal set of weights for a given grid structure and desired tolerance using Chebyshev polynomials. Of course, the ultimate goal is to obtain tilted BH–torus ID that has been self-consistently formed via NR simulations of tilted (magnetised) BHNS mergers (especially with small mass ratios) and to use the tools developed in this thesis to analyse the subsequent post-merger disc evolutions.

Obtaining better ID is the most pressing issue in this future program, as any extension (such as GRMHD or improved microphysics described above) to our simulations will be plagued with the same problems we encountered in this work, related to the initial constraint violations. Even if constraint transporting schemes could cure our problems, the need for accurate initial BH–torus data will remain in order to perform comprehensive parameter space studies of these systems without having to perform the actual merger beforehand. This is, however, a very ambitious and time-consuming project which would require new techniques (general purpose constraint solvers, steady-state tilted and warped accretion disc hydro ID) and is aimed at the long run.

There is one more area in which we can improve our future simulations. All simulations in this thesis have been performed on Cartesian grids, which

are known for being notoriously substandard when used in the evolution of azimuthal flows, such as the ones encountered in accretion discs. Spherical polar coordinates are be much better suited for the GRHD evolution of accretion discs as they are adapted to the topology and symmetries of the flow. Baumgarte et al. [2013] have recently developed an implementation of the BSSN equations in spherical polar coordinates without any symmetry assumptions, which has later been extended to a fully covariant and conformal formulation of the Z4 system by Sanchis-Gual et al. [2014]. For the simulations of self-gravitating scalar fields around collapsing stars reported in Sanchis-Gual et al. [2015], I have developed a new radial coordinate composed of two patches, a geometrical progression in the interior and a hyperbolic cosine outside, allowing to push the outer boundary much further out without the use of prohibitively many radial grid points to achieve a sufficiently high resolution near the origin. We have also experimented with the 3D version of the `Nada` code, having implemented the spacetime variables boundary condition described in Section 4.1 as well as different GW extraction routines via the Weyl scalar Ψ_4. We plan on comparing the spherical `Nada` code and the `ET` in the future, focusing in particular on obtaining gravitational waveforms of the gravitational collapse of a rapidly rotating NS using both codes. This comparison is a short term goal, as the codes are in place and the problem is well defined.

Last but not least, we want to add more functionality to the disc analysis thorn (implementing some of the measures for which we have used the tracers) and, subject to interest from the community, work on making the thorn public to the `ET`.

Part V

Appendices

Appendix A

Hyperbolic partial differential equations

In this appendix we provide a brief introduction to hyperbolic PDEs, as they are central to our numerical integration of the Einstein field equations coupled to the matter evolution via GRHD. We refer the reader to [Courant and Hilbert 1962, Toro 2013, LeVeque 1992] for a detailed analysis of the topic.

We start by classifying second-order PDEs. Consider a general second-order partial differential operator L, acting on the dependent variable $u(x_1, x_2, .., x_n)$ of n independent variables x_n:

$$L[u] = 0. \tag{A.1}$$

We can rewrite this as the double sum of the second-order partial differentials plus terms of lower order partial derivatives:

$$L[u] = m^{AB}\partial_A\partial_B u + \text{terms of lower order} = 0, \tag{A.2}$$

where uppercase latin indices run from 1 to n. $m^{AB}\partial_A\partial_B u$ denotes the *principal part* of the PDE where m^{AB} are the components of the principal part matrix $\boldsymbol{M}$. In the case that the coefficients m^{AB} are constant and real-valued, we can classify the PDE (A.2) depending on the properties of the eigenvalues of the matrix $\boldsymbol{M}$ (see, for instance Courant and Hilbert [1962]):

1. The equation (A.1) is **elliptic** if the eigenvalues of $\boldsymbol{M}$ are real and all positive, or all negative.

2. The equation (A.1) is **parabolic** if the eigenvalues of $\boldsymbol{M}$ are real and all positive, or all negative except one that is 0.

3. The equation (A.1) is **hyperbolic** if $\boldsymbol{M}$ has real eigenvalues with either one positive eigenvalue and the rest are negative, or one negative eigenvalue and the rest are positive.

The classification of the PDE in the general case when m^{AB} are differentiable functions of the independent variables x_n is also described in Courant and Hilbert [1962].

As an example, consider the following PDE in 2 dimensions:

$$\partial_t \partial_t u(x,y,t) - \partial_x \partial_x u(x,y,t) - \partial_y \partial_y u(x,y,t) = 0, \tag{A.3}$$

from which we see immediately that $\boldsymbol{M} = \mathrm{diag}(1,-1,-1)$ with eigenvalues $\lambda_n = \{-1,-1,1\}$. The PDE (A.3), called the *wave equation*, is therefore hyperbolic. Hyperbolic PDEs have a finite speed of information propagation, which means that disturbances will travel away from the source with finite speed and are not immediately felt everywhere. This is in contrast to elliptic equations, where the propagation of information is instantaneous.

A.1 Characterising hyperbolic PDEs

As we have seen in section 2.1 of this thesis, the $3+1$ split has essentially allowed us to reformulate the 4 dimensional Einstein field equations as a first-order quasi-linear hyperbolic system and to treat the time evolution of the gravitational field as a Cauchy initial value problem. We have also seen that the numerical integration of the original $3+1$ system is not stable, which is attributed to the appearance of the Ricci tensor R_{ij} in the evolution equation (2.30) of the extrinsic curvature K_{ij}. To gain some insight and understand why the evolution equations in their original $3+1$ form are not stable, we need a criterion for the hyperbolicity of the evolution system.

In the following, we categorise the hyperbolicity of PDEs, following the classification of the hyperbolicity outlined in Shinkai and Yoneda [2002].

Consider the following system of n first-order, (quasi-) linear PDEs:

$$\partial_t u_A + m^{aB}{}_A(u)\partial_a u_B + S_A(u) = 0, \tag{A.4}$$

where, as above, uppercase latin indices run from 1 to n, and $m^{aB}{}_A$ is a $n \times n$ matrix for a fixed a, where the indices a run over the spatial dimensions of

the system (1 to 3 in our case). The vector $S_A(u)$ is a vector of sources. The matrices ${m^{aB}}_A$ can be understood as block matrices along the diagonal of a larger $3n \times 3n$ matrix $\boldsymbol{M}$:

$$\boldsymbol{M} = \left(\begin{array}{c|c|c} {m^{1B}}_A & 0 & 0 \\ \hline 0 & {m^{2B}}_A & 0 \\ \hline 0 & 0 & {m^{3B}}_A \end{array}\right) \tag{A.5}$$

The classification of the hyperbolicity depends on the spectrum of the *characteristic matrix* $\boldsymbol{M}$ in the following way:

1. The system (A.4) is **weakly hyperbolic** if all eigenvalues of $\boldsymbol{M}$ are real.

2. The system (A.4) is **strongly hyperbolic** if the matrix $\boldsymbol{M}$ is diagonizable ($\boldsymbol{M}$ has $3n$ linearly independent eigenvectors).

3. The system (A.4) is **symmetric hyperbolic** if the matrix $\boldsymbol{M}$ is Hermitian.

Let us analyse the hyperbolicity of the wave equation (A.3). We first need to rewrite the PDE as a system of first-order PDEs. To do this, we introduce the following state vector:

$$U = \begin{bmatrix} \partial_x u \\ \partial_y u \\ \partial_t u \end{bmatrix}, \tag{A.6}$$

so that

$$\partial_t U = \partial_t \begin{bmatrix} \partial_x u \\ \partial_y u \\ \partial_t u \end{bmatrix} = \begin{bmatrix} \partial_t \partial_x u \\ \partial_t \partial_y u \\ \partial_x \partial_x u + \partial_y \partial_y u \end{bmatrix}, \tag{A.7}$$

allowing us to write the first-order system of the form:

$$\partial_t \begin{bmatrix} \partial_x u \\ \partial_y u \\ \partial_t u \end{bmatrix} = \begin{bmatrix} 0 & 0 & 1 \\ 0 & 0 & 0 \\ 1 & 0 & 0 \end{bmatrix} \partial_x \begin{bmatrix} \partial_x u \\ \partial_y u \\ \partial_t u \end{bmatrix} + \begin{bmatrix} 0 & 0 & 0 \\ 0 & 0 & 1 \\ 0 & 1 & 0 \end{bmatrix} \partial_y \begin{bmatrix} \partial_x u \\ \partial_y u \\ \partial_t u \end{bmatrix}, \tag{A.8}$$

which means that the characteristic matrix of $\boldsymbol{M}$ is given by:

$$\boldsymbol{M} = \begin{bmatrix} 0 & 0 & 1 & 0 & 0 & 0 \\ 0 & 0 & 0 & 0 & 0 & 0 \\ 1 & 0 & 0 & 0 & 0 & 0 \\ 0 & 0 & 0 & 0 & 0 & 0 \\ 0 & 0 & 0 & 0 & 0 & 1 \\ 0 & 0 & 0 & 0 & 1 & 0 \end{bmatrix}, \tag{A.9}$$

which has 6 linearly independent eigenvectors and is therefore diagonizable. Furthermore, since $\boldsymbol{M} = \boldsymbol{M}^\dagger$, where $\boldsymbol{M}^\dagger$ is the conjugate transpose of $\boldsymbol{M}$, the matrix is Hermitian and system (A.8) is therefore symmetric hyperbolic.

A.2 The hyperbolicity of the 3+1 evolution equations

To analyse the hyperbolicity of the original $3+1$ evolution equations (2.24) and (2.30), we follow the discussion in Gourgoulhon [2012] and express them first in Gaussian coordinates, for which, as stated earlier, the lapse and shift take the following form: $\alpha = 1,\ \beta^i = 0$. In this gauge, Eqs. (2.24) and (2.30) reduce to:

$$\partial_t \gamma_{ij} = -2\, K_{ij}, \tag{A.10}$$

and

$$\partial_t K_{ij} = R_{ij} + K K_{ij} - 2 K_{ia} K^a{}_j, \tag{A.11}$$

respectively, where we have assumed a vacuum spacetime ($T_{\mu\nu} = 0$) for simplicity. We can therefore substitute the extrinsic curvature in Eq. (A.11) with $-\frac{1}{2}\dot{\gamma}_{ij}$ to arrive at the following equation:

$$\ddot{\gamma}_{ij} + 2R_{ij} + \frac{1}{2}\gamma^{ab}\,\dot{\gamma}_{ab}\,\dot{\gamma}_{ij} - 2\gamma^{ab}\,\dot{\gamma}_{ia}\,\dot{\gamma}_{bj} = 0. \tag{A.12}$$

Remember that the Ricci tensor R_{ij} is essentially a second-order partial differential operator acting on the metric γ_{ij} (which can be seen from its definition (2.39)), thus Eq. (A.12) is basically a wave equation for the metric γ_{ij}, with the additional appearance of mixed partial derivatives of the metric due to the presence of R_{ij}. We will not analyse the hyperbolicity of equation (A.12) directly, but make an heuristic argument based on the investigation of the hyperbolicity of the simple 2 dimensional wave equation (A.3) written as a first-order system when adding a single mixed partial derivative.

To do this, we consider the following PDE where we have added a mixed partial derivative ($\partial_x \partial_y u(x,y,t)$) to Eq. (A.3):

$$\partial_t \partial_t u(x,y,t) - \partial_x \partial_x u(x,y,t) - \partial_y \partial_y u(x,y,t) - \partial_x \partial_y u(x,y,t) = 0. \tag{A.13}$$

As above, we define the state vector U and rewrite (A.13) as a first-order system:

$$\partial_t U = \partial_t \begin{bmatrix} \partial_x u \\ \partial_y u \\ \partial_t u \end{bmatrix} = \begin{bmatrix} \partial_t \partial_x u \\ \partial_t \partial_y u \\ \partial_x \partial_x u + \partial_y \partial_y u + \partial_x \partial_y u \end{bmatrix}, \tag{A.14}$$

so that

$$\partial_t \begin{bmatrix} \partial_x u \\ \partial_y u \\ \partial_t u \end{bmatrix} = \begin{bmatrix} 0 & 0 & 1 \\ 0 & 0 & 0 \\ 1 & 0 & 0 \end{bmatrix} \partial_x \begin{bmatrix} \partial_x u \\ \partial_y u \\ \partial_t u \end{bmatrix} + \begin{bmatrix} 0 & 0 & 0 \\ 0 & 0 & 1 \\ 0 & 1 & 0 \end{bmatrix} \partial_y \begin{bmatrix} \partial_x u \\ \partial_y u \\ \partial_t u \end{bmatrix} + \begin{bmatrix} 0 & 0 & 0 \\ 0 & 0 & 0 \\ 1 & 0 & 0 \end{bmatrix} \partial_y \begin{bmatrix} \partial_x u \\ \partial_y u \\ \partial_t u \end{bmatrix} \tag{A.15}$$

The 9×9 characteristic matrix $\boldsymbol{M}$ of the system is:

$$\boldsymbol{M} = \begin{bmatrix} 0 & 0 & 1 & 0 & 0 & 0 & 0 & 0 & 0 \\ 0 & 0 & 0 & 0 & 0 & 0 & 0 & 0 & 0 \\ 1 & 0 & 0 & 0 & 0 & 0 & 0 & 0 & 0 \\ 0 & 0 & 0 & 0 & 0 & 0 & 0 & 0 & 0 \\ 0 & 0 & 0 & 0 & 0 & 1 & 0 & 0 & 0 \\ 0 & 0 & 0 & 0 & 1 & 0 & 0 & 0 & 0 \\ 0 & 0 & 0 & 0 & 0 & 0 & 0 & 0 & 0 \\ 0 & 0 & 0 & 0 & 0 & 0 & 0 & 0 & 0 \\ 0 & 0 & 0 & 0 & 0 & 0 & 1 & 0 & 0 \end{bmatrix}. \tag{A.16}$$

This matrix has the following set of eigenvalues: $\lambda_n\{-1, -1, 1, 1, 0, 0, 0, 0, 0\}$, which are all real. The characteristic matrix, has not, however, a set of 9 independent eigenvectors and therefore cannot be diagonalised. The first-order system (A.15) is therefore only **weakly hyperbolic**. This shows that the simple addition of a mixed partial derivative to the wave equation (A.3) renders the resulting equation weakly hyperbolic. The appearance of mixed partial derivatives of γ_{ij} in (A.12) due to the presence of R_{ij} therefore lies at the heart of the problem that the original $3 + 1$ evolution equations are not strongly hyperbolic. Investigating the type of hyperbolicity is important, as the Cauchy problem for a weakly hyperbolic equation is not well-posed [Kreiss and Lorenz 1989].

A.3 Conservation laws

There is a very important class of hyperbolic PDEs, called *system of conservation laws*. We call a system of n hyperbolic PDEs a system of conservation laws if it can written in the following form:

$$\partial_t w_A + \partial_a F^{aB}{}_A(w) = 0, \tag{A.17}$$

where w_A are the components of the state vector $\boldsymbol{w}$ of *conserved variables* and $F^{aB}{}_A(w)$ the components of the matrix $\boldsymbol{F}(w)$ of *fluxes*, and uppercase latin indices run from 1 to n. The hyperbolicity of the system (A.17) can be analysed by investigating the spectrum of the characteristic matrix $\boldsymbol{M}$, whose components $m^{aB}{}_A$ are defined as follows:

$$\partial_t w_A + m^{aB}{}_A(w)\partial_a w_B + S_A(w) = 0, \tag{A.18}$$

which means we need to bring the system (A.17) in a form that resembles (A.18). This is achieved by using the chain rule for partial derivatives, allowing us to write (A.17) as:

$$\partial_t w_A + \partial_{w_A} F^{aB}(w)\partial_a w_B = 0, \tag{A.19}$$

where $\partial_{w_A} F^{aB}(w)$ is the Jacobian for the system, a (in three dimensions) $3n \times 3n$ block diagonal matrix with three $n \times n$ matrices along the diagonal. For instance, $\partial_{w_A} F^{1B}(w)$ is given by:

$$\partial_{w_A} F^{1B}(w) = \begin{bmatrix} \frac{\partial F^{11}}{\partial w_1} & \cdots & \frac{\partial F^{11}}{\partial w_n} \\ \vdots & \vdots & \vdots \\ \frac{\partial F^{1n}}{\partial w_1} & \cdots & \frac{\partial F^{1n}}{\partial w_n} \end{bmatrix}, \tag{A.20}$$

and the full characteristic matrix of the system (A.17) is given by:

$$\boldsymbol{M} = \left(\begin{array}{c|c|c} \partial_{w_A} F^{1B}(w) & 0 & 0 \\ \hline 0 & \partial_{w_A} F^{2B}(w) & 0 \\ \hline 0 & 0 & \partial_{w_A} F^{3B}(w) \end{array}\right) \tag{A.21}$$

Appendix B

Implementation details of the disc analysis thorn

The values of the twist $\sigma(r)$ and the tilt $\nu(r)$ are computed for radial shells specified by the user in the `.par` file of the simulation. The integrals are performed by summing the values of the integrand for all grid points that fulfil the following inequality:
`shell_radius[i-1]<r[i,j,k]<shell_radius[i]`, where `shell_radius[i]` is the radius of current shell.

In practice, we setup the three components of the angular momentum vector of each computational cell J_x, J_y and J_z as grid functions, and calculate their value at every point on the grid across the processors of the simulation. If a grid point does not fulfil the equality above, the values of the angular momentum vector components are set to 0. The location of the BH is taken into account using information from the `PunctureTracker` thorn, in the sense that the coordinates in Eq. (4.32) are actually given by:

`x = x - pt_loc_x` and similarly for `y` and `z`.

This processor-local routine is scheduled `nradii` times, where `nradii` is the total number of shells. The total angular momentum vector for each shell is subsequently calculated using a global reduction across all processors. The pseudocode of the computation is shown in the algorithm diagram 1. Note that while the pseudocode in diagram 1 displays the calculation of the fluid angular momentum in each shell as a single procedure, the actual implementation is split in various functions due to the scheduling involved.

Algorithm 1 Shell angular momentum calculation

procedure SHELL ANGULAR MOMENTUM
  shell = nradii ▷ shell is the counter for the specified shells
  while shell $\neq 0$ **do**
    for all i,j,k **do** ▷ loop over all grid points
      $x = x - \mathrm{BH}_x$ ▷ setup coordinate system centred about BH
      $y = y - \mathrm{BH}_y$
      $z = z - \mathrm{BH}_z$
      $r = \sqrt{x^2 + y^2 + z^2}$ ▷ radius at grid point
      if shell_radius[shell $-$ 1] $< r$ **and** $r <=$ shell_radius[shell] **then**
        $J_x(i,j,k) = \sqrt{\gamma}\,\alpha(y\,T^{30} - z\,T^{20})$ ▷ Eqs. (4.32) and (4.33)
        $J_y(i,j,k) = \sqrt{\gamma}\,\alpha(z\,T^{10} - x\,T^{30})$
        $J_z(i,j,k) = \sqrt{\gamma}\,\alpha(x\,T^{20} - y\,T^{10})$
      else ▷ For points outside shell, set J_i to 0
        $J_x(i,j,k) = 0$
        $J_y(i,j,k) = 0$
        $J_z(i,j,k) = 0$
      end if
    end for
    J_x[shell] $= \sum_{i,j,k} J_x(i,j,k)$ ▷ Sum over domain to get J_i(shell)
    J_y[shell] $= \sum_{i,j,k} J_y(i,j,k)$
    J_z[shell] $= \sum_{i,j,k} J_z(i,j,k)$

    J_x[shell] $= J_x$[shell]$\Delta x \Delta y \Delta z$ ▷ Multiply by the coarsest grid spacings to perform volume integration
    J_x[shell] $= J_x$[shell]$\Delta x \Delta y \Delta z$
    J_x[shell] $= J_x$[shell]$\Delta x \Delta y \Delta z$

    shell = shell $-$ 1 ▷ Decrement shell counter
  end while
end procedure

One we have calculated the fluid angular momentum components in each shell, J_i[shell], the values of the twist and tilt angles are computed for all spherical shells. The main functions used in the calculation of the angles are presented in pseudocode in the algorithm diagram 2. In the actual numerical implementation, we do not use the inverse cosine to calculate the angles, as the function becomes very inaccurate when the vectors become close to being parallel or anti-parallel, instead we use the `atan2` function which is free of this deficiency. The tilt $\nu(r)$ is then calculated using the following formula:

$$\nu(r) = \tan^{-1}\left[\, |\hat{\mathbf{S}}_{\mathrm{BH}} \times \hat{\mathbf{J}}_{\mathrm{Disc}}(r)| \,,\, \hat{\mathbf{S}}_{\mathrm{BH}} \cdot \hat{\mathbf{J}}_{\mathrm{Disc}}(r) \right] \tag{B.1}$$

Algorithm 2 Functions for tilt and twist angle calculations (see Fig. 4.1 for a visualisation of the various vectors involved)

function UNIT_VECTOR($\mathbf{v}$) ▷ normalise vector
  return $\mathbf{v}/\mathrm{norm}(\mathbf{v})$
end function
function ANGLE($\mathbf{v1}$,$\mathbf{v2}$) ▷ calculate angle between two vectors
  $\mathbf{v1} = \mathrm{unit\_vector}(\mathbf{v1})$
  $\mathbf{v2} = \mathrm{unit\_vector}(\mathbf{v2})$
  $\mathrm{a} = \mathrm{norm}(\mathbf{v1} \times \mathbf{v2})$
  $\mathrm{b} = \mathbf{v1} \cdot \mathbf{v2}$
  $\mathrm{angle} = \mathrm{atan2}(\mathrm{a}, \mathrm{b})$
  return angle
end function
function SIGNED_ANGLE($\mathbf{v1}$,$\mathbf{v2}$,$\mathbf{v3}$) ▷ calculate signed angle between vectors $\mathbf{v1}$ and $\mathbf{v2}$, ranging from 0 to 2π
  $\mathbf{v1} = \mathrm{unit\_vector}(\mathbf{v1})$
  $\mathbf{v2} = \mathrm{unit\_vector}(\mathbf{v2})$
  $\mathbf{v3} = \mathrm{unit\_vector}(\mathbf{v3})$
  $\mathrm{a} = \mathrm{norm}(\mathbf{v1} \times \mathbf{v2})$
  $\mathrm{b} = \mathbf{v1} \cdot \mathbf{v2}$
  $\mathrm{angle} = \mathrm{angle}(\mathbf{v1}, \mathbf{v2})$
  $\mathrm{sign} = \mathbf{v3} \cdot (\mathbf{v1} \times \mathbf{v2})$
  if $\mathrm{sign} < 0$ **then**
    $\mathrm{angle} = -\mathrm{angle} + 2\pi$
  end if
  return angle
end function
function BH_EQ_PLANE_PROJECT($\mathbf{v1}$,$\mathbf{n}$) ▷ project vector $\mathbf{v1}$ onto the BH equatorial plane
  $\mathbf{v} = \mathbf{v1} - (\mathbf{v1} \cdot \mathbf{n})/\mathrm{norm}(\mathbf{n})^2\mathbf{n}$
  return $\mathbf{v}$
end function
function TWIST($\mathbf{S}$,$\mathbf{J}$[shell]) ▷ calculate the twist angle
  $\mathbf{R} = [[0, -1, 0], [1, 0, 0], [0, 0, 1]]$
  $\mathbf{S}_{xy} = [\mathrm{S}_x, \mathrm{S}_y, 0]$
  $\mathbf{S}_{xy-90} = \mathbf{R} \cdot \mathbf{S}_{xy}$
  $\mathrm{twist} = \mathrm{signed\_angle}(\mathbf{S} \times \mathbf{S}_{xy-90}, \mathrm{BH\_eq\_plane\_project}(\mathbf{J}[\mathrm{shell}], \mathbf{S}), \mathbf{S})$
  return twist
end function

where the hat indicates unit vectors.

For the twist $\sigma(r)$, we need to be more careful. In the formula above, we implicitly assume that $\nu(r) < \pi\,, \forall\, t$, because Eq. (B.1) will always return

angles $\leq \pi$. Although it does not generally make much sense to consider angles $\geq \pi$ between two 3D vectors, because there is an up and down direction, we are nevertheless interested in directional (signed) angles $\geq \pi$ for the twist σ. The reason is that we want to be able to track cumulative twists larger than π. In order to calculate the directional angle $\sigma(r)$ from the reference vector $\mathbf{S}_{\mathrm{BH}} \times \mathbf{S}_{\mathrm{xy-90}}$ to the target vector $\mathrm{P}(\mathbf{J}_{\mathrm{Disc}}(r), \mathbf{S}_{\mathrm{BH}})$ in a fixed sense of rotation, we need a third reference vector that always lies above the plane spanned by the two original vectors. As the plane in which both vectors live is constructed to be the equatorial plane of the BH, we can therefore choose this vector to be $\mathbf{S}_{\mathrm{BH}}$. This information allows us (because the cross product contains this information in the sign it returns) to calculate twist angles in the range $[0, 2\pi]$.

Bibliography

[1] J. Abadie, B. P. Abbott, R. Abbott, M. Abernathy, T. Accadia, F. Acernese, C. Adams, R. Adhikari, P. Ajith, B. Allen, and et al. "Topical Review: Predictions for the rates of compact binary coalescences observable by ground-based gravitational-wave detectors." In: *Class. Quantum Grav.* 27.17 (Sept. 2010), p. 173001.

[2] B. P. Abbott, R. Abbott, T. D. Abbott, M. R. Abernathy, F. Acernese, K. Ackley, C. Adams, T. Adams, P. Addesso, R. X. Adhikari, and et al. "Observation of Gravitational Waves from a Binary Black Hole Merger." In: *Physical Review Letters* 116.6, 061102 (Feb. 2016), p. 061102. arXiv: 1602.03837 [gr-qc].

[3] M. A. Abramowicz, M. Calvani, and L. Nobili. "Runaway instability in accretion disks orbiting black holes." In: *Nature* 302 (Apr. 1983), pp. 597–599.

[4] M. A. Abramowicz, W. Kluźniak, J. E. McClintock, and R. A. Remillard. "The Importance of Discovering a 3:2 Twin-Peak Quasi-periodic Oscillation in an Ultraluminous X-Ray Source, or How to Solve the Puzzle of Intermediate-Mass Black Holes." In: *Astrophys. J. Lett.* 609 (July 2004), pp. L63–L65. eprint: astro-ph/0402012.

[5] F. C. Adams, S. P. Ruden, and F. H. Shu. "Eccentric gravitational instabilities in nearly Keplerian disks." In: *Astrophys. J.* 347 (Dec. 1989), pp. 959–976.

[6] R. X. Adhikari. "Gravitational radiation detection with laser interferometry." In: *Reviews of Modern Physics* 86 (Jan. 2014), pp. 121–151. arXiv: 1305.5188 [gr-qc].

[7] J. Adsuara, I. Cordero-Carrión, P. Cerdá-Durán, V. Mewes, and M. Á. Aloy. "Optimal Scheduled Relaxation Jacobi method." In: *Submitted to Communications in Computational Physics* (2016).

[8] M. Alcubierre. "Hyperbolic slicings of spacetime: singularity avoidance and gauge shocks." In: *Classical and Quantum Gravity* 20 (Feb. 2003), pp. 607–623. eprint: gr-qc/0210050.

[9] M. Alcubierre. *Introduction to 3+1 Numerical Relativity*. Oxford University Press, 2008.

[10] M. Alcubierre and B. Brügmann. "Simple excision of a black hole in 3+1 numerical relativity." In: *Phys. Rev. D* 63.10, 104006 (May 2001), p. 104006. eprint: gr-qc/0008067.

[11] M. Alcubierre, B. Brügmann, P. Diener, M. Koppitz, D. Pollney, E. Seidel, and R. Takahashi. "Gauge conditions for long-term numerical black hole evolutions without excision." In: *Phys. Rev. D* 67.8, 084023 (Apr. 2003), p. 084023. eprint: gr-qc/0206072.

[12] M. Alcubierre, B. Brügmann, T. Dramlitsch, J. A. Font, P. Papadopoulos, E. Seidel, N. Stergioulas, and R. Takahashi. "Towards a stable numerical evolution of strongly gravitating systems in general relativity: The conformal treatments." In: *Phys. Rev. D* 62.4, 044034 (Aug. 2000), p. 044034. eprint: gr-qc/0003071.

[13] D. Alic, C. Bona-Casas, C. Bona, L. Rezzolla, and C. Palenzuela. "Conformal and covariant formulation of the Z4 system with constraint-violation damping." In: *Phys. Rev. D* 85.6, 064040 (Mar. 2012), p. 064040. arXiv: 1106.2254 [gr-qc].

[14] D. Alic, L. Rezzolla, I. Hinder, and P. Mösta. "Dynamical damping terms for symmetry-seeking shift conditions." In: *Classical and Quantum Gravity* 27.24, 245023 (Dec. 2010), p. 245023. arXiv: 1008.2212 [gr-qc].

[15] M. A. Aloy, J. M. Ibáñez, J. M. Martı/, and E. Müller. "GENESIS: A High-Resolution Code for Three-dimensional Relativistic Hydrodynamics." In: *Astrophys. J. Suppl. Ser.* 122 (May 1999), pp. 151–166. eprint: astro-ph/9903352.

[16] M. A. Aloy, H.-T. Janka, and E. Müller. "Relativistic outflows from remnants of compact object mergers and their viability for short gamma-ray bursts." In: *Astron. Astrophys.* 436 (June 2005), pp. 273–311. eprint: astro-ph/0408291.

[17] P. Anninos, D. Bernstein, S. Brandt, J. Libson, J. Massó, E. Seidel, L. Smarr, W.-M. Suen, and P. Walker. "Dynamics of Apparent and Event Horizons." In: *Physical Review Letters* 74 (Jan. 1995), pp. 630–633. eprint: gr-qc/9403011.

[18] R. Arnowitt, S. Deser, and C. W. Misner. "Republication of: The dynamics of general relativity." In: *General Relativity and Gravitation* 40 (Sept. 2008), pp. 1997–2027. eprint: gr-qc/0405109.

[19] A. Ashtekar, C. Beetle, and S. Fairhurst. "Isolated horizons: a generalization of black hole mechanics." In: *Classical and Quantum Gravity* 16 (Feb. 1999), pp. L1–L7. eprint: gr-qc/9812065.

[20] A. Ashtekar and B. Krishnan. "Dynamical horizons and their properties." In: *Phys. Rev. D* 68.10, 104030 (Nov. 2003), p. 104030. eprint: gr-qc/0308033.

[21] A. Ashtekar and B. Krishnan. "Isolated and Dynamical Horizons and Their Applications." In: *Living Reviews in Relativity* 7 (Dec. 2004). eprint: gr-qc/0407042.

[22] M. Babiuc, B. Szilágyi, I. Hawke, and Y. Zlochower. "Gravitational wave extraction based on Cauchy characteristic extraction and characteristic evolution." In: *Classical and Quantum Gravity* 22 (Dec. 2005), pp. 5089–5107. eprint: gr-qc/0501008.

[23] L. Baiotti, R. de Pietri, G. M. Manca, and L. Rezzolla. "Accurate simulations of the dynamical bar-mode instability in full general relativity." In: *Phys. Rev. D* 75.4, 044023 (Feb. 2007), p. 044023. eprint: astro-ph/0609473.

[24] L. Baiotti, I. Hawke, P. J. Montero, F. Löffler, L. Rezzolla, N. Stergioulas, J. A. Font, and E. Seidel. "Three-dimensional relativistic simulations of rotating neutron-star collapse to a Kerr black hole." In: *Phys. Rev. D* 71.2, 024035 (Jan. 2005), p. 024035. eprint: gr-qc/0403029.

[25] L. Baiotti, I. Hawke, and L. Rezzolla. "On the gravitational radiation from the collapse of neutron stars to rotating black holes." In: *Classical and Quantum Gravity* 24 (June 2007), S187–S206. eprint: gr-qc/0701043.

[26] J. G. Baker, J. Centrella, D.-I. Choi, M. Koppitz, and J. van Meter. "Gravitational-Wave Extraction from an Inspiraling Configuration of Merging Black Holes." In: *Physical Review Letters* 96.11, 111102 (Mar. 2006), p. 111102. eprint: gr-qc/0511103.

[27] J. G. Baker, J. R. van Meter, S. T. McWilliams, J. Centrella, and B. J. Kelly. "Consistency of Post-Newtonian Waveforms with Numerical Relativity." In: *Physical Review Letters* 99.18, 181101 (Nov. 2007), p. 181101. eprint: gr-qc/0612024.

[28] J. Baker, M. Campanelli, and C. O. Lousto. "The Lazarus project: A pragmatic approach to binary black hole evolutions." In: *Phys. Rev. D* 65.4, 044001 (Feb. 2002), p. 044001. eprint: gr-qc/0104063.

[29] S. A. Balbus. "Enhanced Angular Momentum Transport in Accretion Disks." In: *Annu. Rev. Astron. Astrophys.* 41 (2003), pp. 555–597. eprint: astro-ph/0306208.

[30] S. A. Balbus and J. F. Hawley. "A powerful local shear instability in weakly magnetized disks. I - Linear analysis. II - Nonlinear evolution." In: *Astrophys. J.* 376 (July 1991), pp. 214–233.

[31] F. Banyuls, J. A. Font, J. M. Ibáñez, J. M. Martí, and J. A. Miralles. "Numerical {3 + 1} General Relativistic Hydrodynamics: A Local Characteristic Approach." In: *Astrophys. J.* 476 (Feb. 1997), pp. 221–231.

[32] J. M. Bardeen and J. A. Petterson. "The Lense-Thirring Effect and Accretion Disks around Kerr Black Holes." In: *Astrophys. J. Lett.* 195 (Jan. 1975), p. L65.

[33] T. W. Baumgarte, P. J. Montero, I. Cordero-Carrión, and E. Müller. "Numerical relativity in spherical polar coordinates: Evolution calculations with the BSSN formulation." In: *Phys. Rev. D* 87.4, 044026 (Feb. 2013), p. 044026. arXiv: 1211.6632 [gr-qc].

[34] T. W. Baumgarte and S. L. Shapiro. "Numerical integration of Einstein's field equations." In: *Phys. Rev. D* 59.2, 024007 (Jan. 1999), p. 024007. eprint: gr-qc/9810065.

[35] T. W. Baumgarte and S. L. Shapiro. *Numerical Relativity: Solving Einstein's Equations on the Computer*. June 2010.

[36] K. Belczynski, M. Dominik, T. Bulik, R. O'Shaughnessy, C. Fryer, and D. E. Holz. "The Effect of Metallicity on the Detection Prospects for Gravitational Waves." In: *Astrophys. J. Lett.* 715 (June 2010), pp. L138–L141. arXiv: 1004.0386 [astro-ph.HE].

[37] K. Belczynski, R. E. Taam, E. Rantsiou, and M. van der Sluys. "Black Hole Spin Evolution: Implications for Short-Hard Gamma-Ray Bursts and Gravitational Wave Detection." In: *Astrophys. J.* 682, 474-486 (July 2008), pp. 474–486. eprint: astro-ph/0703131.

[38] K. Belczynski, G. Wiktorowicz, C. L. Fryer, D. E. Holz, and V. Kalogera. "Missing Black Holes Unveil the Supernova Explosion Mechanism." In: *Astrophys. J.* 757, 91 (Sept. 2012), p. 91. arXiv: 1110.1635.

[39] T. M. Belloni and L. Stella. "Fast Variability from Black-Hole Binaries." In: *Space Science Reviews* 183.1 (2014), pp. 43–60. ISSN: 1572-9672.

[40] M. J. Berger and J. Oliger. "Adaptive Mesh Refinement for Hyperbolic Partial Differential Equations." In: *Journal of Computational Physics* 53 (Mar. 1984), pp. 484–512.

[41] E. Berti, V. Cardoso, and C. M. Will. "Gravitational-wave spectroscopy of massive black holes with the space interferometer LISA." In: *Phys. Rev. D* 73.6, 064030 (Mar. 2006), p. 064030. eprint: gr-qc/0512160.

[42] H. Beyer and O. Sarbach. "Well-posedness of the Baumgarte-Shapiro-Shibata-Nakamura formulation of Einstein's field equations." In: *Phys. Rev. D* 70.10, 104004 (Nov. 2004), p. 104004. eprint: gr-qc/0406003.

[43] O. M. Blaes. "Stabilization of non-axisymmetric instabilities in a rotating flow by accretion on to a central black hole." In: *Mon. Not. R. Astron. Soc.* 227 (Aug. 1987), pp. 975–992.

[44] L. Blanchet, B. R. Iyer, C. M. Will, and A. G. Wiseman. "Gravitational waveforms from inspiralling compact binaries to second-post-Newtonian order." In: *Classical and Quantum Gravity* 13 (Apr. 1996), pp. 575–584. eprint: gr-qc/9602024.

[45] C. Bona, T. Ledvinka, C. Palenzuela, and M. Žáček. "General-covariant evolution formalism for numerical relativity." In: *Phys. Rev. D* 67.10, 104005 (May 2003), p. 104005. eprint: gr-qc/0302083.

[46] C. Bona, J. Massó, E. Seidel, and J. Stela. "New Formalism for Numerical Relativity." In: *Physical Review Letters* 75 (July 1995), pp. 600–603. eprint: gr-qc/9412071.

[47] C. Bona and C. Palenzuela. "Dynamical shift conditions for the Z4 and BSSN formalisms." In: *Phys. Rev. D* 69.10, 104003 (May 2004), p. 104003. eprint: gr-qc/0401019.

[48] S. Bonazzola and E. Gourgoulhon. "A virial identity applied to relativistic stellar models." In: *Classical and Quantum Gravity* 11 (July 1994), pp. 1775–1784.

[49] S. Bonazzola, E. Gourgoulhon, P. Grandclément, and J. Novak. "Constrained scheme for the Einstein equations based on the Dirac gauge and spherical coordinates." In: *Phys. Rev. D* 70.10, 104007 (Nov. 2004), p. 104007. eprint: gr-qc/0307082.

[50] S. Brandt and B. Brügmann. "A Simple Construction of Initial Data for Multiple Black Holes." In: *Physical Review Letters* 78 (May 1997), pp. 3606–3609. eprint: gr-qc/9703066.

[51] D. R. Brill and R. W. Lindquist. "Interaction Energy in Geometrostatics." In: *Physical Review* 131 (July 1963), pp. 471–476.

[52] D. Brown, P. Diener, O. Sarbach, E. Schnetter, and M. Tiglio. "Turducken-ening black holes: An analytical and computational study." In: *Phys. Rev. D* 79.4, 044023 (Feb. 2009), p. 044023. arXiv: 0809.3533 [gr-qc].

[53] B. Brügmann, J. A. González, M. Hannam, S. Husa, and U. Sperhake. "Exploring black hole superkicks." In: *Phys. Rev. D* 77.12, 124047 (June 2008), p. 124047. arXiv: 0707.0135 [gr-qc].

[54] B. Brügmann, W. Tichy, and N. Jansen. "Numerical Simulation of Orbiting Black Holes." In: *Physical Review Letters* 92.21, 211101 (May 2004), p. 211101. eprint: gr-qc/0312112.

[55] `Cactus Computational Toolkit`. http://www.cactuscode.org/.

[56] G. Allen, T. Goodale, G. Lanfermann, T. Radke, D. Rideout, and J. Thornburg. *Cactus Users' Guide*. 2011. URL: http://www.cactuscode.org/Guides/Stable/UsersGuide/UsersGuideStable.pdf.

[57] M. Campanelli, C. O. Lousto, P. Marronetti, and Y. Zlochower. "Accurate Evolutions of Orbiting Black-Hole Binaries without Excision." In: *Physical Review Letters* 96.11, 111101 (Mar. 2006), p. 111101. eprint: gr-qc/0511048.

[58] M. Campanelli, C. O. Lousto, and Y. Zlochower. "Spinning-black-hole binaries: The orbital hang-up." In: *Phys. Rev. D* 74.4, 041501 (Aug. 2006), p. 041501. eprint: gr-qc/0604012.

[59] M. Campanelli, C. O. Lousto, Y. Zlochower, B. Krishnan, and D. Merritt. "Spin flips and precession in black-hole-binary mergers." In: *Phys. Rev. D* 75.6, 064030 (Mar. 2007), p. 064030. eprint: gr-qc/0612076.

[60] `Carpet`. http://carpetcode.org.

[61] S. Chandrasekhar. "The Stability of Non-Dissipative Couette Flow in Hydromagnetics." In: *Proceedings of the National Academy of Science* 46 (Feb. 1960), pp. 253–257.

[62] Y. Choquet-Bruhat. "Théorème d'existence pour certains systèmes d'équations aux dérivées partielles non linéaires." In: *Acta Mathematica, Volume 88, Issue 1, pp 141-225* 88 (1952).

[63] Y. Choquet-Bruhat and T. Ruggeri. "Hyperbolicity of the 3+1 system of Einstein equations." In: *Communications in Mathematical Physics* 89 (June 1983), pp. 269–275.

[64] D. Christodoulou. "Reversible and Irreversible Transformations in Black-Hole Physics." In: *Physical Review Letters* 25 (Nov. 1970), pp. 1596–1597.

[65] D. M. Christodoulou and R. Narayan. "The stability of accretion tori. IV - Fission and fragmentation of slender, self-gravitating annuli." In: *Astrophys. J.* 388 (Apr. 1992), pp. 451–466.

[66] P. Colella and P. R. Woodward. "The Piecewise Parabolic Method (PPM) for Gas-Dynamical Simulations." In: *Journal of Computational Physics* 54 (Sept. 1984), pp. 174–201.

[67] G. B. Cook, M. W. Choptuik, M. R. Dubal, S. Klasky, R. A. Matzner, and S. R. Oliveira. "Three-dimensional initial data for the collision of two black holes." In: *Phys. Rev. D* 47 (Feb. 1993), pp. 1471–1490.

[68] I. Cordero-Carrión, P. Cerdá-Durán, H. Dimmelmeier, J. L. Jaramillo, J. Novak, and E. Gourgoulhon. "Improved constrained scheme for the Einstein equations: An approach to the uniqueness issue." In: *Phys. Rev. D* 79.2, 024017 (Jan. 2009), p. 024017. arXiv: 0809.2325 [gr-qc].

[69] R. Courant and D. Hilbert. *Methods of mathematical physics. Vol. II: Partial differential equations.(Vol. II by R. Courant.)* 1962.

[70] F. Daigne and J. A. Font. "The runaway instability of thick discs around black holes - II. Non-constant angular momentum discs." In: *Mon. Not. R. Astron. Soc.* 349 (Apr. 2004), pp. 841–868. eprint: astro-ph/0311618.

[71] F. Daigne and R. Mochkovitch. "Gamma-ray bursts and the runaway instability of thick discs around black holes." In: *Mon. Not. R. Astron. Soc.* 285 (Mar. 1997), pp. L15–L19.

[72] G. Darmois. "Les équations de la gravitation einsteinienne." In: *Mémorial des sciences mathématiques* 25 (1927), pp. 1–48.

[73] M. Demianski and P. B. Ivanov. "The dynamics of twisted accretion disc around a Kerr black hole." In: *Astron. Astrophys.* 324 (Aug. 1997), pp. 829–834.

[74] K. A. Dennison, T. W. Baumgarte, and P. J. Montero. "Trumpet Slices in Kerr Spacetimes." In: *Physical Review Letters* 113.26, 261101 (Dec. 2014), p. 261101. arXiv: 1409.1887 [gr-qc].

[75] P. A. M. Dirac. "Forms of Relativistic Dynamics." In: *Rev. Mod. Phys.* 21.3 (July 1949), pp. 392–399.

[76] M. Dominik, K. Belczynski, C. Fryer, D. E. Holz, E. Berti, T. Bulik, I. Mandel, and R. O'Shaughnessy. "Double Compact Objects. II. Cosmological Merger Rates." In: *Astrophys. J.* 779, 72 (Dec. 2013), p. 72.

[77] M. Dominik, E. Berti, R. O'Shaughnessy, I. Mandel, K. Belczynski, C. Fryer, D. E. Holz, T. Bulik, and F. Pannarale. "Double Compact Objects III: Gravitational-wave Detection Rates." In: *Astrophys. J.* 806, 263 (June 2015), p. 263. arXiv: 1405.7016 [astro-ph.HE].

[78] R. Donat and A. Marquina. "Capturing Shock Reflections: An Improved Flux Formula." In: *J. Comp. Phys.* 125 (Apr. 1996), pp. 42–58.

[79] O. Dreyer, B. Krishnan, D. Shoemaker, and E. Schnetter. "Introduction to isolated horizons in numerical relativity." In: *Phys. Rev. D* 67.2, 024018 (Jan. 2003), p. 024018. eprint: gr-qc/0206008.

[80] B. Einfeldt. "On Godunov-type methods for gas dynamics." In: *SIAM Journal on Numerical Analysis* 25.2 (1988), pp. 294–318.

[81] `Einstein Toolkit`. http://einsteintoolkit.org/.

[82] A. Einstein. "Die Feldgleichungen der Gravitation." In: *Sitzungsberichte der Königlich Preußischen Akademie der Wissenschaften (Berlin), Seite 844-847.* (1915).

[83] A. Einstein. "Die Grundlage der allgemeinen Relativitätstheorie." In: *Annalen der Physik* 354 (1916), pp. 769–822.

[84] A. Einstein. "Über Gravitationswellen." In: *Sitzungsberichte der Königlich Preußischen Akademie der Wissenschaften (Berlin), Seite 154-167.* (1918).

[85] T. Ertl, H.-T. Janka, S. E. Woosley, T. Sukhbold, and M. Ugliano. "A Two-parameter Criterion for Classifying the Explodability of Massive Stars by the Neutrino-driven Mechanism." In: *Astrophys. J.* 818, 124 (Feb. 2016), p. 124. arXiv: 1503.07522 [astro-ph.SR].

[86] Z. B. Etienne, J. A. Faber, Y. T. Liu, S. L. Shapiro, K. Taniguchi, and T. W. Baumgarte. "Fully general relativistic simulations of black hole-neutron star mergers." In: *Phys. Rev. D* 77.8, 084002 (Apr. 2008), p. 084002. arXiv: 0712.2460.

[87] J. A. Faber, T. W. Baumgarte, Z. B. Etienne, S. L. Shapiro, and K. Taniguchi. "Relativistic hydrodynamics in the presence of puncture black holes." In: *Phys. Rev. D* 76.10, 104021 (Nov. 2007), p. 104021. arXiv: 0708.2436 [gr-qc].

[88] J. A. Faber and F. A. Rasio. "Binary Neutron Star Mergers." In: *Living Reviews in Relativity* 15 (July 2012). arXiv: 1204.3858 [gr-qc].

[89] B. D. Farris, P. Duffell, A. I. MacFadyen, and Z. Haiman. "Binary Black Hole Accretion from a Circumbinary Disk: Gas Dynamics inside the Central Cavity." In: *Astrophys. J.* 783, 134 (Mar. 2014), p. 134. arXiv: 1310.0492 [astro-ph.HE].

[90] A. E. Fischer and J. E. Marsden. "The Einstein Equations of Evolution-A Geometric Approach." In: *J. Math. Phys.* 13 (Apr. 1972), pp. 546–568.

[91] É. É. Flanagan and S. A. Hughes. "Measuring gravitational waves from binary black hole coalescences. I. Signal to noise for inspiral, merger, and ringdown." In: *Phys. Rev. D* 57 (Apr. 1998), pp. 4535–4565. eprint: gr-qc/9701039.

[92] J. A. Font. "Numerical Hydrodynamics and Magnetohydrodynamics in General Relativity." In: *Living Reviews in Relativity* 11 (Sept. 2008).

[93] J. A. Font and F. Daigne. "The runaway instability of thick discs around black holes - I. The constant angular momentum case." In: *Mon. Not. R. Astron. Soc.* 334 (Aug. 2002), pp. 383–400. eprint: astro-ph/0203403.

[94] F. Foucart. "Black-hole-neutron-star mergers: Disk mass predictions." In: *Phys. Rev. D* 86.12, 124007 (Dec. 2012), p. 124007. arXiv: 1207.6304 [astro-ph.HE].

[95] F. Foucart, M. B. Deaton, M. D. Duez, L. E. Kidder, I. MacDonald, C. D. Ott, H. P. Pfeiffer, M. A. Scheel, B. Szilagyi, and S. A. Teukolsky. "Black-hole-neutron-star mergers at realistic mass ratios: Equation of state and spin orientation effects." In: *Phys. Rev. D* 87.8, 084006 (Apr. 2013), p. 084006. arXiv: 1212.4810 [gr-qc].

[96] F. Foucart, M. B. Deaton, M. D. Duez, E. O'Connor, C. D. Ott, R. Haas, L. E. Kidder, H. P. Pfeiffer, M. A. Scheel, and B. Szilagyi. "Neutron star-black hole mergers with a nuclear equation of state and neutrino cooling: Dependence in the binary parameters." In: *Phys. Rev. D* 90.2, 024026 (July 2014), p. 024026. arXiv: 1405.1121 [astro-ph.HE].

[97] F. Foucart, M. D. Duez, L. E. Kidder, and S. A. Teukolsky. "Black hole-neutron star mergers: Effects of the orientation of the black hole spin." In: *Phys. Rev. D* 83.2, 024005 (Jan. 2011), p. 024005. arXiv: 1007.4203 [astro-ph.HE].

[98] F. Foucart and D. Lai. "Evolution of linear warps in accretion discs and applications to protoplanetary discs in binaries." In: *Mon. Not. R. Astron. Soc.* 445 (Dec. 2014), pp. 1731–1744. arXiv: 1406.3331 [astro-ph.EP].

[99] P. C. Fragile and P. Anninos. "Hydrodynamic Simulations of Tilted Thick-Disk Accretion onto a Kerr Black Hole." In: *Astrophys. J.* 623 (Apr. 2005), pp. 347–361. eprint: astro-ph/0403356.

[100] P. C. Fragile, O. M. Blaes, P. Anninos, and J. D. Salmonson. "Global General Relativistic Magnetohydrodynamic Simulation of a Tilted Black Hole Accretion Disk." In: *Astrophys. J.* 668 (Oct. 2007), pp. 417–429. arXiv: 0706.4303.

[101] P. C. Fragile, G. J. Mathews, and J. R. Wilson. "Bardeen-Petterson Effect and Quasi-periodic Oscillations in X-Ray Binaries." In: *Astrophys. J.* 553 (June 2001), pp. 955–959. eprint: astro-ph/0007478.

[102] T. Fragos, M. Tremmel, E. Rantsiou, and K. Belczynski. "Black Hole Spin-Orbit Misalignment in Galactic X-ray Binaries." In: *Astrophys. J. Lett.* 719 (Aug. 2010), pp. L79–L83. arXiv: 1001.1107 [astro-ph.HE].

[103] A. Franchini, G. Lodato, and S. Facchini. "Lense-Thirring precession around supermassive black holes during tidal disruption events." In: *Mon. Not. R. Astron. Soc.* 455 (Jan. 2016), pp. 1946–1956. arXiv: 1510.04879 [astro-ph.HE].

[104] H. Friedrich. "Hyperbolic reductions for Einstein's equations." In: *Classical and Quantum Gravity* 13 (June 1996), pp. 1451–1469.

[105] C. L. Fryer, K. Belczynski, G. Wiktorowicz, M. Dominik, V. Kalogera, and D. E. Holz. "Compact Remnant Mass Function: Dependence on the Explosion Mechanism and Metallicity." In: *Astrophys. J.* 749, 91 (Apr. 2012), p. 91. arXiv: 1110.1726 [astro-ph.SR].

[106] C. L. Fryer, S. E. Woosley, M. Herant, and M. B. Davies. "Merging White Dwarf/Black Hole Binaries and Gamma-Ray Bursts." In: *Astrophys. J.* 520 (Aug. 1999), pp. 650–660. eprint: astro-ph/9808094.

[107] W. Fu and D. Lai. "Papaloizou-Pringle instability of magnetized accretion tori." In: *Mon. Not. R. Astron. Soc.* 410 (Jan. 2011), pp. 1617–1630. arXiv: 1006.3824 [astro-ph.HE].

[108] F. Galeazzi, W. Kastaun, L. Rezzolla, and J. A. Font. "Implementation of a simplified approach to radiative transfer in general relativity." In: *Phys. Rev. D* 88.6, 064009 (Sept. 2013), p. 064009. arXiv: 1306.4953 [gr-qc].

[109] D. Garfinkle, C. Gundlach, and D. Hilditch. "Comments on Bona Massó-type slicing conditions in long-term black hole evolutions." In: *Classical and Quantum Gravity* 25.7, 075007 (Apr. 2008), p. 075007. arXiv: 0707.0726 [gr-qc].

[110] B. Giacomazzo and R. Perna. "Formation of Stable Magnetars from Binary Neutron Star Mergers." In: *Astrophys. J. Lett.* 771, L26 (July 2013), p. L26. arXiv: 1306.1608 [astro-ph.HE].

[111] S. K. Godunov. "A difference method for numerical calculation of discontinuous solutions of the equations of hydrodynamics." In: *Mat. Sb.* 89.3 (1959), pp. 271–306.

[112] R. Gold and B. Brügmann. "Eccentric black hole mergers and zoom-whirl behavior from elliptic inspirals to hyperbolic encounters." In: *Phys. Rev. D* 88.6, 064051 (Sept. 2013), p. 064051. arXiv: 1209.4085 [gr-qc].

[113] R. Gold, V. Paschalidis, Z. B. Etienne, S. L. Shapiro, and H. P. Pfeiffer. "Accretion disks around binary black holes of unequal mass: General relativistic magnetohydrodynamic simulations near decoupling." In: *Phys. Rev. D* 89.6, 064060 (Mar. 2014), p. 064060. arXiv: 1312.0600 [astro-ph.HE].

[114] T. Goodale, G. Allen, G. Lanfermann, J. Massó, T. Radke, E. Seidel, and J. Shalf. "High Performance Computing for Computational Science — VECPAR 2002: 5th International Conference Porto, Portugal, June 26–28, 2002 Selected Papers and Invited Talks." In: ed. by J. M. L. M. Palma, A. A. Sousa, J. Dongarra, and V. Hernández. Berlin, Heidelberg: Springer Berlin Heidelberg, 2003. Chap. The Cactus Framework and Toolkit: Design and Applications, pp. 197–227. ISBN: 978-3-540-36569-3.

[115] J. Goodman, R. Narayan, and P. Goldreich. "The stability of accretion tori. II - Non-linear evolution to discrete planets." In: *Mon. Not. R. Astron. Soc.* 225 (Apr. 1987), pp. 695–711.

[116] J. Goodman and R. R. Rafikov. "Planetary Torques as the Viscosity of Protoplanetary Disks." In: *Astrophys. J.* 552 (May 2001), pp. 793–802. eprint: astro-ph/0010576.

[117] E. Gourgoulhon, ed. *3+1 Formalism in General Relativity*. Vol. 846. Lecture Notes in Physics, Springer. 2012.

[118] E. Gourgoulhon and S. Bonazzola. "A formulation of the virial theorem in general relativity." In: *Classical and Quantum Gravity* 11 (Feb. 1994), pp. 443–452.

[119] C. Gundlach and J. M. Martín-García. "Well-posedness of formulations of the Einstein equations with dynamical lapse and shift conditions." In: *Phys. Rev. D* 74.2, 024016 (July 2006), p. 024016. eprint: gr-qc/0604035.

[120] I. Hachisu, J. E. Tohline, and Y. Eriguchi. "Fragmentation of rapidly rotating gas clouds. I - A universal criterion for fragmentation." In: *Astrophys. J.* 323 (Dec. 1987), pp. 592–613.

[121] M. Hannam, S. Husa, D. Pollney, B. Brügmann, and N. Ó. Murchadha. "Geometry and Regularity of Moving Punctures." In: *Physical Review Letters* 99.24, 241102 (Dec. 2007), p. 241102. eprint: gr-qc/0606099.

[122] A. Harten, B. Engquist, S. Osher, and S. R. Chakravarthy. "Uniformly high order accurate essentially non-oscillatory schemes, III." In: *Upwind and High-Resolution Schemes*. Springer, 1987, pp. 218–290.

[123] A. Harten, P. D. Lax, and B. v. Leer. "On upstream differencing and Godunov-type schemes for hyperbolic conservation laws." In: *SIAM review* 25.1 (1983), pp. 35–61.

[124] S. W. Hawking and G. F. R. Ellis. *The Large Scale Structure of Space-Time*. 1975.

[125] J. F. Hawley. "Non-linear evolution of a non-axisymmetric disc instability." In: *Mon. Not. R. Astron. Soc.* 225 (Apr. 1987), pp. 677–694.

[126] J. F. Hawley. "Three-dimensional simulations of black hole tori." In: *Astrophys. J.* 381 (Nov. 1991), pp. 496–507.

[127] M. H. M. Heemskerk, J. C. Papaloizou, and G. J. Savonije. "Non-linear development of M = 1 instabilities in a self-gravitating gaseous disc." In: *Astron. Astrophys.* 260 (July 1992), pp. 161–174.

[128] A. Heger, N. Langer, and S. E. Woosley. "Presupernova Evolution of Rotating Massive Stars. I. Numerical Method and Evolution of the Internal Stellar Structure." In: *Astrophys. J.* 528 (Jan. 2000), pp. 368–396. eprint: astro-ph/9904132.

[129] T. Heinemann and J. C. B. Papaloizou. "A weakly non-linear theory for spiral density waves excited by accretion disc turbulence." In: *Mon. Not. R. Astron. Soc.* 419 (Jan. 2012), pp. 1085–1096. arXiv: 1109.2907 [astro-ph.EP].

[130] K. B. Henisey, O. M. Blaes, and P. C. Fragile. "Variability from Non-axisymmetric Fluctuations Interacting with Standing Shocks in Tilted Black Hole Accretion Disks." In: *Astrophys. J.* 761, 18 (Dec. 2012), p. 18. arXiv: 1211.2273 [astro-ph.HE].

[131] S. Hild. "Beyond the second generation of laser-interferometric gravitational wave observatories." In: *Classical and Quantum Gravity* 29.12, 124006 (June 2012), p. 124006. arXiv: 1111.6277 [gr-qc].

[132] I. Hinder. "The current status of binary black hole simulations in numerical relativity." In: *Classical and Quantum Gravity* 27.11, 114004 (June 2010), p. 114004. arXiv: 1001.5161 [gr-qc].

[133] I. Hinder, B. Wardell, and E. Bentivegna. "Falloff of the Weyl scalars in binary black hole spacetimes." In: *Phys. Rev. D* 84.2, 024036 (July 2011), p. 024036. arXiv: 1105.0781 [gr-qc].

[134] K. Hotokezaka, K. Kiuchi, K. Kyutoku, T. Muranushi, Y.-i. Sekiguchi, M. Shibata, and K. Taniguchi. "Remnant massive neutron stars of binary neutron star mergers: Evolution process and gravitational waveform." In: *Phys. Rev. D* 88.4, 044026 (Aug. 2013), p. 044026. arXiv: 1307.5888 [astro-ph.HE].

[135] K. Hotokezaka, K. Kiuchi, K. Kyutoku, H. Okawa, Y.-i. Sekiguchi, M. Shibata, and K. Taniguchi. "Mass ejection from the merger of binary neutron stars." In: *Phys. Rev. D* 87.2, 024001 (Jan. 2013), p. 024001. arXiv: 1212.0905 [astro-ph.HE].

[136] R. A. Hulse and J. H. Taylor. "Discovery of a pulsar in a binary system." In: *Astrophys. J. Lett.* 195 (Jan. 1975), pp. L51–L53.

[137] S. Husa, I. Hinder, and C. Lechner. "Kranc: a Mathematica package to generate numerical codes for tensorial evolution equations." In: *Computer Physics Communications* 174 (June 2006), pp. 983–1004. eprint: gr-qc/0404023.

[138] J. M. Hyman. "Method of lines solution of partial differential equations." In: (1976).

[139] P. B. Ivanov and A. F. Illarionov. "The oscillatory shape of the stationary twisted disc around a Kerr black hole." In: *Mon. Not. R. Astron. Soc.* 285 (Feb. 1997), pp. 394–402.

[140] H.-T. Janka, T. Eberl, M. Ruffert, and C. L. Fryer. "Black Hole-Neutron Star Mergers as Central Engines of Gamma-Ray Bursts." In: *Astrophys. J. Lett.* 527 (Dec. 1999), pp. L39–L42. eprint: astro-ph/9908290.

[141] J. L. Jaramillo and E. Gourgoulhon. "Mass and Angular Momentum in General Relativity." In: *Mass and Motion in General Relativity*. Ed. by L. Blanchet, A. Spallicci, and B. Whiting. 2011, pp. 87–124.

[142] W. Kastaun and F. Galeazzi. "Properties of hypermassive neutron stars formed in mergers of spinning binaries." In: *Phys. Rev. D* 91.6, 064027 (Mar. 2015), p. 064027. arXiv: 1411.7975 [gr-qc].

[143] J. Katz. "A note on Komar's anomalous factor." In: *Classical and Quantum Gravity* 2 (May 1985), pp. 423–425.

[144] K. Kawaguchi, K. Kyutoku, H. Nakano, H. Okawa, M. Shibata, and K. Taniguchi. "Black hole-neutron star binary merger: Dependence on black hole spin orientation and equation of state." In: *Phys. Rev. D* 92.2, 024014 (July 2015), p. 024014. arXiv: 1506.05473 [astro-ph.HE].

[145] R. P. Kerr. "Gravitational Field of a Spinning Mass as an Example of Algebraically Special Metrics." In: *Physical Review Letters* 11 (Sept. 1963), pp. 237–238.

[146] L. E. Kidder. "Coalescing binary systems of compact objects to (post)$^{5/2}$-Newtonian order. V. Spin effects." In: *Phys. Rev. D* 52 (July 1995), pp. 821–847. eprint: gr-qc/9506022.

[147] A. R. King, S. H. Lubow, G. I. Ogilvie, and J. E. Pringle. "Aligning spinning black holes and accretion discs." In: *Mon. Not. R. Astron. Soc.* 363 (Oct. 2005), pp. 49–56. eprint: astro-ph/0507098.

[148] K. Kiuchi, P. Cerdá-Durán, K. Kyutoku, Y. Sekiguchi, and M. Shibata. "Efficient magnetic-field amplification due to the Kelvin-Helmholtz instability in binary neutron star mergers." In: *Phys. Rev. D* 92.12, 124034 (Dec. 2015), p. 124034. arXiv: 1509.09205 [astro-ph.HE].

[149] K. Kiuchi, Y. Sekiguchi, K. Kyutoku, M. Shibata, K. Taniguchi, and T. Wada. "High resolution magnetohydrodynamic simulation of black hole-neutron star merger: Mass ejection and short gamma ray bursts." In: *Phys. Rev. D* 92.6, 064034 (Sept. 2015), p. 064034. arXiv: 1506.06811 [astro-ph.HE].

[150] K. Kiuchi, M. Shibata, P. J. Montero, and J. A. Font. "Gravitational Waves from the Papaloizou-Pringle Instability in Black-Hole-Torus Systems." In: *Physical Review Letters* 106.25, 251102 (June 2011), p. 251102. arXiv: 1105.5035 [astro-ph.HE].

[151] A. Komar. "Covariant Conservation Laws in General Relativity." In: *Physical Review* 113 (Feb. 1959), pp. 934–936.

[152] A. Komar. "Necessity of Singularities in the Solution of the Field Equations of General Relativity." In: *Physical Review* 104 (Oct. 1956), pp. 544–546.

[153] O. Korobkin, E. B. Abdikamalov, E. Schnetter, N. Stergioulas, and B. Zink. "Stability of general-relativistic accretion disks." In: *Phys. Rev. D* 83.4, 043007 (Feb. 2011), p. 043007. arXiv: 1011.3010 [astro-ph.HE].

[154] O. Korobkin, E. Abdikamalov, N. Stergioulas, E. Schnetter, B. Zink, S. Rosswog, and C. D. Ott. "The runaway instability in general relativistic accretion discs." In: *Mon. Not. R. Astron. Soc.* 431 (May 2013), pp. 349–354. arXiv: 1210.1214 [astro-ph.HE].

[155] Y. Kozai. "Secular perturbations of asteroids with high inclination and eccentricity." In: *Astrophys. J.* 67 (Nov. 1962), p. 591.

[156] D. Kramer and E. Schmutzer. *Exact solutions of Einstein's field equations*. 1980.

[157] L. Kreidberg, C. D. Bailyn, W. M. Farr, and V. Kalogera. "Mass Measurements of Black Holes in X-Ray Transients: Is There a Mass Gap?" In: *Astrophys. J.* 757, 36 (Sept. 2012), p. 36. arXiv: 1205.1805 [astro-ph.HE].

[158] H.-O. Kreiss and J. Lorenz. *Initial-boundary value problems and the Navier-Stokes equations*. Vol. 47. Siam, 1989.

[159] K. V. Kucha and C. G. Torre. "Gaussian reference fluid and interpretation of quantum geometrodynamics." In: *Phys. Rev. D* 43 (Jan. 1991), pp. 419–441.

[160] K. Kyutoku, H. Okawa, M. Shibata, and K. Taniguchi. "Gravitational waves from spinning black hole-neutron star binaries: dependence on black hole spins and on neutron star equations of state." In: *Phys. Rev. D* 84.6, 064018 (Sept. 2011), p. 064018. arXiv: 1108.1189 [astro-ph.HE].

[161] D. Lai and D. Tsang. "Corotational instability of inertial-acoustic modes in black hole accretion discs and quasi-periodic oscillations." In: *Mon. Not. R. Astron. Soc.* 393 (Mar. 2009), pp. 979–991. arXiv: 0810.0203.

[162] P. Lax and B. Wendroff. "Systems of conservation laws." In: *Commun. Pure Appl. Math.* 13.2 (1960), pp. 217–237.

[163] J. Lense and H. Thirring. "Über den Einfluß der Eigenrotation der Zentralkörper auf die Bewegung der Planeten und Monde nach der Einsteinschen Gravitationstheorie." In: *Physikalische Zeitschrift* 19 (1918).

[164] R. J. LeVeque. *Numerical methods for conservation laws*. Vol. 132. Springer, 1992.

[165] L.-X. Li, J. Goodman, and R. Narayan. "Nonaxisymmetric g-Mode and p-Mode Instability in a Hydrodynamic Thin Accretion Disk." In: *Astrophys. J.* 593 (Aug. 2003), pp. 980–991. eprint: astro-ph/0210455.

[166] J. Libson, J. Massó, E. Seidel, W.-M. Suen, and P. Walker. "Event horizons in numerical relativity: Methods and tests." In: *Phys. Rev. D* 53 (Apr. 1996), pp. 4335–4350. eprint: gr-qc/9412068.

[167] A. Lichnerowicz. "L'intégration des équations de la gravitation relativiste et le probleme des n corps." In: *J. Math. Pures Appl* 23.37 (1944), p. 4.

[168] M. L. Lidov. "The evolution of orbits of artificial satellites of planets under the action of gravitational perturbations of external bodies." In: *Planet. Space Sci.* 9 (Oct. 1962), pp. 719–759.

[169] LIGO Scientific Collaboration, J. Aasi, B. P. Abbott, R. Abbott, T. Abbott, M. R. Abernathy, K. Ackley, C. Adams, T. Adams, P. Addesso, and et al. "Advanced LIGO." In: *Classical and Quantum Gravity* 32.7, 074001 (Apr. 2015), p. 074001. arXiv: 1411.4547 [gr-qc].

[170] Y. T. Liu, Z. B. Etienne, and S. L. Shapiro. "Evolution of near-extremal-spin black holes using the moving puncture technique." In: *Phys. Rev. D* 80.12, 121503 (Dec. 2009), p. 121503. arXiv: 1001.4077 [gr-qc].

[171] F. Löffler, J. Faber, E. Bentivegna, T. Bode, P. Diener, R. Haas, I. Hinder, B. C. Mundim, C. D. Ott, E. Schnetter, G. Allen, M. Campanelli, and P. Laguna. "The Einstein Toolkit: a community computational infrastructure for relativistic astrophysics." In: *Classical and Quantum Gravity* 29.11, 115001 (June 2012), p. 115001. arXiv: 1111.3344 [gr-qc].

[172] F. Löffler, L. Rezzolla, and M. Ansorg. "Numerical evolutions of a black hole-neutron star system in full general relativity: Head-on collision." In: *Phys. Rev. D* 74.10, 104018 (Nov. 2006), p. 104018. eprint: gr-qc/0606104.

[173] C. O. Lousto, H. Nakano, Y. Zlochower, B. C. Mundim, and M. Campanelli. "Study of conformally flat initial data for highly spinning black holes and their early evolutions." In: *Phys. Rev. D* 85.12, 124013 (June 2012), p. 124013. arXiv: 1203.3223 [gr-qc].

[174] S. H. Lubow, G. I. Ogilvie, and J. E. Pringle. "The evolution of a warped disc around a Kerr black hole." In: *Mon. Not. R. Astron. Soc.* 337 (Dec. 2002), pp. 706–712. eprint: astro-ph/0208206.

[175] T. J. Maccarone. "On the misalignment of jets in microquasars." In: *Mon. Not. R. Astron. Soc.* 336 (Nov. 2002), pp. 1371–1376. eprint: astro-ph/0209105.

[176] A. I. MacFadyen and M. Milosavljević. "An Eccentric Circumbinary Accretion Disk and the Detection of Binary Massive Black Holes." In: *Astrophys. J.* 672, 83-93 (Jan. 2008), pp. 83–93. eprint: astro-ph/0607467.

[177] M. Machida and R. Matsumoto. "Excitation of Low-Frequency QPOs in Black-Hole Accretion Flows." In: *Publ. Astron. Soc. Jpn* 60 (June 2008), pp. 613–626. arXiv: 0802.3779.

[178] P. Marronetti, W. Tichy, B. Brügmann, J. González, and U. Sperhake. "High-spin binary black hole mergers." In: *Phys. Rev. D* 77.6, 064010 (Mar. 2008), p. 064010. arXiv: 0709.2160 [gr-qc].

[179] R. G. Martin, C. Nixon, S. H. Lubow, P. J. Armitage, D. J. Price, S. Doğan, and A. King. "The Kozai-Lidov Mechanism in Hydrodynamical Disks." In: *Astrophys. J. Lett.* 792, L33 (Sept. 2014), p. L33. arXiv: 1409.1226 [astro-ph.EP].

[180] F. Masset and M. Tagger. "Non-linear coupling of spiral waves in disk galaxies: a numerical study." In: *Astron. Astrophys.* 322 (June 1997), pp. 442–454. eprint: astro-ph/9902125.

[181] G. P. Mazur, O. Zanotti, A. Sądowski, B. Mishra, and W. Kluźniak. "Oscillations of radiation pressure supported tori near black holes." In: *Mon. Not. R. Astron. Soc.* 456 (Mar. 2016), pp. 3245–3252. arXiv: 1510.08810 [astro-ph.HE].

[182] M. Méndez, M. van der Klis, E. C. Ford, R. Wijnands, and J. van Paradijs. "Dependence of the Frequency of the Kilohertz Quasi-periodic Oscillationson X-Ray Count Rate and Colors in 4U 1608-52." In: *Astrophys. J. Lett.* 511 (Jan. 1999), pp. L49–L52. eprint: astro-ph/9811261.

[183] D. Merritt and E. Vasiliev. "Spin evolution of supermassive black holes and galactic nuclei." In: *Phys. Rev. D* 86.10, 102002 (Nov. 2012), p. 102002. arXiv: 1208.6274 [astro-ph.GA].

[184] V. Mewes, J. A. Font, and P. J. Montero. "Measuring the black hole spin direction in 3D Cartesian numerical relativity simulations." In: *Phys. Rev. D* 91.12, 124043 (June 2015), p. 124043. arXiv: 1505.07225 [gr-qc].

[185] V. Mewes, P. J. Montero, N. Stergioulas, F. Galeazzi, and J. A. Font. "General Relativistic Simulations of Accretion Disks Around Tilted Kerr Black Holes." In: *Astrophys. Space Sci. Proc.* 40 (2015). Springer International Publishing Cham, pp. 121–127.

[186] V. Mewes, J. A. Font, F. Galeazzi, P. J. Montero, and N. Stergioulas. "Numerical relativity simulations of thick accretion disks around tilted Kerr black holes." In: *Phys. Rev. D* 93 (6 Mar. 2016), p. 064055.

[187] J. Miller, L. Barsotti, S. Vitale, P. Fritschel, M. Evans, and D. Sigg. "Prospects for doubling the range of Advanced LIGO." In: *Phys. Rev. D* 91.6, 062005 (Mar. 2015), p. 062005. arXiv: 1410.5882 [gr-qc].

[188] B. Mishra, F. H. Vincent, A. Manousakis, P. C. Fragile, T. Paumard, and W. Kluźniak. "Quasi-periodic oscillations from relativistic hydrodynamical slender tori." In: *ArXiv e-prints* (Oct. 2015). arXiv: 1510.07414 [astro-ph.HE].

[189] V. Moncrief. "Gravitational perturbations of spherically symmetric systems. I. The exterior problem." In: *Annals of Physics* 88 (Dec. 1974), pp. 323–342.

[190] P. J. Montero, J. A. Font, and M. Shibata. "Influence of Self-Gravity on the Runaway Instability of Black-Hole-Torus Systems." In: *Physical Review Letters* 104.19, 191101 (May 2010), p. 191101. arXiv: 1004.3102 [gr-qc].

[191] P. J. Montero and O. Zanotti. "Oscillations of relativistic axisymmetric tori and implications for modelling kHz-QPOs in neutron star X-ray binaries." In: *Mon. Not. R. Astron. Soc.* 419 (Jan. 2012), pp. 1507–1514. arXiv: 1107.2546 [astro-ph.SR].

[192] P. Mösta, B. C. Mundim, J. A. Faber, R. Haas, S. C. Noble, T. Bode, F. Löffler, C. D. Ott, C. Reisswig, and E. Schnetter. "GRHydro: a new open-source general-relativistic magnetohydrodynamics code for the Einstein toolkit." In: *Classical and Quantum Gravity* 31.1, 015005 (Jan. 2014), p. 015005. arXiv: 1304.5544 [gr-qc].

[193] B. C. Mundim, B. J. Kelly, Y. Zlochower, H. Nakano, and M. Campanelli. "Hybrid black-hole binary initial data." In: *Classical and Quantum Gravity* 28.13, 134003 (July 2011), p. 134003. arXiv: 1012.0886 [gr-qc].

[194] A. Nagar and L. Rezzolla. "Gauge-invariant non-spherical metric perturbations of Schwarzschild black-hole spacetimes." In: *Classical and Quantum Gravity* 22 (Aug. 2005), R167–R192. eprint: gr-qc/0502064.

[195] K. Nakamura, T. Kajino, G. J. Mathews, S. Sato, and S. Harikae. "r-process nucleosynthesis in the MHD+neutrino-heated collapsar jet." In: *Astron. Astrophys.* 582, A34 (Oct. 2015), A34.

[196] T. Nakamura, K. Oohara, and Y. Kojima. "General Relativistic Collapse to Black Holes and Gravitational Waves from Black Holes." In: *Progress of Theoretical Physics Supplement* 90 (1987), pp. 1–218.

[197] R. Nealon, C. Nixon, D. J. Price, and A. King. "Apsidal precession, disc breaking and viscosity in warped discs." In: *Mon. Not. R. Astron. Soc.* 455 (Jan. 2016), pp. L62–L66. arXiv: 1510.02525 [astro-ph.HE].

[198] D. Neilsen, S. L. Liebling, M. Anderson, L. Lehner, E. O'Connor, and C. Palenzuela. "Magnetized neutron stars with realistic equations of state and neutrino cooling." In: *Phys. Rev. D* 89.10, 104029 (May 2014), p. 104029.

[199] R. P. Nelson and J. C. B. Papaloizou. "Hydrodynamic simulations of the Bardeen-Petterson effect." In: *Mon. Not. R. Astron. Soc.* 315 (July 2000), pp. 570–586. eprint: astro-ph/0001439.

[200] E. Newman and R. Penrose. "An Approach to Gravitational Radiation by a Method of Spin Coefficients." In: *Journal of Mathematical Physics* 3 (May 1962), pp. 566–578.

[201] N. Ó Murchadha and J. W. York. "Gravitational energy." In: *Phys. Rev. D* 10 (Oct. 1974), pp. 2345–2357.

[202] H. Okawa, H. Witek, and V. Cardoso. "Black holes and fundamental fields in numerical relativity: Initial data construction and evolution of bound states." In: *Phys. Rev. D* 89.10, 104032 (May 2014), p. 104032. arXiv: 1401.1548 [gr-qc].

[203] R. Owen. "Final remnant of binary black hole mergers: Multipolar analysis." In: *Phys. Rev. D* 80.8, 084012 (Oct. 2009), p. 084012. arXiv: 0907.0280 [gr-qc].

[204] J. C. B. Papaloizou and D. N. C. Lin. "Theory Of Accretion Disks I: Angular Momentum Transport Processes." In: *Annu. Rev. Astron. Astrophys.* 33 (1995), pp. 505–540.

[205] J. C. B. Papaloizou and J. E. Pringle. "The dynamical stability of differentially rotating discs. II." In: *Mon. Not. R. Astron. Soc.* 213 (Apr. 1985), pp. 799–820.

[206] J. C. B. Papaloizou and J. E. Pringle. "The dynamical stability of differentially rotating discs with constant specific angular momentum." In: *Mon. Not. R. Astron. Soc.* 208 (June 1984), pp. 721–750.

[207] V. Paschalidis, W. E. East, F. Pretorius, and S. L. Shapiro. "One-arm spiral instability in hypermassive neutron stars formed by dynamical-capture binary neutron star mergers." In: *Phys. Rev. D* 92.12, 121502 (Dec. 2015), p. 121502. arXiv: 1510.03432 [astro-ph.HE].

[208] V. Paschalidis, Y. T. Liu, Z. Etienne, and S. L. Shapiro. "Merger of binary white dwarf-neutron stars: Simulations in full general relativity." In: *Phys. Rev. D* 84.10, 104032 (Nov. 2011), p. 104032. arXiv: 1109.5177 [astro-ph.HE].

[209] V. Paschalidis, M. Ruiz, and S. L. Shapiro. "Relativistic Simulations of Black Hole-Neutron Star Coalescence: The Jet Emerges." In: *Astrophys. J. Lett.* 806, L14 (June 2015), p. L14. arXiv: 1410.7392 [astro-ph.HE].

[210] D. Pollney, C. Reisswig, E. Schnetter, N. Dorband, and P. Diener. "High accuracy binary black hole simulations with an extended wave zone." In: *Phys. Rev. D* 83.4, 044045 (Feb. 2011), p. 044045. arXiv: 0910.3803 [gr-qc].

[211] R. Popham, S. E. Woosley, and C. Fryer. "Hyperaccreting Black Holes and Gamma-Ray Bursts." In: *Astrophys. J.* 518 (June 1999), pp. 356–374. eprint: astro-ph/9807028.

[212] F. Pretorius. "Evolution of Binary Black-Hole Spacetimes." In: *Physical Review Letters* 95.12, 121101 (Sept. 2005), p. 121101. eprint: gr-qc/0507014.

[213] F. Pretorius. "Numerical relativity using a generalized harmonic decomposition." In: *Classical and Quantum Gravity* 22 (Jan. 2005), pp. 425–451. eprint: gr-qc/0407110.

[214] C. Raskin, E. Scannapieco, C. Fryer, G. Rockefeller, and F. X. Timmes. "Remnants of Binary White Dwarf Mergers." In: *Astrophys. J.* 746, 62 (Feb. 2012), p. 62. arXiv: 1112.1420 [astro-ph.HE].

[215] J. S. Read, C. Markakis, M. Shibata, K. Uryū, J. D. E. Creighton, and J. L. Friedman. "Measuring the neutron star equation of state with gravitational wave observations." In: *Phys. Rev. D* 79.12, 124033 (June 2009), p. 124033. arXiv: 0901.3258 [gr-qc].

[216] M. J. Rees. "Relativistic jets and beams in radio galaxies." In: *Nature* 275 (Oct. 1978), p. 516.

[217] M. J. Rees and P. Meszaros. "Unsteady outflow models for cosmological gamma-ray bursts." In: *Astrophys. J. Lett.* 430 (Aug. 1994), pp. L93–L96. eprint: astro-ph/9404038.

[218] G. Reifenberger and W. Tichy. "Alternatives to standard puncture initial data for binary black hole evolution." In: *Phys. Rev. D* 86.6, 064003 (Sept. 2012), p. 064003. arXiv: 1205.5502 [gr-qc].

[219] C. Reisswig, N. T. Bishop, D. Pollney, and B. Szilágyi. "Unambiguous Determination of Gravitational Waveforms from Binary Black Hole Mergers." In: *Physical Review Letters* 103.22, 221101 (Nov. 2009), p. 221101. arXiv: 0907.2637 [gr-qc].

[220] C. Reisswig, R. Haas, C. D. Ott, E. Abdikamalov, P. Mösta, D. Pollney, and E. Schnetter. "Three-dimensional general-relativistic hydrodynamic simulations of binary neutron star coalescence and stellar collapse with multipatch grids." In: *Phys. Rev. D* 87.6, 064023 (Mar. 2013), p. 064023. arXiv: 1212.1191 [astro-ph.HE].

[221] C. Reisswig, C. D. Ott, U. Sperhake, and E. Schnetter. "Gravitational wave extraction in simulations of rotating stellar core collapse." In: *Phys. Rev. D* 83.6, 064008 (Mar. 2011), p. 064008. arXiv: 1012.0595 [gr-qc].

[222] C. Reisswig and D. Pollney. "Notes on the integration of numerical relativity waveforms." In: *Classical and Quantum Gravity* 28.19, 195015 (Oct. 2011), p. 195015. arXiv: 1006.1632 [gr-qc].

[223] R. A. Remillard and J. E. McClintock. "X-Ray Properties of Black-Hole Binaries." In: *Annu. Rev. Astron. Astrophys.* 44 (Sept. 2006), pp. 49–92. eprint: astro-ph/0606352.

[224] L. Rezzolla, L. Baiotti, B. Giacomazzo, D. Link, and J. A. Font. "Accurate evolutions of unequal-mass neutron-star binaries: properties of the torus and short GRB engines." In: *Classical and Quantum Gravity* 27.11, 114105 (June 2010), p. 114105. arXiv: 1001.3074 [gr-qc].

[225] L. Rezzolla, S. Yoshida, T. J. Maccarone, and O. Zanotti. "A new simple model for high-frequency quasi-periodic oscillations in black hole candidates." In: *Mon. Not. R. Astron. Soc.* 344 (Sept. 2003), pp. L37–L41. eprint: astro-ph/0307487.

[226] P. L. Roe. "Approximate Riemann solvers, parameter vectors, and difference schemes." In: *J. Comp. Phys.* 43.2 (1981), pp. 357–372.

[227] C. Roedig, A. Sesana, M. Dotti, J. Cuadra, P. Amaro-Seoane, and F. Haardt. "Evolution of binary black holes in self gravitating discs. Dissecting the torques." In: *Astron. Astrophys.* 545, A127 (Sept. 2012), A127. arXiv: 1202.6063 [astro-ph.CO].

[228] N. Sanchis-Gual, J. C. Degollado, P. J. Montero, J. A. Font, and V. Mewes. "Quasistationary solutions of self-gravitating scalar fields around collapsing stars." In: *Phys. Rev. D* 92.8, 083001 (Oct. 2015), p. 083001. arXiv: 1507.08437 [gr-qc].

[229] N. Sanchis-Gual, P. J. Montero, J. A. Font, E. Müller, and T. W. Baumgarte. "Fully covariant and conformal formulation of the Z4 system in a reference-metric approach: Comparison with the BSSN formulation in spherical symmetry." In: *Phys. Rev. D* 89.10, 104033 (May 2014), p. 104033. arXiv: 1403.3653 [gr-qc].

[230] P. A. G. Scheuer and R. Feiler. "The realignment of a black hole misaligned with its accretion disc." In: *Mon. Not. R. Astron. Soc.* 282 (Sept. 1996), p. 291.

[231] E. Schnetter. "Time step size limitation introduced by the BSSN Gamma Driver." In: *Classical and Quantum Gravity* 27.16, 167001 (Aug. 2010), p. 167001. arXiv: 1003.0859 [gr-qc].

[232] E. Schnetter, P. Diener, E. N. Dorband, and M. Tiglio. "A multi-block infrastructure for three-dimensional time-dependent numerical relativity." In: *Classical and Quantum Gravity* 23 (Aug. 2006), S553–S578. eprint: gr-qc/0602104.

[233] E. Schnetter, S. H. Hawley, and I. Hawke. "Evolutions in 3D numerical relativity using fixed mesh refinement." In: *Classical and Quantum Gravity* 21 (Mar. 2004), pp. 1465–1488. eprint: gr-qc/0310042.

[234] E. Schnetter, B. Krishnan, and F. Beyer. "Introduction to dynamical horizons in numerical relativity." In: *Phys. Rev. D* 74.2, 024028 (July 2006), p. 024028. eprint: gr-qc/0604015.

[235] K. Schwarzschild. "Über das Gravitationsfeld eines Massenpunktes nach der Einsteinschen Theorie." In: *Sitzungsberichte der Königlich Preußischen Akad. der Wissenschaften* (1916).

[236] E. Seidel and W.-M. Suen. "Towards a singularity-proof scheme in numerical relativity." In: *Physical Review Letters* 69 (Sept. 1992), pp. 1845–1848. eprint: gr-qc/9210016.

[237] Y. Sekiguchi, K. Kiuchi, K. Kyutoku, and M. Shibata. "Dynamical mass ejection from binary neutron star mergers: Radiation-hydrodynamics study in general relativity." In: *Phys. Rev. D* 91.6, 064059 (Mar. 2015), p. 064059.

[238] J. M. M. Senovilla. “Singularity Theorems and Their Consequences.” In: *General Relativity and Gravitation* 30 (May 1998), pp. 701–848.

[239] S. L. Shapiro and S. A. Teukolsky. *Black Holes, White Dwarfs and Neutron Stars: The Physics of Compact Objects*. June 1986, p. 672.

[240] M. Shibata, M. D. Duez, Y. T. Liu, S. L. Shapiro, and B. C. Stephens. “Magnetized Hypermassive Neutron-Star Collapse: A Central Engine for Short Gamma-Ray Bursts.” In: *Physical Review Letters* 96.3, 031102 (Jan. 2006), p. 031102. eprint: astro-ph/0511142.

[241] M. Shibata and T. Nakamura. “Evolution of three-dimensional gravitational waves: Harmonic slicing case.” In: *Phys. Rev. D* 52 (Nov. 1995), pp. 5428–5444.

[242] M. Shibata and K. Taniguchi. “Coalescence of Black Hole-Neutron Star Binaries.” In: *Living Reviews in Relativity* 14 (Aug. 2011).

[243] M. Shibata and K. Uryū. “Merger of black hole-neutron star binaries: Nonspinning black hole case.” In: *Phys. Rev. D* 74.12, 121503 (Dec. 2006), p. 121503. eprint: gr-qc/0612142.

[244] M. Shibata and K. Uryū. “Simulation of merging binary neutron stars in full general relativity: $\Gamma=2$ case.” In: *Phys. Rev. D* 61.6, 064001 (Mar. 2000), p. 064001. eprint: gr-qc/9911058.

[245] H.-a. Shinkai and G. Yoneda. “Re-formulating the Einstein equations for stable numerical simulations: Formulation Problem in Numerical Relativity.” In: *ArXiv General Relativity and Quantum Cosmology e-prints* (Sept. 2002). eprint: gr-qc/0209111.

[246] C.-W. Shu and S. Osher. “Efficient Implementation of Essentially Non-oscillatory Shock-Capturing Schemes.” In: *Journal of Computational Physics* 77 (Aug. 1988), pp. 439–471.

[247] L. Smarr. “Mass Formula for Kerr Black Holes.” In: *Physical Review Letters* 30 (Mar. 1973), pp. 521–521.

[248] L. Smarr and J. W. York Jr. “Kinematical conditions in the construction of spacetime.” In: *Phys. Rev. D* 17 (May 1978), pp. 2529–2551.

[249] N. Stergioulas. “Black hole spacetimes with self-gravitating, massive accretion tori.” In: *Journal of Physics Conference Series* 283.1, 012036 (Feb. 2011), p. 012036.

[250] N. Stone, A. Loeb, and E. Berger. “Pulsations in short gamma ray bursts from black hole-neutron star mergers.” In: *Phys. Rev. D* 87.8, 084053 (Apr. 2013), p. 084053. arXiv: 1209.4097 [astro-ph.HE].

[251] L. B. Szabados. “Quasi-Local Energy-Momentum and Angular Momentum in General Relativity.” In: *Living Reviews in Relativity* 12 (June 2009).

[252] B. Szilágyi, D. Pollney, L. Rezzolla, J. Thornburg, and J. Winicour. “An explicit harmonic code for black-hole evolution using excision.” In: *Classical and Quantum Gravity* 24 (June 2007), S275–S293. eprint: gr-qc/0612150.

[253] M. Tagger and P. Varnière. "Accretion-Ejection Instability, MHD Rossby Wave Instability, Diskoseismology, and the High-Frequency QPOs of Microquasars." In: *Astrophys. J.* 652 (Dec. 2006), pp. 1457–1465. eprint: astro-ph/0608123.

[254] J. H. Taylor and J. M. Weisberg. "A new test of general relativity - Gravitational radiation and the binary pulsar PSR 1913+16." In: *Astrophys. J.* 253 (Feb. 1982), pp. 908–920.

[255] J. Thornburg. "A Fast Apparent-Horizon Finder for 3-Dimensional Cartesian Grids in Numerical Relativity." In: *The Astrophysics of Gravitational Wave Sources*. Ed. by J. M. Centrella. Vol. 686. American Institute of Physics Conference Series. Oct. 2003, pp. 247–252.

[256] J. Thornburg. "Event and Apparent Horizon Finders for 3+1 Numerical Relativity." In: *Living Reviews in Relativity* 10 (June 2007).

[257] J. Thornburg, P. Diener, D. Pollney, L. Rezzolla, E. Schnetter, E. Seidel, and R. Takahashi. "Are moving punctures equivalent to moving black holes?" In: *Classical and Quantum Gravity* 24 (Aug. 2007), pp. 3911–3918. eprint: gr-qc/0701038.

[258] A. Toomre. "On the gravitational stability of a disk of stars." In: *Astrophys. J.* 139 (May 1964), pp. 1217–1238.

[259] E. F. Toro. *Riemann solvers and numerical methods for fluid dynamics: a practical introduction*. Springer Science & Business Media, 2013.

[260] C. Travaglio, W. Hillebrandt, M. Reinecke, and F.-K. Thielemann. "Nucleosynthesis in multi-dimensional SN Ia explosions." In: *Astron. Astrophys.* 425 (Oct. 2004), pp. 1029–1040. eprint: astro-ph/0406281.

[261] M. Ugliano, H.-T. Janka, A. Marek, and A. Arcones. "Progenitor-explosion Connection and Remnant Birth Masses for Neutrino-driven Supernovae of Iron-core Progenitors." In: *Astrophys. J.* 757, 69 (Sept. 2012), p. 69. arXiv: 1205.3657 [astro-ph.SR].

[262] M. van der Klis. "Rapid X-ray Variability." In: *Compact stellar X-ray sources*. Ed. by W. H. G. Lewin and M. van der Klis. Apr. 2006, pp. 39–112.

[263] J. R. van Meter, J. G. Baker, M. Koppitz, and D.-I. Choi. "How to move a black hole without excision: Gauge conditions for the numerical evolution of a moving puncture." In: *Phys. Rev. D* 73.12, 124011 (June 2006), p. 124011. eprint: gr-qc/0605030.

[264] J. van Paradijs, W. Penninx, and W. H. G. Lewin. "On the relation between X-ray burst properties and the persistent X-ray luminosity." In: *Mon. Not. R. Astron. Soc.* 233 (July 1988), pp. 437–450.

[265] M. H. van Putten. "Proposed Source of Gravitational Radiation from a Torus around a Black Hole." In: *Physical Review Letters* 87.9, 091101 (Aug. 2001), p. 091101. eprint: astro-ph/0107007.

[266] E. Velikhov. "Stability of an ideally conducting liquid flowing between rotating cylinders in a magnetic field." In: *Zhur. Eksptl'. i Teoret. Fiz.* 36 (1959).

[267] M. Visser. "The Kerr spacetime: A brief introduction." In: (June 2007). arXiv: 0706.0622.

[268] R. M. Wald and V. Iyer. "Trapped surfaces in the Schwarzschild geometry and cosmic censorship." In: *Phys. Rev. D* 44 (Dec. 1991), R3719–R3722.

[269] S. Weinberg. *Gravitation and cosmology: principles and applications of the general theory of relativity*. Vol. 1. Wiley New York, 1972.

[270] J. Winicour. "Characteristic Evolution and Matching." In: *Living Reviews in Relativity* 15 (Jan. 2012).

[271] L. Witten. "Gravitation: An introduction to current research." In: (1961).

[272] S. E. Woosley. "Gamma-ray bursts from stellar mass accretion disks around black holes." In: *Astrophys. J.* 405 (Mar. 1993), pp. 273–277.

[273] X. I. Yang and R. Mittal. "Acceleration of the Jacobi iterative method by factors exceeding 100 using scheduled relaxation." In: *Journal of Computational Physics* 274 (2014), pp. 695–708.

[274] H.-J. Yo, T. W. Baumgarte, and S. L. Shapiro. "Improved numerical stability of stationary black hole evolution calculations." In: *Phys. Rev. D* 66.8, 084026 (Oct. 2002), p. 084026. eprint: gr-qc/0209066.

[275] J. W. York Jr. "Initial data for collisions of black holes and other gravitational miscellany." In: *Frontiers in Numerical Relativity*. Ed. by C. R. Evans, L. S. Finn, and D. W. Hobill. 1989, pp. 89–109.

[276] E. Zeidler. *Quantum Field Theory III: Gauge Theory: A Bridge between Mathematicians and Physicists*. Springer Science & Business Media, 2011.

[277] X.-L. Zhou, W. Yuan, H.-W. Pan, and Z. Liu. "Universal Scaling of the 3:2 Twin-peak Quasi-periodic Oscillation Frequencies With Black Hole Mass and Spin Revisited." In: *Astrophys. J. Lett.* 798, L5 (Jan. 2015), p. L5. arXiv: 1411.7731 [astro-ph.HE].

[278] M. Zimmermann and E. Szedenits Jr. "Gravitational waves from rotating and precessing rigid bodies - Simple models and applications to pulsars." In: *Phys. Rev. D* 20 (July 1979), pp. 351–355.

[279] Y. Zlochower, M. Ponce, and C. O. Lousto. "Accuracy issues for numerical waveforms." In: *Phys. Rev. D* 86.10, 104056 (Nov. 2012), p. 104056. arXiv: 1208.5494 [gr-qc].

[280] W. H. Zurek and W. Benz. "Redistribution of angular momentum by nonaxisymmetric instabilities in a thick accretion disk." In: *Astrophys. J.* 308 (Sept. 1986), pp. 123–133.